Bioinspired by Nature, Designed for Flow: Engineering Functional Interfaces for Small-Caliber Vascular Grafts

Gabriele Obino

ISBN: 978-94-93483-96-5

Printed by Proefschrift specialist

Bioinspired by Nature, Designed for Flow: Engineering Functional Interfaces for Small-Caliber Vascular Grafts

Dissertation

to obtain the degree of Doctor at Maastricht University, on the authority of the Rector Magnificus, Prof. Dr. Pamela Habibović, and the degree of Doctor in Life Sciences and Biotechnologies at the University of Sassari, on the authority of the Rector Prof. Gavino Mariotti,
in accordance with the decision of the Board of Deans,
to be defended in public on Wednesday 18th March 2026 at 10:00 hours

by

Gabriele Obino

Supervisors
Prof. Dr. Lorenzo Moroni (Maastricht University, the Netherlands)
Dr. Antonio Junior Lepedda (University of Sassari, Italy)

Assessment Committee
Chair:
Prof. Dr. Martijn van Griensven (Maastricht University, the
Netherlands)

Members:
Dr. Claudia Crosio (University of Sassari, Italy)
Prof. Dr. Abhay Pandit (National University of Galway, Ireland)
Prof. Dr. Joris Ivo Rotmans (Leiden University Medical Centre
Netherlands)
Dr. Niloofar Tahmasebi Birgani (Maastricht University, the
Netherlands)

Table of Contents

		Page
Chapter 1	General Introduction	7
Chapter 2	Marine Sulfated Polysaccharides as Biofunctional Agents for Enhancing Hemocompatibility and Endothelialization of Tissue-Engineered Vascular Grafts	15
Chapter 3	Purification of an acidic polysaccharide with anticoagulant activity from the marine sponge *Sarcotragus spinosulus*	47
Chapter 4	Marine-Derived Sulfated Polysaccharides Enhance Hemocompatibility and Endothelialization of Nanofibrous PCL for Vascular Graft applications	77
Chapter 5	Tunable Bioresorbable Scaffolds with Marine Sulfated Polysaccharides for SmallCaliber Vascular Grafts: A Multi-Layered Strategy Combining Electrospinning and 4-Axis Printing	121
Chapter 6	Incorporation of Notoginsenoside Fc into PCL Scaffolds to Enhance Endothelialization and Inhibit Platelet Aggregation	179
Chapter 7	General discussion	209
Chapter 8	Thesis Impact	225
Appendix	Summary/Samenvatting Acknowledgments Publications Biography	235

Chapter 1
General Introduction

This chapter presents an overview of the research conducted during this PhD and a summary of the experimental work described in the following chapters

Introduction

Cardiovascular diseases remain the leading cause of death worldwide, accounting for an estimated 19.4 million deaths per year [1]. Among them, coronary artery disease (CAD) and peripheral artery disease (PAD) are major conditions requiring surgical interventions that often involve the replacement or bypass of blood vessels [2,3]. When the affected vessels have an internal diameter smaller than 6 mm—commonly defined as small-caliber blood vessels—their replacement poses a critical clinical challenge [4].

Currently, the gold standard for vascular replacement is the use of autologous grafts, most frequently the internal mammary artery (IMA) or the saphenous vein. These grafts are widely used in coronary artery bypass grafting (CABG) and peripheral artery bypass surgery [5]. However, not all patients are suitable candidates for autologous transplantation due to prior harvesting, poor vessel quality, or comorbidities such as diabetes, advanced age, or vascular disease. In these cases, the therapeutic options are severely limited. When autologous vessels are unavailable, patients often rely on aggressive pharmacological management with antiplatelet or anticoagulant therapies, which are not always effective and may be contraindicated due to bleeding risks, heparin-induced thrombocytopenia, or drug intolerance.

For large-diameter vessels such as the aorta, synthetic prostheses made of polyethylene terephthalate (Dacron®) or expanded polytetrafluoroethylene (ePTFE, Gore-Tex®) are routinely used with high success rates. These materials exhibit good long-term performance in high-flow, large-diameter settings, where the risk of thrombosis is relatively low. However, their use in small-caliber applications has been largely unsuccessful due to rapid thrombus formation, intimal hyperplasia, and low long-term patency [6]. In fact, grafts below 6 mm in diameter almost invariably fail within months after implantation.

Given these limitations, tissue engineering has emerged as the most promising strategy to create functional and durable small caliber blood vessel substitutes [7]. The goal is to fabricate bioresorbable scaffolds capable of providing initial mechanical support while offering a hemocompatible surface that encourages host cell adhesion, infiltration, and remodeling. Over time, the scaffold should degrade and be replaced by native extracellular matrix (ECM), ultimately giving rise to a living, functional blood vessel.

The development of small-caliber blood vessels substitutes remains particularly demanding owing to the stringent physiological and biomechanical requirements that an ideal graft must fulfill. Foremost among

these is the need for a non-thrombogenic lumen surface capable of preventing platelet adhesion, activation, and subsequent thrombus formation [6]. In addition, the mechanical compliance of the graft must be carefully tailored to closely match that of the native vessel to avoid flow disturbances and the onset of intimal hyperplasia, with the optimal compliance varying between veins, elastic arteries, and muscular arteries. Adequate suture retention and burst strength are also critical to ensure sufficient mechanical integrity for safe surgical handling without risk of tearing [8]. Simultaneously, the graft must provide adequate leak tightness to prevent blood leakage, while maintaining controlled porosity that enables cellular infiltration and supports gradual vascular remodeling. Finally, the scaffold material must exhibit both biocompatibility and the capacity to undergo constructive remodeling by promoting complete endothelialization, smooth muscle cell colonization, and extracellular matrix deposition, while degrading at a rate that remains synchronized with neotissue formation. The greatest remaining challenge lies in the engineering of a hemocompatible luminal surface that directly prevents thrombosis, while indirectly achieving this through complete and rapid endothelialization [6].

To address this challenge, multiple strategies have been explored. Surface modifications, including heparin coatings [9], nitric oxide (NO)-releasing molecules [10], and antithrombotic peptides, reduce platelet adhesion and thrombus formation while enhancing endothelial cell (EC) proliferation and function. Biofunctionalization approaches, such as immobilization of cell-adhesive peptides, growth factors (e.g., VEGF), and protein coatings, selectively promote EC adhesion and accelerate endothelialization. Material innovations, including hydrogels, alternative fiber orientations, and novel polymers, improve hemocompatibility and support EC growth. Pre-endothelialized grafts, seeded with endothelial or progenitor cells, including induced pluripotent stem cells (iPSCs) derived cells, show promise for *in situ* endothelialization but face translational and scalability challenges [4]. Despite these advances, no single approach has yet yielded a fully effective and clinically reliable small-caliber vascular graft. Achieving a stable, confluent endothelial layer that simultaneously resists thrombosis and replicates native vessel behavior remains the central challenge.

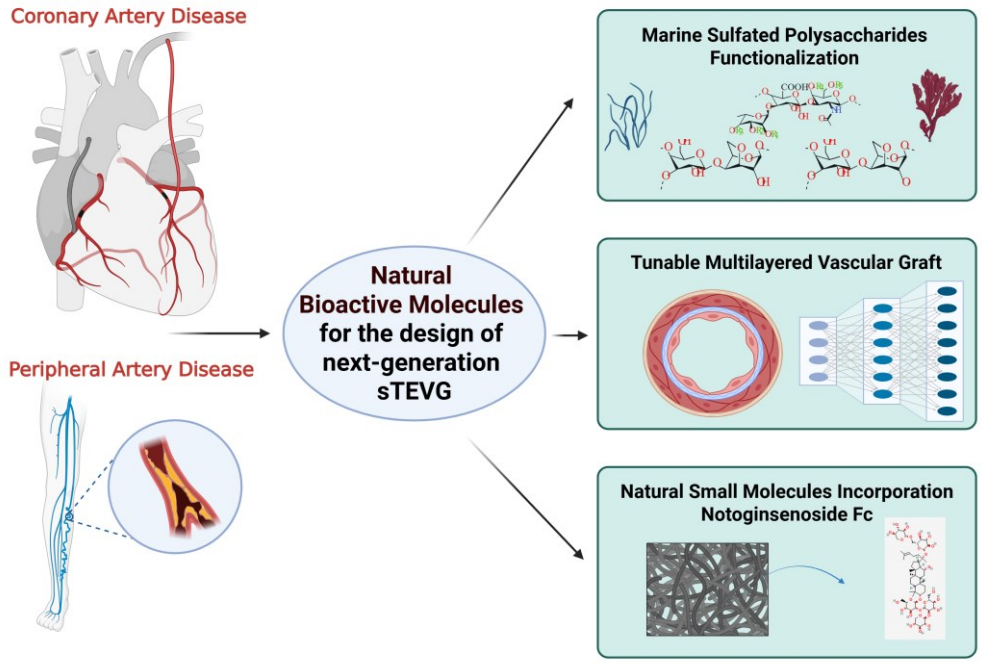

Figure 1.1. Conceptual overview of next-generation small-caliber tissue-engineered vascular grafts (sTEVGs) integrating natural bioactive molecules. Strategies include marine sulfated polysaccharides functionalization, tunable multilayered graft design, and incorporation of small molecules such as Notoginsenoside Fc to enhance hemocompatibility and regeneration in cardiovascular diseases. Figure partially created with BioRender.com under academic license.

This thesis investigates the use of marine sulfated polysaccharides (MSPs) and other natural bioactive molecules for the design of next-generation small-caliber vascular grafts (Figure 1.1). Specifically:

Chapter 2 provides a comprehensive review of MSPs as biofunctional agents for enhancing hemocompatibility and endothelialization in tissue-engineered vascular grafts. MSPs, including fucoidans, carrageenans, and fucosylated chondroitin sulfates (FCS), have attracted increasing attention due to their structural resemblance to glycosaminoglycans such as heparin, which endows them with anticoagulant, anti-inflammatory, and pro-endothelial properties. Sourced from marine organisms such as sea cucumbers (*Holothuria tubulosa*) and sponges (*Sarcotragus spinosulus*), these molecules can interfere with multiple steps of the coagulation cascade, reduce platelet adhesion, and mimic

the endothelial glycocalyx. Importantly, they can be sustainably sourced from marine environments, offering a viable alternative to other bioactive sulfated polysaccharides.

Chapter 3 reports the purification and structural characterization of anticoagulant MSPs from *Holothuria tubulosa* and *Sarcotragus spinosulus*, and evaluates their anticoagulant activity. Using anion exchange chromatography, different fractions of sulfated polysaccharides were isolated, and their molecular structure, anticoagulant activity, and preliminary cytotoxicity on human dermal fibroblasts were assessed. Two fractions demonstrated strong anticoagulant activity comparable to unfractionated heparin and were selected for further functional studies in Chapter 4.

Chapter 4 describes the functionalization of electrospun poly(ε-caprolactone) (PCL) scaffolds with the selected MSP fractions. Functionalized scaffolds exhibited enhanced hemocompatibility, as shown by reduced platelet adhesion, and improved endothelialization, achieving complete endothelial cell coverage within 2–4 days. Importantly, the anticoagulant activity observed in solution was preserved after scaffold functionalization, as confirmed by aPTT and PT assays. These results demonstrate that MSPs can be used to design an engineered surface that improves both hemocompatibility and endothelialization of electrospun PCL scaffolds, establishing a foundation for vascular scaffold fabrication.

Chapter 5 presents the development of multilayer bioresorbable vascular grafts with MSP-functionalized PCL. By combining electrospinning with 4-axis printing, scaffolds with tunable mechanical properties, high burst strength, and structural integrity suitable for arterial applications were produced. The study also examined smooth muscle cells, as well as endothelial cells, behavior on these grafts. While heparin-functionalized scaffolds inhibited SMC proliferation and induced disorganized morphology, MSP-functionalized scaffolds supported SMC spreading, alignment, and contractile phenotype, with abundant α-SMA fibers. These findings indicate that MSP-functionalized grafts not only promote rapid endothelialization, but also support stable medial integration, addressing two critical requirements for long-term graft patency and function.

Chapter 6 explores an additional strategy for enhancing hemocompatibility and biocompatibility by embedding Notoginsenoside Fc (NgFc), a natural saponin, into electrospun PCL scaffolds for controlled release. This chapter provides proof of concept for NgFc as a bioactive agent to improve anti-thrombogenicity. Future work will focus on optimizing NgFc release through

polymer blending and combining it with established agents such as heparin or fucosylated chondroitin sulfate to further enhance graft performance.
Chapter 7 places the main findings of this thesis in the context of the current state of the art, discussing their significance and highlighting the remaining challenges for clinical translation of these vascular constructs. Future directions to advance the field are also proposed. Finally, **Chapter 8** outlines the scientific and societal impact of the work presented, emphasizing its potential contribution to vascular tissue engineering and regenerative medicine.

References

[1] Martin SS, Aday AW, Allen NB, Almarzooq ZI, Anderson CAM, Arora P, et al. 2025 Heart Disease and Stroke Statistics: A Report of US and Global Data From the American Heart Association. Circulation. 151 (2025). https://doi.org/10.1161/CIR.0000000000001303.

[2] R. Bauersachs, U. Zeymer, J.B. Brière, C. Marre, K. Bowrin, M. Huelsebeck, Burden of Coronary Artery Disease and Peripheral Artery Disease: A Literature Review, Cardiovasc Ther 2019 (2019). https://doi.org/10.1155/2019/8295054.

[3] M. Drozd, M. Pujades-Rodriguez, F. Sun, K.N. Franks, P.J. Lillie, K.K. Witte, M.T. Kearney, R.M. Cubbon, Causes of death in people with cardiovascular disease: A uk biobank cohort study, J Am Heart Assoc 10 (2021). https://doi.org/10.1161/JAHA.121.023188.

[4] J. Ji, H. Xu, C. Li, J. Luo, Small-Caliber Tissue-Engineered Vascular Grafts Based on Human-Induced Pluripotent Stem Cells: Progress and Challenges, Tissue Eng Part B Rev 29 (2023) 441–455. https://doi.org/10.1089/ten.teb.2023.0005.

[5] R. Scott, E.H. Blackstone, P.M. McCarthy, B.W. Lytle, F.D. Loop, J.A. White, D.M. Cosgrove, Isolated bypass grafting of the left internal thoracic artery to the left anterior descending coronary artery late consequences of incomplete revascularization, Journal of Thoracic and Cardiovascular Surgery 120 (2000) 173–184. https://doi.org/10.1067/mtc.2000.107280.

[6] Y. Zhuang, C. Zhang, M. Cheng, J. Huang, Q. Liu, G. Yuan, K. Lin, H. Yu, Challenges and strategies for in situ endothelialization and long-term lumen patency of vascular grafts, Bioact Mater 6 (2021) 1791–1809. https://doi.org/10.1016/j.bioactmat.2020.11.028.

[7] M.X. Li, Q.Q. Wei, H.L. Mo, Y. Ren, W. Zhang, H.J. Lu, Y.K. Joung, Challenges and advances in materials and fabrication technologies of small-diameter vascular grafts, Biomater Res 27 (2023). https://doi.org/10.1186/s40824-023-00399-2.

[8] D.B. Camasão, D. Mantovani, The mechanical characterization of blood vessels and their substitutes in the continuous quest for physiological-relevant performances. A critical review, Mater Today Bio 10 (2021). https://doi.org/10.1016/j.mtbio.2021.100106.

[9] S.Y. Zhou, L. Li, E. Xie, M.X. Li, J.H. Cao, X. Bin Yang, D.Y. Wu, Small-diameter PCL/PU vascular graft modified with heparin-aspirin compound for preventing the occurrence of acute thrombosis, Int J Biol Macromol 249 (2023). https://doi.org/10.1016/j.ijbiomac.2023.126058.

[10] H. Zhang, G.M. Annich, J. Miskulin, K. Osterholzer, S.I. Merz, R.H. Bartlett, M.E. Meyerhoff, Nitric oxide releasing silicone rubbers with improved blood compatibility: preparation, characterization, and in vivo evaluation, 2002.

Chapter 2
Marine Sulfated Polysaccharides as Biofunctional Agents for Enhancing Hemocompatibility and Endothelialization of Tissue-Engineered Vascular Grafts.

Gabriele Obino [a,b], Antonio J. Lepedda [a] and Lorenzo Moroni [b].

[a]Department of Biomedical Sciences, University of Sassari, Viale San Pietro, 43b, 07100 Sassari, Italy
[b]MERLN Institute for Technology-Inspired Regenerative Medicine, Complex Tissue Regeneration Department, Maastricht University, 6200 MD Maastricht, The Netherlands

Abstract

Small-diameter vascular grafts (≤6 mm) continue to face high failure rates due to thrombosis, intimal hyperplasia, and inadequate endothelialization. While bioresorbable and hybrid materials offer promising alternatives to conventional prostheses, challenges in hemocompatibility and host integration remain. Marine sulfated polysaccharides (MSPs)—including fucoidans, carrageenans, and fucosylated chondroitin sulfates—have emerged as biofunctional agents capable of modulating coagulation, inflammation, and vascular cell behavior. These structurally diverse, highly sulfated glycans mimic features of the native endothelial glycocalyx, enabling interactions with coagulation factors and promoting endothelial regeneration. This review brings together current insights into MSPs structure–function relationships, anticoagulant mechanisms, and endothelial support, and discusses how these features can be strategically harnessed for vascular graft design and clinical translation. We examine recent strategies for MSPs functionalization of electrospun and 3D-printed scaffolds and evaluate emerging evidence from in vitro and in vivo studies. Finally, we explore current challenges and future directions for the clinical application of MSP-functionalized vascular biomaterials. Collectively, these insights position marine sulfated polysaccharides as a versatile and underexplored class of biomolecules with the potential to address long-standing barriers in vascular tissue engineering.

Keywords

Marine sulfated polysaccharides (MSPs); Fucosylated chondroitin sulfate (FCS); Small-diameter vascular graft (sTEVG); Vascular regeneration; Scaffold biofunctionalization; Hemocompatibility

Introduction

The development of small-diameter (≤6 mm) tissue engineered vascular grafts (sTEVG) remains a critical and unresolved challenge in cardiovascular tissue engineering [1,2]. Conventional synthetic prostheses, such as expanded polytetrafluoroethylene (ePTFE) and Dacron, frequently fail due to early thrombosis, intimal hyperplasia, and insufficient endothelialization [3,4], resulting in low long-term patency rates [5,6]. Various strategies have been pursued to improve hemocompatibility of vascular prostheses, including the functionalization of graft surfaces with anticoagulant agents [7], mainly

heparin [8]; yet, these approaches have only marginally improved clinical outcomes [9]. Resorbable small-caliber grafts have emerged as a promising alternative, offering the potential for *in situ* tissue regeneration through host cell recruitment and extracellular matrix (ECM) deposition, while supporting endothelialization to reduce thrombotic risk [10,11]. However, their clinical translation has been hindered by limitations such as the lack of reliable autologous cell sources, immunogenicity, and incomplete integration with host tissue. Additionally, many synthetic resorbable materials exhibit poor endothelial cell colonization and a high thrombogenic profile [12–15]. To address these shortcomings, hybrid constructs combining synthetic polymers with natural materials have been developed, which improve cell adhesion but often compromise mechanical performance and fail to fully address thrombogenicity [16–18]. Mechanical integrity and degradation kinetics must be precisely tuned: vascular grafts must retain sufficient structural strength to support early neo-tissue formation while degrading in a manner that permits timely cell infiltration and ECM remodeling. Compliance mismatch between the graft and native vessels further contributes to long-term failure, highlighting the need for biomaterials that recapitulate the biomechanical properties of native vessels [19–24].

Despite significant advances in antithrombotic pharmacotherapy and surface engineering, the development of durable, off-the-shelf vascular grafts that fully replicate the biological and functional performance of native vessels is challenging using current materials [10,11,25]. One emerging strategy is the biofunctionalization of vascular scaffolds with bioactive molecules that mimic the extracellular environment and actively modulate host responses [26]. Among these, marine-derived sulfated polysaccharides—including fucoidans, fucosylated chondroitin sulfate, and carrageenans—have attracted growing interest due to their structural similarities to glycosaminoglycans found in vertebrates, such as heparin, and their wide-ranging biological activities [27]. Sourced from diverse marine invertebrates and algae—including echinoderms, sponges, and seaweeds—these polysaccharides possess unique sulfation patterns and carbohydrate backbones [28,29], which account for the anticoagulant [30], antithrombotic [31,32], anti-inflammatory [33], pro-endothelial [34] or anti-tumoral [35] properties. Their evolutionary adaptation in extreme marine environments has given rise to structurally diverse, highly bioactive compounds, many of which are amenable to scalable extraction or

synthetic optimization. Unlike mammalian heparin, marine-derived polysaccharides offer additional advantages such as reduced immunogenicity, non-mammalian origin, and distinctive biologically functional profiles.

This review synthesizes recent advances in the use of marine sulfated polysaccharides (MSPs) as biofunctional agents for vascular biomaterials. We examine their sources, structural features, and mechanisms of hemocompatibility, along with strategies for their incorporation into tissue-engineered vascular scaffolds. Finally, we discuss translational challenges and future directions, positioning these marine biopolymers as promising candidates in the development of next-generation, bioactive vascular grafts.

Marine Sulfated Polysaccharides: Sources and Structural Features

To address the still unmet challenges of effective sTEVG development, research has increasingly turned to naturally derived bioactive materials. Among these, MSPs stand out for their structural resemblance to glycosaminoglycans and their ability to regulate vascular responses. The following section provides an overview of their marine origins and distinctive structural features.

Origins and Diversity

MSPs are a structurally diverse class of biomolecules derived from a wide array of marine organisms, including brown and red algae, sea cucumbers, and sponges (Figure 1). Each class is characterized by distinct monosaccharide compositions, bonding motifs, and sulfation patterns that underline their unique biological activities [36,37].

Among the most studied are fucoidans, primarily extracted from brown seaweeds such as *Fucus vesiculosus*, *Laminaria digitata*, *Saccharina latissima*, and *Cladosiphon okamuranus* [38–40]. These polysaccharides are typically rich in α-L-fucose residues, which are variably substituted with O-sulfate groups, giving rise to highly branched, heterogeneous structures.

Carrageenans, another major group, are linear sulfated galactans found in red algae (phylum *Rhodophyta*) [41] such as *Chondrus crispus*, *Eucheuma spp*., *Gigartina stellata*, *Iridaea*, *Hypnea*, *Solieria*, *Agardhiella*, and *Sarconema* [42,43]. They consist of repeating disaccharide units of D-galactose linked via

alternating β-(1→4) and α-(1→3) glycosidic bonds, with sulfation ranging from zero to three sulfate groups per disaccharide.

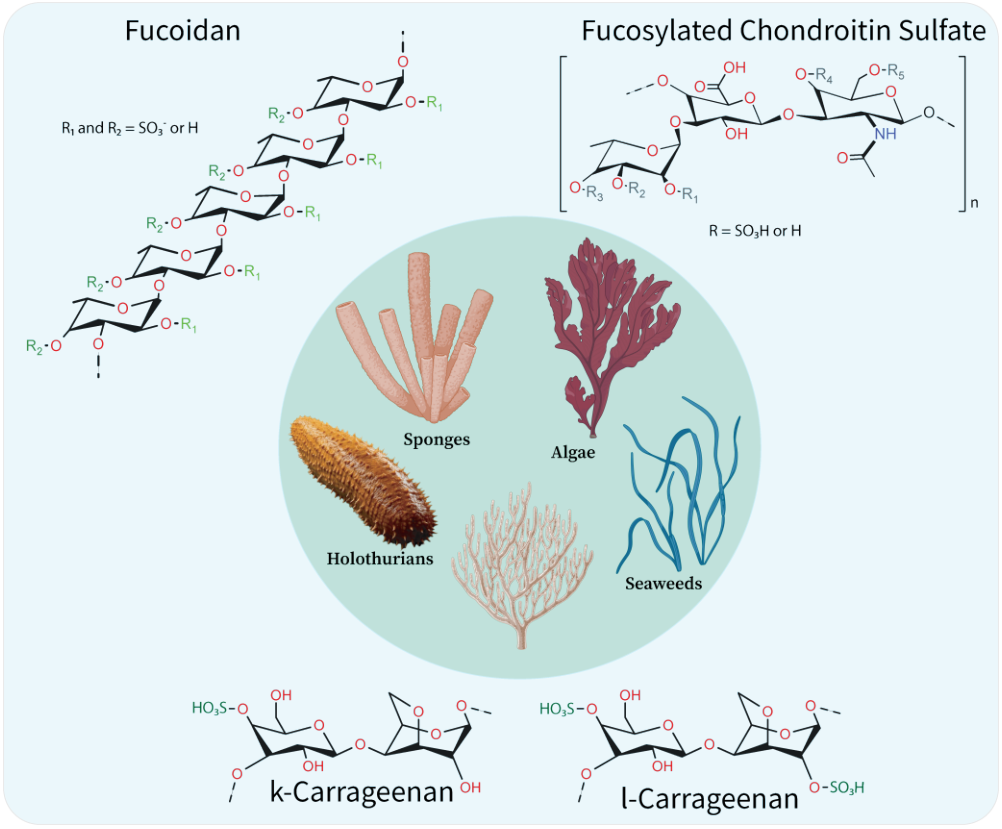

Figure 2.1. Representative chemical structures and marine sources of sulfated polysaccharides. Marine-derived glycans, including fucoidan, fucosylated chondroitin sulfate, and carrageenans (κ- and ι-forms), exhibit structural diversity arising from variable sulfation patterns, glycosidic linkages, and monosaccharide compositions. These polysaccharides are predominantly extracted from algae, seaweeds, sponges, and holothurians, and have attracted increasing attention due to their broad spectrum of bioactivities. Figure partially created with BioRender.com under academic license.

At least ten structurally distinct carrageenan types have been identified, each with specific biological and rheological properties [44].
Arguably, the most structurally complex and biologically potent MSPs are the fucosylated chondroitin sulfates (FCS), primarily sourced from sea cucumbers (class *Holothuroidea*) [45]. These unique glycosaminoglycans consist of a

chondroitin sulfate backbone composed of repeating disaccharide units of β-D-glucuronic acid and N-acetylgalactosamine, branched with sulfated α-L-fucose residues at defined positions [46]. FCSs display species-specific structural variation, particularly in the degree and position of sulfation—commonly at the 2-O, 4-O, and 6-O positions of fucose and backbone sugars—which greatly influence their bioactivity. A growing number of sea cucumber species have been characterized as FCS sources, including *Holothuria tubulosa* [30], *Holothuria stellati* [47], *Massinium magnum* [48], *Holothuria scabra* [49], *Eupentacta fraudatrix* [50], *Cucumaria frondosa* [51], *Cucumaria syracusana* [52], *Acaudina leucoprocta* [53], *Holothuria leucospilota* [54], *Holothuria Mexicana* [55], *Apostichopus japonicus, Actinopyga mauritiana* [56], *Stichopus chloronotus, Stichopus horrens* [57] *and Hemioedema spectabilis* [58]. Considering their wide array of biological activities, FCS oligosaccharides have also been chemically synthetized [59]

Marine GAGs and GAG-mimetics (such as sulfated fucans and galactans) display a much broader range of monosaccharide composition, sulfation patterns, and backbone structures than mammalian GAGs, even within the same class of molecule [60]. This diversity is especially pronounced in marine invertebrates and algae, leading to unique and structurally distinct polysaccharides compared to their mammalian counterparts [61,62]. Their sulfate content varies widely—fucoidans, for example, can contain between 9% and 40% sulfate by weight, depending on species, seasonal factors, and extraction methodologies [63]. Their molecular weights are equally diverse, spanning from tens to several hundred kilodaltons, contributing to variability in physicochemical and biological properties. In contrast, mammalian heparin—the clinical gold standard for anticoagulation—is a relatively well-defined GAG composed of repeating disaccharide units of α-L-iduronic acid (or β-D-glucuronic acid) and α-D-glucosamine, with specific sulfation at the N-, 2-O-, and 6-O-positions. Despite some batch-to-batch variability and the presence of minor GAG contaminants, pharmaceutical-grade heparin displays a much narrower structural and functional profile [64]. By comparison, marine polysaccharides feature a broader array of carbohydrate backbones and sulfation motifs. Fucoidans typically consist of α-(1→3)- and/or α-(1→4)-linked L-fucose units bearing sulfate groups at the 2-O, 3-O, and 4-O positions [65]. Carrageenans, with alternating α- and β-galactose residues, can possess up to three sulfate groups per disaccharide, leading to highly anionic structures [43,66]. FCSs exhibit a chondroitin sulfate core with 3-linked, variably

sulfated α-L-fucose branches, often carrying multiple sulfates at distinct positions (e.g., 2-O, 3-O, 4-O) on both the side chains and the backbone [45].

Table 1. Overview of the main structural motifs and anticoagulant activities of representative sulfated polysaccharides. Marine-derived polysaccharides such as fucoidan, carrageenan, and fucosylated chondroitin sulfate display diverse backbones and sulfation patterns compared with mammalian heparin, resulting in variable anticoagulant potency.

Polysaccharide	***Source***	***Backbone***	***Sulfation Pattern***	***Anticoagulant Activity***
Fucoidan *[39]*	Brown algae	α-L-Fucan (1→3, 1→4)	Variable (C2, C4 sulfation)	Generally high
Carrageenan *[42,43]*	Red algae	Alternating D-galactose (α(1→3), β(1→4))	0–3 sulfates per disaccharide	Low–moderate (κ/ι/λ vary)
Fucosylated Chondroitin Sulfate *[30,45,46]*	Sea cucumber	Chondroitin sulfate core + sulfated α-L-Fuc branches	Fucose: 2-*O*,4-*O*,6-*O* sulfation; core: 4-*O*,6-*O*	High (effective ATIII/HCII activation)
Heparin *[67]*	Mammalian (pig intestines)	α-L-iduronic acid or β-D-glucuronic acid + *N*-acetylated glucosamine or *N*-sulfated glucosamine	Highly sulfated: 2-*O*,6-*O*, N-sulfation	Very high
Acidic Glycogen *[68]*	Aplysina fulva (Sea sponge)	(1→4)-linked α-D-Glc (90%) +HexUA (10%)	5% of Sulfated D-Glc; 50% of sulfated non-reducing ends	Not yet investigated

This diversity in monosaccharide composition, glycosidic linkages, and sulfation patterns underpins the broad spectrum of biological activities observed for marine-derived sulfated polysaccharides, particularly in modulating coagulation, inflammation, and endothelial function. A comparative overview of key structural motifs and associated anticoagulant activities is presented in Table 1.

Structure–Anticoagulation Relationships

As the structure plays a defining role in bioactivity, the mechanistic basis of MSPs anticoagulant function lies in their specific interactions with the coagulation cascade and platelets. How do these glycans influence clotting pathways and cellular responses at the blood–material interface? The structural diversity of MSPs—reflected in their sugar backbones, molecular weights, and sulfation motifs—is key to their functional behavior [69]. The anticoagulant potency of MSPs is closely linked to their structural features, particularly the degree and pattern of sulfation. Higher sulfate content generally enhances anticoagulant activity, but the specific position of sulfate groups on sugar residues is also critical. For example, sulfation at certain positions (such as C-2/C-4 of rhamnose or galactose units) significantly increases the ability to inhibit coagulation factors [70–74]. The molecular weight of these polysaccharides also plays a role: higher molecular weight fractions tend to show stronger anticoagulant effects, while depolymerization can reduce activity [59,73–75]. Additionally, unique structural motifs—such as the presence of L-fucose branching, and uronic acid residues—can modulate binding to coagulation proteins and influence the mechanism of action [76–79]. In particular, the 2,4-disulfated fucosyl branches [80,81] and mostly the sulfation at position 4 of the fucosyl branches is important for coagulation inhibition, as suggested by computational studies [82].

Specific Interactions with the Coagulation Cascade

Blood coagulation is a tightly regulated cascade of enzymatic reactions that culminates in the formation of a stable fibrin clot (Figure 2). This cascade is classically divided into three interconnected pathways: the intrinsic, extrinsic, and common pathways. The extrinsic pathway is rapidly activated by external trauma that exposes tissue factor (TF) to circulating factor VII, forming a TF–VIIa complex that directly activates factor X. The intrinsic pathway, on the other hand, is initiated by contact with negatively charged surfaces, leading to sequential activation of factors XII, XI, IX, and VIII, ultimately converging at factor X. Both pathways feed into the common pathway, where activated factor X (Xa) converts prothrombin (factor II) into thrombin (factor IIa), which in turn converts fibrinogen into fibrin, forming the structural backbone of a clot [83,84]. MSPs exert anticoagulant effects primarily by potentiating serpin inhibitors such as antithrombin III (ATIII) and heparin cofactor II (HCII), leading to accelerated inhibition of thrombin (factor IIa) and factor Xa within the common pathway [85–87]. Certain sulfated galactoarabinan and

arabinogalactan structures from green algae strongly inhibit intrinsic pathway factors (XII, XI, IX, VIII) and promote thrombin and factor Xa inhibition via ATIII and HCII [71,72,88].

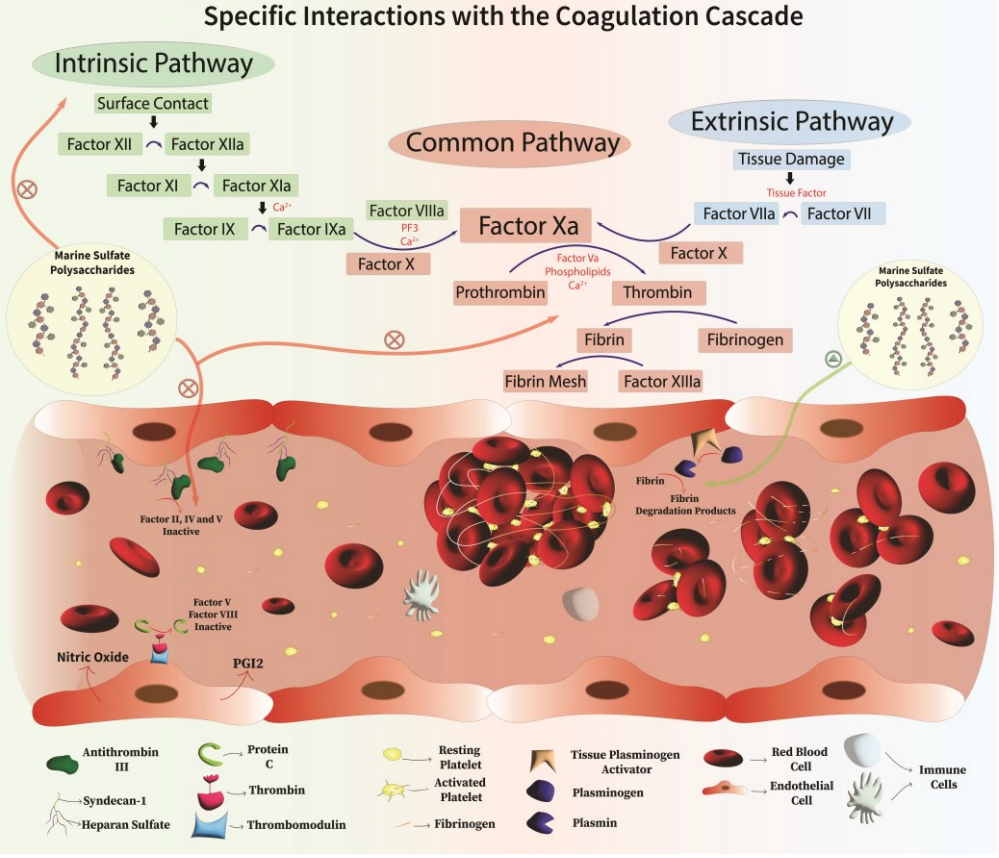

Figure 2.2. Schematic representation of the coagulation cascade and the modulatory effects of MSPs. The coagulation process proceeds through two main initiation routes—the intrinsic pathway (triggered by surface contact) and the extrinsic pathway (activated by tissue damage)—which converge at the common pathway, leading to the activation of Factor Xa and subsequent conversion of prothrombin to thrombin. Thrombin then cleaves fibrinogen into fibrin, which polymerizes into a fibrin mesh stabilized by Factor XIIIa, ultimately resulting in clot formation. MSPs can interfere with this process at multiple stages, particularly by inhibiting thrombin generation, Factor Xa activity, and fibrin formation, thereby reducing clot stability.

Some MSPs also enhance plasminogen activation, contributing to thrombolytic activity and clot breakdown [74,89]. While initial attraction is largely electrostatic, specific binding and activation are regulated by the stereochemical properties of the polysaccharide, including sulfation pattern, degree of sulfation, and backbone structure, rather than simply overall negative charge [72,90,91].

Effects on Platelet Adhesion and Aggregation

MSPs exhibit anticoagulant activity not only through interactions with coagulation cascade proteins but also by significantly inhibiting platelet adhesion and aggregation (Figure 3). Unlike native vascular endothelium, biomaterial surfaces lack natural adhesive ligands and rapidly adsorb plasma proteins upon blood contact (the Vroman effect), including fibrinogen, albumin, fibronectin, and von Willebrand factor (vWF). The conformation of these adsorbed proteins—particularly fibrinogen—is a key determinant of platelet adhesion. Current evidence indicates that platelet adhesion is governed more by protein conformational changes than by the absolute amount of protein adsorbed. Unfolded fibrinogen exposes cryptic binding sites for platelet integrins, notably αIIbβ3, which can result in stronger platelet adhesion compared to native tissue [12,92–94].

Although GpIb–vWF interactions can still occur if vWF is adsorbed and partially unfolded on the biomaterial surface, platelet adhesion on artificial materials is often dominated by direct fibrinogen–integrin interactions due to the higher plasma concentration of fibrinogen. In native vessels, the initial tethering of platelets under flow is mediated by GpIbα binding to the A1 domain of vWF immobilized on collagen. On biomaterials, this mechanism is less prominent unless vWF is appropriately adsorbed and conformationally active. Surface characteristics—such as chemistry, roughness, and hydrophobicity—strongly influence protein adsorption and conformation, thereby modulating platelet adhesion. Strategies including hydrophilic coatings, nanoscale topographies, and endothelialization (e.g., HUVEC monolayers) have been shown to mitigate platelet adhesion by maintaining protein conformation or replicating the antithrombotic properties of native endothelium [95–98].

MSPs also interfere with P-selectin-mediated interactions and collagen-induced platelet activation. By attenuating P-selectin–dependent platelet–

leukocyte crosstalk, MSPs can reduce downstream vascular inflammation and thrombus propagation. This dual functionality—combining anticoagulant and anti-inflammatory effects—positions MSPs as promising biologically functional agents for vascular grafts and other blood-contacting devices [99–101]. While P-selectin is not directly involved in the initial platelet adhesion to surfaces, its expression on activated platelets and endothelial cells plays a critical role in later stages of thrombus formation and in linking platelet activation to immune cell recruitment via P-selectin Glycoprotein Ligand-1 (PSGL-1).

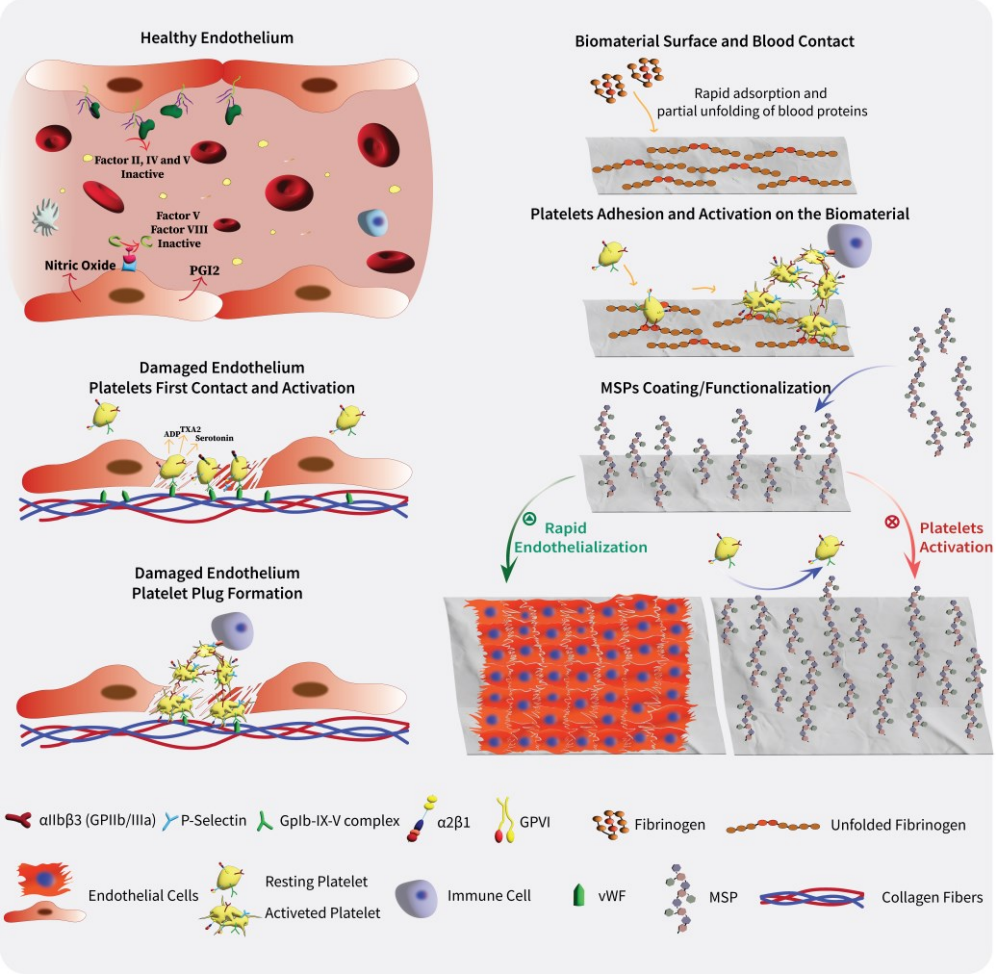

Figure 2.3. Comparison of hemostatic responses in healthy endothelium versus biomaterial surfaces, and the modulatory role of MSPs. Under

physiological conditions, the healthy endothelium maintains blood fluidity by releasing nitric oxide (NO) and prostacyclin (PGI_2), and by keeping coagulation factors (II, IV, and V) in their inactive state, thereby preventing platelet activation. In contrast, endothelial damage exposes subendothelial collagen, triggering platelet adhesion through receptors such as GPIb-IX-V, αIIbβ3, α2β1, and GPVI, followed by platelet activation and platelet plug formation. Similarly, when blood contacts a biomaterial surface, rapid adsorption and partial unfolding of plasma proteins (e.g., fibrinogen, von Willebrand factor) initiate platelet adhesion and activation, potentially leading to thrombus formation. Functionalization of biomaterials with MSPs can modulate this response: (i) by inhibiting platelet adhesion and activation, reducing thrombotic risk, and (ii) by promoting rapid endothelialization, thereby restoring an antithrombotic surface similar to native endothelium. This dual mechanism highlights the therapeutic relevance of MSPs-based coatings for the development of hemocompatible vascular grafts.

Modulation of endothelialization

Marine sulfated polysaccharides exhibit structural similarities to mammalian glycosaminoglycans (GAGs) but possess distinct sulfation patterns and carbohydrate backbones that confer potent anticoagulant properties [102]. Beyond their role in coagulation, these polysaccharides have also been shown to promote endothelial cell adhesion, proliferation, and functional maturation [103]. Earlier mechanistic studies on related sulfated glycoconjugates—particularly sulfatides—demonstrated that these molecules can mediate cell adhesion through highly specific interactions with extracellular matrix proteins such as laminin and thrombospondin [104]. These interactions are not merely adhesive but functionally significant: sulfatide–laminin binding supports both cell attachment and spreading, whereas sulfatide–thrombospondin binding enables initial adhesion without promoting cell spreading, suggesting distinct roles in regulating cellular behavior [105]. Such findings underscore that sulfated glycolipids and polysaccharides do not act as passive structural elements, but instead actively modulate cellular responses through selective, structure-dependent recognition of matrix components. This supports the emerging view that marine sulfated polysaccharides can serve as functional analogs of the endothelial glycocalyx, influencing not only hemocompatibility but also vascular regeneration.

Immunomodulation and Inflammatory Control

Beyond hemocompatibility, marine sulfated polysaccharides (MSPs) exhibit notable immunomodulatory activity [106], a key factor in the success of vascular implants. Effective immunoregulation is essential in vascular tissue engineering, where promoting M2 macrophage polarization—linked to anti-inflammatory and tissue-regenerative functions—while suppressing the pro-inflammatory M1 phenotype, is critical for constructive remodeling [107,108]. Certain fucoidans have been shown to modulate macrophage phenotype and reduce pro-inflammatory cytokine expression to levels comparable to the anti-inflammatory cytokine IL-10, suggesting a role in dampening post-implantation inflammation [109]. Additionally, MSPs can interact directly with immune cells: sulfated glycans from marine sources have been reported to bind specific receptors on macrophages and lymphocytes, triggering intracellular signaling cascades that modulate immune cell proliferation and cytokine production [110–112]. These immunoregulatory functions may help mitigate the foreign body response, enhance tissue remodeling, and support long-term graft acceptance.

Pro-Angiogenic Support via Growth Factor Modulation

The capacity of MSPs to modulate pro-angiogenic signaling also holds relevance for graft integration and long-term function. Several MSPs, particularly fucoidans, have demonstrated the ability to bind and stabilize key angiogenic growth factors such as vascular endothelial growth factor (VEGF) and fibroblast growth factor (FGF). By mimicking heparan sulfate, fucoidans prolong the half-life of these growth factors and enhance their receptor-mediated signaling [113,114].

In the context of TEVGs, such interactions may support the recruitment of endothelial cells to the graft lumen and promote localized neovascularization at the graft–host interface—processes essential for restoring perfusion and promoting functional anastomosis. Experimental studies have shown that fucoidan can enhance endothelial cell tube formation *in vitro* and stimulate neovascularization *in vivo* [115,116], reinforcing its potential role in improving vascular integration of bioengineered grafts.

Scientific Potential and Therapeutic Promise

Multiple *in vitro* and *in vivo* studies show low toxicity and good cell compatibility of MSP, making them suitable for biomedical applications

[117,118]. Marine sulfated polysaccharides (MSPs) represent a compelling alternative to conventional anticoagulants like heparin, offering multiple advantages. Sourced from marine algae and invertebrates rather than mammalians, such as swine or bovine, they avoid risks of zoonotic contamination, prion transmission, and batch variability commonly associated with mammalian-derived heparin [119–121]. Moreover, MSPs exhibit high structural diversity, particularly in their sulfation patterns and molecular weights, which allows for the fine-tuning of anticoagulant potency and specificity—for example, selectively enhancing inhibition of factor Xa or thrombin (IIa) depending on sulfation degree and position [39,74].

MSPs such as fucoidan, generally, demonstrate low intrinsic toxicity and may present a lower bleeding risk compared to unfractionated heparin, making them attractive candidates for safer anticoagulant therapies. This is because their anticoagulant effect is mediated by weaker, multi-target interactions —such as partial inhibition of thrombin or factor Xa via both antithrombin III (ATIII) and heparin cofactor II (HCII) rather than the strong, high-affinity binding seen with heparin, reducing the risk of uncontrolled bleeding [122,123]. Low molecular weight fucoidan (LMWF) fractions often exhibit additional antiplatelet or antiproliferative effects, by interfering with P-selectin–mediated platelet adhesion. LMWF also inhibits growth factor signaling in vascular smooth muscle cells, contributing to antiproliferative effects and potentially reducing restenosis risk after vascular injury [124,125].

Importantly, their reduced risk of heparin-induced thrombocytopenia (HIT), combined with customizable bioactivity, positions marine polysaccharides as promising scaffolds for the next generation of anticoagulant and vascular graft functionalization strategies. Ongoing research into their structure–function relationships and mechanistic pathways will be critical to unlocking their full therapeutic potential and accelerating their translation into clinical applications.

Given their unique structural features and multifunctional bioactivity, MSPs are increasingly recognized as promising candidates for applications in regenerative medicine and biomedical engineering. In particular, their integration into surface-modified sTEVG has attracted growing interest as a strategy to overcome some of the major limitations associated with current synthetic grafts—specifically, early thrombosis, poor endothelialization, and inflammation. This review specifically highlights the potential of MSPs to bio-

functionalize the luminal surface of sTEVG, leveraging their anticoagulant and anti-platelet aggregation properties to mitigate thrombus formation. The highly anionic character of these polysaccharides, resulting from dense and site-specific sulfation, closely mimics the negative charge of the native endothelial glycocalyx, which plays a pivotal role in preventing activation of the intrinsic coagulation cascade [126,127]. By emulating this natural biochemical barrier, MSPs may exert targeted anticoagulant effects without provoking off-target coagulation or systemic anticoagulation side effects. Their structural motifs are thought to support selective interactions with coagulation factors (e.g., thrombin, factor Xa) while minimizing nonspecific protein adsorption and activation [128]. In addition to their hemocompatibility, MSPs can contribute to a bioactive microenvironment conducive to vascular regeneration. Their negatively charged domains, similarly to heparin, may be capable of binding and stabilizing —in an active conformation— pro-angiogenic growth factors such as VEGF and FGF, enhancing local bioavailability and promoting endothelial cell recruitment and proliferation [91,129,130]. Furthermore, their carbohydrate-rich surfaces may provide specific adhesion sites for integrin-mediated cell attachment and colonization, further supporting endothelialization of the graft.

Importantly, several MSPs also exhibit anti-inflammatory and antimicrobial properties, which could help reduce post-implantation inflammation and prevent graft-related infections—two critical complications in the long-term success of vascular implants [1]. The stereochemistry and sulfation patterns of MSPs are central to these biointeractions, supporting the view that these marine-derived molecules can act as functional analogs of the endothelial surface, offering a versatile and tunable platform for next-generation vascular biomaterials.

Marine Sulfated Polysaccharides Integration into Vascular Grafts

Realizing the therapeutic promise of MSPs requires effective integration into vascular scaffold systems. In the following sections, we highlight current approaches for functionalizing sTEVGs with MSPs and evaluate how these designs influence biological performance and clinical applicability. Marine sulfated glycans – especially fucoidans and FCS – provide a potent

combination of antithrombotic and pro-endothelial cues that can be leveraged to improve small-diameter vascular grafts [34].

Scaffold Technologies for MSPs Integration: Advantages and Features

Electrospinning and 3D printing techniques offer unique advantages for the fabrication of engineered vascular grafts with MSP integration. Electrospinning generates nanofibrous scaffolds with high surface-to-volume ratios, mimicking the architecture of the native extracellular matrix and providing abundant binding sites for sulfated polysaccharides and for cell colonization [5,25]. 3D printing, on the other hand, enables precise control of lumen geometry, porosity, and multilayer architectures, which are essential to balance mechanical strength with endothelialization potential [131]. Together, these technologies produce reproducible, tunable supports that can stably incorporate MSPs while preserving compliance and long-term patency features that are difficult to achieve with conventional vascular prostheses.

Functionalization Strategies for MSP Integration

Engineering the luminal surface of vascular grafts with MSPs has already yielded promising results, with several studies demonstrating comparable or superior performance to traditional heparin-based coatings in terms of inhibition of platelet activation and hemocompatibility [34,132].

To harness the bioactivity of marine sulfated polysaccharides, researchers have developed a variety of graft functionalization strategies. One notable example involves the covalent incorporation of fucoidan into poly(vinyl alcohol) (PVA) hydrogels using sodium trimetaphosphate (STMP) as a crosslinking agent, resulting in a stable PVA–fucoidan composite that preserves the native mechanical properties of the polymer [133]. This functionalization significantly enhanced endothelial cell adhesion and proliferation while reducing platelet adhesion and thrombin generation *in vitro*. Moreover, in a rabbit carotid artery model, the fucoidan-functionalized grafts achieved superior patency compared to commercial ePTFE grafts after one month of implantation, demonstrating the translational potential of this approach [133]. Similarly, Bračič et al. studied the use of fucoidan and carrageenan, when applied as surface coatings on polyester substrates, effectively reduced nonspecific protein adsorption and mitigated thrombogenic activation. However, their capacity to support endothelial cell proliferation and exert direct anticoagulant effects *in vitro* was more limited than that of heparin and

dextran sulfate coatings, which offered a more favorable balance between hemocompatibility and endothelialization [134].

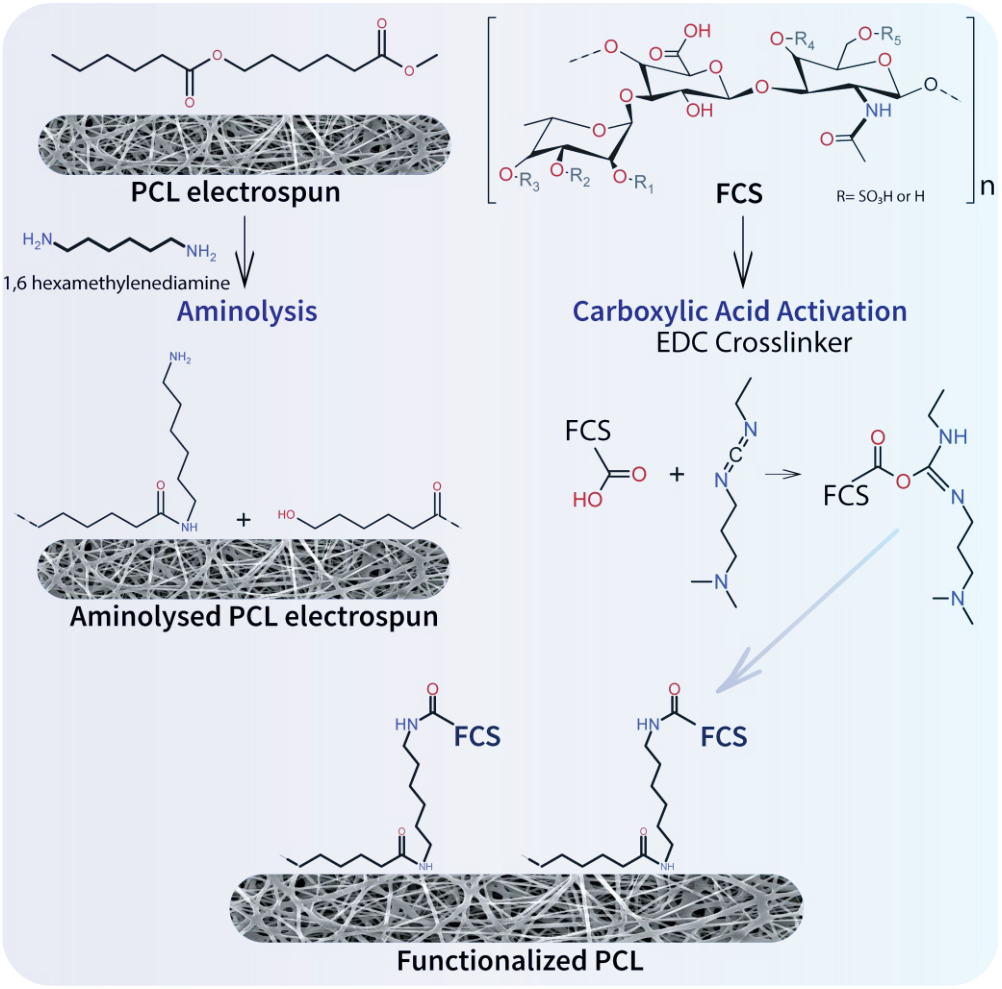

Figure 2.4. Schematic representation of PCL electrospun scaffold functionalization with sulfated polysaccharides. PCL fibers are first subjected to aminolysis using 1,6-hexamethylenediamine, introducing surface amine groups. In parallel, sulfated polysaccharides (FCS) are activated at their carboxylic acid residues via EDC crosslinking chemistry. The activated polysaccharides are then covalently conjugated to the aminolyzed PCL scaffold, resulting in a functionalized surface presenting bioactive FCS motifs.

This difference may reflect the lower degree or distinct pattern of sulfation in fucoidan and carrageenan, which could reduce their ability to bind and present growth factors or coagulation mediators as effectively as FCS or heparin. In another strategy, polyelectrolyte multilayers composed of laminin and fucoidan were constructed via layer-by-layer (LbL) self-assembly. These constructs used fucoidan as the terminal layer to minimize platelet adhesion, while laminin-rich surfaces promoted HUVEC attachment and spreading [135]. Recently, FCS from *Holothuria tubulosa*, along with a structurally related sulfated polysaccharide from the sponge *Sarcotragus spinosulus*, were covalently bound to electrospun PCL scaffolds via EDC/NHS chemistry (Figure 4). This chemical modification generated a stable, hydrophilic, and negatively charged surface that mimics key features of the native endothelial glycocalyx. The resulting scaffolds significantly reduced platelet adhesion and supported endothelial cell viability and monolayer formation, further demonstrating the potential of MSPs to enhance both hemocompatibility and endothelialization in small-diameter vascular grafts [34]. While simple physical adsorption or dip-coating can confer bioactivity, these methods typically yield weaker surface retention and limited durability. The choice between covalent binding, LbL assembly, or adsorption should be guided by the desired stability, release profile, and functional longevity of the graft.

In Vitro Studies

Recent *in vitro* studies have demonstrated that MSPs can be efficiently and stably immobilized on electrospun PCL scaffolds, yielding marked improvements in hemocompatibility and endothelialization. For example, chemically crosslinked FCS from *Holothuria tubulosa* and a sulfated polysaccharide from *Sarcotragus spinosulus* were shown to significantly accelerate the formation of a confluent endothelial monolayer compared with unmodified PCL or PCL functionalized with unfractionated porcine heparin. In addition to enhanced endothelial coverage, MSPs-functionalized scaffolds exhibited a pronounced reduction in platelet adhesion and activation [34]. A very recent study by the same team further highlighted the impact of surface chemistry on vascular cell behavior [131]. The authors, who developed a tunable multi-layered PCL-based sTEVG functionalized with FCS from *Holothuria tubulosa,* evidenced as, while heparin-functionalized grafts inhibited SMC proliferation and induced a spherical cell morphology with disorganized cytoskeletal architecture, consistent with literature [136,137],

FCS-modified scaffolds supported robust SMC spreading, alignment, and contractile phenotype, with abundant α-SMA fibers, as well as the formation of a mature endothelium on the luminal surface. Together, these findings suggest that MSP functionalized vascular grafts not only promote rapid endothelialization but also foster stable medial integration, addressing two critical requirements for long-term graft patency and function [131].

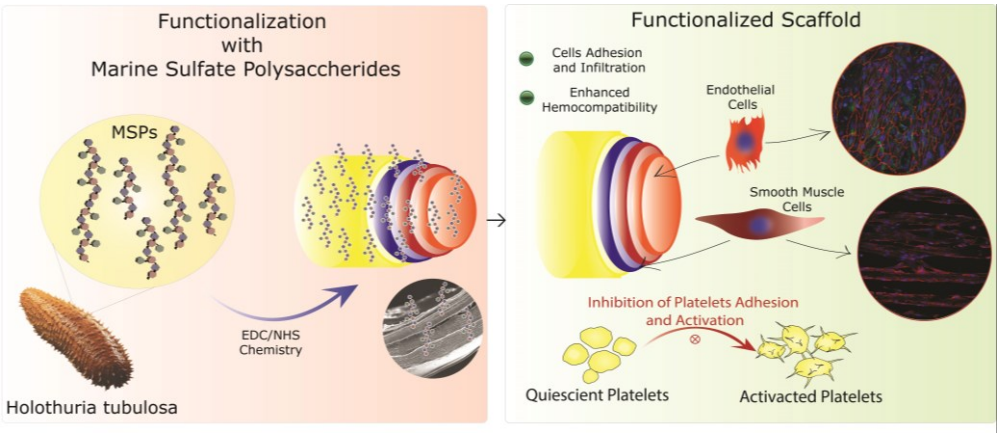

Figure 2.5. Functionalization of multi-layered vascular scaffolds, obtained by a combination of electrospinning and 4-Axis printing, with MSPs. Covalent crosslink of MSPs from *Holothuria tubulosa* onto polymeric scaffolds (EDC/NHS chemistry) creates a bioactive interface that inhibits platelet activation while driving endothelialization and smooth muscle cell integration, key determinants of long-term graft patency (modified from Obino et al [34,131]).

In Vivo Evidence and Translational Progress

While the integration of MSPs into sTEVGs remains at an early stage, emerging *in vivo* evidence indicates encouraging translational potential. In a rabbit carotid artery model, fucoidan-functionalized polyvinyl alcohol (PVA) grafts maintained full patency and supported endothelialization, whereas unmodified grafts occluded rapidly due to thrombotic events. Moreover, fucoidan-coated grafts significantly reduced intimal hyperplasia, suggesting improved vascular healing and remodeling [133]. In a subsequent study by the same team, the combination of fucoidan functionalization with luminal micro-gratings further enhanced in situ endothelialization, resulting in substantially

increased endothelial coverage along the graft lumen and improved graft patency in the same rabbit carotid artery model [138]. These findings underscore the translational relevance of integrating MPS-based biochemical cues with topographical guidance to overcome the limited endothelialization of synthetic vascular grafts. Similarly, by short-term implantation in chick chorioallantoic membrane, fucoidan–PCL nanofibrous meshes were shown to promote angiogenesis, further supporting the regenerative potential of MSP-based materials [103].

A critical translational requirement is the preservation of mechanical integrity following MSP incorporation. Encouragingly, MSPs functionalization—whether via surface adsorption, covalent conjugation, or blending—does not compromise graft mechanical properties within the ranges tested. Fucoidan incorporation did not alter the crosslinking density or tensile strength of PVA scaffolds [133], and electrospun PCL grafts retained porosity and burst strength after MSP coating [131].

From a regulatory and clinical perspective, MSPs-functionalized grafts benefit from inherent biodegradability and favorable blood-contact compatibility. MSPs such as fucoidan and fucosylated chondroitin sulfate are naturally cleared by enzymatic degradation and exhibit minimal cytotoxicity, immunogenicity, or allergenicity in preliminary studies. However, rigorous preclinical evaluation remains essential to confirm long-term safety, particularly regarding immunomodulation and degradation byproducts.

Manufacturing challenges persist, notably batch-to-batch consistency, endotoxin-free purification, and precise characterization of sulfation and molecular weight. These hurdles are magnified when sourcing MSPs from wild marine organisms; this issue could be overcome by a sustainable aquaculture approach that combines species from different trophic levels in a way that mimics natural ecosystems (Integrated Multi-Trophic Aquaculture). This could allow large-scale production of raw material while reducing waste and contributing to bioremediation. Regulatory approval will necessitate classification as a combination product, with extensive biocompatibility, sterility, and efficacy testing. While fucoidan is marketed as an FDA-approved dietary supplement, no MSP has yet received approval for therapeutic or device applications [139].

Future Perspectives

The future of scaffold functionalization for vascular regeneration lies in the convergence of biomimetic materials, immunomodulation, advanced fabrication technologies, and smart, multifunctional systems, with a strong emphasis on translational research and clinical validation. MSPs have moved beyond proof-of-concept and now consistently demonstrate anticoagulant, antiplatelet, and pro-endothelial activity when integrated into vascular grafts. The challenge ahead is not whether MSPs are bioactive, but how to harness that bioactivity in a standardized, tunable, and clinically reproducible way. Establishing clear correlations between sulfation motifs, molecular weight, and defined biological outcomes under physiological flow will be essential for rational design.

On the translational side, manufacturing and regulatory hurdles remain major barriers. Natural extracts are intrinsically heterogeneous, with batch-to-batch variability in sulfation, backbone composition, and molecular weight. Sustainable sourcing (e.g., aquaculture, biorefinery pipelines) or synthetic analogues will be required for scalability and reproducibility. Regulatory approval will also demand harmonized protocols for characterization, sterility, and large-animal validation, as most current studies remain short-term and small-scale. While preclinical results are promising, future research must address challenges in scaling up, long-term patency, and performance in disease or aging models. Large animal studies and clinical trials will be essential to validate the translational potential of these advanced scaffolds.

Looking forward, MSPs should be envisioned not as replacements for heparin or other mammalian GAGs, but as versatile, lumen-facing biointerfaces capable of modulating thrombosis, endothelialization, inflammation, and even local angiogenesis. A particularly exciting frontier is the possibility of tailoring MSP functionalization to the different stages of graft healing. One could envision distinct MSP chemistries deployed sequentially with highly sulfated domains to ensure immediate hemocompatibility, followed by less sulfated motifs that favor endothelial migration, and later structural variants that stabilize mature endothelium and dampen inflammation. Time-dependent presentation, achieved through degradable linkers or stimuli-responsive release, could transform MSPs into dynamic instructive cues rather than static coatings.

Another promising direction is the use of layer-by-layer functionalization to reflect the natural complexity of the vessel wall. For instance, luminal MSPs might be optimized for endothelial quiescence, medial MSPs for preserving contractile SMC phenotype, and adventitial MSPs for guiding fibroblast remodeling or local angiogenesis. Such stratified design would create a cross-talk among the biomaterial and multiple cell types, orchestrating vascular regeneration in a spatiotemporally controlled manner. Moreover, MSPs could act as smart linkers, exploiting their sulfate-dependent binding affinities to anchor and release growth factors, peptides, or extracellular vesicles locally. This would enable spatially programmed reservoirs that deliver bioactive signals only where needed, such as at sites of flow disturbance or high inflammatory burden.

If a clear understanding of structure–function relationships, reproducible manufacturing, and long-term validation will be achieved, MSPs could evolve into a new class of precision biomolecules for vascular medicine: not static coatings, but adaptive biointerfaces capable of guiding complex cellular processes across time, space, and tissue compartments.

Conclusion

In conclusion, recent findings validate the core premise that MSPs coating, functionalization or incorporation can impart antithrombotic and pro-endothelial properties to synthetic vascular grafts without compromising mechanical performance. As structure–function relationships become clearer, rational design of MSP-functionalized scaffolds may overcome long-standing limitations in small-diameter TEVGs. With continued progress in standardization, safety validation, and regulatory navigation, MSPs hold strong potential to transform vascular biomaterials and advance the field of regenerative medicine.

References

[1] Y. Zhuang, C. Zhang, M. Cheng, J. Huang, Q. Liu, G. Yuan, K. Lin, H. Yu, Challenges and strategies for in situ endothelialization and long-term lumen patency of vascular grafts, Bioact. Mater. 6 (2021) 1791–1809. https://doi.org/10.1016/j.bioactmat.2020.11.028.

[2] H.P. Ferreira, L. Moroni, H. Bergmeister, I.C. Gonçalves, Engineering antithrombogenic surfaces in synthetic small-diameter vascular grafts: A review of passive strategies, Acta Biomater. 209 (2026) 64–88. https://doi.org/10.1016/j.actbio.2025.10.038.

[3] D.G. Seifu, A. Purnama, K. Mequanint, D. Mantovani, Small-diameter vascular tissue engineering, Nat. Rev. Cardiol. 10 (2013) 410–421. https://doi.org/10.1038/nrcardio.2013.77.

[4] J.M. Seeger, W.M. Abbott, A.M. Callow, W.M. Moore, R.M. Rutherford, F.M. Veith, Evaluation and performance standards for arterial prostheses, J. Vasc. Surg. 17 (1993) 746–756. https://doi.org/10.1067/mva.1993.45222.

[5] M.X. Li, Q.Q. Wei, H.L. Mo, Y. Ren, W. Zhang, H.J. Lu, Y.K. Joung, Challenges and advances in materials and fabrication technologies of small-diameter vascular grafts, Biomater. Res. 27 (2023). https://doi.org/10.1186/s40824-023-00399-2.

[6] D.B. Camasão, D. Mantovani, The mechanical characterization of blood vessels and their substitutes in the continuous quest for physiological-relevant performances. A critical review, Mater. Today Bio 10 (2021). https://doi.org/10.1016/j.mtbio.2021.100106.

[7] S. Zhang, Z. Deng, Y. Wang, C. Zhao, A Review of Anticoagulant Surface Modification Strategies for Blood-Contacting Materials: From Inertness to Bioinspired and Biointegration, Coatings 15 (2025). https://doi.org/10.3390/coatings15121486.

[8] A.J. Lepedda, G. Nieddu, M. Formato, M.B. Baker, J. Fernández-Pérez, L. Moroni, Glycosaminoglycans: From Vascular Physiology to Tissue Engineering Applications, Front. Chem. 9 (2021). https://doi.org/10.3389/fchem.2021.680836.

[9] J.M.M. Heyligers, H.J.M. Verhagen, J.I. Rotmans, C. Weeterings, P.G. De Groot, F.L. Moll, T. Lisman, Heparin immobilization reduces thrombogenicity of small-caliber expanded polytetrafluoroethylene grafts, J. Vasc. Surg. 43 (2006) 587–591. https://doi.org/10.1016/j.jvs.2005.10.038.

[10] A. Fayon, P. Menu, R. El Omar, Cellularized small-caliber tissue-engineered vascular grafts: looking for the ultimate gold standard, NPJ Regen. Med. 6 (2021). https://doi.org/10.1038/s41536-021-00155-x.

[11] J. Ji, H. Xu, C. Li, J. Luo, Small-Caliber Tissue-Engineered Vascular Grafts Based on Human-Induced Pluripotent Stem Cells: Progress and Challenges, Tissue Eng. Part B Rev. 29 (2023) 441–455. https://doi.org/10.1089/ten.teb.2023.0005.

[12] B. Sivaraman, R.A. Latour, The relationship between platelet adhesion on surfaces and the structure versus the amount of adsorbed fibrinogen, Biomaterials 31 (2010) 832–839. https://doi.org/10.1016/j.biomaterials.2009.10.008.

[13] A.P. Rickel, X. Deng, D. Engebretson, Z. Hong, Electrospun nanofiber scaffold for vascular tissue engineering, Materials Science and Engineering C 129 (2021). https://doi.org/10.1016/j.msec.2021.112373.

[14] G.G. Flores-Rojas, B. Gómez-Lazaro, F. López-Saucedo, R. Vera-Graziano, E. Bucio, E. Mendizábal, Electrospun Scaffolds for Tissue Engineering: A Review, Macromol 3 (2023) 524–553. https://doi.org/10.3390/macromol3030031.

[15] V.M. Merkle, D. Martin, M. Hutchinson, P.L. Tran, A. Behrens, S. Hossainy, J. Sheriff, D. Bluestein, X. Wu, M.J. Slepian, Hemocompatibility of poly(vinyl alcohol)-gelatin core-shell electrospun nanofibers: A scaffold for modulating platelet deposition and activation, ACS Appl. Mater. Interfaces 7 (2015) 8302–8312. https://doi.org/10.1021/acsami.5b01671.

[16] H. Wu, L. Yang, R. Luo, L. Li, T. Zheng, K. Huang, Y. Qin, X. Yang, X. Zhang, Y. Wang, A drug-free cardiovascular stent functionalized with tailored collagen supports in-situ healing of vascular tissues, Nat. Commun. 15 (2024). https://doi.org/10.1038/s41467-024-44902-2.

[17] M. Shojaee, C.A. Bashur, Compositions Including Synthetic and Natural Blends for Integration and Structural Integrity: Engineered for Different Vascular Graft Applications, Adv. Healthc. Mater. 6 (2017). https://doi.org/10.1002/adhm.201700001.

[18] P. Mallis, A. Kostakis, C. Stavropoulos-Giokas, E. Michalopoulos, Future perspectives in small-diameter vascular graft engineering, Bioengineering 7 (2020) 1–40. https://doi.org/10.3390/bioengineering7040160.

[19] W.M. Abbott, J. Megerman, J.E. Hasson, G. L'Italien, D.F. Warnock, Effect of compliance mismatch on vascular graft patency, J. Vasc. Surg. 5 (1987) 376–382. https://doi.org/10.1067/mva.1987.avs0050376.

[20] R.M. Nezarati, M.B. Eifert, D.K. Dempsey, E. Cosgriff-Hernandez, Electrospun vascular grafts with improved compliance matching to native vessels, J. Biomed. Mater. Res. B Appl. Biomater. 103 (2015) 313–323. https://doi.org/10.1002/jbm.b.33201.

[21] E.A. Tamimi, D.C. Ardila, B.D. Ensley, R.S. Kellar, J.P. Vande Geest, Computationally optimizing the compliance of multilayered biomimetic tissue engineered vascular grafts, J. Biomech. Eng. 141 (2019). https://doi.org/10.1115/1.4042902.

[22] K.J. Furdella, S. Higuchi, A. Behrangzade, K. Kim, W.R. Wagner, J.P. Vande Geest, In-vivo assessment of a tissue engineered vascular graft computationally optimized for target vessel compliance, Acta Biomater. 123 (2021) 298–311. https://doi.org/10.1016/j.actbio.2020.12.058.

[23] S. Ozdemir, J. Oztemur, H. Sezgin, I. Yalcin-Enis, THE EFFECT OF POLYMER TYPE AND FIBER ORIENTATION ON THE COMPLIANCE PROPERTIES OF ELECTROSPUN VASCULAR GRAFTS, Vlakna a Textil 30 (2023) 67–71. https://doi.org/10.15240/tul/008/2023-1-011.

[24] A. Post, P. Diaz-Rodriguez, B. Balouch, S. Paulsen, S. Wu, J. Miller, M. Hahn, E. Cosgriff-Hernandez, Elucidating the role of graft compliance mismatch on intimal hyperplasia using an ex vivo organ culture model, Acta Biomater. 89 (2019) 84–94. https://doi.org/10.1016/j.actbio.2019.03.025.

[25] A. Hasan, A. Memic, N. Annabi, M. Hossain, A. Paul, M.R. Dokmeci, F. Dehghani, A. Khademhosseini, Electrospun scaffolds for tissue engineering of vascular grafts, Acta Biomater. 10 (2014) 11–25. https://doi.org/10.1016/j.actbio.2013.08.022.

[26] N.A. Jarad, A. Chami, J.I. Weitz, T.F. Didar, Advancements in surface modification strategies of vascular grafts to improve biocompatibility and tissue integration, Exploration of BioMat-X 1 (2024) 241–265. https://doi.org/10.37349/ebmx.2024.00018.

[27] Y. Wang, X. Guo, C. Huang, C. Shi, X. Xiang, Biomedical potency and mechanisms of marine polysaccharides and oligosaccharides: A review, Int. J. Biol. Macromol. 265 (2024). https://doi.org/10.1016/j.ijbiomac.2024.131007.

[28] V.H. Pomin, P.A.S. Mourão, Specific sulfation and glycosylation-a structural combination for the anticoagulation of marine carbohydrates, Front. Cell. Infect. Microbiol. 5 (2014). https://doi.org/10.3389/fcimb.2014.00033.

[29] V.H. Pomin, An overview about the structure-function relationship of marine sulfated homopolysaccharides with regular chemical structures, Biopolymers 91 (2009) 601–609. https://doi.org/10.1002/bip.21200.

[30] G. Nieddu, G. Obino, C. Ciampelli, A. Brunetti, T. Cubeddu, R. Manconi, G.A. Stocchino, G.A. Deiana, M. Formato, A.J. Lepedda, Purification of an Acidic Polysaccharide with Anticoagulant Activity from the Marine Sponge Sarcotragus spinosulus, Mar. Drugs 22 (2024). https://doi.org/10.3390/md22030139.

[31] F. Carvalhal, R.R. Cristelo, D.I.S.P. Resende, M.M.M. Pinto, E. Sousa, M. Correia-Da-Silva, Antithrombotics from the sea: Polysaccharides and beyond, Mar. Drugs 17 (2019). https://doi.org/10.3390/md17030170.

[32] P.A.S. Mourão, Perspective on the use of sulfated polysaccharides from marine organisms as a source of new antithrombotic drugs, Mar. Drugs 13 (2015) 2770–2784. https://doi.org/10.3390/md13052770.
[33] R.C.F. Cheung, T.B. Ng, J.H. Wong, Y. Chen, W.Y. Chan, Marine natural products with anti-inflammatory activity, Appl. Microbiol. Biotechnol. 100 (2016) 1645–1666. https://doi.org/10.1007/s00253-015-7244-3.
[34] G. Obino, G. Nieddu, M. Nagy, H. Ippel, T. Cubeddu, H.M.H. Spronk, T.M. Hackeng, M. Formato, A.J. Lepedda, L. Moroni, Marine-derived sulfated polysaccharides enhance hemocompatibility and endothelialization of nanofibrous PCL for vascular graft applications, Cell Biomaterials (2025) 100155. https://doi.org/10.1016/j.celbio.2025.100155.
[35] C. Ciampelli, S. Mangani, G. Nieddu, M. Formato, P. Ioannou, S. Kremmydas, N. Karamanos, A.J. Lepedda, Effects of Acidic Polysaccharide-Enriched Extracts from Holothuria tubulosa on Two- and Three-Dimensional Invasive Breast Cancer Cell Models, Biology (Basel). 14 (2025). https://doi.org/10.3390/biology14040334.
[36] Y. Dai, K. Qiao, D. Li, P. Isingizwe, H. Liu, Y. Liu, K. Lim, T. Woodfield, G. Liu, J. Hu, J. Yuan, J. Tang, X. Cui, Plant-Derived Biomaterials and Their Potential in Cardiac Tissue Repair, Adv. Healthc. Mater. 12 (2023). https://doi.org/10.1002/adhm.202202827.
[37] A. Hossain, D. Dave, F. Shahidi, Sulfated polysaccharides in sea cucumbers and their biological properties: A review, Int. J. Biol. Macromol. 253 (2023). https://doi.org/10.1016/j.ijbiomac.2023.127329.
[38] B. Li, F. Lu, X. Wei, R. Zhao, Fucoidan: Structure and bioactivity, Molecules 13 (2008) 1671–1695. https://doi.org/10.3390/molecules13081671.
[39] Y. Yao, E.K.F. Yim, Fucoidan for cardiovascular application and the factors mediating its activities, Carbohydr. Polym. 270 (2021). https://doi.org/10.1016/j.carbpol.2021.118347.
[40] N.E. Ustyuzhanina, N.A. Ushakova, K.A. Zyuzina, M.I. Bilan, A.L. Elizarova, O. V. Somonova, A. V. Madzhuga, V.B. Krylov, M.E. Preobrazhenskaya, A.I. Usov, M. V. Kiselevskiy, N.E. Nifantiev, Influence of fucoidans on hemostatic system, Mar. Drugs 11 (2013) 2444–2458. https://doi.org/10.3390/md11072444.
[41] A.K. Khan, A.U. Saba, S. Nawazish, F. Akhtar, R. Rashid, S. Mir, B. Nasir, F. Iqbal, S. Afzal, F. Pervaiz, G. Murtaza, Carrageenan based bionanocomposites as drug delivery tool with special emphasis on the influence of ferromagnetic nanoparticles, Oxid. Med. Cell. Longev. 2017 (2017). https://doi.org/10.1155/2017/8158315.
[42] Y. Chen, M.-L. Liao, D.E. Dunstan, The rheology of K 1-k-carrageenan as a weak gel, *50(2), 109–116.* doi:10.1016/s0144-8617(02)00009-7.
[43] F. van de Velde; S.H. Knutsen; A.I. Usov; H.S. Rollema; A.S. Cerezo. (2002). *1H and 13C high resolution NMR spectroscopy of carrageenans: application in research and industry. , 13(3), 0–92.* doi:10.1016/s0924-2244(02)00066-3.
[44] A. Jafari, M. Farahani, M. Sedighi, N. Rabiee, H. Savoji, Carrageenans for tissue engineering and regenerative medicine applications: A review, Carbohydr. Polym. 281 (2022). https://doi.org/10.1016/j.carbpol.2021.119045.
[45] A.L. Felix, S.M. Penno, F.F. Bezerra, P.A.S. Mourão, Fucosylated chondroitin sulfate, an intriguing polysaccharide from sea cucumber: past, present, and future, Glycobiology 35 (2025). https://doi.org/10.1093/glycob/cwae098.
[46] H. Xu, Q. Zhou, B. Liu, F. Chen, M. Wang, Holothurian fucosylated chondroitin sulfates and their potential benefits for human health: Structures and biological activities, Carbohydr. Polym. 275 (2022). https://doi.org/10.1016/j.carbpol.2021.118691.
[47] N.E. Ustyuzhanina, M.I. Bilan, A.S. Dmitrenok, N.E. Nifantiev, A.I. Usov, Fucosylated chondroitin sulfates from the sea cucumbers Holothuria tubulosa and Holothuria stellati, Carbohydr. Polym. 200 (2018) 1–5. https://doi.org/10.1016/j.carbpol.2018.07.035.

[48] N.E. Ustyuzhanina, M.I. Bilan, A.S. Dmitrenok, E.Y. Borodina, V.A. Stonik, N.E. Nifantiev, A.I. Usov, A highly regular fucosylated chondroitin sulfate from the sea cucumber Massinium magnum: Structure and effects on coagulation, Carbohydr. Polym. 167 (2017) 20–26. https://doi.org/10.1016/j.carbpol.2017.02.101.
[49] L. Yang, Y. Wang, S. Yang, Z. Lv, Separation, purification, structures and anticoagulant activities of fucosylated chondroitin sulfates from Holothuria scabra, Int. J. Biol. Macromol. 108 (2018) 710–718. https://doi.org/10.1016/j.ijbiomac.2017.11.058.
[50] N.E. Ustyuzhanina, M.I. Bilan, A.S. Dmitrenok, N.E. Nifantiev, A.I. Usov, Two fucosylated chondroitin sulfates from the sea cucumber Eupentacta fraudatrix, Carbohydr. Polym. 164 (2017) 8–12. https://doi.org/10.1016/j.carbpol.2017.01.034.
[51] N.E. Ustyuzhanina, M.I. Bilan, A.S. Dmitrenok, A.S. Shashkov, N.E. Nifantiev, A.I. Usov, The structure of a fucosylated chondroitin sulfate from the sea cucumber Cucumaria frondosa, Carbohydr. Polym. 165 (2017) 7–12. https://doi.org/10.1016/j.carbpol.2017.02.003.
[52] L. Chahed, R. Balti, S. Elhiss, N. Bouchemal, N. Ajzenberg, V. Ollivier, F. Chaubet, R.M. Maaroufi, M. Ben Mansour, Anticoagulant activity of fucosylated chondroitin sulfate isolated from Cucumaria syracusana, Process Biochemistry 91 (2020) 149–157. https://doi.org/10.1016/j.procbio.2019.12.006.
[53] P. Tian, D. Zhou, C. Ji, C. Niu, Y. Chen, Y. Chen, Characterization and anticoagulant activity of a fucosylated chondroitin sulfate from the sea cucumber Acaudina leucoprocta, Process Biochemistry 147 (2024) 130–136. https://doi.org/10.1016/j.procbio.2024.08.007.
[54] P. Qiu, F. Wu, L. Yi, L. Chen, Y. Jin, X. Ding, Y. Ouyang, Y. Yao, Y. Jiang, Z. Zhang, Structure characterization of a heavily fucosylated chondroitin sulfate from sea cucumber (H. leucospilota) with bottom-up strategies, Carbohydr. Polym. 240 (2020). https://doi.org/10.1016/j.carbpol.2020.116337.
[55] J. Mou, C. Wang, W. Li, J. Yang, Purification, structural characterization and anticoagulant properties of fucosylated chondroitin sulfate isolated from Holothuria mexicana, Int. J. Biol. Macromol. 98 (2017) 208–215. https://doi.org/10.1016/j.ijbiomac.2017.01.123.
[56] N.E. Ustyuzhanina, M.I. Bilan, A.S. Dmitrenok, E.A. Tsvetkova, A.S. Shashkov, V.A. Stonik, N.E. Nifantiev, A.I. Usov, Structural characterization of fucosylated chondroitin sulfates from sea cucumbers Apostichopus japonicus and Actinopyga mauritiana, Carbohydr. Polym. 153 (2016) 399–405. https://doi.org/10.1016/j.carbpol.2016.07.076.
[57] N.E. Ustyuzhanina, M.I. Bilan, A.S. Dmitrenok, A.S. Shashkov, N.E. Nifantiev, A.I. Usov, Two structurally similar fucosylated chondroitin sulfates from the holothurian species Stichopus chloronotus and Stichopus horrens, Carbohydr. Polym. 189 (2018) 10–14. https://doi.org/10.1016/j.carbpol.2018.02.008.
[58] N.E. Ustyuzhanina, M.I. Bilan, A.S. Dmitrenok, A.S. Shashkov, N.M.A. Ponce, C.A. Stortz, N.E. Nifantiev, A.I. Usov, Fucosylated chondroitin sulfate from the sea cucumber Hemioedema spectabilis: Structure and influence on cell adhesion and tubulogenesis, Carbohydr. Polym. 234 (2020). https://doi.org/10.1016/j.carbpol.2020.115895.
[59] P. Xu, B. Yu, L. Zhang, B. Liu, Chemical synthesis of fucosylated chondroitin sulfate oligosaccharides, Journal of Organic Chemistry 85 (2020) 15908–15919. https://doi.org/10.1021/acs.joc.0c01009.
[60] A.A. Vasconcelos, V.H. Pomin, The sea as a rich source of structurally unique glycosaminoglycans and mimetics, Microorganisms 5 (2017). https://doi.org/10.3390/microorganisms5030051.
[61] V.H. Pomin, NMR structural determination of unique invertebrate glycosaminoglycans endowed with medical properties, Carbohydr. Res. 413 (2015) 41–50. https://doi.org/10.1016/j.carres.2015.05.004.
[62] V.H. Pomin, P.A.S. Mourão, Structure, biology, evolution, and medical importance of sulfated fucans and galactans, Glycobiology 18 (2008) 1016–1027. https://doi.org/10.1093/glycob/cwn085.
[63] O.N. Pozharitskaya, E.D. Obluchinskaya, A.N. Shikov, Mechanisms of bioactivities of fucoidan from the brown seaweed fucus vesiculosus L. Of the barents sea, Mar. Drugs 18 (2020). https://doi.org/10.3390/md18050275.

[64] A. Babuty, A. Zykwinska, S.A. Samsonov, N. Candia, C. Veinstein, M. Pugnière, T.H.G. Ngo, C. Sinquin, J. Muñoz-Garcia, S. Colliec-Jouault, D. Heymann, Anticoagulant Potential of Modified Sulfated Exopolysaccharides from Deep-Sea Bacteria: Toward Non-Animal Heparin Alternatives, Polysaccharides 6 (2025) 54. https://doi.org/10.3390/polysaccharides6020054.

[65] Y. Yao, E.K.F. Yim, Fucoidan for cardiovascular application and the factors mediating its activities, Carbohydr. Polym. 270 (2021). https://doi.org/10.1016/j.carbpol.2021.118347.

[66] E. V Sokolova, A.O. Barabanova, V.A. Homenko, T.F. Solov'eva, R.N. Bogdanovich, I.M. Yermak, In Vitro and Ex Vivo Studies of Antioxidant Activity of Carrageenans, Sulfated Polysaccharides from Red Algae, 2010.

[67] E. Gray, J. Hogwood, B. Mulloy, The Anticoagulant and Antithrombotic Mechanisms of Heparin, in: 2012: pp. 43–61. https://doi.org/10.1007/978-3-642-23056-1_3.

[68] M.S. Zierer, R.P. Vieira, B. Mulloy, P.A.S. Mourso, A novel acidic glycogen extracted from the marine sponge Aplysina fulva (Porifera-Demospongiae), 1995.

[69] K. Li, R. Li, Y. Liu, G. Li, S. Liu, Diversity, mechanism and structure-activity relationships of marine anticoagulant-active polysaccharides: A review, Int. J. Biol. Macromol. 306 (2025). https://doi.org/10.1016/j.ijbiomac.2025.141742.

[70] L. Qin, Y. Yang, W. Mao, Anticoagulant Property of a Sulfated Polysaccharide with Unique Structural Characteristics from the Green Alga Chaetomorpha aerea, Mar. Drugs 21 (2023). https://doi.org/10.3390/md21020088.

[71] S. Cao, X. He, L. Qin, M. He, Y. Yang, Z. Liu, W. Mao, Anticoagulant and antithrombotic properties in vitro and in vivo of a novel sulfated polysaccharide from marine green alga Monostroma nitidum, Mar. Drugs 17 (2019). https://doi.org/10.3390/md17040247.

[72] M. He, Y. Yang, Z. Shao, J. Zhang, C. Feng, L. Wang, W. Mao, Chemical structure and anticoagulant property of a novel sulfated polysaccharide from the green alga cladophora oligoclada, Mar. Drugs 19 (2021). https://doi.org/10.3390/md19100554.

[73] L. Peipei, Z. Qinghong, C. Yin, H. Pengfei, Z. Junjie, Structure and anticoagulant activity of a galactoarabinan sulfate polysaccharide and its oligosaccharide from the green algae, Codium fragile, Int. J. Biol. Macromol. 279 (2024). https://doi.org/10.1016/j.ijbiomac.2024.135255.

[74] Q. Chen, M. Zhang, Y. Liu, W. Liu, C. Peng, L. Zheng, Sulfated Polysaccharides with Anticoagulant Potential: A Review Focusing on Structure-Activity Relationship and Action Mechanism, Chem. Biodivers. 21 (2024). https://doi.org/10.1002/cbdv.202400152.

[75] R. Chen, W. Wang, R. Yin, Y. Pan, C. Xu, N. Gao, X. Luo, J. Zhao, Structural Characterization and Anticoagulant Activities of a Keratan Sulfate-like Polysaccharide from the Sea Cucumber Holothuria fuscopunctata, Mar. Drugs 21 (2023). https://doi.org/10.3390/md21120632.

[76] N.E. Ustyuzhanina, M.I. Bilan, N.Y. Anisimova, S.P. Nikogosova, A.S. Dmitrenok, E.A. Tsvetkova, E.G. Panina, N.P. Sanamyan, S.A. Avilov, V.A. Stonik, M. V. Kiselevskiy, A.I. Usov, N.E. Nifantiev, Fucosylated Chondroitin Sulfates with Rare Disaccharide Branches from the Sea Cucumbers Psolus peronii and Holothuria nobilis: Structures and Influence on Hematopoiesis, Pharmaceuticals 16 (2023). https://doi.org/10.3390/ph16121673.

[77] C.G. Panagos, D.S. Thomson, C. Moss, A.D. Hughes, M.S. Kelly, Y. Liu, W. Chai, R. Venkatasamy, D. Spina, C.P. Page, J. Hogwood, R.J. Woods, B. Mulloy, C.D. Bavington, D. Uhrín, Fucosylated chondroitin sulfates from the body wall of the sea cucumber Holothuria forskali: Conformation, selectin binding, and biological activity, Journal of Biological Chemistry 289 (2014) 28284–28298. https://doi.org/10.1074/jbc.M114.572297.

[78] N.E. Ustyuzhanina, M.I. Bilan, N.Y. Anisimova, S.P. Nikogosova, A.S. Dmitrenok, E.A. Tsvetkova, E.G. Panina, N.P. Sanamyan, S.A. Avilov, V.A. Stonik, M. V. Kiselevskiy, A.I. Usov, N.E. Nifantiev, Fucosylated Chondroitin Sulfates with Rare Disaccharide Branches from the Sea Cucumbers Psolus

peronii and Holothuria nobilis: Structures and Influence on Hematopoiesis, Pharmaceuticals 16 (2023). https://doi.org/10.3390/ph16121673.
[79] V.H. Pomin, Holothurian fucosylated chondroitin sulfate, Mar. Drugs 12 (2014) 232–254. https://doi.org/10.3390/md12010232.
[80] S. Chen, G. Li, N. Wu, X. Guo, N. Liao, X. Ye, D. Liu, C. Xue, W. Chai, Sulfation pattern of the fucose branch is important for the anticoagulant and antithrombotic activities of fucosylated chondroitin sulfates, Biochim. Biophys. Acta Gen. Subj. 1830 (2013) 3054–3066. https://doi.org/10.1016/j.bbagen.2013.01.001.
[81] S. Chen, C. Xue, L. Yin, Q. Tang, G. Yu, W. Chai, Comparison of structures and anticoagulant activities of fucosylated chondroitin sulfates from different sea cucumbers, Carbohydr. Polym. 83 (2011) 688–696. https://doi.org/10.1016/j.carbpol.2010.08.040.
[82] A.G. Gerbst, N.E. Ustyuzhanina, N.E. Nifantiev, Computational study of the possible formation of the ternary complex between thrombin, antithrombin III and fucosylated chondroitin sulfates, Mendeleev Communications 25 (2015) 420–421. https://doi.org/10.1016/j.mencom.2015.11.006.
[83] Green D. (2006). Coagulation cascade. *Hemodialysis international. International Symposium on Home Hemodialysis*, *10 Suppl 2*, S2–S4. https://doi.org/10.1111/j.1542-4758.2006.00119.x
[84] R. Chaudhry, R.B. Killeen, H.M. Babiker, Physiology, Coagulation Pathways, 2025.
[85] W. Zhang, W. Jin, V.H. Pomin, F. Zhang, R.J. Linhardt, Interactions of marine sulfated glycans with antithrombin and platelet factor 4, Front. Mol. Biosci. 9 (2022). https://doi.org/10.3389/fmolb.2022.954752.
[86] N.E. Ustyuzhanina, M.I. Bilan, A.S. Dmitrenok, E.Y. Borodina, V.A. Stonik, N.E. Nifantiev, A.I. Usov, A highly regular fucosylated chondroitin sulfate from the sea cucumber Massinium magnum: Structure and effects on coagulation, Carbohydr. Polym. 167 (2017) 20–26. https://doi.org/10.1016/j.carbpol.2017.02.101.
[87] P.A.S. Mourã, M.S. Pereira, M.S.G. Pavã, B. Mulloy, D.M. Tollefsen, M.-C. Mowinckel, U. Abildgaard, Structure and Anticoagulant Activity of a Fucosylated Chondroitin Sulfate from Echinoderm SULFATED FUCOSE BRANCHES ON THE POLYSACCHARIDE ACCOUNT FOR ITS HIGH ANTICOAGULANT ACTION*, 1996.
[88] L. Qin, M. He, Y. Yang, Z. Fu, C. Tang, Z. Shao, J. Zhang, W. Mao, Anticoagulant-active sulfated arabinogalactan from Chaetomorpha linum: Structural characterization and action on coagulation factors, Carbohydr. Polym. 242 (2020). https://doi.org/10.1016/j.carbpol.2020.116394.
[89] X. Liu, X. He, W. Mao, S. Cao, L. Qin, M. He, X. He, W. Mao, Anticoagulant properties of a green algal rhamnan-type sulfated polysaccharide and its low-molecular-weight fragments prepared by mild acid degradation, Mar. Drugs 16 (2018). https://doi.org/10.3390/md16110445.
[90] V.H. Pomin, P. Antônio, S. Mourão, Structure versus anticoagulant and antithrombotic actions of marine sulfated polysaccharides, Revista Brasileira de Farmacognosia Brazilian Journal of Pharmacognosy 22 921–928. https://doi.org/10.1590/S0102.
[91] S. Alizadeh, Z. Ameri, H. Daemi, M. Pezeshki-Modaress, Sulfated polysaccharide as biomimetic biopolymers for tissue engineering scaffolds fabrication: Challenges and opportunities, Carbohydr. Polym. 336 (2024). https://doi.org/10.1016/j.carbpol.2024.122124.
[92] T.A. Horbett, Fibrinogen adsorption to biomaterials, J. Biomed. Mater. Res. A 106 (2018) 2777–2788. https://doi.org/10.1002/jbm.a.36460.
[93] L. Yang, L. Han, Q. Liu, Y. Xu, L. Jia, Galloyl groups-regulated fibrinogen conformation: Understanding antiplatelet adhesion on tannic acid coating, Acta Biomater. 64 (2017) 187–199. https://doi.org/10.1016/j.actbio.2017.09.034.
[94] I. Firkowska-Boden, K.D. Jandt, C. Helbing, T.J. Dauben, M. Pieper, How nanotopography-induced conformational changes of fibrinogen affect platelet adhesion and activation, Langmuir 36 (2020) 11573–11580. https://doi.org/10.1021/acs.langmuir.0c02094.

[95] J.B.M. Rocha Neto, F. Copes, P. Chevallier, R.S. Vieira, J.V.L. da Silva, D. Mantovani, M.M. Beppu, Polysaccharide-based layer-by-layer nanoarchitectonics with sulfated chitosan for tuning anti-thrombogenic properties, Colloids Surf. B Biointerfaces 213 (2022). https://doi.org/10.1016/j.colsurfb.2022.112359.

[96] L.C. Xu, M.E. Meyerhoff, C.A. Siedlecki, Blood coagulation response and bacterial adhesion to biomimetic polyurethane biomaterials prepared with surface texturing and nitric oxide release, Acta Biomater. 84 (2019) 77–87. https://doi.org/10.1016/j.actbio.2018.11.035.

[97] M.A. Haque, D. Murakami, T. Anada, M. Tanaka, Poly(2-Methoxyethyl Acrylate) (PMEA)-Coated Anti-Platelet Adhesive Surfaces to Mimic Native Blood Vessels through HUVECs Attachment, Migration, and Monolayer Formation, Coatings 12 (2022). https://doi.org/10.3390/coatings12060869.

[98] D. Fan, X. Liu, H. Chen, Endothelium-Mimicking Materials: A "Rising Star" for Antithrombosis, ACS Appl. Mater. Interfaces 16 (2024) 53343–53371. https://doi.org/10.1021/acsami.4c12117.

[99] Y. Pan, H. Sun, X. Gu, S. Li, S. Yang, L. Zhang, H. Mao, P. Wang, S. Yang, R. Yin, Z. Zuo, J. Zhao, Oligosaccharide-assisted resolution of holothurian fucosylated chondroitin sulfate for fine structure and P-selectin inhibition, Carbohydr. Polym. 351 (2025). https://doi.org/10.1016/j.carbpol.2024.123145.

[100] E. V. Sokolova, A.O. Byankina, A.A. Kalitnik, Y.H. Kim, L.N. Bogdanovich, T.F. Solov'Eva, I.M. Yermak, Influence of red algal sulfated polysaccharides on blood coagulation and platelets activation in vitro, J. Biomed. Mater. Res. A 102 (2014) 1431–1438. https://doi.org/10.1002/jbm.a.34827.

[101] F.D. da S. Chagas, G.C. Lima, V.I.N. dos Santos, L.E.C. Costa, W.M. de Sousa, V.G. Sombra, D.F. de Araújo, F.C.N. Barros, E. Marinho-Soriano, J.P. de Andrade Feitosa, R.C.M. de Paula, M.G. Pereira, A.L.P. Freitas, Sulfated polysaccharide from the red algae Gelidiella acerosa: Anticoagulant, antiplatelet and antithrombotic effects, Int. J. Biol. Macromol. 159 (2020) 415–421. https://doi.org/10.1016/j.ijbiomac.2020.05.012.

[102] Y. Wang, M. Xing, Q. Cao, A. Ji, H. Liang, S. Song, Biological activities of fucoidan and the factors mediating its therapeutic effects: A review of recent studies, Mar. Drugs 17 (2019). https://doi.org/10.3390/md17030183.

[103] L.L. Reys, S.S. Silva, C. Oliveira, N.M. Neves, A. Martins, R.L. Reis, T.H. Silva, Angiogenic potential of airbrushed fucoidan/polycaprolactone nanofibrous meshes, Int. J. Biol. Macromol. 183 (2021) 695–706. https://doi.org/10.1016/j.ijbiomac.2021.04.166.

[104] D.D. Roberts, V. Ginsburg', Sulfated Glycolipids and Cell Adhesion, 1988.

[105] E. Vilanova, C.C. Coutinho, P.A.S. Mourão, Sulfated polysaccharides from marine sponges (Porifera): An ancestor cell-cell adhesion event based on the carbohydrate-carbohydrate interaction, Glycobiology 19 (2009) 860–867. https://doi.org/10.1093/glycob/cwp059.

[106] O. Siddiqua Prova, S. Afrin, T.A. Tabish, M. Rizwan, Fucoidan based hydrogel biomaterials for tissue engineering, Biomater. Sci. 13 (2025) 6572–6597. https://doi.org/10.1039/D5BM00676G.

[107] F. Zhang, M.W. King, Immunomodulation Strategies for the Successful Regeneration of a Tissue-Engineered Vascular Graft, Adv. Healthc. Mater. 11 (2022). https://doi.org/10.1002/adhm.202200045.

[108] S.D. Sommerfeld, X. Zhou, J.C. Mejías, B.C. Oh, D.R. Maestas, G.J. Furtmüller, P.A. Laffont, J.H. Elisseeff, G. Brandacher, Biomaterials-based immunomodulation enhances survival of murine vascularized composite allografts, Biomater. Sci. 11 (2023) 4022–4031. https://doi.org/10.1039/d2bm01845d.

[109] M.L. Amin, D. Mawad, S. Dokos, P. Koshy, P.J. Martens, C.C. Sorrell, Immunomodulatory properties of photopolymerizable fucoidan and carrageenans, Carbohydr. Polym. 230 (2020). https://doi.org/10.1016/j.carbpol.2019.115691.

[110] L.Y.C. Madruga, M.J. Kipper, Expanding the Repertoire of Electrospinning: New and Emerging Biopolymers, Techniques, and Applications, Adv. Healthc. Mater. 11 (2022). https://doi.org/10.1002/adhm.202101979.

[111] Y. Geng, L. Xing, M. Sun, F. Su, Immunomodulatory effects of sulfated polysaccharides of pine pollen on mouse macrophages, Int. J. Biol. Macromol. 91 (2016) 846–855. https://doi.org/10.1016/j.ijbiomac.2016.06.021.
[112] L. Huang, M. Shen, G.A. Morris, J. Xie, Sulfated polysaccharides: Immunomodulation and signaling mechanisms, Trends Food Sci. Technol. 92 (2019) 1–11. https://doi.org/10.1016/j.tifs.2019.08.008.
[113] A. Purnama, R. Aid-Launais, O. Haddad, M. Maire, D. Mantovani, D. Letourneur, H. Hlawaty, C. Le Visage, Fucoidan in a 3D scaffold interacts with vascular endothelial growth factor and promotes neovascularization in mice, Drug Deliv. Transl. Res. 5 (2015) 187–197. https://doi.org/10.1007/s13346-013-0177-4.
[114] S. Matou, D. Helley, D. Chabut, A. Bros, A.-M. Fischer, Effect of fucoidan on fibroblast growth factor-2-induced angiogenesis in vitro. (2002). 106(4-5), 0–221. doi:10.1016/s0049-3848(02)00136-6
[115] C. Bouvard, I. Galy-Fauroux, F. Grelac, W. Carpentier, A. Lokajczyk, S. Gandrille, S. Colliec-Jouault, A.M. Fischer, D. Helley, Low-molecular-weight fucoidan induces endothelial cell migration via the PI3K/AKT pathway and modulates the transcription of genes involved in angiogenesis, Mar. Drugs 13 (2015) 7446–7462. https://doi.org/10.3390/md13127075.
[116] N. Marinval, P. Sabboural, O. Haddad, M. Maire, K. Bassand, F. Geinguenaud, N. Djaker, K. Ben Akrout, M.L. De La Chapelle, R. Robert, O. Oudar, E. Guyot, C. Laguillier-Morizot, A. Sutton, C. Chauvierre, F. Chaubet, N. Charnaux, H. Hlawaty, Identification of a pro-angiogenic potential and cellular uptake mechanism of a LMW highly sulfated fraction of fucoidan from Ascophyllum nodosum, Mar. Drugs 14 (2016). https://doi.org/10.3390/md14100185.
[117] G. Jiao, G. Yu, J. Zhang, H.S. Ewart, Chemical structures and bioactivities of sulfated polysaccharides from marine algae, Mar. Drugs 9 (2011) 196–233. https://doi.org/10.3390/md9020196.
[118] M.S. Arokiarajan, R. Thirunavukkarasu, J. Joseph, O. Ekaterina, W. Aruni, Advance research in biomedical applications on marine sulfated polysaccharide, Int. J. Biol. Macromol. 194 (2022) 870–881. https://doi.org/10.1016/j.ijbiomac.2021.11.142.
[119] S.N. Baytas, R.J. Linhardt, Advances in the preparation and synthesis of heparin and related products, Drug Discov. Today 25 (2020) 2095–2109. https://doi.org/10.1016/j.drudis.2020.09.011.
[120] M. Douaisi, E.E. Paskaleva, L. Fu, N. Grover, C.L. McManaman, S. Varghese, P.R. Brodfuehrer, J.M. Gibson, I. de Joode, K. Xia, M.I. Brier, T.J. Simmons, P. Datta, F. Zhang, A. Onishi, M. Hirakane, D. Mori, R.J. Linhardt, J.S. Dordick, Synthesis of bioengineered heparin chemically and biologically similar to porcine-derived products and convertible to low MW heparin, Proc. Natl. Acad. Sci. U. S. A. 121 (2024). https://doi.org/10.1073/pnas.2315586121.
[121] A. Babuty, A. Zykwinska, S.A. Samsonov, N. Candia, C. Veinstein, M. Pugnière, T.H.G. Ngo, C. Sinquin, J. Muñoz-Garcia, S. Colliec-Jouault, D. Heymann, Anticoagulant Potential of Modified Sulfated Exopolysaccharides from Deep-Sea Bacteria: Toward Non-Animal Heparin Alternatives, Polysaccharides 6 (2025) 54. https://doi.org/10.3390/polysaccharides6020054.
[122] S.C. Chen, X. Qin, N. Xiong, L. Lin, Y. Wu, Q. Li, D. Sun, D.C. Xiong, C.E. Callmann, M. Wu, X.S. Ye, Comprehensive synthesis and anticoagulant evaluation of a diverse fucoidan library, Nat. Commun. 16 (2025) 4364. https://doi.org/10.1038/s41467-025-59632-2.
[123] W. Zhang, W. Jin, V.H. Pomin, F. Zhang, R.J. Linhardt, Interactions of marine sulfated glycans with antithrombin and platelet factor 4, Front. Mol. Biosci. 9 (2022). https://doi.org/10.3389/fmolb.2022.954752.
[124] E. Durand, D. Helley, A. Al Haj Zen, C. Dujols, P. Bruneval, S. Colliec-Jouault, A.M. Fischer, A. Lafont, Effect of low molecular weight fucoidan and low molecular weight heparin in a rabbit model of arterial thrombosis, J. Vasc. Res. 45 (2008) 529–537. https://doi.org/10.1159/000129687.
[125] K. Wang, X. Xu, Q. Wei, Q. Yang, J. Zhao, Y. Wang, X. Li, K. Ji, S. Song, Application of fucoidan as treatment for cardiovascular and cerebrovascular diseases, Ther. Adv. Chronic Dis. 13 (2022). https://doi.org/10.1177/20406223221076891.

[126] C.A. Foote, R.N. Soares, F.I. Ramirez-Perez, T. Ghiarone, A. Aroor, C. Manrique-Acevedo, J. Padilla, L. Martinez-Lemus, Endothelial Glycocalyx, Compr. Physiol. 12 (2022). https://doi.org/10.1002/cphy.c210029.

[127] D. Pretorius, R.P. Richter, T. Anand, J.C. Cardenas, J.R. Richter, Alterations in heparan sulfate proteoglycan synthesis and sulfation and the impact on vascular endothelial function, Matrix Biol. Plus 16 (2022). https://doi.org/10.1016/j.mbplus.2022.100121.

[128] Eble, Johannes. (2009). *Editorial [Hot Topic: The Extracellular Matrix in Health and Disease. Current Pharmaceutical Design, 15(12), 1275–1276.* doi:10.2174/138161209787846694.

[129] S.E. Sakiyama-Elbert, Incorporation of heparin into biomaterials, Acta Biomater. 10 (2014) 1581–1587. https://doi.org/10.1016/j.actbio.2013.08.045.

[130] S. Aslani, M. Kabiri, S. HosseinZadeh, H. Hanaee-Ahvaz, E.S. Taherzadeh, M. Soleimani, The applications of heparin in vascular tissue engineering, Microvasc. Res. 131 (2020). https://doi.org/10.1016/j.mvr.2020.104027.

[131] G. Obino, A. Sensini, T. ten Brink, G. Nieddu, T. Bodet, G.A. Deiana, M. van Griensven, M. Formato, A.J. Lepedda, L. Moroni, Tunable Bioresorbable Scaffolds With Marine Sulfated Polysaccharides for Small-Caliber Vascular Grafts: A Multi-Layered Strategy Combining Electrospinning and 4-Axis Printing, Adv. Healthc. Mater. (2026). https://doi.org/10.1002/adhm.202505314.

[132] S.Y. Zhou, L. Li, E. Xie, M.X. Li, J.H. Cao, X. Bin Yang, D.Y. Wu, Small-diameter PCL/PU vascular graft modified with heparin-aspirin compound for preventing the occurrence of acute thrombosis, Int. J. Biol. Macromol. 249 (2023). https://doi.org/10.1016/j.ijbiomac.2023.126058.

[133] Y. Yao, A.M. Zaw, D.E.J. Anderson, M.T. Hinds, E.K.F. Yim, Fucoidan functionalization on poly(vinyl alcohol) hydrogels for improved endothelialization and hemocompatibility, Biomaterials 249 (2020). https://doi.org/10.1016/j.biomaterials.2020.120011.

[134] M. Bračič, B.M. Nagy, O. Plohl, F. Lackner, T. Steindorfer, R.C. Fischer, T. Heinze, A. Olschewski, K.S. Kleinschek, C. Nagaraj, T. Mohan, Antithrombogenic polysaccharide coatings to improve hemocompatibility, protein-repellence, and endothelial cell response, IScience 27 (2024). https://doi.org/10.1016/j.isci.2024.110692.

[135] Y. Wang, C. Ye, H. Su, J. Wang, Y. Wang, H. Wang, A. Zhao, N. Huang, Layer-by-layer self-assembled laminin/fucoidan films: Towards better hemocompatibility and endothelialization, RSC Adv. 6 (2016) 56048–56055. https://doi.org/10.1039/c6ra02070d.

[136] A.C. Gilotti, W. Nimlamool, R. Pugh, J.B. Slee, T.C. Barthol, E.A. Miller, L.J. Lowe-Krentz, Heparin responses in vascular smooth muscle cells involve cGMP-dependent protein kinase (PKG), J. Cell. Physiol. 229 (2014) 2142–2152. https://doi.org/10.1002/jcp.24677.

[137] K. Lundmark, P.K. Tran, M.G. Kinsella, A.W. Clowes, T.N. Wight, U. Hedin, Perlecan inhibits smooth muscle cell adhesion to fibronectin: Role of heparan sulfate, J. Cell. Physiol. 188 (2001) 67–74. https://doi.org/10.1002/jcp.1094.

[138] Y. Yao, A.M. Zaw, D.E.J. Anderson, Y.J. Jeong, J. Kunihiro, M.T. Hinds, E.K.F. Yim, Fucoidan and topography modification improved in situ endothelialization on acellular synthetic vascular grafts, Bioact. Mater. 22 (2023) 535–550. https://doi.org/10.1016/j.bioactmat.2022.10.011.

[139] A. Citkowska, M. Szekalska, K. Winnicka, Possibilities of fucoidan utilization in the development of pharmaceutical dosage forms, Mar. Drugs 17 (2019). https://doi.org/10.3390/md17080458.

Chapter 3
Purification of an acidic polysaccharide with anticoagulant activity from the marine sponge *Sarcotragus spinosulus*

Gabriele Nieddu[1 *], Gabriele Obino[1,2 *], Cristina Ciampelli[1], Antonio Brunetti[1], Tiziana Cubeddu[3], Renata Manconi[3], Giacinta Angela Stocchino[3], Giovanni Andrea Deiana[4,5], Marilena Formato[1] and Antonio Junior Lepedda[1]

* These authors contributed equally to this work

[1]Department of Biomedical Sciences, University of Sassari, Viale San Pietro, 43b, Sassari - 07100, Italy
[2]MERLN Institute for Technology-Inspired Regenerative Medicine, Complex Tissue Regeneration Department, Maastricht University, Maastricht, 6200 MD, The Netherlands
[3]Department of Veterinary Medicine, University of Sassari, Via Vienna 2, Sassari - 07100, Italy
[4]Department of Medicine, Surgery and Pharmacy, University of Sassari, Viale San Pietro, 43b, Sassari - 07100, Italy
[5]Struttura Complessa Laboratorio Unico di Analisi cliniche chimico-ematologiche, Azienda Ospedaliera Universitaria, Sassari - 07100, Italy

The content of this chapter has been published in *Marine Drugs*
DOI: 10.3390/md22030139

Abstract

Thromboembolic conditions are the most common causes of death in developed countries. Anticoagulant therapy is the treatment of choice, being heparinoids and warfarin the most adopted drugs. Sulphated polysaccharides extracted from marine organisms have been demonstrated to be effective alternatives, blocking thrombus formation by inhibiting some factors involved in the coagulation cascade. In this study, four acidic glycan fractions from the marine sponge *Sarcotragus spinosulus* were purified by anion exchange chromatography and their anticoagulant properties were investigated through APTT and PT assays, and compared with both standard glycosaminoglycans and holothurian sulphated polysaccharides. Moreover, their topographic localization was assessed through histological analysis and their cytocompatibility was tested on a human fibroblast cell line. A positive correlation between the amount of acid glycans and the inhibitory effect towards both the intrinsic and extrinsic coagulation pathways was observed. The most effective anticoagulant activity was exhibited by a highly charged fraction, which accounted for almost half (about 40%) of the total hexuronate containing polysaccharides. Its preliminary structural characterization, performed through infrared spectroscopy and nuclear magnetic resonance, suggested that it may consist of a fucosylated chondroitin sulphate, whose unique structure may be responsible for the anticoagulant activity reported herein for the first time.

Keywords: fucosylated chondroitin sulphate; marine invertebrates; anticoagulant activity; sustainable spongiculture; Porifera

Introduction

Coagulation, also known as clotting, is a dynamic biochemical process responsible for stopping bleeding and promoting healing after blood vessel injury [1]. It involves the activation of a series of coagulation factors interacting in a precise sequence, to form a clot at the site of injury. This process is essential for the survival of organisms, as it prevents excessive blood loss and maintains blood vessel integrity [2]. The balance between factors that promote and inhibit the formation of the clot is called hemostasis, a term that literally means “stop of bleeding” and comes from the two ancient Greek words heme and stasis, which stand for blood and to stop, respectively [3].

The first theories describing blood coagulation processes are dated back to the 1960's, when the hypotheses of two theories called the "waterfall" and "cascade" were proposed by Davie and Ratnoff [4], as well as by Macfarlane [5], explaining how a series of inactive enzymes can be activated one after the other, like a cascade, ultimately leading to the formation of a blood clot [6].
The coagulation process can be divided into three main pathways: the extrinsic, the intrinsic, and the common pathway. The first one is activated by tissue factor (TF), abundantly expressed by both adventitial cells surrounding blood vessels and subendothelial tissues [7] and exposed as a consequence of tissue damage, which binds with and activates factor VII [8], finally leading to the formation of a fibrin clot. On the other hand, the intrinsic pathway, also known as the contact pathway, is triggered by negatively charged surfaces coming into contact with factor XII, which is converted into its active conformation and can, in turn, activate factor XI and sequentially factor IX, which binds with factor VIII [9, 10]. Both pathways converge on the common pathway, by activating factor X, which forms a complex with its cofactor (factor V), tissue phospholipids, platelet phospholipids, and calcium, thus creating a stable clot [2].
All these events are tightly regulated to prevent excessive clotting, which can lead to life-threatening conditions such as deep vein thrombosis, pulmonary embolism, stroke, and other complications associated with vascular related diseases, which represent the most common cause of death in developed countries [11-13]. At the same time, it is also important to maintain adequate clotting to prevent excessive bleeding, particularly during surgery or injury [14].
The identification of new natural molecules with anticoagulant activity is a key issue, as it can lead to the development of new drugs able to prevent excessive clotting without increasing the risk of bleeding and avoiding other side effects. Currently, the most widely used drugs for therapeutic purposes are warfarin, heparin (Hep), and Hep-derivatives, whose ability to prevent excessive coagulation is effective despite some considerable side effects, such as nausea, vomiting, abdominal pain, thrombocytopenia, significant hemorrhagic episodes, bruising, osteoporosis, and changes in lipid metabolism [15-17]. Furthermore, since clinically used Hep and its low molecular weight forms are commonly of porcine or bovine origin, some patients may not be prone to its use, for example, due to religious beliefs or nutritional habits. To overcome all these problems, alternative molecules purified from different sources have been tested so far, prospecting promising results [10, 18-20].

In this context, it has been widely reported that marine organisms are a rich source of bioactive compounds, potentially useful for various medical applications. Among them, sulphated polysaccharides show interesting biological properties, similarly to those reported for mammalian glycosaminoglycans (GAGs) [21], including anticoagulant [19], antimalarial [22], antitumoral [23], anti-HIV-1 [24], as well as anti-inflammatory [25] activities. More in detail, anticoagulant properties have been reported for fucoidan purified from holothurians [26], and seaweeds [27, 28], as well as for fucosylated chondroitin sulphate (FCS), which, as yet, has been found only in the holothurians body wall [29, 30]. These latter, by selectively interfering with intrinsic coagulation pathway with negligible bleeding risk if compared to heparinoids and warfarin, represent a very promising alternative to commonly used anticoagulant drugs [31].

Other marine invertebrates, such as Porifera, have been proven to produce a wide array of bioactive compounds potentially useful for both pharmaceutical and commercial applications [10, 32-35].

A wide diversity of sulphated polysaccharides is synthesized by different species of marine sponges; their structural heterogeneity and complexity, concerning the molecular masses, the relative proportions of constituent sugars, and especially the sulphation degree has been related to their biological role as cell adhesion factors involved in species-specific cell re-aggregation [36-43].

The usefulness of sponge acid polysaccharides for medical applications in the context of cardiovascular diseases has not been investigated so far.

This study focused on the proteolytic extraction of acidic glycans from the marine sponge *Sarcotragus spinosulus*, their purification by anion-exchange chromatography, and the evaluation of their anticoagulant activity. Furthermore, their distribution in the extracellular matrix (ECM) was determined by histological analysis and their cytocompatibility was determined on a human skin fibroblast cell line.

Corresponding polysaccharides fractions were obtained by the same purification procedures from the body wall of *Holothuria tubulosa*, one of the most abundant Mediterranean sea cucumber species, and were used, in this study, as a positive control for coagulation assays, since it has been widely demonstrated that some hexuronate-containing glycans, particularly sulphated fucoidans [44] and FCSs [45, 46] extracted from several holothurians species, represent efficient inhibitors of the coagulation cascade. The structural

characterization of the sponge acidic glycan fraction with the highest anticoagulant potential was assessed via FTIR and NMR.

Results and Discussion

All data collected for *S. spinosulus* were compared with those obtained from the marine invertebrate *H. tubulosa*, for which the presence of acidic polysaccharides able to interfere with the coagulation cascade has been reported by various studies [20, 26].

Histological analysis

Sarcotragus spinosulus

The sponge body, lined by the epidermis, was characterized by two districts i.e., an outer district (ectosome) rich in canals and cavities (aquiferous system) and an inner district (endosome/choanosome) with choanocyte chambers, cavities, and canals. Both districts were filled by extracellular matrix (ECM) harboring different types of isolated cells. The ECM layout was supported by a densely structured collagenic skeletal networks (filamentous and fibrous) and scanty exogenous mineral structures.

The ECM staining with Alcian blue highlighted varying intensities of blue-turquoise in both body districts, where cell nuclei were pinkish. In particular, (i) the sub-epidermis area and (ii) the outlines of cavities and canals (aquiferous system) were intensely blue-turquoise (Figure 3.1). At the inner district (endosome/choanosome), the ECM was blue-turquoise as well, but somewhat less intensely colored than that of the ectosome district (Figure 3.1, panels A and C). The skeletal networks were made of light blue to uncolored filaments and light pinkish to uncolored fibers, the latter sometimes with light blue-turquoise areas (Figure 3.1. A, E).

These results suggest that ECM of *S. spinosulus* is particularly rich in acidic glycans confirming data from literature [47]. Although sponges are the most basal and oldest metazoans, their extracellular matrix (ECM), similarly to that of higher taxa, is mostly composed of collagen and proteoglycan-like molecules, together with minor amounts of structural proteins. According to recent literature, the poriferan polysaccharidic chains of the proteoglycan-like molecules differ from classical mammalian glycosaminoglycans [42, 48].

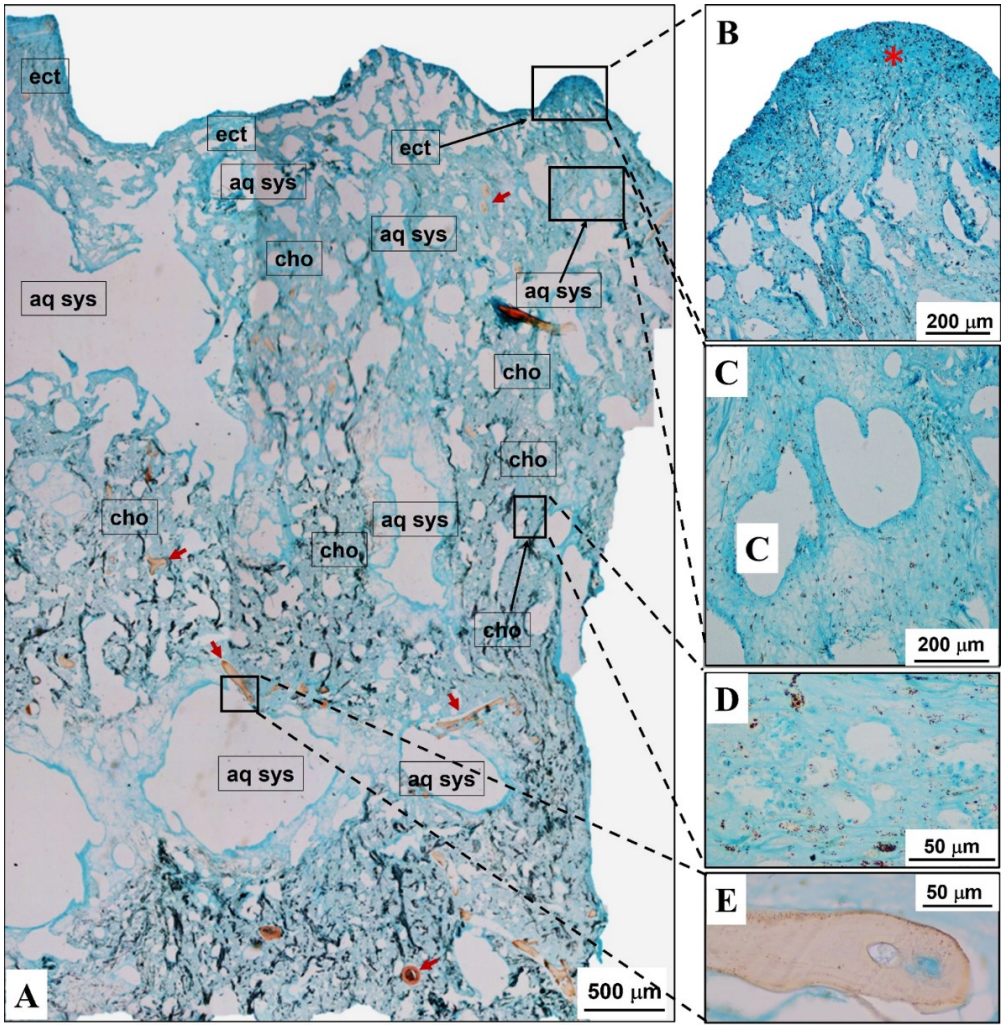

Figure 3.1. *Sarcotragus spinosulus* (Porifera, *Irciniidae*) as a model of body plan architecture in a marine basal Metazoa. (A) Acidic glycans topographic distribution (evidenced by Alcian blue staining) in the ubiquitous ECM highlighted as a range of light blue to blue-turquoise shades at the level of both outer (ectosome, namely ect) and inner (endosome/choanosome, namely cho) body districts. (B) Outer body district (ectosome) with the dermal membrane compact layout (intensely blue-turquoise, red asterisk) and the less colored underlying layer rich of canals and cavities (inner ectosome). Cells with nuclei as pinkish spots. (C) Intensely blue-turquoise shades focus the aquiferous system (aq sys) outlines (cavities and canals, endosome/choanosome) surrounding a less colored ECM. Cells with nuclei as pinkish spots. (D)

Choanocyte chambers within a light blue ECM (endosome/choanosome). (E) Acidic glycans within the skeletal fibers (black arrow).

Holothuria tubulosa

The sea cucumber body wall district was characterized by (i) an epidermis covered by a thin acellular cuticle, and (ii) a dermis connective tissue with few cells embedded in an extremely abundant ECM occupying most of the wall's thickness (Figure 3.2 A). Below the dermis, two muscular layers internally lined the perivisceral coelom (body cavity) i.e., a circular muscles layer and a layer composed by five pairs of longitudinal muscles (Figure 3.2, panels A and D). The body wall was crossed by the pedicellar canals of the aquiferous vascular system (Figure 3.2, panels A and C). The cuticle and dermis were intensely blue-turquoise colored on staining with Alcian blue (Figure 3.2). The epidermis was less intensely colored (Figure 3.2 B). The ECM delimiting the aquiferous pedicellar canals was slightly more colored than the surrounding dermis ECM (Figure 3.2, panels A and C). Also, the ECM compact layer supporting the circular muscles was more colored than the surrounding dermis (Figure 3.2, panels A and D). A light blue turquoise stain was evident within circular and longitudinal muscles (Figure 3.2, panels C and D).

The abundant presence of polysaccharides in the ECM of sea cucumber body wall previously reported [49, 50] has been confirmed in the present study, as evidenced by the intense blue-turquoise staining, indicative of a high amount of acidic glycans in this body district of holothurians.

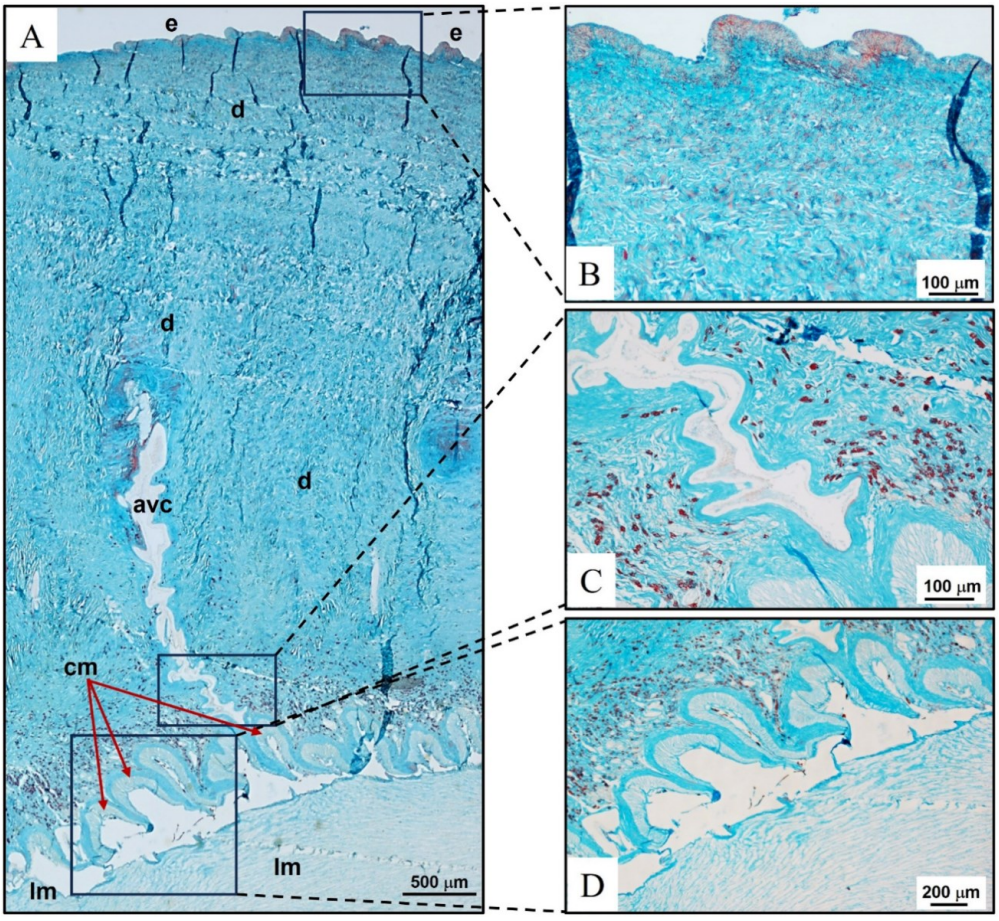

Figure 3.2. *Holothuria tubulosa* (Echinodermata, *Holothuriidae*) as a model of body wall architecture in a complex marine invertebrate (Metazoa). (A) Architecture of the body wall district. Compact dermis with extremely abundant ECM occupying most of the wall's thickness. (B) Intensely blue-turquoise colored thin acellular cuticle and dermis on staining with Alcian blue. The epidermis was less intensely colored. (C) Outline of a pedicellar canal (aquiferous vascular system) more colored than the surrounding body wall dermis ECM. (D) Circular muscles supported by a compact, coat-like ECM more colored than the surrounding dermis. A light blue turquoise stain is evident in circular and longitudinal muscles. Epidermidis (e), dermis (d), aquiferous vascular system (avc), circular muscles (cm), longitudinal muscles (lm).

Purification and Biochemical Analyses

Following papain extraction from the ECM of both species, four polysaccharide fractions were obtained by anion exchange chromatography, by increasing ionic strength step wisely (0.5 M, 1.0M, 1,5M, and 2.0 M LiCl concentration). Each fraction was analyzed for its hexuronate content and subjected to qualitative analysis by electrophoretic techniques. For the sake of clarity, each of the fractions purified from both marine invertebrates was assigned an acronym composed of the initials of the systematic name and number, from 1 to 4, corresponding to the sequential elution order.

Quantitative analysis

All purified fractions were quantified using the carbazole assay as described beyond, yielding positive results for each fraction eluted from all specimens. As reported in Table 3.1, the total yield of hexuronate-containing glycans isolated from *S. spinosulus* was 2.234 mg/g dry weight. Concurrently, considerable variability in the content of uronic acid (UA) was registered for each fraction purified. In particular, the most abundant glycan fractions are represented by Ss3 (43.78 %) and Ss1 (40.15 %).
On the other hand, the total amount of hexuronate-containing glycans extracted from the holothurian body wall was more than double the amount from sponge samples, and mainly represented by Ht3 fraction (86.82 %).

Table 3.1. Yield of each purified fraction, based on the weight of dehydrated delipidated tissue (DDT) from *Sarcotragus spinosulus* (Ss) and *Holothuria tubulosa* (Ht). Data are reported as mean ± standard deviation (*1 n = 18, § n = 7).

Fraction	Total yield (mg UA /g DDT)	Yield (mg UA / g DDT)	Fraction % over total glycans purified
Ss1*	2.234	0.897 ± 0.018	40.15
Ss2*		0.289 ± 0.011	12.94
Ss3*		0.978 ± 0.072	43.78
Ss4*		0.070 ± 0.005	3.13
Ht1§	5.068	0.332 ± 0.010	6.55
Ht2§		0.226 ± 0.017	4.46
Ht3§		4.400 ± 0.115	86.82
Ht4§		0.110 ± 0.010	2.17

Overall, quantitative data indicated that the distribution of hexuronate-containing polysaccharides in the *S. spinosulus* fractions was different compared to *H. tubulosa* fractions, the high-charge and low-charge molecular species being in similar proportions (Table 3.1).

Electrophoretic profiles

Preliminary structural characterization of hexuronate-containing glycan fractions was performed through comparative analysis of electrophoretic profiles on polyacrylamide gel.

Carbohydrate electrophoresis (C-PAGE) allows for the separation of polysaccharides based on their molecular masses; moreover, the treatment with the cationic carbocyanine dye Stains-all stains polysaccharides with specific colors, which turn from blue to purple to yellow as the degree of sulphation increases [51].

All acidic glycan fractions purified from both marine invertebrates consisted of a wide range of molecular weight polysaccharides. Each electrophoretic lane appeared somewhat smeared, a feature also observed for the standard polysaccharides (Figure 3.3).

Moreover, thanks to metachromasia phenomenon caused by the dye used, it could be appreciated that different eluted fractions exhibited different degrees of sulphation, which increased together with the ionic strength of the elution buffer used.

By comparing the colors of sponge fractions lanes with those of standard glycans, it was possible to perceive that Ss1 showed a color shade between that of the non-sulphated high and low molecular weight hyaluronic acid and fucoidan, thus suggesting a very low sulphation degree. Moreover, fraction Ss2 showed a profile similar to fucoidan standard, while Ss3 and Ss4, exhibited a more purplish color with respect to fucoidan but less yellowish than chondroitin sulphate (CS), dermatan sulphate (DS), heparin (Hep), and enoxaparin (E-Hep), suggesting that they were composed of less sulphated glycans, compared to standard glycosaminoglycans. Overall, by comparing corresponding fractions obtained from *S. spinosulus* and *H. tubulosa*, we detected similar patterns for Ss3 and Ht3 only, with the holothurian polysaccharide being considerably more sulphated.

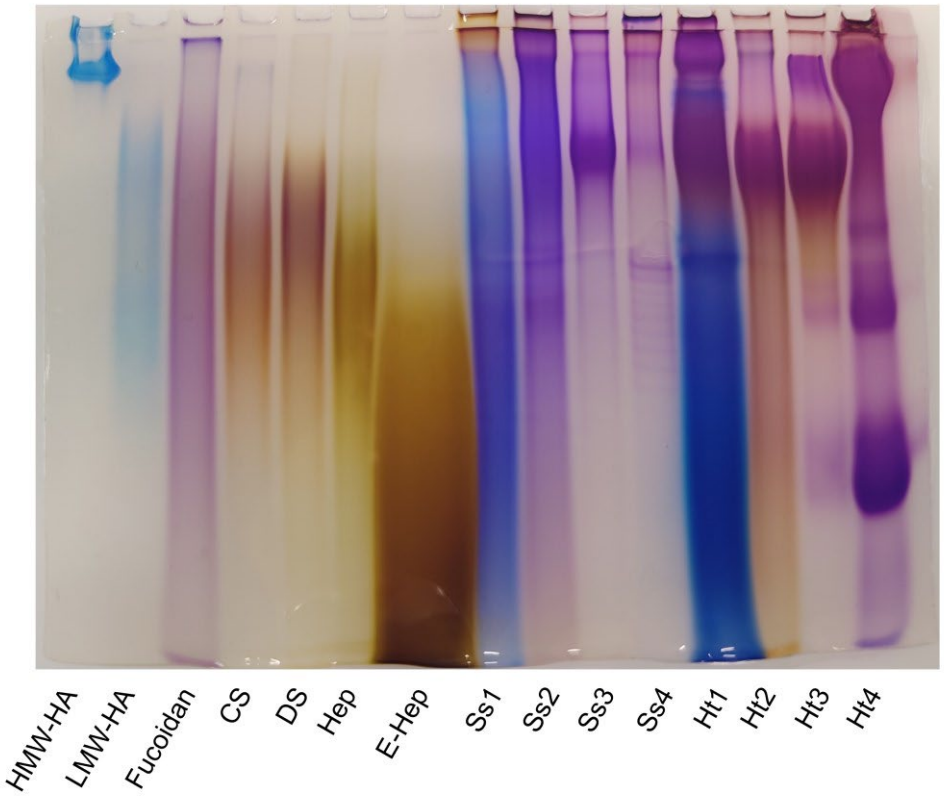

Figure 3.3. Electrophoretic profiles of standard polysaccharides (high molecular weight hyaluronic acid (HMW-HA), low molecular weight hyaluronic acid (LMW-HA), fucoidan, chondroitin sulphate (CS), dermatan sulphate (DS), heparin (Hep), and enoxaparin (E-Hep)) and purified fractions from *S. spinosulus* (Ss1-Ss4) and *H. tubulosa* (Ht1-Ht4).

In vitro cytocompatibility assessment

A preliminary evaluation of the cytocompatibility of each hexuronate-containing glycans fraction purified from *S. spinosulus* was performed herein, for the first time, on Human Fibroblasts, well known to be a model for cell proliferation and adhesion studies, to evaluate their potential side effects on cellular metabolic activity. Reduction potential, positively correlated with cell viability, was evaluated by using PrestoBlue™ reagent, in triplicate for each condition at each timepoint.

Overall, the data obtained showed that all hexuronate-containing fractions purified from *S. spinosulus* did not have remarkable effects on cell viability or proliferation, as no significant changes in reducing potential were observed for any of the assayed concentrations, after 96 and 168 hours of incubation, with respect to untreated controls (Figure 3.4).

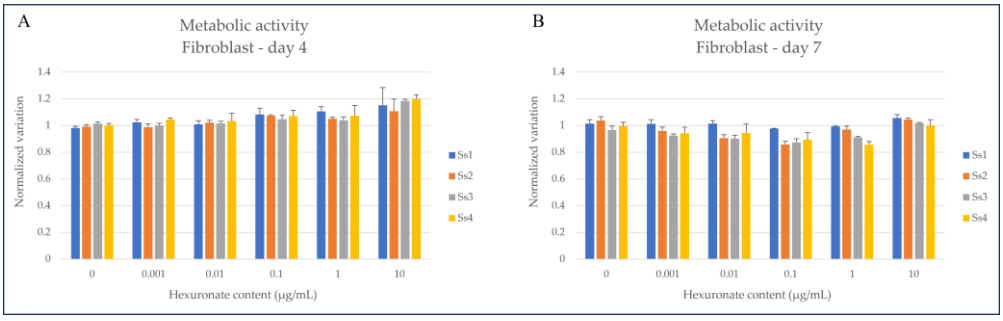

Figure 3.4. Metabolic activity of Human Fibroblast cell line incubated with purified fractions from *S. spinosulus*, measured after 4 and 7 days (panel A and B, respectively). Each eluate was tested at different concentrations, ranging from 0.001 µg/mL to 10 µg/mL, and fluorescence was measured after incubation with PrestoBlue™ reagent.

Anticoagulant Activity of Purified Glycan Fractions

The acidic glycans purified from *S. spinosulus* were herein assessed for their potential activity, *in vitro*, towards the coagulation cascade. The ability of purified fractions from *S. spinosulus* to prolong the clotting time for both the intrinsic and extrinsic pathway of the coagulation cascade was evaluated, using activated partial thromboplastin time (APTT) and prothrombin time (PT) assays respectively, and compared with standard glycosaminoglycans (GAGs) (Hep, E-Hep, CS + DS, and CS), and *H. tubulosa* fractions, assuming both Hep and E-Hep as positive controls.

Inhibition of the Intrinsic Pathway of Coagulation

Figure 3.5 reports the effects of purified fractions from *S. spinosulus* (Ss1-Ss4), compared to both standard GAGs and *H. tubulosa* (Ht1-Ht4) glycans, on the intrinsic cascade of coagulation. As expected, data concerning standard GAGs were consistent with literature, confirming that Hep, together with its low-molecular weight fragments, were the most effective compounds able to inhibit clot formation [52], whereas low or no effects were evidenced for both CS + DS and CS, as previously described [53]. Regarding the four sponge fractions,

no activity was evidenced for the first one, whereas Ss2, Ss3, and Ss4 showed variable inhibitory effects. More in detail, Ss2 fraction showed a limited effect at 25 µg/ml, whereas Ss3 and Ss4 fractions were found to be the most effective inhibitors of the intrinsic pathway at 10 – 25 µg/ml and 25 µg/ml, respectively, with results between those recorded for Hep and E-Hep. By comparing each other the fractions obtained from the two species, those from holothurian samples were more effective in inhibiting coagulation. Indeed, Ht2, Ht3, and Ht4 had remarkable effects, as their inhibitory potential was higher than that of E-Hep, although lower than unfractionated Hep, in agreement with data reported elsewhere [20, 26].

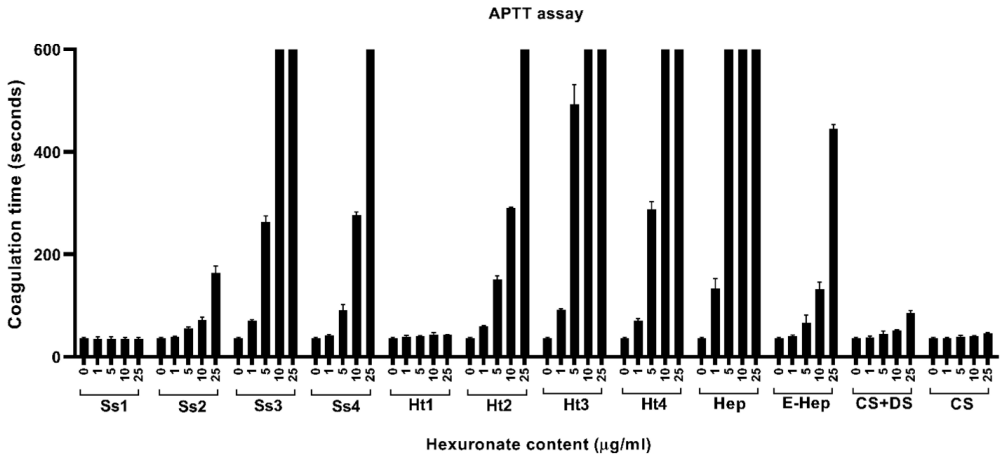

Figure 3.5. *In vitro* anticoagulant activity on intrinsic pathway of acidic glycans fractions purified from *S. spinosulus* (Ss1-Ss4) and *H. tubulosa* (Ht1-Ht4), and standard GAGs. Values are reported as mean ± SD.

As far as we know, the obtained data indicated, for the first time, that acidic polysaccharides from marine sponges, similarly to that extracted from sea cucumbers, can interfere selectively with the contact pathways, even with a lower activity compared to Hep.

Inhibition of the Extrinsic Pathway of Coagulation

Figure 3.6 reports the effects of both standard GAGs and purified fractions from sponge (Ss1-Ss4) and holothurian (Ht1-Ht4) on the extrinsic cascade of coagulation. Among the standard GAGs, only Hep showed inhibitory activity whereas, as expected, no significant effects on PT assay were evidenced for E-Hep, due to the low concentrations used, as indicated by the manufacturer, and

stated elsewhere [54], and for CS + DS and CS. With regards to the purified fractions, only Ss3, and Ss4 were found to be able to slightly extend the PT, with an activity comparable to that observed for Ht3, and Ht4, in agreement with previous papers reporting that holothurian most negatively charged fractions have an inhibitory effect, although reduced with respect to Hep, on the extrinsic pathway [55-57].

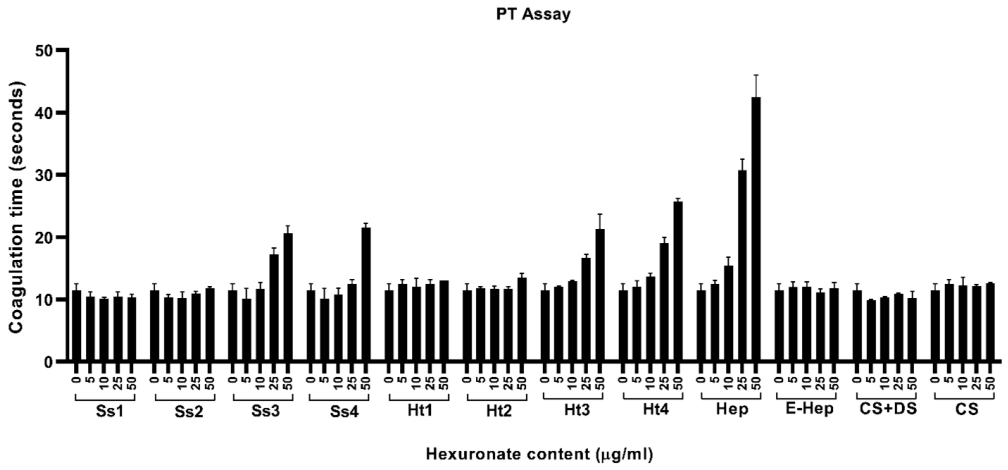

Figure 3.6. *In vitro* anticoagulant activity on extrinsic pathway of acidic glycans fractions purified from *S. spinosulus* (Ss1-Ss4) and *H. tubulosa* (Ht1-Ht4), and standard GAGs. Values are reported as mean ± SD.

All these results were consistent with literature, indicating that sea cucumbers contain FCS with strong anticoagulant activity, particularly on the intrinsic pathway [58]. The anticoagulant properties that we have described for some purified fractions from *S. spinosulus*, may be due to peculiar structural features including saccharide composition, chain length, sulfation pattern, and glycosidic bonds.
Since the fraction that demonstrated to be more effective in inhibiting the formation of the clot, towards both the intrinsic and extrinsic pathway, was Ss3, we decided to elucidate its structure, by means of spectroscopic analyses.

Structural Characterization via FTIR and NMR Spectroscopy

Fourier Transform Infrared (FTIR) Spectroscopy

FTIR spectra of the fractions showing the most remarkable anticoagulant activity from both *S. spinosulus* and *H. tubulosa*, and of CS and fucoidan

standards, were collected between 400 cm-1 and 4000 cm-1, as reported in Figure 3.7. The different signals obtained from standard polysaccharides and the purified fractions showed a high percentage of matching. In fact, a significant absorbance at around 570 cm-1, 1025 cm-1, 1220 cm-1, 1370 cm-1, was detected for every sample, corresponding, respectively, to S-O stretching vibration [59], C–O and C–C stretching vibrations of pyranose ring, demonstrated to be common to all polysaccharides [60, 61], symmetric stretching of S=O [62], uronic acid O-C=O bending or, alternatively, CH3 group bending of L-fucopyranosyl [63, 64]; all these signals are distinctive of polysaccharides, thus proving that the adopted method was effective for the purification of acidic glycans from different sources.

Signals at around 720 cm-1, 930 cm-1, 1130 cm-1, 1160 cm-1, 1417 cm-1, 2945 cm-1, were collected, corresponding to C-H bending, to the presence of 3,6-anhydro-D-galactose [61], to C-C-C symmetric vibrations of glycosidic linkage cycles [26], to C-O-C glycosidic linkage group [64], to O-C=O uronic acid presence [26], and to C-H stretching vibrations [57], respectively. All these characteristic absorptions suggest that the backbone of the glycans present in the third fraction of both *S. spinosulus* and *H. tubulosa* is similar to CS, since they all contain glucuronic acid, and that the differences observed may be due to the presence of fucosyl branches in Ss3 and Ht3 polysaccharides, as suggested by the signal detected at 962 cm-1, corresponding to both asymmetric and symmetric vibrations of methyl groups in fucose residues, as reported by previous studies [65].

As highlighted by some signals recorded at 677 cm-1, as well as in the region of 800-840 cm-1, the third fraction from both *S. spinosulus* and *H. tubulosa* contains polysaccharides with a high degree of sulphation, besides containing a secondary amine, as evidenced by the signal recorded at 1544 cm-1 and 1555 cm-1, for Ss3 and Ht3 respectively, corresponding to C-N vibrations of N-acetyl group [64].

Overall, the analysis of acquired spectra, corroborated by both FTIR and NMR data from the literature, allowed us to determine characteristics absorption bands, likely corresponding to FCS polysaccharide chain, consisting of the repeating trisaccharide unit N-Acetyl-D-glucosamine and D-glucuronic acid backbone branched with L-Fucose, previously reported to be exclusive of the body wall of several sea cucumber species. Therefore, FTIR data suggest the presence of the branched acidic glycan FCS in the complex three-dimensional dynamic network that surrounds and provides structural support to sponge cells.

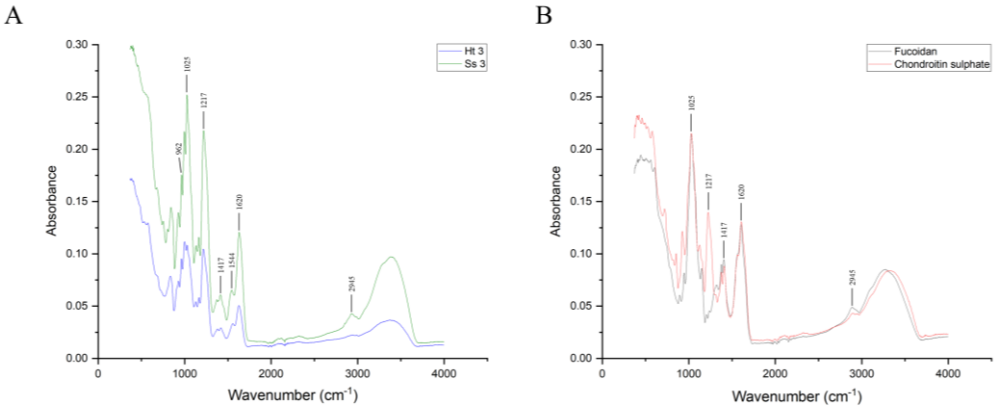

Figure 3.7. FTIR spectra of Ss3 (green), and Ht3 (blue) fractions of *S. spinosulus* and *H. tubulosa* (A), and of standard fucoidan (black), and CS (red) (B).

Nuclear Magnetic Resonance (NMR) Analysis

A preliminary analysis was conducted by proton (1H) nuclear magnetic resonance (NMR). Recorded signals indicated that the purified fractions Ss3 and Ht3 showed characteristic signals of fucose (Fuc), N-Acetylgalactosamine (GalNAc), and hexuronic acid. (Figure 3.8). Signals recorded at δ 1.21 ppm were assigned to unsulphated Fuc (Fuc) [66, 67], at δ 2.00 ppm to GalNAc [67-69], and at δ 3.59 to non-substituted glucuronic acid (GlcA) residues [66]. Another significant signal was detected, in both spectra, at δ 0.85 ppm, corresponding to a methyl group matching with the presence of Fuc residues. Moreover, Ss3 spectrum presented a further peak at δ 3.39, corresponding to H-2 of non-substituted GlcA residues [66], thus confirming the presence of hexuronic acid in the structure of this polysaccharide fraction.

No information on branching, sulphation degree, or molar ratio of monosaccharides were obtained from the structural analyses performed. Although, data recorded by NMR confirmed results obtained by infrared spectroscopy, indicating that Ss3 and Ht3 polysaccharides share common structural features, these findings deserve further confirmation due to the great heterogeneity and complexity described for poriferan ECM polysaccharides.

Species-specific variations in both chemical composition and molecular masses of sulphated polysaccharides have been reported [37, 42]. This wide structural diversity probably reflects their pivotal role in sponge ECM organization and in the well known sponge adaptive strategies, such as cell

totipotence, cell dedifferentiation, chronic morphogenesis, and modular/clonal organization of body plan [36, 38-41, 43].

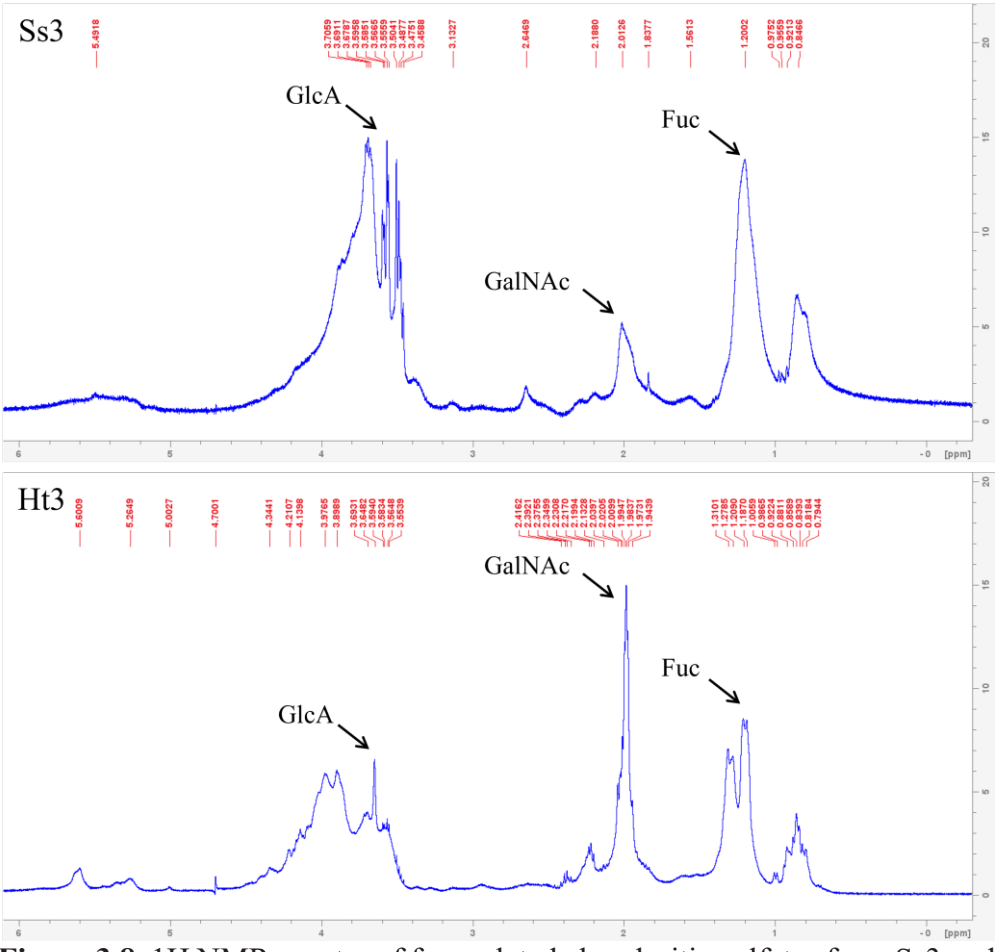

Figure 3.8. 1H NMR spectra of fucosylated chondroitin sulfates from Ss3 and Ht3.

Materials and Methods

Chemicals and Equipments

High molecular weight hyaluronic acid (HMW-HA) sodium salt from Streptococcus equi (1,500,000-1,750,000 Da), low molecular weight hyaluronic acid (LMW-HA) sodium salt from Streptococcus equi (8,000-15,000 Da), chondroitin sulphate (CS) sodium salt from bovine trachea, dermatan sulphate (DS) from porcine intestinal mucosa, heparan sulphate (HS) sodium salt from bovine kidney, heparin (Hep) sodium salt from porcine intestinal mucosa, fucoidan from marine brown algae *Macrocystis pyrifera*, glycerol, Stains-all, cresol red, deuterium oxide, trizma base (Tris), lithium chloride, sodium acetate, acrylamide/bis-acrylamide 30 % solution (29:1), alcian blue 8GX, diethylami-noethyl-(DEAE)Sephacel, ethylenediaminetetraacetic acid (EDTA), L-cysteine, neutral red, and glucuronolactone were purchased from Merck (Merck KGaA, Darmstadt, Germany). Ethanol was bought from Honeywell International Inc (Charlotte, North Carolina, USA). Papain, sulphuric acid, magnesium chloride, Dulbecco's Modified Eagle Medium (DMEM) high glucose, GlutaMAX™ Supplement, Fetal Bovine Serum (FBS), Phosphate buffer saline (PBS), PrestoBlue™ Cell Viability Reagent, were acquired from Thermo Fisher Scientific Inc. (Waltham, Massachusetts, USA). A low molecular weight heparin (E-Hep), namely enoxaparin, which trade name is Clexane®, was purchased from Sanofi (Paris, France), while activated partial thromboplastin time (APTT) (Dade® Actin® FSL), and prothrombin time (PT) (Dade® Innovin®) assay kits were purchased from Siemens Healthcare GMBH (Erlangen, Germany). Coagulation control plasma was from Biolab Diagnostics (Sant'Antonio Abate, Italy). Formic acid, formalin, acetone, sodium tetraborate decahydrate, carbazole, and acetic acid were from Carlo Erba Reagents GMBH (Emmendingen, Germany). Human fibroblast (CRL-2522 ATCC®) cell line was collected from American Type Culture Collection (Rockville, Maryland, USA). Amicon Ultra-15 Centrifugal Filter Units were produced by Millipore (Massachusetts, USA). Xylene, and paraffin were from Bio-Optica Milano spa (Milano, Italy). Econo-Column chromatography columns, GS-800 calibrated densitometer, Mini Protean II cell vertical slab gel electrophoresis apparatus were acquired from Bio-Rad laboratories (Hercules, California, USA). VictorX5 Multimode Plate Reader was bought from PerkinElmer (Waltham, Massachusetts, USA). Bruker alpha compact FT-IR spectrometer and Bruker Avance III 400 MHz NMR spectrometer were from

Bruker (Karlsruhe, Germany). Edwards Modulyo Freeze Dryer was from Edwards Vacuum (Burgess Hill, United Kingdom). Nikon ECLIPSE 80i Light Microscope, Nikon Digital-Sight DS-FI camera, and Nikon D3100 reflex camera were acquired from Nikon Corporation (Tokyo, Japan).

Experimental Models

Sarcotragus spinosulus Schmidt, 1862 (Porifera, Dictyoceratida, Irciniidae) is a sessile, benthic, basal Metazoa with no organs and true tissues. It is a *photophilous* demosponge inhabiting Mediterranean shallow waters, with asymmetric, massive, rounded growth form. Its body surface, brownish in color, black to dark grey *in vivo*, is irregularly conulose and entirely covered by a dermal membrane; the interior is orange to light brown. The three-dimensional collagenic (horny) endoskeleton with a complex architecture is embedded in the amorphous jelly-like extracellular matrix (ECM) of the entire sponge body [40].

Holothuria tubulosa Gmelin, 1791 (*Echinodermata, Holothuroidea, Holothuriidae*) is a benthic, sedentary, complex Metazoa living in the Mediterranean Sea (surface to 100 m depth). Its bilateral body is roughly cylindrical along the oroaboral axis, dark brown, with numerous conical papillae [61]. The body wall of connective tissue rich of ECM, with embedded calcareous skeletal ossicles, encircles the coelom in which internal organs are localized.

Sponge and Holothurian Sample Harvesting

Reared specimens of *S. spinosulus* were collected from a sustainable, shallow water experimental sponge culture plant [62,63] harboured in the Tramariglio Cove (40°35'32.47"N 8°10'11.50"E, Capo Caccia - Isola Piana Marine Protected Area, Northern Sardinian Sea, Western Mediterranean). Wild specimens of *H. tubulosa* were collected along the Porto Torres coast (40°50'17.781" N 8°24'33.955" E, Asinara Gulf, Northern Sardinian Sea, Western Mediterranean). All specimens of sponges and holothurians were immediately kept in sea water in refrigerated bags and transferred to the Sassari University laboratories.

Histological Analyses

Representative body fragments of *S. spinosulus* were dissected, after hypothermia, by means of a scalpel. For downstream histological evaluation, samples were fixed in formalin 10 %, at room temperature, before being fully

dehydrated in ascending ethanol series, cleared in xylene, and embedded in paraffin.

Specimens of *H. tubulosa* were killed by hypothermia and body wall fragments were fixed in formalin 10 %, at room temperature, then rinsed in distilled water and decalcified, in formic acid 8 % for 24 h, to remove skeletal ossicles. After decalcification, samples were rinsed in distilled water and then dehydrated in an ascending ethanol series, cleared in xylene, and embedded in paraffin.

Sponges and holothurians samples were sectioned at intervals of 3 µm and stained with Alcian blue (pH 2.5) to verify the presence and topographic distribution of acidic glycans, and counterstained with neutral red to detect nuclei of cells. Slides were examined under a Nikon ECLIPSE 80i Light Microscope, and microphotographs were taken with a Nikon Digital-Sight DS-FI camera.

Acidic Glycans Purification

Body fragments (n = 18) of *S. spinosulus* and body wall fragments (n = 7) of *H. tubulosa* were put in absolute ethanol for 120 h, at 4 °C, and then finely minced, before being incubated in acetone for 24 h, in order to achieve complete dehydration and delipidation. Samples were centrifuged at 5,000 x g for 15 min and the supernatant was discarded. After complete acetone evaporation, dehydrated and delipidated tissue (DDT) was rehydrated, with 0.1 M sodium acetate buffer, pH 6.0, containing 5 mM EDTA, and 5 mM cysteine (15 mL per gram of tissue), at 4 °C for 24 h. Proteolytic treatment was performed, by adding 1 U of papain per mg of DDT, at 56 °C for 48 hours; enzyme activity was stopped by boiling the mixture, at 100 °C, for 5 min. After centrifugation at 5,000 x g for 10 min, the supernatant was recovered and immediately loaded into a chromatography column packed with DEAE-Sephacel anion exchange resin (10 mL of resin per gram of digested tissue), previously equilibrated with 50 mM sodium acetate, pH 6.0. The same buffer was used to wash the column until absorbance, measured at 280 nm, was less than 0.05. Acidic glycans were fractionated by performing four separate elution steps using 20 mM Tris-HCl buffer, pH 8.6, containing alternatively 0.5 M, 1 M, 1.5 M, and 2 M lithium chloride. Eluates were concentrated and dialyzed against deionized water, by means of Amicon Ultra-15 Centrifugal Filter Units with 3 kDa cut-off, according to manufacturer's instructions. The following acronyms have been assigned to each purified fraction, to indicate the four different elutions: 0.5 M fraction from *S. spinosulus* and *H. tubulosa*, Ss1 and Ht1, respectively; 1 M fraction from *S. spinosulus* and *H. tubulosa*,

Ss2 and Ht2, respectively; 1.5 M fraction from *S. spinosulus* and *H. tubulosa*, Ss3 and Ht3, respectively; 2 M fraction from *S. spinosulus* and *H. tubulosa*, Ss4 and Ht4, respectively. All samples were assayed in duplicate.

Hexuronic Acid Quantification

Each eluate was assayed for uronic acid (UA) content, by the method of Bitter and Muir [64], using glucuronolactone as standard, as reported elsewhere [65]. Briefly, 250 μL of either standard (from 5 to 40 µg UA/mL) or eluate were added with 1.25 mL of 25 mM sodium tetraborate decahydrate in concentrated sulphuric acid, and incubated at 85 °C for 10 min. Afterwards, 50 μL of carbazole were added and, following 15 min boiling, absorbance was read at 530 nm.

C-PAGE

Carbohydrate electrophoresis [51] was carried out in a Mini Protean II cell vertical slab gel electrophoresis apparatus, using 13.5 % T, 3 % C polyacrylamide running gels, overlaid with 5 % T, 3 % C stacking gel, using 40 mM acetic acid, 40 mM Tris-HCl, pH 7.8, solution as running buffer. A volume corresponding to 2.5 µg, in terms of UA, of each standard polysaccharide and glycan fraction was freeze-dried and then resolubilized in 10 µL of 62.5 mM Tris-HCl, pH 7.8, 10 % glycerol, and 0.002 % cresol red, and loaded into the wells. Run was performed at 50 V for the first 10 min and then at 120 V until the dye front reached the bottom of the gel. Staining was performed by incubating every gel with 50 mL of a solution of 50 % ethanol containing 0.005 % Stains-all dye, overnight and in the dark, at room temperature. Gels were rehydrated with distilled water before being photographed with a Nikon D3100 reflex camera and acquired using GS-800 calibrated densitometer.

Cell Culture and Metabolic Activity Assay

Cytocompatibility of all fractions of acidic glycans purified from *S. spinosulus* was assessed, *in vitro*, on human skin fibroblasts cell line (ATCC, CRL-2522), to preliminary evaluate the biological effects of these compounds. More in detail, metabolic activity was evaluated by means of PrestoBlue™ Cell Viability Reagent, according to manufacturer's instructions. Briefly, 5 x 104 cells/well were suspended in 90 µL of DMEM added with 10 % FBS, seeded in a 96-well plate, and treated with 10 µL of complete culture medium

containing different polysaccharide final concentrations (0.001, 0.01, 0.1, 1, and 10 μg/mL, expressed as UA content). Untreated cells were used as control. At every time point, 11 μL of PrestoBlue™ were added to each well, and well-plates were incubated, at 37 °C, 5 % CO2. After 45 min, the solution of PrestoBlue™/DMEM+10 % FBS was transferred into a new well plate, and fluorescence was measured with the excitation/emission wavelengths set at 540/590 nm, with VictorX5 multilabel counter. Cells were rinsed with PBS, and 100 μl of new culture media containing 10 % FBS together with the abovementioned concentrations of acidic glycans, were added to each well. Experiments were performed in triplicate.

Coagulation Assays

The anticoagulant activity of the four eluted fractions from *S. spinosulus* was evaluated *in vitro* and compared with that of *H. tubulosa* purified glycans, as well as standard glycosaminoglycans (GAGs), including Hep, E-Hep, as well as CS and DS, using commercially available kits by Siemens Healthcare. In particular, activated partial thromboplastin time (APTT) (Dade® Actin® FSL), and prothrombin time (PT) (Dade® Inno-vin®) assays were performed to evaluate the inhibition of the intrinsic and extrinsic coagulation pathways, respectively. Commercial human coagulation control plasma was used for all coagulation tests.

Four dilutions of each sample were prepared and tested, in order to assess the effects of these polysaccharides on the inhibition of clot formation. In particular, APTT assay was performed with the following concentrations of either standard GAGs or purified glycans: 1 μg/mL, 5 μg/mL, 10 μg/mL, and 25 μg/mL, while the impact on the extrinsic pathway of the coagulation cascade was assayed for concentrations of 5 μg/mL, 10 μg/mL, 25 μg/mL, and 50 μg/mL.

APTT assay was carried out according to manufacturer's guidelines. Briefly, 100 μL of plasma, previously added with purified polysaccharides or standard GAGs, were mixed with 100 μL of prewarmed FSL reagent and incubated, at 37 °C, for 3 min; then, 100 μL of a prewarmed 25 mM calcium chloride solution were added, and the resulting fibrin clot formation time was measured by optical detection.

PT assay was performed following producer's instructions, as well. More in detail, 100 μL of plasma, containing purified acidic glycans or standard GAGs, were incubated at 37 °C for 1 minute and 200 μL of prewarmed Dade®

Innovin® Reagent were added. Clot formation time was measured by optical detection.
All measurements were conducted in triplicate and the results were reported as mean and standard deviation.

Fourier Transform Infrared (FTIR) Spectroscopy

Hexuronate-containing fractions with remarkable anticoagulant properties, as well as standard fucoidan and CS, were freeze-dried overnight, followed by Fourier transform infrared spectroscopy (FTIR) analyses. Spectra were collected using a Bruker Alpha spectrometer, with 128 scans at a spectral resolution of 2 cm-1.
All measurements were performed in the range of 400-4000 cm-1, at room temperature. Data were acquired and processed by Bruker Opus software, release 8.7.

Nuclear Magnetic Resonance (NMR) Spectroscopy

NMR spectra were recorded on a Bruker Avance III 400 MHz spectrometer (1H NMR: 400.13 MHz). A volume corresponding to 10 mg of both Ss3 and Ht3 fractions was freeze-dried and dissolved in 650 µL of 99.9% D2O. Measurements were performed at 298 K, with HOD suppression by pre-saturation. Signals were analyzed by TopSpin 4.3.0 software (Bruker).

Conclusions

In this study, four acidic polysaccharides fractions purified from the marine sponge *Sarcotragus spinosulus* were analyzed, to evaluate their biological activity towards the coagulation pathway, besides determining their localization and abundance in the extracellular matrix (ECM), as well as assessing their cytocompatibility, *in vitro*. Histological analyses on representative sponge samples allowed us to confirm that Porifera ECM is rich in acidic glycans.
All purified fractions were proven to contain hexuronic acid, although in variable proportions. A preliminary assessment, in terms of sulphate content, was performed by C-PAGE, confirming that sulphation degree increased together with the ionic strength of the buffer used for elution. Additionally, cytocompatibility of all sponge fractions was evaluated on a human cell line, showing no remarkable negative effects on cell viability, thus suggesting that these glycans did not interfere with essential metabolic pathways. Further

experiments will be carried out to assess the full biocompatibility of these acidic glycans *in vivo*.

Moreover, the ability to inhibit the coagulation process was evaluated for each of the four sponge fractions, and the results indicated that the third and fourth hexuronate-containing fractions were able to strongly interfere with the intrinsic pathway of the coagulation cascade, showing effects comparable to the activities obtained for heparin (Hep) and enoxaparin (E-Hep). The same fractions also showed inhibitory activity, albeit to a lesser extent, on the extrinsic pathway. In this context, our results can have a valuable impact, as sulphated polysaccharides from marine invertebrates have been shown to possess beneficial and adjustable anticoagulant activity, even though with a lower activity with respect to Hep.

Both FTIR and NMR analyses performed on Ss3 fraction suggested that, by comparing obtained spectra with those from Ht3 and with data reported in literature, the most abundant polysaccharide contained hexuronic acid, N-Acetylgalactosamine, and fucose, indicative of a fucosylated chondroitin sulphate.

Altogether, the results presented in this paper demonstrate, for the first time, the presence of acidic glycans with anticoagulant activity in ECM of keratose sponges belonging to genus *Sarcotragus*, whose structure showed similarities with fucosylated chondroitin sulphate extracted from sea cucumbers body wall. Further investigations will be carried out, aiming at confirming the obtained results, performing more detailed structural analyses, and assessing the clear structure–activity relationship of the sponge acidic polysaccharides, besides evaluating which coagulation factors are inhibited by these glycans.

The great diversity and metabolite complexity of marine sponges, as a key renewable source in sustainable shallow water plants, could represent a useful tool for applications in bioinspired bioactive compounds science and technologies. The present findings suggest that the fucosylated chondroitin sulphate fraction purified from *S. spinosulus* could be a candidate new anticoagulant drug, useful as a substitute for currently adopted antithrombotics.

Author Contributions: Conceptualization: G.N., G.O., M.F., A.J.L.; Methodology: G.N., G.O., A.J.L.; Validation: G.O., Formal analysis: G.N., G.O., A.J.L.; Investigation: G.N., G.O., C.C., A.B., T.C., R.M., G.A.S., Resources: A.B., T.C., R.M., G.A.S., G.A.D., M.F., A.J.L.; Data curation: G.N., G.O., C.C., T.C., R.M., Writing – original draft: G.N., T.C., R.M., M.F.,

A.J.L.; Writing – review & editing: G.N., G.O., C.C., A.B., T.C., R.M., G.A.S., G.A.D., M.F., A.J.L.; Visualization: G.N., G.O., C.C., G.A.S., Supervision: M.F., A.J.L.; Project administration: G.N., G.O., A.J.L.; Funding acquisition: M.F., A.J.L..

Funding: G.N.: M.F. and A.J.L. thank the Fondazione di Sardegna (BANDO FONDAZIONE DI SARDEGNA 2022 E 2023—PROGETTI DI RICERCA DI BASE DIPARTIMENTALI (D.R.16/2022)) and the European Union (PROGETTI DI RICERCA INTERDISCIPLINARE – DM 737/2021, RISORSE 2021 – 2022, Finanziato dall'Unione europea – NextGenerationEU) for their financial support.

Acknowledgement: We thank Dr. Maria Orecchioni (Department of Chemical, Physical, Mathematical and Natural Sciences, University of Sassari, Italy) for the NMR spectra. The authors are grateful to CIRTEBEC - Centro Interuniversitario di Ricerca sulle Tecnologie per i Beni Culturali - GAUSS Laboratories of the Università degli Studi di Sassari for providing instrumentations.

Data Availability Statement: The data presented in this study are available on request from the corresponding authors.

Conflicts of Interest: The authors declare no conflicts of interest.

References

[1] Chaudhry, R., S.M. Usama, and H.M. Babiker, *Physiology, Coagulation Pathways*, in *StatPearls*. 2023: Treasure Island (FL) ineligible companies. Disclosure: Syed Muhammad Usama declares no relevant financial relationships with ineligible companies. Disclosure: Hani Babiker declares no relevant financial relationships with ineligible companies.

[2] Palta, S., R. Saroa, and A. Palta, *Overview of the coagulation system.* Indian J Anaesth, 2014. 58(5): p. 515-23.

[3] Thornton, P. and J. Douglas, *Coagulation in pregnancy.* Best Pract Res Clin Obstet Gynaecol, 2010. 24(3): p. 339-52.

[4] Davie, E.W. and O.D. Ratnoff, *Waterfall Sequence for Intrinsic Blood Clotting.* Science, 1964. 145(3638): p. 1310-2.

[5] Macfarlane, R.G., *An Enzyme Cascade in the Blood Clotting Mechanism, and Its Function as a Biochemical Amplifier.* Nature, 1964. 202: p. 498-9.

[6] Achneck, H.E., et al., *Pathophysiology of bleeding and clotting in the cardiac surgery patient: from vascular endothelium to circulatory assist device surface.* Circulation, 2010. 122(20): p. 2068-77.

[7] Smith, S.A., R.J. Travers, and J.H. Morrissey, *How it all starts: Initiation of the clotting cascade.* Crit Rev Biochem Mol Biol, 2015. 50(4): p. 326-36.

[8] Lasne, D., B. Jude, and S. Susen, *From normal to pathological hemostasis.* Can J Anaesth, 2006. 53(6 Suppl): p. S2-11.

[9] He, S., et al., *The Clotting Trigger Is an Important Determinant for the Coagulation Pathway In Vivo or In Vitro-Inference from Data Review.* Semin Thromb Hemost, 2021. 47(1): p. 63-73.

[10] Carvalhal, F., et al., *Antithrombotics from the Sea: Polysaccharides and Beyond.* Mar Drugs, 2019. 17(3).

[11] Ashorobi, D., M.A. Ameer, and R. Fernandez, *Thrombosis*, in *StatPearls*. 2023.

[12] Goldhaber, S.Z. and H. Bounameaux, *Pulmonary embolism and deep vein thrombosis.* Lancet, 2012. 379(9828): p. 1835-46.

[13] Montano, A., D.F. Hanley, and J.C. Hemphill, 3rd, *Hemorrhagic stroke.* Handb Clin Neurol, 2021. 176: p. 229-248.

[14] Curnow, J., L. Pasalic, and E.J. Favaloro, *Why Do Patients Bleed?* Surg J (N Y), 2016. 2(1): p. e29-e43.

[15] Garcia, D.A., et al., *Parenteral anticoagulants: Antithrombotic Therapy and Prevention of Thrombosis, 9th ed: American College of Chest Physicians Evidence-Based Clinical Practice Guidelines.* Chest, 2012. 141(2 Suppl): p. e24S-e43S.

[16] Alban, S., *Adverse effects of heparin.* Handb Exp Pharmacol, 2012(207): p. 211-63.

[17] Patel, S., et al., *Warfarin*, in *StatPearls*. 2023.

[18] Vasconcelos, A.A. and V.H. Pomin, *Marine Carbohydrate-Based Compounds with Medicinal Properties.* Mar Drugs, 2018. 16(7).

[19] Cao, S., et al., *Anticoagulant and Antithrombotic Properties in Vitro and in Vivo of a Novel Sulfated Polysaccharide from Marine Green Alga Monostroma nitidum.* Mar Drugs, 2019. 17(4).

[20] Yang, L., et al., *Separation, purification, structures and anticoagulant activities of fucosylated chondroitin sulfates from Holothuria scabra.* Int J Biol Macromol, 2018. 108: p. 710-718.
[21] Senni, K., et al., *Marine polysaccharides: a source of bioactive molecules for cell therapy and tissue engineering.* Mar Drugs, 2011. 9(9): p. 1664-1681.
[22] Marques, J., et al., *Marine organism sulfated polysaccharides exhibiting significant antimalarial activity and inhibition of red blood cell invasion by Plasmodium.* Sci Rep, 2016. 6: p. 24368.
[23] Khalifa, S.A.M., et al., *Marine Natural Products: A Source of Novel Anticancer Drugs.* Mar Drugs, 2019. 17(9).
[24] Sanniyasi, E., et al., *In vitro anti-HIV-1 activity of the bioactive compound extracted and purified from two different marine macroalgae (seaweeds) (Dictyota bartayesiana J.V.Lamouroux and Turbinaria decurrens Bory).* Sci Rep, 2019. 9(1): p. 12185.
[25] Jayawardena, T.U., et al., *Anti-Inflammatory Effects of Sulfated Polysaccharide from Sargassum Swartzii in Macrophages via Blocking TLR/NF-Kappab Signal Transduction.* Mar Drugs, 2020. 18(12).
[26] Mansour, M.B., et al., *Primary structure and anticoagulant activity of fucoidan from the sea cucumber Holothuria polii.* Int J Biol Macromol, 2019. 121: p. 1145-1153.
[27] Luthuli, S., et al., *Therapeutic Effects of Fucoidan: A Review on Recent Studies.* Mar Drugs, 2019. 17(9).
[28] Zhao, Y., et al., *Fucoidan Extracted from Undaria pinnatifida: Source for Nutraceuticals/Functional Foods.* Mar Drugs, 2018. 16(9).
[29] Xu, H., et al., *Holothurian fucosylated chondroitin sulfates and their potential benefits for human health: Structures and biological activities.* Carbohydr Polym, 2022. 275: p. 118691.
[30] Zhang, L., et al., *Chemical Synthesis of Fucosylated Chondroitin Sulfate Oligosaccharides.* J Org Chem, 2020. 85(24): p. 15908-15919.
[31] Xiao, C., et al., *Nonasaccharide Inhibits Intrinsic Factor Xase Complex by Binding to Factor IXa and Disrupting Factor IXa-Factor VIIIa Interactions.* Thromb Haemost, 2019. 119(5): p. 705-715.
[32] Langasco, R., et al., *Natural collagenic skeleton of marine sponges in pharmaceutics: Innovative biomaterial for topical drug delivery.* Mater Sci Eng C Mater Biol Appl, 2017. 70(Pt 1): p. 710-720.
[33] Huang, X., et al., *Streptomyces tirandamycinicus sp. nov., a Novel Marine Sponge-Derived Actinobacterium With Antibacterial Potential Against Streptococcus agalactiae.* Front Microbiol, 2019. 10: p. 482.
[34] Anjum, K., et al., *Marine Sponges as a Drug Treasure.* Biomol Ther (Seoul), 2016. 24(4): p. 347-62.
[35] Murray, P.M., et al., *Sustainable production of biologically active molecules of marine based origin.* N Biotechnol, 2013. 30(6): p. 839-50.
[36] Spillmann, D., et al., *Characterization of a novel sulfated carbohydrate unit implicated in the carbohydrate-carbohydrate-mediated cell aggregation of the marine sponge Microciona prolifera.* J Biol Chem, 1995. 270(10): p. 5089-97.
[37] Guerardel, Y., et al., *Molecular fingerprinting of carbohydrate structure phenotypes of three porifera proteoglycan-like glyconectins.* J Biol Chem, 2004. 279(15): p. 15591-603.

[38] Misevic, G.N., et al., *Molecular recognition between glyconectins as an adhesion self-assembly pathway to multicellularity.* J Biol Chem, 2004. 279(15): p. 15579-90.
[39] Carvalho de Souza, A., et al., *Adhesion forces in the self-recognition of oligosaccharide epitopes of the proteoglycan aggregation factor of the marine sponge Microciona prolifera.* Glycoconj J, 2009. 26(4): p. 457-65.
[40] Vilanova, E., et al., *Sulfated polysaccharides from marine sponges: conspicuous distribution among different cell types and involvement on formation of in vitro cell aggregates.* Cell Tissue Res, 2010. 340(3): p. 523-31.
[41] Vilanova, E., C.C. Coutinho, and P.A. Mourao, *Sulfated polysaccharides from marine sponges (Porifera): an ancestor cell-cell adhesion event based on the carbohydrate-carbohydrate interaction.* Glycobiology, 2009. 19(8): p. 860-7.
[42] Zierer, M.S. and P.A. Mourao, *A wide diversity of sulfated polysaccharides are synthesized by different species of marine sponges.* Carbohydr Res, 2000. 328(2): p. 209-16.
[43] Vilanova, E., et al., *Carbohydrate-Carbohydrate Interactions Mediated by Sulfate Esters and Calcium Provide the Cell Adhesion Required for the Emergence of Early Metazoans.* J Biol Chem, 2016. 291(18): p. 9425-37.
[44] Ustyuzhanina, N.E., et al., *Influence of fucoidans on hemostatic system.* Mar Drugs, 2013. 11(7): p. 2444-58.
[45] Li, H., et al., *Low-molecular-weight fucosylated glycosaminoglycan and its oligosaccharides from sea cucumber as novel anticoagulants: A review.* Carbohydr Polym, 2021. 251: p. 117034.
[46] Ustyuzhanina, N.E., et al., *Depolymerization of a fucosylated chondroitin sulfate from Cucumaria japonica: Structure and activity of the product.* Carbohydr Polym, 2022. 281: p. 119072.
[47] Stocchino, G.A., et al., *Sponges architecture by colour: new insights into the fibres morphogenesis, skeletal spatial layout and morpho-anatomical traits of a marine horny sponge species (Porifera).* The European Zoological Journal, 2021. 88(1): p. 237-253.
[48] Yamada, S., K. Sugahara, and S. Ozbek, *Evolution of glycosaminoglycans: Comparative biochemical study.* Commun Integr Biol, 2011. 4(2): p. 150-8.
[49] Khotimchenko, Y., *Pharmacological Potential of Sea Cucumbers.* Int J Mol Sci, 2018. 19(5).
[50] Hossain, A., D. Dave, and F. Shahidi, *Sulfated polysaccharides in sea cucumbers and their biological properties: A review.* Int J Biol Macromol, 2023. 253(Pt 7): p. 127329.
[51] Andrade, J.P.S., et al., *A color-code for glycosaminoglycans identification by means of polyacrylamide gel electrophoresis stained with the cationic carbocyanine dye Stains-all.* Electrophoresis, 2018. 39(4): p. 666-669.
[52] Sobieraj, D.M., et al., *Comparative effectiveness of low-molecular-weight heparins versus other anticoagulants in major orthopedic surgery: a systematic review and meta-analysis.* Pharmacotherapy, 2012. 32(9): p. 799-808.
[53] Bougatef, H., et al., *Purification, compositional analysis, and anticoagulant capacity of chondroitin sulfate/dermatan sulfate from bone of corb (Sciaena umbra).* Int J Biol Macromol, 2019. 134: p. 405-412.
[54] Tobu, M., et al., *Influence of different anticoagulant agents on fibrinopeptide a generation.* Clin Appl Thromb Hemost, 2003. 9(4): p. 273-92.

[55] Gao, N., et al., *Purification, structural characterization and anticoagulant activities of four sulfated polysaccharides from sea cucumber Holothuria fuscopunctata.* Int J Biol Macromol, 2020. 164: p. 3421-3428.
[56] Ma, Y., et al., *Five distinct fucan sulfates from sea cucumber Pattalus mollis: Purification, structural characterization and anticoagulant activities.* Int J Biol Macromol, 2021. 186: p. 535-543.
[57] Li, X., et al., *A regular fucan sulfate from Stichopus herrmanni and its peroxide depolymerization: Structure and anticoagulant activity.* Carbohydr Polym, 2021. 256: p. 117513.
[58] Ustyuzhanina, N.E., et al., *Fucosylated Chondroitin Sulfates from the Sea Cucumbers Paracaudina chilensis and Holothuria hilla: Structures and Anticoagulant Activity.* Mar Drugs, 2020. 18(11).
[59] Shang, F., et al., *Structural analysis and anticoagulant activities of three highly regular fucan sulfates as novel intrinsic factor Xase inhibitors.* Carbohydr Polym, 2018. 195: p. 257-266.
[60] Shi, D., et al., *Comparison of hydrothermal depolymerization and oligosaccharide profile of fucoidan and fucosylated chondroitin sulfate from Holothuria floridana.* Int J Biol Macromol, 2019. 132: p. 738-747.
[61] Pereira, L., S.F. Gheda, and P.J.A. Ribeiro-Claro, *Analysis by Vibrational Spectroscopy of Seaweed Polysaccharides with Potential Use in Food, Pharmaceutical, and Cosmetic Industries.* International Journal of Carbohydrate Chemistry, 2013. 2013: p. 537202.
[62] Vandanjon, L., et al., *The Use of FTIR Spectroscopy as a Tool for the Seasonal Variation Analysis and for the Quality Control of Polysaccharides from Seaweeds.* Mar Drugs, 2023. 21(9).
[63] Ben Mansour, M., et al., *Characterization and anticoagulant activity of a fucosylated chondroitin sulfate with unusually procoagulant effect from sea cucumber.* Carbohydr Polym, 2017. 174: p. 760-771.
[64] Myron, P., S. Siddiquee, and S.A. Azad, *Partial structural studies of fucosylated chondroitin sulfate (FuCS) using attenuated total reflection fourier transform infrared spectroscopy (ATR-FTIR) and chemometrics.* Vibrational Spectroscopy, 2017. 89: p. 26-36.
[65] Cai, Y., et al., *An anticoagulant fucan sulfate with hexasaccharide repeating units from the sea cucumber Holothuria albiventer.* Carbohydr Res, 2018. 464: p. 12-18.
[66] Mourao, P.A., et al., *Structure and anticoagulant activity of a fucosylated chondroitin sulfate from echinoderm. Sulfated fucose branches on the polysaccharide account for its high anticoagulant action.* J Biol Chem, 1996. 271(39): p. 23973-84.
[67] Yang, W., et al., *NMR characterization and anticoagulant activity of the oligosaccharides from the fucosylated glycosaminoglycan isolated from Holothuria coluber.* Carbohydrate Polymers, 2020. 233: p. 115844.
[68] Ustyuzhanina, N.E., et al., *Fucosylated Chondroitin Sulfates with Rare Disaccharide Branches from the Sea Cucumbers Psolus peronii and Holothuria nobilis: Structures and Influence on Hematopoiesis.* Pharmaceuticals, 2023. 16(12): p. 1673.
[69] Ustyuzhanina, N.E., et al., *Fucosylated chondroitin sulfates from the sea cucumbers Holothuria tubulosa and Holothuria stellati.* Carbohydrate Polymers, 2018. 200: p. 1-5.

Chapter 4
Marine-Derived Sulfated Polysaccharides Enhance Hemocompatibility and Endothelialization of Nanofibrous PCL for Vascular Graft applications

Gabriele Obino[a,b*], Gabriele Nieddu[a*], Magdolna Nagy[c], Hans Ippel[c], Tiziana Cubeddu[d], Henri M. H. Spronk[c], Tilman M. Hackeng[c], Marilena Formato[a], Antonio J. Lepedda[a**] and Lorenzo Moroni[b**]

*GO and GN contributed equally to this work

**AJL and LM contributed equally to this work

[a]Department of Biomedical Sciences, University of Sassari, Viale San Pietro, 43b, 07100 Sassari, Italy
[b]MERLN Institute for Technology-Inspired Regenerative Medicine, Complex Tissue Regeneration Department, Maastricht University, 6200 MD Maastricht, The Netherlands
[c]Department of Biochemistry, Cardiovascular Research Institute Maastricht (CARIM), Maastricht University, Universiteitssingel 50, 6229 ER, Maastricht, The Netherlands
[d]Department of Veterinary Medicine, University of Sassari, Via Vienna 2, 07100 Sassari, Italy

The content of this chapter has been published in *Cell Biomaterials*
DOI:10.1016/j.celbio.2025.100155

Abstract

Despite the growing need for small-caliber tissue-engineered vascular grafts (sTEVGs), no clinically approved substitutes exist, largely due to thrombotic failure. We recently purified a fucosylated chondroitin sulfate from two marine invertebrates, *Holothuria tubulosa* (Ht) and *Sarcotragus spinosulus* (Ss), which showed strong anticoagulant activity and *in vitro* cytocompatibility. This study aimed to develop nanofibrous PCL electrospun scaffolds functionalized with these marine polysaccharides to improve hemocompatibility and endothelialization. The functionalized scaffolds exhibited anticoagulant and anti-platelet properties and supported endothelial cell colonization. Human microvascular endothelial cells cultured on the scaffolds formed a confluent monolayer within four days, confirmed by VE-Cadherin and von Willebrand Factor expression. These results demonstrate that cross-linking PCL scaffolds with sulfated marine polysaccharides is a promising strategy for overcoming current sTEVG limitations.

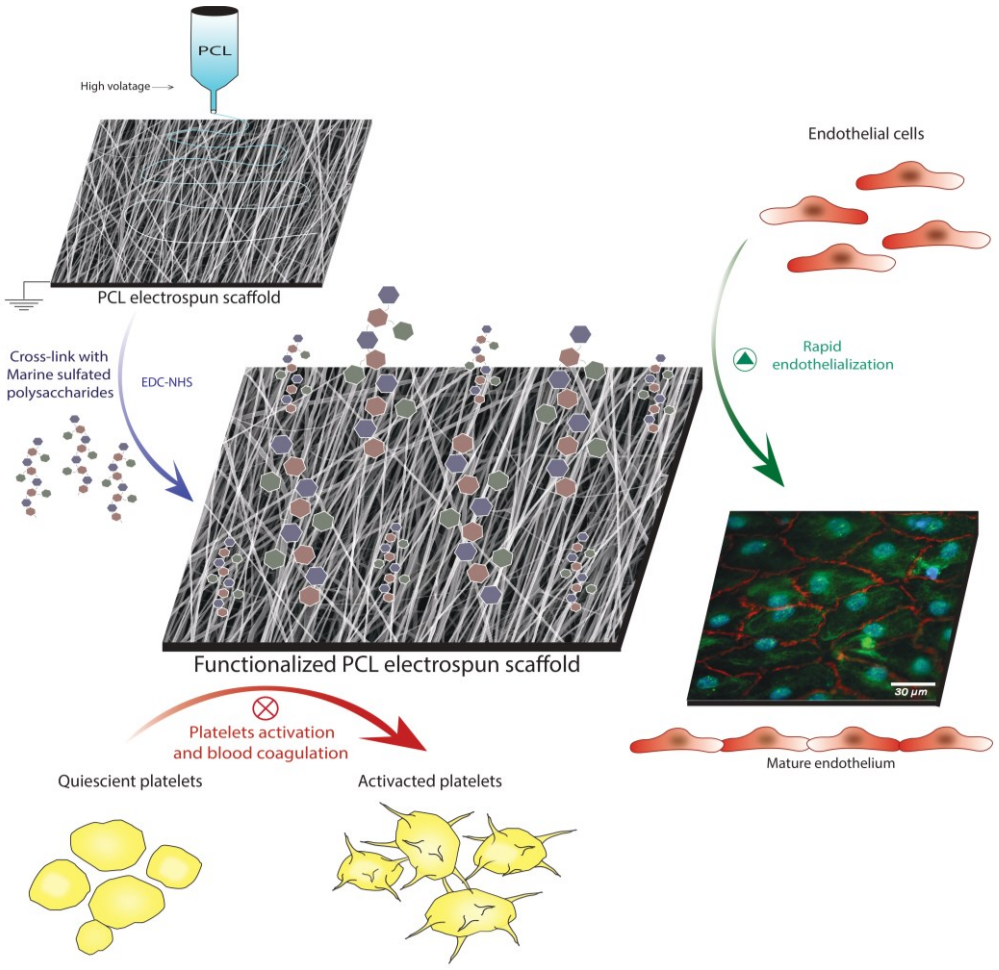

Graphical Abstract: Schematic representation of the functionalization of electrospun PCL scaffolds with marine sulfated polysaccharides to enhance hemocompatibility and endothelialization.

Introduction

Grafts approved for clinical use are currently limited to medium and large caliber vessels, such as the aorta and major arteries. Commonly employed materials include polyethylene terephthalate (PET) and expanded polytetrafluoroethylene (ePTFE) [1–4]. However, there is no synthetic option available for small caliber substitutes fabrication [5], posing a significant challenge, as coronary artery disease and peripheral artery disease are leading causes of mortality globally [6]. Concerning coronary arteries, bypass grafting is mainly performed by using autologous blood vessels, typically the saphenous vein or the mammary artery. However, this procedure is constrained by the limited availability of healthy vessels in such patients and the invasive harvesting procedures [7]. Accordingly, a major challenge is to design small-caliber tissue-engineered vascular grafts (sTEVG) that combine mechanical properties similar to natural blood vessels with biocompatibility, controlled biodegradability, and a specific combination of molecular signals allowing for vascular regeneration, besides being readily available as off-the-shelf product. Hemocompatibility and endothelialization are two critical factors for the success of vascular grafts. High hemocompatibility prevents blood clotting and inflammation, while rapid and stable endothelialization forms a protective lining that mimics natural blood vessels, reducing thrombosis and improving long-term graft patency.

Various fabrication strategies have been used to obtain biocompatible nanofibrous scaffolds tailored for small-caliber blood vessels. Among the most promising approaches, electrospinning, 3D bioprinting, and solvent casting/particulate leaching have emerged as leading techniques for sTEVG fabrication. Electrospinning represents a versatile technique for creating nanofibers that mimic the structure of the extracellular matrix (ECM) of blood vessels, providing scaffolds with favorable mechanical properties and a high surface-to-volume ratio [8–11].

Several synthetic polymers, such as poly(Ɛ-caprolactone) (PCL), poly(lactic-co-glycolic acid) (PLGA), and polyurethane (PU), have been widely used to produce nanofiber sTEVG because of their mechanical strength and tunable degradation rates. However, none of them encloses all the properties required for an ideal sTEVG. In fact, synthetic polymers are typically hydrophobic, hindering rapid endothelialization of the graft, and lead to thrombosis due to interactions between blood proteins and the material surface [12,13]. Addressing these challenges, recent studies have focused on surface functionalization and coating using bioactive natural molecules, such as

collagen, elastin, fibrinogen, silk fibroin, alginate, chitosan, dextran, glycosaminoglycans, and selected growth factors, to enhance graft performance. This strategy has been shown to effectively promote rapid endothelialization. However, the coating itself can, under certain conditions, contribute to thrombogenesis [14,15]. These molecules may also stimulate cell migration and angiogenesis, further enhancing graft integration with surrounding tissue and promoting long-term patency [16,17].
Among them, Heparin has been one of the most widely used [18]. Besides the anti-coagulant activity, its highly negative charge allows to bind and stabilize growth factors such as VEGF and FGF2 [19–21], and to increase the hydrophilicity of the sTEVG, significantly improving its performance by refining anticoagulant properties, promoting endothelialization, and enhancing tissue integration [14,15]. Although heparin is a strong anticoagulant, it may not fully prevent platelet adhesion and aggregation on its own, but the effect is stronger when combined with other antiplatelet agents or advanced coatings [20].
Some sulfated polysaccharides from marine organisms showed interesting anticoagulant and antiplatelet aggregation properties, including the fucosylated chondroitin sulfate found exclusively in some Holothurian species [22–26]. In this respect, we have recently purified a fucosylated chondroitin sulfate from the Mediterranean sponge *Sarcotragus spinosulus* (Ss) and the echinoderm *Holothuria tubulosa* (Ht) showing inhibitory activity towards both the intrinsic and extrinsic pathways of coagulation, *in vitro* [27].
This study presents an innovative strategy that leverages the unique bioactive properties of these polysaccharides to functionalize electrospun PCL scaffolds. The engineered constructs demonstrate improved *in vitro* hemocompatibility and endothelialization, as well as decreased platelet adhesion. These results effectively overcome key challenges in sTEVG design, marking a noteworthy advancement in vascular tissue engineering.

Results

NMR Spectroscopy

The ^{1}H-NMR spectrum of polysaccharides extracted from Ht was comparable to previously reported spectra for fucosylated chondroitin sulfate from other *Holothuria* species, confirming its structural identity. The ^{1}H-NMR spectra (Figure S4.1) of both Ht and Ss revealed common structural features, including signals corresponding to N-acetylgalactosamine (GalNAc) and Fucose (Fuc)

residues. However, ^{1}H spectra of Ss sugar protons displayed broader resonances. In addition, notable difference between Ht and Ss was observed for the ^{1}H peak clustered around 2.1 ppm, likely attributable to multiple GalNAc acetyl groups. The relative peak intensity was significantly higher in the Ht spectrum, suggesting a greater abundance of GalNAc residues.
Sulfation patterns were partially identified in both polysaccharides: the Ss polysaccharide exhibited C4 sulfation of fucose, whereas the Ht polysaccharide showed more complex sulfation, with fucose residues sulfated at C2, C4, and in some cases at both positions (Figure S4.2, S4.3, S4.4). Based on the Ss NMR spectra, two distinct Fuc spin systems could be fully assigned, starting from the methyl group of Fuc C6, with one Fuc residue sulfated at C4. However, at least five additional Fuc spin systems with distinct substitution patterns were identified, which showed broad, correlated signals and thus remained only partially assignable. This diverse sulfation pattern is consistent with the structural complexity commonly observed in marine polysaccharides [27]. The presence of fucosylated chondroitin sulfate in Ht was further confirmed by its close match to known ^{13}C carbon NMR data in the literature [28,29]. While both polysaccharides share fundamental structural components, the more intricate sulfation patterns and stronger peak intensities in Ht distinguish it from Ss, potentially leading to differences in their biological activities.

Physicochemical Properties of Electrospun Scaffolds

The electrospun PCL scaffolds were thoroughly characterized to evaluate their potential for vascular tissue engineering applications. SEM analysis revealed the presence of both random and aligned fibers with smooth surfaces and uniform diameters (Figures S4.5A and B), averaging 872 ± 690 nm and 608 ± 422 nm (Figure S4.6), respectively.
The successful functionalization of the PCL scaffolds with the marine sulfated polysaccharides, Ht and Ss, was confirmed using Attenuated Total Reflectance Fourier Transform Infrared Spectroscopy (ATR-FTIR). The ATR-FTIR analysis revealed characteristic peaks at 3400 cm^{-1} and 1650 cm^{-1}, indicating effective crosslinking with EDC/NHS chemistry due to the presence of –OH and -NH stretching (3400 cm^{-1}) and of the amide stretching (1650 cm^{-1}) present in the scaffolds functionalized with Ht, Ss and Hep (Figure 4.1).

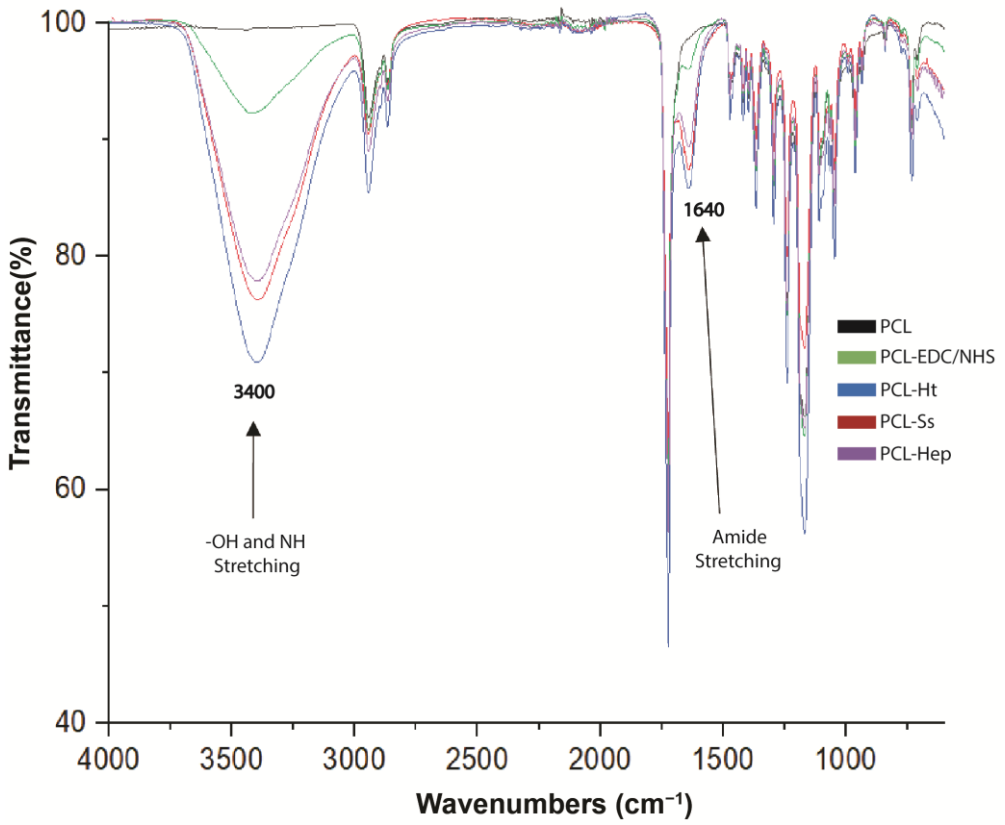

Figure 4.1. ATR-FTIR spectra of naked PCL, aminolyzed PCL treated with EDC/NHS (PCL-EDC/NHS), PCL functionalized with Hep (PCL-Hep), or with polysaccharides from Ht (PCL-Ht) and Ss (PCL-Ss).

Results from the TBO assay revealed that scaffolds incubated in PBS at 37 °C for 30 days exhibited no significant change in the amount of surface-bound sulfated polysaccharides compared to baseline measurements, demonstrating the robust stability of the covalent crosslinking achieved via EDC/NHS chemistry (Figure 4.2A). Additionally, scaffolds stored for 12 months at room temperature under dry conditions maintained levels of bound polysaccharides that were comparable to those of freshly functionalized scaffolds, despite a slight statistically significant difference likely due to variations in batch functionalization efficiency (Figure 4.2B). Notably, the amount of hexuronic acid used for functionalization was consistent across all conditions, the use of marine sulfated polysaccharides resulted in a higher binding efficiency, with a

higher concentration of molecules attached per scaffold (Figure 4.2B and 4.2C). Moreover, the crosslinking enhanced the scaffold's hydrophilicity, as demonstrated by a significant reduction in water contact angles from 125° ± 2°, for naked PCL, to 55.5° ± 3° and < 10°, for PCL-Ht and PCL-Ss, respectively (Figure 4.2D).

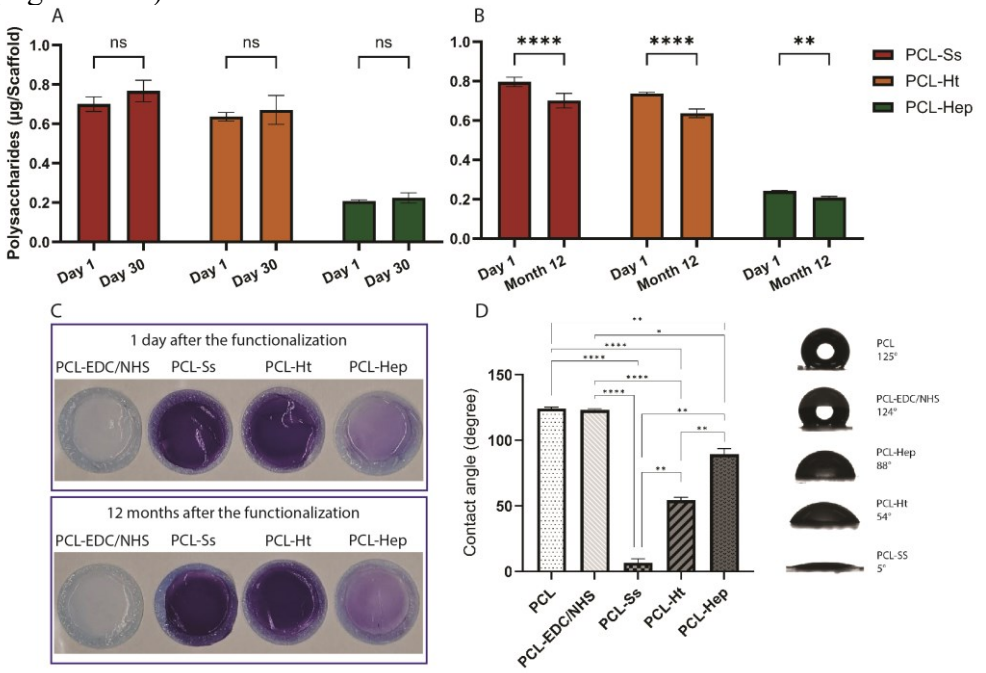

Figure 4.2. TBO staining of functionalized scaffolds and surface wettability of modified scaffolds. A) Quantification of sulfate polysaccharides before and after incubation in PBS for 30 days at 37 °C. B) Quantification of sulfated polysaccharides before and after storage for 12 months. D)Water contact angle (WCA) analysis on PCL, PCL-EDC/NHS, PCL-Ss, PCL-Ht and PCL-Hep. *p<0.05, **p < 0.01, **** p < 0.0001.

Coagulation Assays

The impact of polysaccharide functionalization on scaffold-induced plasma coagulation was examined through activated partial thromboplastin time (aPTT) and prothrombin time (PT) assays. Notably, scaffolds functionalized with polysaccharides extended PPP coagulation time in both assays compared to untreated controls, evidencing an inhibitory effect on both intrinsic (aPTT) and extrinsic (PT) coagulation pathways (Figure 4.3). Specifically, in the aPTT

assay, PPP pre-incubated with heparin-functionalized scaffolds exhibited the most substantial increase in coagulation time, followed by scaffolds treated with the polysaccharides from Ss and Ht (Figure 3A). The PT assay showed a slight, yet statistically significant, effect of polysaccharides from Ss and Ht (Figure 4.3B).

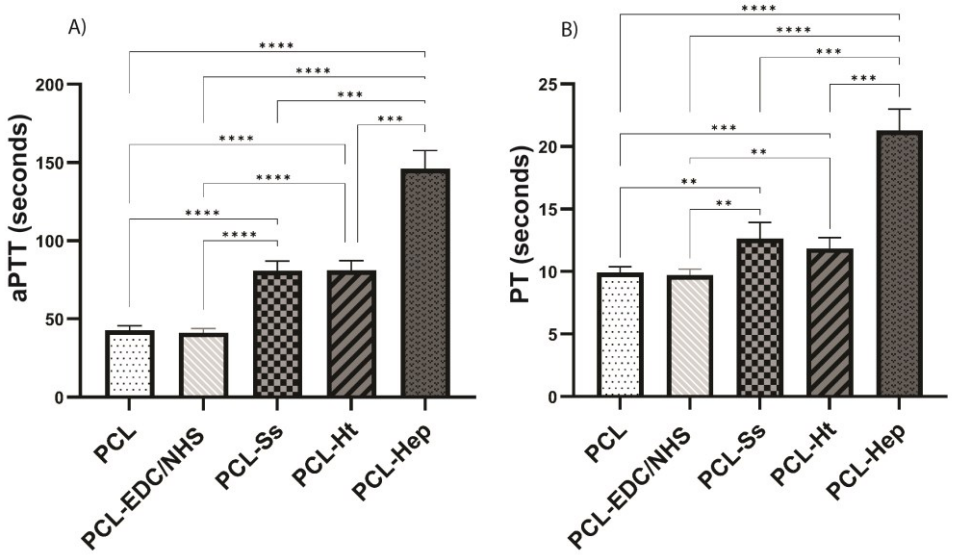

Figure 4.3. Clotting time analysis. Histograms reporting PPP clotting time, following incubation with scaffolds, with regards to the intrinsic (aPTT assay) (A) and extrinsic (PT assay) (B) coagulation assays. **p < 0.01, *** p < 0.001, **** p < 0.0001.

Platelets Adhesion Assays

Platelet adhesion was evaluated, after static incubation of scaffolds with PRP, using the LDH assay. A significant decrease in platelets attached to the surface of PCL-Ss or PCL-Ht, compared to the controls (PCL and/or PCL EDC/NHS), was evidenced. Conversely, PCL functionalization with heparin did not show any significant reduction in platelet adhesion (figure 4.4).

These findings were further validated by fluorescent microscopy using Phalloidin staining and SEM analysis, which confirmed reduced platelet coverage on PCL-Ss and PCL-Ht with respect to both controls and PCL-Heparin (figure 4.5). Moreover, the images revealed distinct differences in platelet morphology and aggregation: platelets on PCL-Collagen and PCL-EDC/NHS scaffolds appeared more aggregated and activated, showing

extended filopodia and pronounced elongations that indicate enhanced cytoskeletal reorganization and robust adhesion to the scaffold, whereas those on PCL-BSA and scaffolds treated with sulfated polysaccharides exhibited a more spherical, non-aggregated morphology. These morphological differences were even more pronounced at higher magnification (5000× and 14000×; figure S4.7).

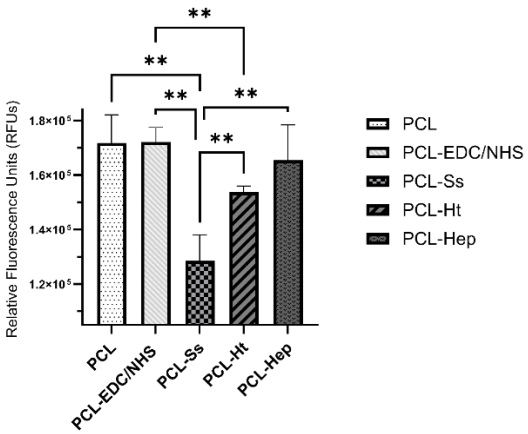

Figure 4.4. Quantification of platelet adhesion by LDH assay. ** $p < 0.01$.

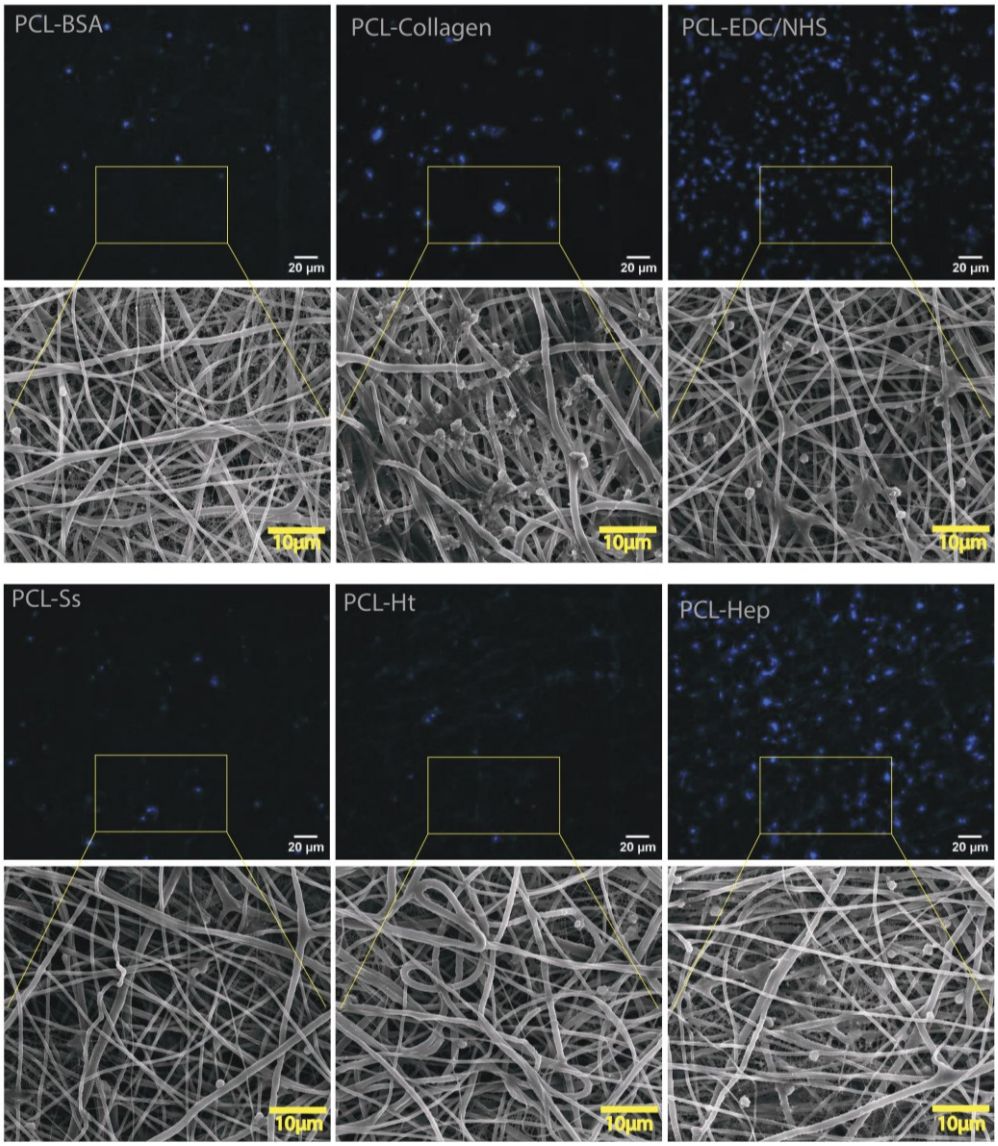

Figure 4.5. Platelets adhesion on scaffolds after 2 hours of static incubation at 37 °C with PRP. Platelets adherent to PCL-BSA, PCL-Collagen, PCL-EDC/NHS, PCL-Ss, PCL-Ht, and PCL-Hep were evidenced by Blue-fluorescence microscopy (Phalloidin staining, 60× magnification, scale bar: 20 µm). Corresponding SEM images were obtained to assess platelet morphology and distribution on fibers (2000× magnification, scale bar: 10 µm).

Cell Culture on Scaffolds: Metabolic Activity and Proliferation.

Endothelial cell colonization and proliferation on scaffolds treated with marine sulfated polysaccharides (Ht and Ss) were significantly enhanced, as evidenced by proliferation and metabolic activity assays (figure 4.6A and 4.6B, respectively), as well as immunohistochemistry (figures 4.7 and 4.8). At 24 hours post-seeding (Day 1), cell numbers were significantly higher on the PCL-Ht and PCL-Ss compared to the other conditions, indicating enhanced cell colonization on scaffolds treated with marine polysaccharides. This trend persisted at Day 4, with significantly higher DNA content on PCL-Ht and PCL-Ss. By Day 7, DNA content on these scaffolds remained elevated, consistent with the increased metabolic activity. However, by Day 14, the differences in DNA content among the various conditions began to decrease. By Day 21, all scaffolds exhibited similar cell numbers, with the only notable difference being between the PCL and PCL-Hep. hMVECs cultured on scaffolds treated with marine polysaccharides showed a significantly increased metabolic activity at days 1, 4, and 7. Interestingly, from day 14 onwards the metabolic activity of cells cultured on PCL, PCL-EDC/NHS or PCL-Hep was higher compared to both PCL-Ss and PCL-Ht. This suggests that hMVECs growing on scaffolds functionalized with marine polysaccharides reached a quiescent status earlier, while cells growing in a less biocompatible environment required a longer time to activate, proliferate and form a mature endothelium.

hMVECs achieved rapid and complete endothelialization on PCL-Ss and PCL-Ht scaffolds by day 4, as shown in Figures S4.8 and S4.9. In contrast, full endothelialization of the PCL, PCL-EDC/NHS, and PCL-Hep scaffolds was only observed by day 21. Notably, cells cultured on scaffolds functionalized with marine polysaccharides exhibited distinct morphological changes, characterized by a more spread-out configuration and the formation of mature adherent junctions, as indicated by VE-cadherin staining (Figures 4.7 and 4.8). Furthermore, hMVECs grown on aligned nanofibers developed an organized, aligned morphology (Figure 8), closely resembling the native endothelial alignment observed in blood vessels (alignment quantification reported in Figure S4.10).

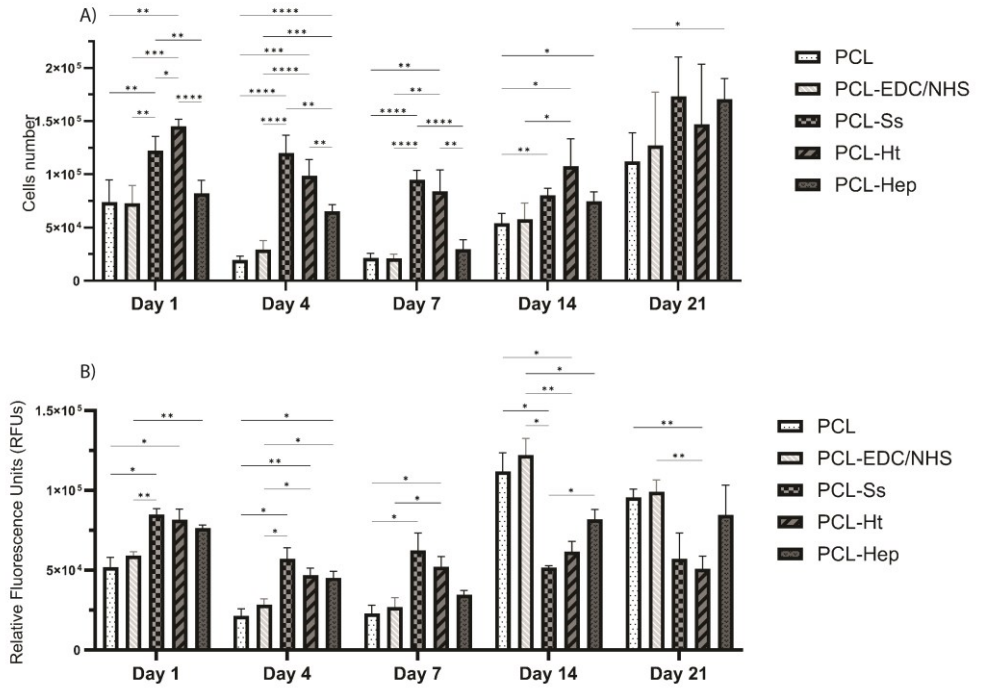

Figure 4.6. hMVEC proliferation and metabolic activity. Proliferation (A) and metabolic activity (B) assays results on hMVECs during 21-day culture on naked PCL, PCL-EDC/NHS, PCL-Hep, PCL-Ht, and PCL-Ss. *p < 0.05, **p < 0.01, *** p < 0.001, **** p < 0.0001

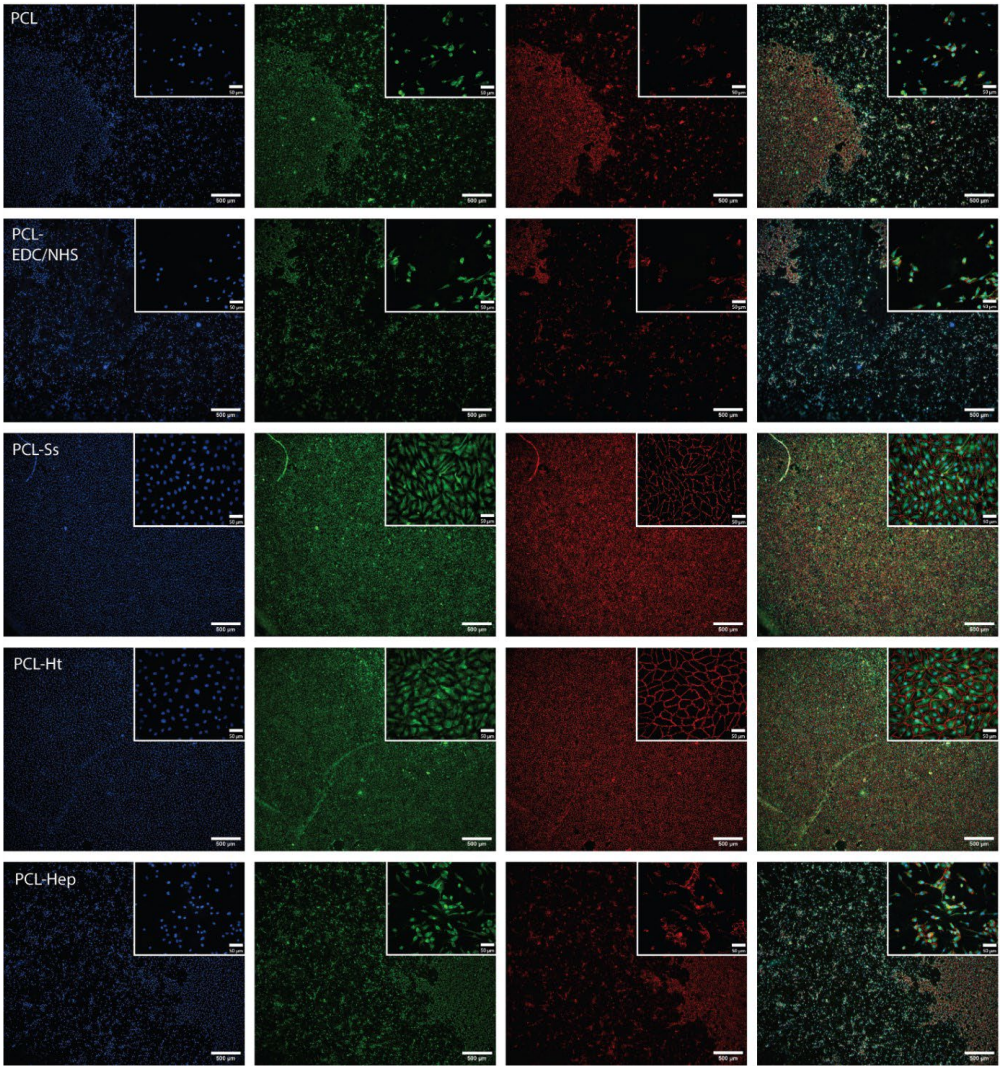

Figure 4.7. Immunostaining of human microvascular endothelial cells (hMVECs) after 7 days of culture on random fiber scaffolds treated with marine sulfated polysaccharides from Ss (PCL-Ss) and Ht (PCL-Ht), Hep (PCL-Hep), and two controls (PCL and PCL-EDC/NHS). Cells were stained with DAPI (blue), von Willebrand Factor (VWF, green), and Ve-Cadherin (Ve-Cad, red). Magnification 4x (scale bar 500 μm) and in insets 40x (scale bar 50 μm).

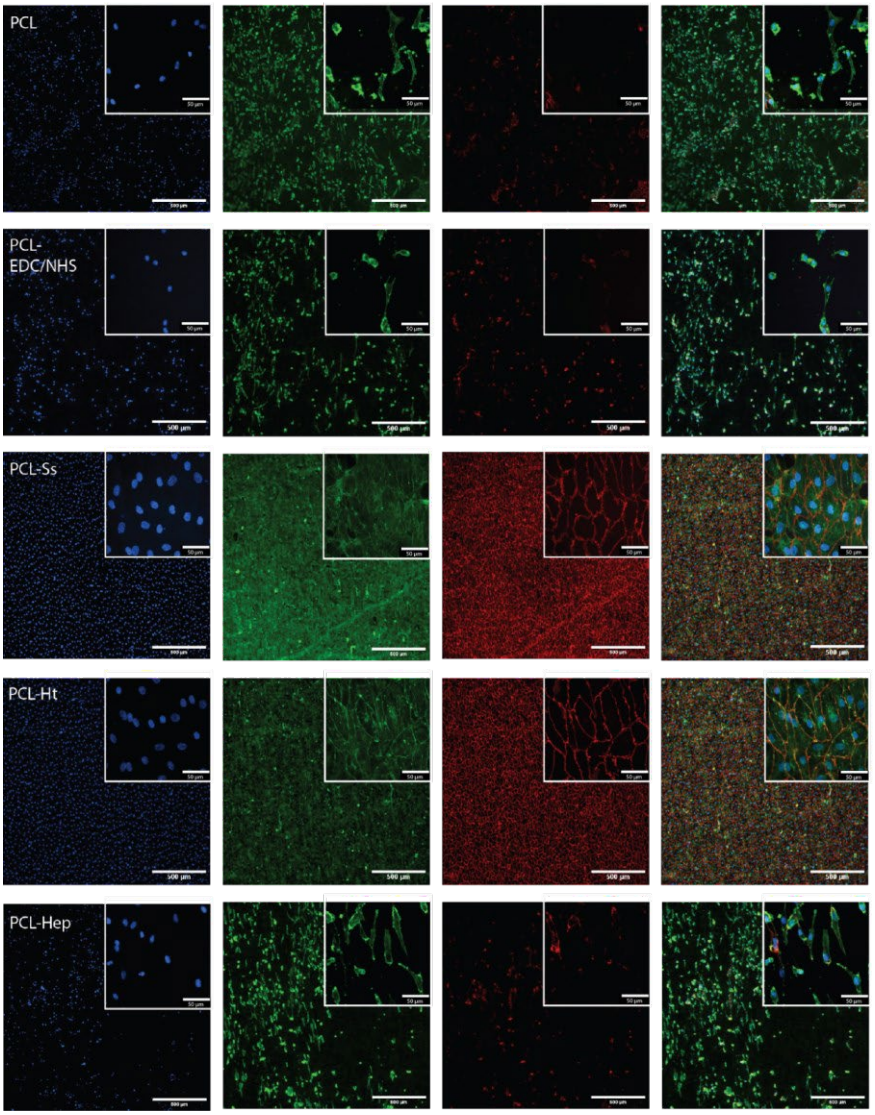

Figure 4.8. Immunostaining of human microvascular endothelial cells (hMVECs) after 7 days of culture on aligned fiber scaffolds treated with marine sulfated polysaccharides from Ss (PCL-Ss) and Ht (PCL-Ht), Hep (PCL-Hep), and two controls (PCL and PCL-EDC/NHS). Cells were stained with Ve-Cadherin (red), Phalloidin (green), and DAPI (blue). The alignment of the scaffold fibers facilitated the polarization of endothelial cells in the direction of the fibers, from the top to the bottom. Magnification 4x (scale bar 500 µm) and in insets 40x (scale bar 50 µm).

Discussion

Among the polymers used for electrospun scaffolds fabrication, PCL is the most used for vascular applications [15]. PCL's properties—biocompatibility, slow biodegradation, low cost, extensive *in vivo* knowledge, and ease of handling with various printing techniques—make it an attractive choice for producing bioresorbable synthetic blood vessel grafts [30–32]. Producing fibers with morphology, orientation, and size that resemble natural ECM fibers facilitates optimal interactions between cells and the scaffold. With regard to vasculature, endothelial cells exhibit a prominent polarization along the direction of blood flow in native vessels, resulting in a monolayer of axially oriented cells. Aligned electrospun nanofibers have been shown to guide endothelial cell orientation effectively in tissue engineering applications, by mimicking the physiological effects of shear stress [33] [34].

However, PCL's inherent hydrophobicity poses significant challenges, including poor endothelialization, inadequate cell compatibility, and the risk of non-specific protein adsorption leading to platelet activation and clot formation, ultimately resulting in graft failure [35,36]. Surface modification is crucial for enhancing scaffold properties for tissue engineering applications. Heparin incorporation is the most widely-used approach to increase biocompatibility and hemocompatibility [19–21,37].

Previous research has reported the in-solution anticoagulant properties of several marine-derived polysaccharides [27]. Mourão et al. evidenced the anticoagulant properties of fucosylated chondroitin sulfate from sea cucumbers, proposing its potential as heparin substitute [38]. Zhang et al. stressed on the anticoagulant effects of sulfated glycans from marine sources and their interaction with important coagulation proteins [39]. The research by Sokolova et al. on red algal sulfated polysaccharides influencing blood coagulation and *in vitro* platelet activation provides insights into how heparin and carrageenan affect platelet adhesion [40].

In this study, PCL electrospun scaffolds were functionalized for the first time with marine sulfated polysaccharides extracted from the Mediterranean sponge *Ss* and the echinoderm *Ht*, whose anticoagulant properties have been recently discovered [27]. The functionalization remained stable over time, in both dry and physiological conditions, and significantly improved the biocompatibility and hemocompatibility of the scaffolds.

Interestingly, these polysaccharides retained their anticoagulant properties even when covalently bound to PCL fibers, representing a promising approach for vascular regeneration. Indeed, both the intrinsic and extrinsic coagulation

pathways were shown to be affected by PPP incubation with PCL-Ss or PCL-Ht compared to controls. The complex structures of marine polysaccharides allow unique interactions with coagulation factors, enhancing anticoagulation and inhibiting platelets activation, adhesion and aggregation. Key structural features influencing these properties include monosaccharide composition, degree and pattern of sulfation, molecular weight, and types of glycosidic bonds [41]. Furthermore, our findings show that PCL functionalization with these bioactive molecules effectively modulates platelet adhesion, highlighting their potential as a novel anti-thrombotic strategy in vascular tissue engineering, particularly for the fabrication of sTEVG.

Although several researchers have combined PCL with other synthetic or natural polymers such as collagen, fibrin, and elastin to improve the biocompatibility of electrospun scaffolds [42], developing a graft able to maintain its integrity and patency by preventing thrombosis and intimal hyperplasia still represents a challenge [15]. With regards to scaffold population by endothelial cells, our results clearly show a substantial improvement in cell adhesion, colonization, and rapid endothelialization of the PCL fibers, thanks to the surface coating by these bioactive compounds. Specifically, PCL functionalization with Ht polysaccharides led to nearly complete endothelial cell coverage within 24 hours, with the formation of mature adherent junctions, evidenced through VE-cadherin staining, by day 4. Likewise, PCL-Ss proved to be effective as endothelial cells reached confluence by day 7, following significant scaffold coverage by day 4. In contrast, hMVECs seeded on unmodified PCL scaffolds, as well as on those treated with EDC/NHS or heparin, showed poorer initial adhesion and a rounded morphology at day 1, features typically associated with weak substrate interaction. This likely contributed to an apparent reduction in DNA content at days 4 and 7, reflecting the detachment of less adherent cells during the early adaptation phase. Such transient decreases in cell number are not uncommon when cells are exposed to synthetic environments, where only those capable of forming stronger focal adhesions remain, elongate, and eventually proliferate. Accordingly, this early cell loss was far less evident on the biofunctionalized scaffolds, where rapid and stable adhesion led to more consistent DNA levels and earlier endothelialization. These trends were supported by both immunofluorescence imaging and morphological analyses, which revealed progressive elongation and reduced circularity over time, consistent with rapid enhanced cell–scaffold interactions and cytoskeletal reorganization. In stark contrast, unmodified PCL scaffolds, as well as those

treated with EDC/NHS crosslinking agents or heparin, required up to 21 days to reach a comparable level of endothelial cell coverage. This evidence was further confirmed by both metabolic and proliferation assays showing an early step of fast cell growth followed by the achievement of a quiescent mature state on our bioactive materials. Moreover, aligned electrospun scaffolds effectively guided the orientation of hMVECs on their surfaces along the direction of the nanofibers, closely mimicking the natural alignment of ECs in blood vessels.

Our findings show that incorporating marine sulfated polysaccharides into PCL scaffolds improve hydrophilicity, enhance anti-thrombogenic properties, and facilitate rapid endothelialization. The ability of these polysaccharides to accelerate the formation of a functional endothelial monolayer is particularly advantageous, as it provides a critical barrier that prevents thrombus formation by minimizing direct contact between blood proteins and the underlying synthetic matrix, reducing the risk of thrombogenesis [43,44]. The improved endothelialization is crucial for the long-term success of sTEVG, as it ensures the formation of a stable and functional vascular graft. Moreover, the use of naturally derived marine polysaccharides offers an innovative approach that not only improves hemocompatibility and biocompatibility, but it is also in line with the principle of blue economy, which emphasizes sustainable use of ocean resources for economic growth, improved livelihoods, and ecosystem health. By utilizing marine-derived biomaterials, this approach supports the sustainable harvesting of marine resources and promotes the development of high-value biomedical products from renewable and ecologically responsible sources, thereby contributing to the trend toward using bioactive, renewable materials in biomedical applications [45–49].

Future research should focus on the design and fabrication of tubular sTEVG using these polysaccharides and on comprehensive *in vivo* studies to validate these promising *in vitro* results, further elucidating the mechanisms by which these marine polysaccharides interact with vascular cells and blood components. Additionally, exploring the use of other marine-derived polysaccharides with unique bioactive properties could expand the scope of this strategy, providing new avenues for optimizing TEVGs. Understanding the long-term behavior of these functionalized grafts in physiological environments, including their biodegradation profiles and their integration with native tissue, will be crucial for translating these findings into clinical applications.

Conclusion

This research contributes to the expanding body of knowledge on the therapeutic applications of acidic polysaccharides in regenerative medicine, demonstrating that the incorporation of these marine-derived polymers into a synthetic matrix may enhance its cytocompatibility and anti-thrombotic properties. Furthermore, our study suggests that these compounds have the potential to serve as effective alternatives to conventional anticoagulants such as heparin. The incorporation of these polysaccharides could play a pivotal role in the development of safer and more effective vascular grafts, potentially leading to better clinical outcomes for patients requiring vascular interventions. This approach holds great promises for improving the performance and longevity of tissue-engineered vascular grafts, addressing key challenges associated with PCL's inherent properties.

Methods

Materials

All reagents and chemicals used in this study were of analytical grade from Merck Group (KGaA, Darmstadt, Germany), unless otherwise stated.5.2. Scaffolds Preparation and Characterization

Electrospun PCL Fibers Preparation

The electrospinning solution was prepared by dissolving 13% (w/v) PCL (80 kDa MW) in hexafluoro-2-propanol (Biosolve B.V., the Netherlands) overnight under stirring conditions. Electrospun scaffolds were obtained after 45 minutes of electrospinning using the following parameters: voltage, 18.5 kV; working distance between the needle tip and the collector, 15 cm; and flow rate, 1 mL/h. A stainless steel 6 cm diameter mandrel was used as collector. To produce random fibers, the mandrel speed was set at 500 rpm, whereas aligned fibers were obtained at 5800 rpm. During electrospinning, a blunt 20-gauge stainless steel hypodermic needle (internal diameter 0.8 mm, Unimed, Switzerland) was set to move along the length of the collector to ensure homogeneous deposition of the PCL fibers.
All processes were carried out under controlled conditions, maintaining a temperature of 25 °C and a relative humidity of 35%.

Scanning Electron Microscopy (SEM) Investigation

For the characterization of both morphology and size of the fibers, a thin layer of gold coating (Quorum Technologies SC7620, UK) was applied over the samples. Images were captured by using a JSM-IT200 microscope (Jeol ltd., the Netherlands) at 2000× magnification, with an accelerating voltage of 100 kV and a working distance of 11 mm. The subsequent image processing and analysis was performed to determine fiber diameter (n = 3 samples × 35 measurements each) by using Fiji image processing package (GNU General Public License).

Marine Sulfated Polysaccharides Purification

Sulfated polysaccharides were purified as previously described by Nieddu et al. [27]. Briefly, body fragments (n = 18) of the sponge *Sarcotragus spinosulus* (Ss) and body wall fragments (n = 7) of the echinoderm *Holothuria tubulosa* (Ht) were immersed in absolute ethanol for 120 hours at 4 °C. Then, samples were finely minced and incubated in acetone for 24 hours to achieve complete dehydration and delipidation. Samples were centrifuged at 5000 g for 15 minutes, and the supernatant was discarded. After complete acetone evaporation, the dehydrated and delipidated tissue (DDT) was rehydrated with 0.1 M sodium acetate buffer, pH 6.0, containing 5 mM EDTA and 5 mM cysteine (15 mL per gram of tissue) at 4 °C for 24 hours. Proteolytic treatment was performed by adding 1 U of papain (Themo Fisher Scientific Inc. Waltham, MA, USA) per mg of DDT at 56 °C for 48 hours. Enzyme activity was stopped by boiling the mixture at 100 °C for 5 minutes. After centrifugation at 5000× g for 10 minutes, the supernatant was recovered and immediately loaded into a chromatography column packed with diethylaminoethyl-(DEAE) -Sephacel anion-exchange resin (10 mL of resin per gram of digested tissue), previously equilibrated with 50 mM sodium acetate, pH 6.0. The column was washed with the same buffer until absorbance at 280 nm was less than 0.05 OD. Acidic polysaccharides were fractionated by performing four elution steps using 20 mM Tris-HCl buffer, pH 8.6, containing 0.5 M, 1 M, 1.5 M, and 2 M lithium chloride, respectively. Eluates were concentrated and dialyzed against deionized water using Amicon Ultra-15 Centrifugal Filter Units with a 3 kDa cut-off, according to the manufacturer's instructions. For subsequent experiments, the polysaccharides eluted with 1.5 M lithium chloride were used for scaffold functionalization. Hereafter, for the sake of simplicity, they were referred to as Ss (1.5 M fraction from *Sarcotragus spinosulus*) and Ht (1.5 M fraction from *Holothuria tubulosa*).

Hexuronic Acid Quantification

The uronic acid (UA) content of each eluate was determined using the Bitter and Muir method [50], with glucuronolactone as the standard [51]. Briefly, 250 µL of either the standard solution (ranging from 5 to 40 µg UA/mL) or the eluate was mixed with 1.25 mL of 25 mM sodium tetraborate decahydrate in concentrated sulfuric acid. The mixture was incubated at 85 °C for 10 minutes. Following incubation, 50 µL of carbazole was added, and the solution was boiled for an additional 15 minutes. The absorbance was then measured at 530 nm.

NMR-Analysis

The purified samples were lyophilized to obtain a powdered form, and approximately 5 mg of each sample was dissolved in deuterium oxide (D_2O) to a final concentration of 8.3 mg/mL. The solutions were vortexed and sonicated to ensure complete dissolution before NMR analysis. NMR spectra were recorded on a Bruker Avance III HD 700 MHz spectrometer equipped with an H/C/N triple-resonance probe and an x/y/z triple-axis pulse field gradient unit. ^{1}H-NMR and ^{13}C-NMR spectra were acquired at 25 °C and/or 53 °C using the standard 1D *zgpr* and *zgpg* Bruker pulse sequences. The samples were buffered in 50 mM potassium phosphate (pH 6.9) to enable direct comparisons between the two polysaccharides, Ht and Ss. For resonance assignment and structural elucidation of the Ht and Ss polysaccharides, a set of 2D NMR spectra were acquired, namely: DIPSI (25 and 70 ms mixing times), NOESY (100 ms mixing time), gradient enhanced HSQC ^{13}C-^{1}H, gradient enhanced relay HSQC ^{13}C-^{1}H-DIPSI (70 ms mixing time), and gradient HMBC ^{13}C-^{1}H (optimized for detection of long-range nJCH couplings of 10 Hz), all taken from the standard Bruker pulse sequence library. Furthermore, low power presaturation of residual water in the D_2O samples was applied in 1D ^{1}H spectra and during the relaxation delay of DIPSI and NOESY spectra.

All spectra were processed using Bruker TopSpin 3.6.5 software, with baseline correction of 1D spectra performed using a 5th-order polynomial function followed by integration. Processed 2D spectra were converted and analyzed using Sparky 3.114 software [52]. The obtained spectra were analyzed to identify key functional groups, signal multiplicity, chemical shifts, and coupling constants. Polysaccharide structural features, such as monosaccharide composition, glycosidic linkages, and sulfation patterns, were

deduced based on the NMR chemical shift data and compared to literature values.

PCL Aminolysis and EDC/NHS Crosslinking

PCL scaffolds underwent aminolysis to introduce amine groups on their surface, followed by crosslinking of bioactive molecules through N-(3-dimethylaminopropyl)-N'-ethylcarbodiimide hydrochloride/N-hydroxysuccinimide (EDC/NHS) chemistry. The aminolysis was performed by incubating the scaffolds with a 6% (w/v) solution of 1,6-hexamethylenediamine (HMDA) in 2-propanol for 2 hours at 37 °C. Following aminolysis, the scaffolds were washed three times with 2-propanol to remove residual HMDA and then transferred to new 24-well plates where they were washed three additional times with distilled water to ensure thorough cleaning. 166 µg-UA/mL of purified polysaccharides (Ht or Ss) or unfractionated heparin (Hep) were solubilized in a 0.1 M solution of EDC/NHS in 2-(N-morpholino)ethanesulfonic acid (MES) buffer at pH 5. This solution was incubated for 40 minutes to activate the carboxylic groups of the polysaccharides. Then, each scaffold was incubated with 300 µL of the solution containing the activated polysaccharides at room temperature for 24 hours to allow crosslinking, followed by thorough washing to remove any unreacted reagents and to ensure the stability of the crosslinked structure.

ATR-FTIR Analysis

The chemical composition of the electrospun scaffolds was analyzed using Attenuated Total Reflection-Fourier transform infrared spectroscopy (ATR-FTIR) with a Nicolet™ iS50 spectrometer (Thermo Fisher Scientific, the Netherlands). The analysis was performed in the range of 400–4000 cm^{-1} with a resolution of 0.5 cm^{-1} to identify functional groups and verify crosslinking.
Prior to measurement, the electrospun scaffolds were carefully cut into small, flat pieces and placed on the ATR crystal. Gentle pressure was applied to achieve optimal contact. The spectra were collected by averaging 32 scans to improve the signal-to-noise ratio. Naked PCL scaffolds, scaffolds treated with EDC/NHS, as well as scaffolds crosslinked with marine sulfated polysaccharides or heparin, were analyzed to verify the actual crosslinking. Background spectra were recorded under the same conditions and subtracted from the sample spectra to eliminate any contribution from atmospheric CO_2 and water vapor. The resulting spectra were analyzed to identify characteristic peaks corresponding to the functional groups present in the scaffolds.

Toluidine Blue O (TBO) Assay: Quantification and Stability of Sulfated Polysaccharides on Scaffolds

Surface functionalization of PCL-Ss, PCL-Ht, and PCL-Hep scaffolds was evaluated by means of a slightly modified Toluidine Blue O (TBO) assay [53], using PCL-EDC/NHS scaffolds as control. In brief, each scaffold was immersed in a TBO working solution (0.04% w/v in aqueous 0.01 M HCl 0.2 M NaCl) and incubated for 1 hour under continuous shaking to ensure thorough dye interaction. Following incubation, the TBO solution was removed, and the scaffolds were washed five times with a washing solution (0.2 M NaCl solution) to eliminate non-specifically bound dye. The scaffolds were then transferred to an elution solution, consisting of 50% ethanol in 0.01 M HCl, until the complete extraction of the bound TBO. The released dye was quantified by measuring its absorbance at 630 nm using a UV-Vis plate reader (CLARIOstar Plus. Ortenberg, Germany), and the amount of sulfated polysaccharides was determined by referencing a calibration curve. For standard curve preparation, 1 mL of the TBO working solution was combined with 100 µL of a Hep solution of known concentrations (0 µg/ml; 0.5 µg/ml; 1 µg/ml; 2.5 µg/ml). This mixture was incubated at 37 °C with gentle shaking for 1 hour, during which the Hep–TBO complex spontaneously formed and precipitated. The mixture was then centrifuged at 300 rcf for 10 minutes, after which the supernatant was discarded. The precipitate was carefully rinsed five times with the washing solution to ensure complete removal of any unbound TBO. Finally, 1 mL of the elution solution was added to dissolve the precipitate, releasing the bound TBO, and the absorbance of the resulting solution was measured at 630 nm. To assess the stability of the functionalization, the assay was performed under two different conditions: first, by comparing scaffolds that were functionalized one year prior with freshly functionalized scaffolds, and second, by comparing scaffolds incubated in PBS at 37 °C for 30 days with those stored under dry conditions.

Water Contact Angle Measurement

The water contact angle (WCA) of the electrospun scaffolds was measured to evaluate their surface hydrophilicity using a drop shape analyzer (Krüss DSA25S, Germany). A 4 µL droplet of distilled water was carefully deposited onto the surface of each scaffold using a precision micro-syringe. Each experiment was recorded over a period of 90 seconds at a rate of 1 frame per second using a high-resolution camera and was subsequently analyzed to measure the water contact angles.

Coagulation assays

Blood samples were collected from healthy donors without any bleeding disorder, with informed consent in accordance with the Declaration of Helsinki, using 3.2% sodium citrate as an anticoagulant. For coagulation assays, blood was centrifuged at 1500 g for 15 minutes to obtain platelet-poor plasma (PPP). The PPP was collected and utilized for coagulation assays on scaffold surfaces. Naked scaffolds, EDC/NHS-treated or functionalized with Hep, Ss, and Ht polysaccharides were placed in a sterile 24-well plate and incubated with 220 µL of PPP on an orbital shaker at 37 °C for 30 minutes. Subsequently, PPP from each well was collected and immediately subjected to activated partial thromboplastin time (aPTT) and prothrombin time (PT) assays. For the aPTT assay, PPP was processed as follows: 100 µL of PPP from each well was combined with 100 µL of Dade® Actin® FSL Activated PTT Reagent (Siemens) and incubated at 37 °C for 3 minutes. Then, 100 µL of 25 mM calcium chloride was added, and the clot formation time was measured. With regard to PT assay, 200 µL of preheated Dade® Innovin® reagent (Siemens) was added to 100 µL of PPP for 1 minute at 37 °C, and clotting time was recorded accordingly.

Platelet Adhesion Assays

For platelet adhesion assays, 3.2% sodium citrate anticoagulated blood was centrifuged at 250 g for 15 minutes to isolate the platelet-rich plasma (PRP). The supernatant consisting of the PRP was carefully collected, and the platelet concentration was adjusted to 100 x 10^9 platelets per liter with autologous PPP. Platelet adhesion was assessed by adding 300 µL of the PRP to each scaffold in a 24-well plate followed by incubation at 37 °C for 1 hour, to allow platelets to adhere. Then, scaffolds were gently rinsed three times with phosphate-buffered saline (PBS) to remove any non-adherent platelet. This washing step was crucial to minimize background and ensure that only platelets firmly attached to the scaffold surface were counted.

Lactate Dehydrogenase (LDH) Assay

PCL, PCL-EDC/NHS, PCL-Ht, PCL-Ss, and PCL-Hep Scaffolds were treated with a lysis buffer containing 0.9% Triton X-100 to disrupt cell membranes and release intracellular LDH from the cytosol of platelets adhered to the scaffold surface. LDH in the supernatant was quantitatively assayed by means of the fluorescence-based CyQUANT™ LDH Cytotoxicity Assay Kit (ThermoFisher Scientific).

Platelets Fluorescence Microscopy and SEM Analysis: PCL-EDC/NHS, PCL-Ht, PCL-Ss, and PCL-Hep Scaffolds PCL-BSA and PCL-Collagen

Scaffolds were first fixed using a 1% (w/v) paraformaldehyde (PFA) solution in phosphate-buffered saline (PBS) to preserve their structural integrity and immobilize adhered platelets. Subsequently, platelets were permeabilized with a 1% sodium dodecyl sulfate (SDS) solution in PBS to enable staining of intracellular components.

For the staining procedure, scaffolds were incubated with CF647 Phalloidin (Biotium; 1:200) to visualize F-actin cytoskeletal structures, providing insights into platelet adhesion and morphology on the scaffold surfaces.

After staining, scaffolds were thoroughly rinsed with PBS followed by fluorescence microscopy analysis using Nikon Eclipse Ti2 Inverted Microscope (Nikon Corporation, Tokyo, Japan) and picture were elaborated using ImageJ Fiji image analysis software.

For SEM analysis scaffolds were fixed in 2.5% glutaraldehyde in phosphate buffer, followed by post-fixation in 1% osmium tetroxide in 0.1 M sodium cacodylate buffer for 1 hour. Samples were then dehydrated through a graded ethanol series (70%, 90%, 100%), and a thin gold coating was applied using a Quorum Technologies SC7620 sputter coater (UK). SEM images were captured using a JSM-IT200 microscope (Jeol Ltd., The Netherlands), providing high-resolution visualization of platelet morphology and scaffold surface characteristics. Analyses were performed on PCL-EDC/NHS, PCL-Ht, PCL-Ss, and PCL-Hep Scaffolds as well as PCL scaffolds coated with a 5% BSA solution in PBS (PCL-BSA) or a 100 µg/ml Type I Bovine collagen (Advanced Biomatrix) solution in 27 mM sodium acetate and 13 mM acetic acid (PCL-Collagen) overnight as further controls.

Biocompatibility Assays

Adult Human Dermal Microvascular Endothelial Cells (hMVECs) were purchased from Lonza (Basel, Switzerland; catalog n. CC-2543). The cells were cultured according to the manufacturer's guidelines in Microvascular Endothelial cell Growth Medium (EGM-2 MV, Lonza, Basel, Switzerland; catalog n. CC-3202).

Scaffolds were placed in 24-well plates and underwent chemical sterilization by immersion in 70% ethanol three times for 15 minutes each [54]. After sterilization, scaffolds were completely air-dried and rinsed with PBS. Subsequently, scaffolds were secured at the bottom of the wells using a rubber O-ring. hMVECs were seeded onto the scaffolds at a density of 130,000 cells

per scaffold. The cells were cultured for 21 days under standard conditions (37 °C, 5% CO_2), with medium changed every 48 hours. At various time points (day 1, day 4, day 7, day 14, and day 21 post-seeding), cell metabolic activity, proliferation, and morphology/differentiation were evaluated to assess scaffold biocompatibility and cellular response.

Proliferation: CyQuant DNA Assay

For DNA quantification, scaffolds were frozen at -80 °C to facilitate cell lysis, until analysis. CyQuant DNA Assay was performed according to the manufacturer's instructions (Thermo Fisher Scientific). Following thawing, scaffolds were incubated with cell-lysis buffer followed by the CyQuant dye binding solution, and fluorescence was measured using a microplate reader at an excitation wavelength of 485 nm and an emission wavelength of 530 nm. The DNA content was quantified based on a standard curve generated using known concentrations of DNA standards provided in the kit. DNA content was quantified in nanograms per scaffold and reported as cells number per scaffold assuming that approximately 6.6 pg of DNA is present in each cell [55].

Metabolic Activity: PrestoBlue Assay

To assess metabolic activity, PrestoBlue reagent (Thermo Fisher Scientific) was used. At every time point, scaffolds were incubated with 450 µL of PrestoBlue solution for 45 minutes at 37 °C, 5% CO_2. Then, 200 µL of the solution was transferred into a black bottom 96-well plate and fluorescence intensity was measured using a microplate reader (CLARIOstar Plus. Ortenberg, Germany) at an excitation wavelength of 560 nm and an emission wavelength of 590 nm, according to the manufacturer's instructions.

hMVECs Immunofluorescence Microscopy Analysis

Scaffolds were washed with PBS to remove residual medium, followed by cell fixation with 3.7% (w/v) paraformaldehyde for 15 minutes. Then, scaffolds were further washed with PBS and cells permeabilized using 0.1% Triton X-100. To block nonspecific binding sites, scaffolds were incubated with a PBS solution containing 3% (w/v) bovine serum albumin (BSA) and 0.05% (v/v) Tween-20 (blocking solution), for 30 minutes.

Scaffolds were then incubated overnight at 4°C with primary antibodies, including an anti-von Willebrand Factor (vWF) antibody produced in rabbit (1:200 dilution; Sigma-Aldrich; Cat. No. F3520) and Alexa Fluor® 647 Mouse Anti-Human CD144-Vascular Endothelial Cadherin (VE-Cad) (1:1000

dilution; BD Pharmingen™; Cat. No. 561567) in blocking solution. After three washes of 5 minutes each with PBS containing 0.05% Tween-20 on an orbital shaker, scaffolds were incubated for 15 minutes with Phalloidin (1:1000 dilution; Thermo Fisher Scientific, Waltham, MA, USA; Cat. No. A12379), to stain actin filaments, and DAPI (1:1000 dilution; Thermo Fisher Scientific; Cat. No. 10184322), to stain cell nuclei. Donkey anti-Rabbit IgG secondary antibody, Alexa Fluor™ 488 (1:1000 dilution; Thermo Fisher Scientific; Cat. No. A-21206), was then applied at room temperature for 1 hour to detect the vWF primary antibody. Finally, scaffolds were washed with PBS to remove unbound secondary antibodies and mounted onto glass slides for visualization using a Nikon Eclipse Ti2 Inverted Microscope (Nikon Corporation, Tokyo, Japan). Immunostaining images were analyzed using ImageJ (Fiji) software, with cell orientation quantified through the OrientationJ plug-in.

Statistical Analysis

Statistical analysis was performed using GraphPad Prism version 10.0. Data from metabolic activity assays and DNA quantification were analyzed for statistical significance. Differences among multiple groups at various time points were assessed using a 2-way ANOVA analysis followed by Tukey's multiple comparisons test. An ordinary one-way ANOVA followed by Tukey's multiple comparisons test was conducted for the aPTT, PT, LDH assay, and WCA data. A p-value of less than 0.05 was considered statistically significant (*p-value < 0.05; **p-value < 0.01; ***p-value < 0.001; ****p-value < 0.0001). Results are presented as the mean ± standard deviation (SD) of at least three independent experiments.

RESOURCE AVAILABILITY

Lead contact

Further information and requests for resources and materials should be directed to and will be fulfilled by the lead contact, Lorenzo Moroni (l.moroni@maastrichtuniversity.nl).

Materials availability

This study did not generate new unique reagents.

Polysaccharides purified from *Holothuria tubulosa* and *Sarcotragus spinosulus* used in this work are not commercially available. However, the purification methods are thoroughly described in this manuscript and in our previous publications.

Data and code availability

The data presented in this work are available from the lead contact upon reasonable request.

Acknowledgements

The authors wish to thank Renata Manconi and Giacinta Angela Stocchino from the Department of Veterinary Medicine, University of Sassari, for providing *Sarcotragus spinosulus* specimens and *Holothuria tubulosa* taxonomy. The authors also thank Tim ten Brink for his assistance in analyzing imaging samples. The animal study protocol was approved by Regione Autonoma della Sardegna (RAS AOO 06-01-00 Autor. Pesca Scient n.13 Prot. Uscita n. 26518 del 25 October 2024). This work was supported by the European Union — NextGenerationEU (DM 737/2021, RISORSE 2021–2022, 2022-2023) [CUP J55F21004240001], and by the Dutch Heart Foundation [03-006-2022-0052].

Authorship contributions

G.O.: Conceptualization, Methodology, Formal analysis, Investigation, Writing – Original Draft, Visualization. **G.N.**: Conceptualization, Formal analysis, Validation, Writing – Review & Editing. **M.N.**: Methodology, Investigation, Resources, Writing – Review & Editing. **H.M.H.S.**: Validation, Writing – Review & Editing. **H.I.**: Methodology, Investigation, Writing – Review & Editing. **T.M.H.**: Validation. **M.F.**: Funding acquisition, Supervision. **T.C.**: Resources. **A.J. L.**: Conceptualization, Resources, Writing – Original Draft, Writing – Review & Editing, Supervision, Project administration, Funding acquisition. **L.M.**: Conceptualization, Resources, Writing – Original Draft, Writing – Review & Editing, Supervision, Project administration, Funding acquisition.

Declaration of interests

All authors declare no conflict of interest regarding the publication of this paper.

Supporting Information

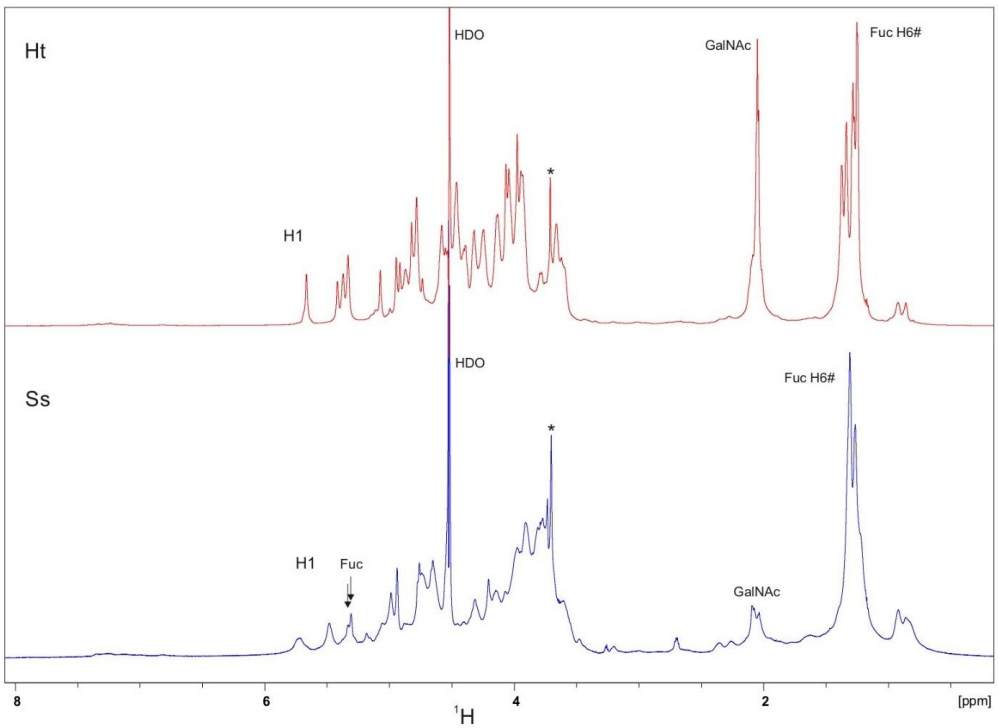

Figure S4.1. 1D ^{1}H nuclear magnetic resonance (NMR) spectra of sulfated polysaccharides extracted from *Holothuria tubulosa* (Ht, red) and *Sarcotragus spinosulus* (Ss, blue) in D_2O, recorded at 53 °C (700 MHz). The spectra differ markedly but share the characteristic methyl signal at 1.3 ppm, attributed to the methyl H6# groups of fucose units. Additional peaks observed in the 0.8–0.9 ppm region correspond to methyl groups of amino acids such as Val, Ile, and Leu, suggesting the presence of short peptide fragments. Asterisks indicate impurities unrelated to the polysaccharides.

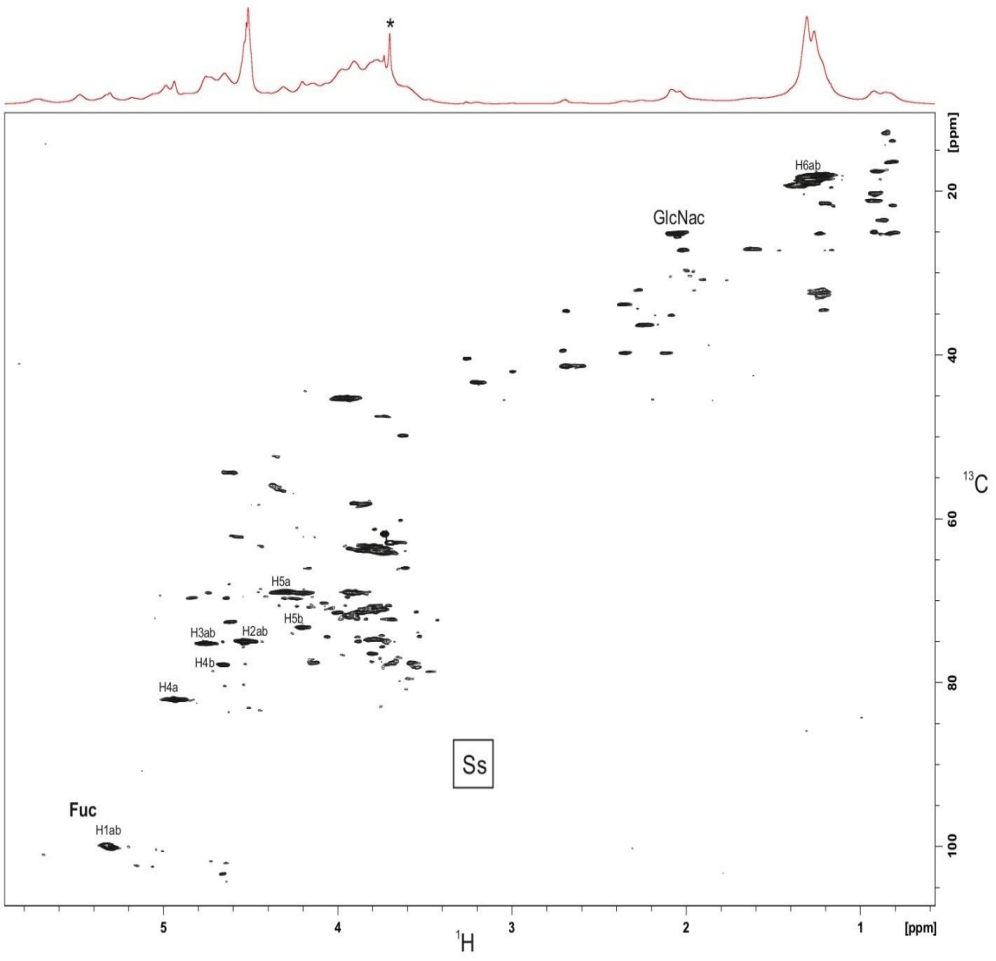

Figure S4.2. 1D ^{1}H spectrum and 2D HSQC ^{13}C–^{1}H NMR spectrum of sulfated polysaccharides extracted from *Sarcotragus spinosulus* (Ss), recorded in D_2O at 53 °C. Resonance assignments were made for two distinct fucose spin systems, labeled a and b, with atom identifiers from H1 to H6.

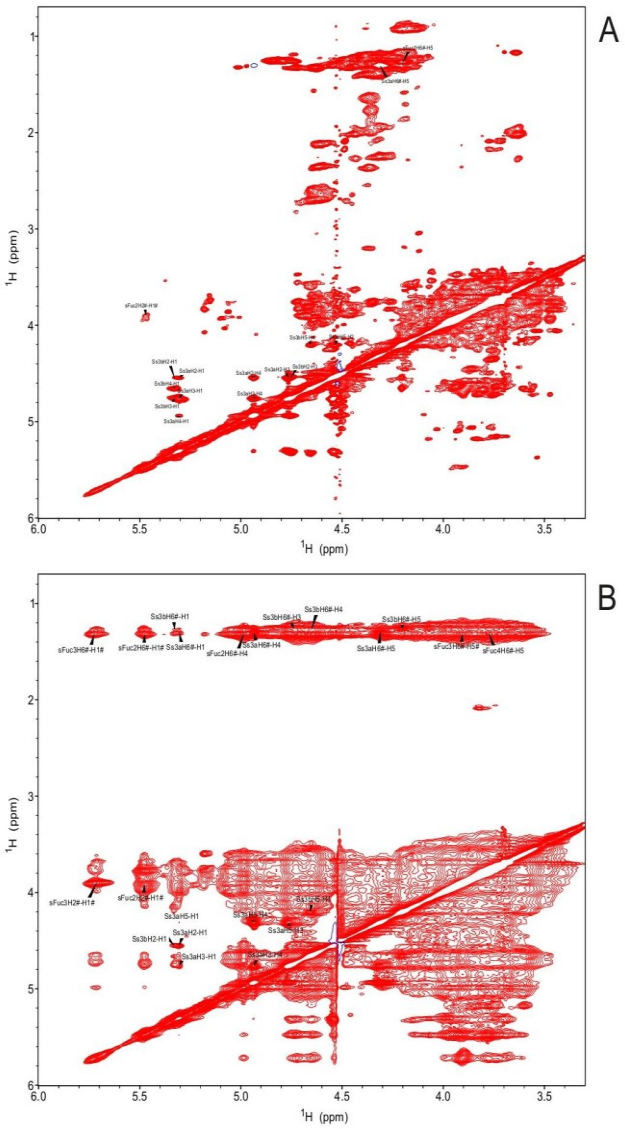

Figure S4.3. 2D DIPSI and NOESY NMR spectra of sulfated polysaccharides extracted from *Sarcotragus spinosulus* (Ss), recorded in D_2O at 53 °C. A) 2D DIPSI spectrum (70 ms mixing time); B) 2D NOESY spectrum (100 ms mixing time), both showing the aliphatic sugar region. Labeled cross-peaks indicate assigned fucose spin systems, including Ss3a, Ss3b, and sFuc1 to sFuc4.

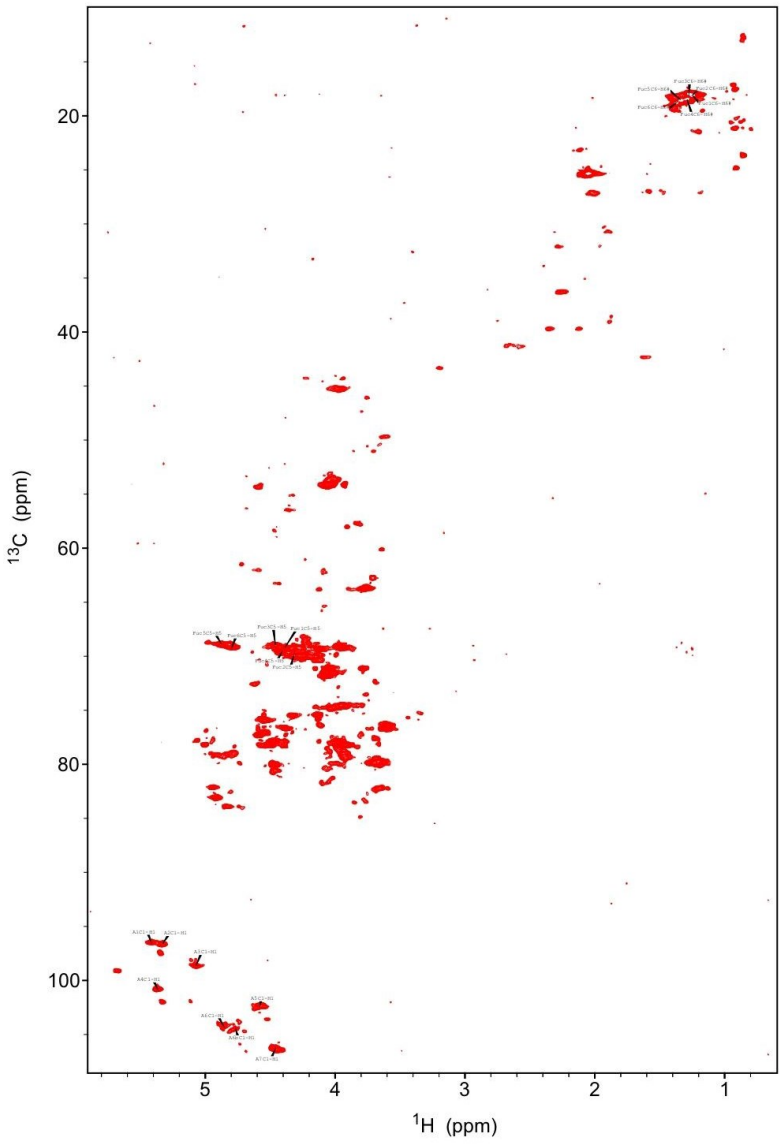

Figure S4.4. 2D HSQC ^{13}C–^{1}H NMR spectrum of sulfated polysaccharides extracted from *Holothuria tubulosa* (Ht), recorded in D_2O at 53 °C. Identified anomeric sugar protons H1 are labelled by A numbers, while connected H5/C5 and H6/C6 methyl resonance positions of fucose sugars, that are belonging to the six most abundant Fucose residues in Ht, are indicated by labels, namely Fuc1 to Fuc6.

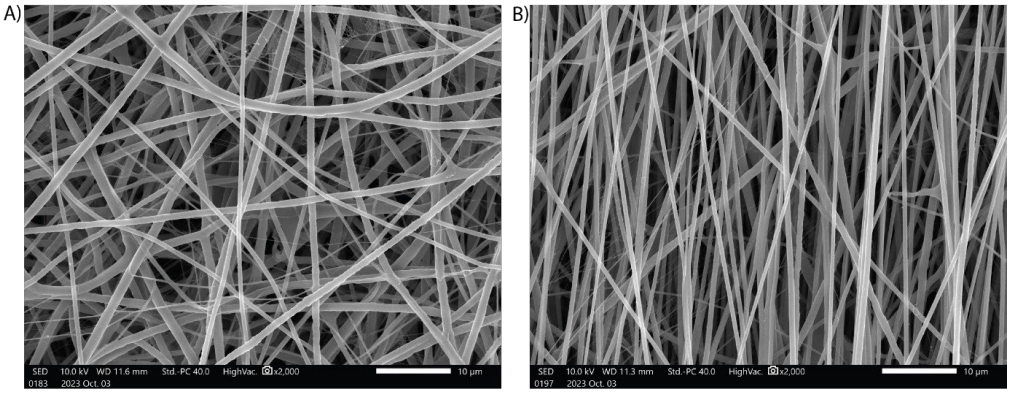

Figure S4.5. Ultramicroscopic morphological features of electrospun PCL nanofibers. SEM images of Random (A) and Aligned fibers (B), magnification 2000X.

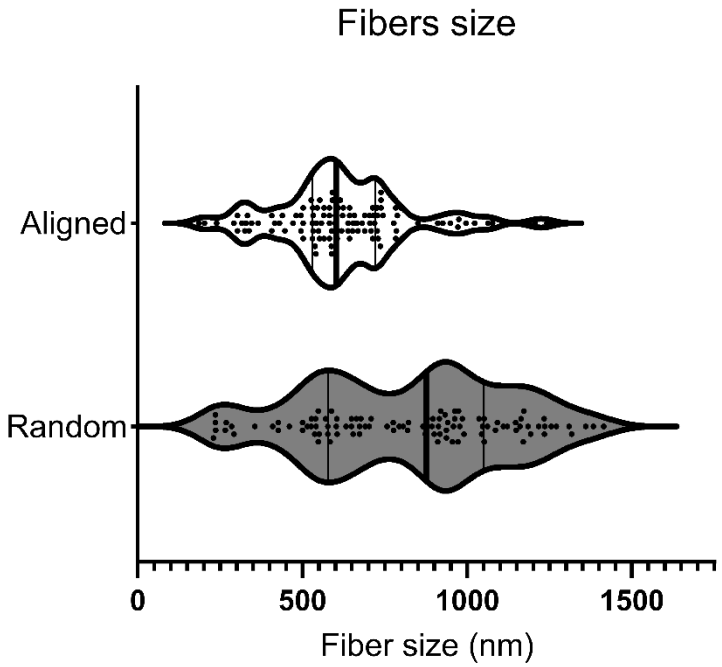

Figure S4.6. Fiber size distribution in aligned and random PCL electrospun scaffolds.

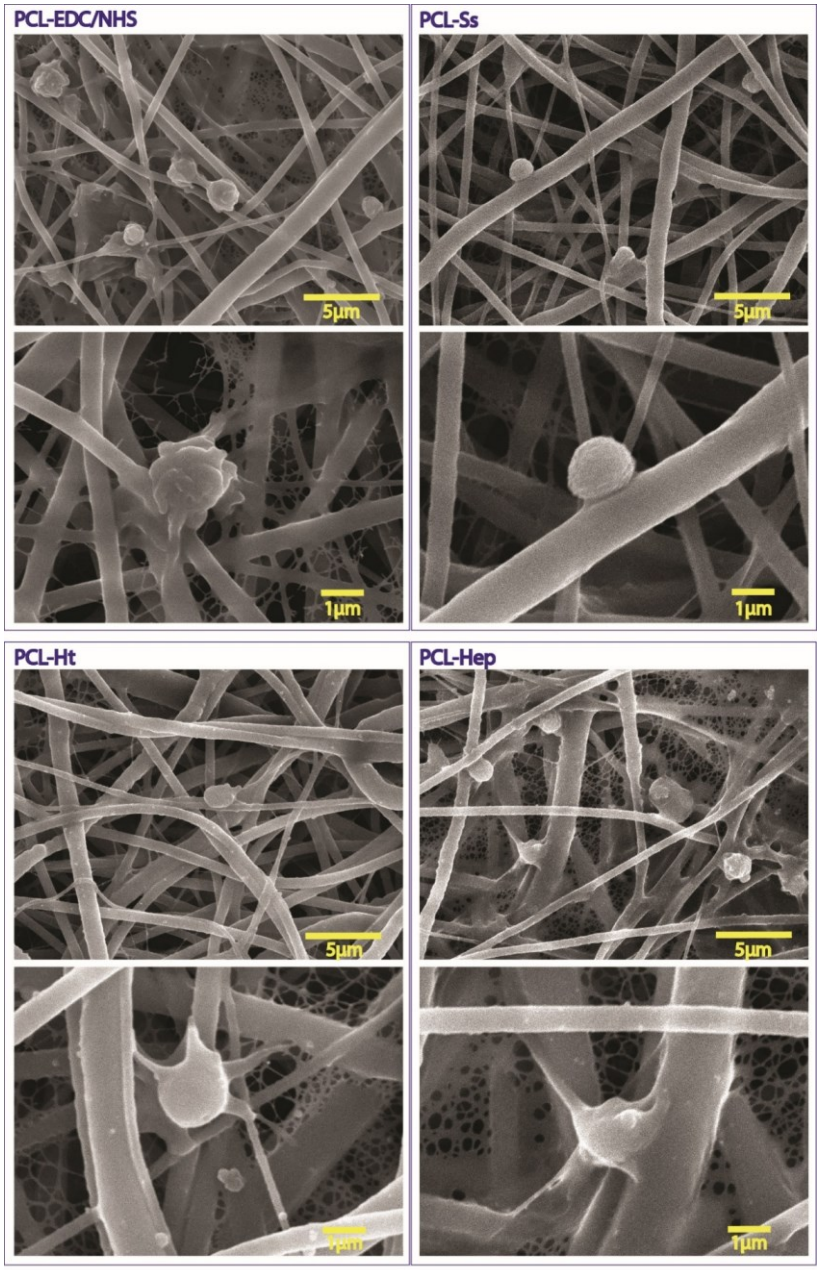

Figure S4.7. SEM high magnification of platelets adhesion and morphology on scaffolds after 1 hour of static incubation at 37°C with PRP. Platelets adherent to PCL-BSA, PCL-Collagen, PCL-EDC/NHS, PCL-Ss, PCL-Ht, and PCL-Hep (5000x and 14000x magnification, scale bar: 5 µm and 1µm).

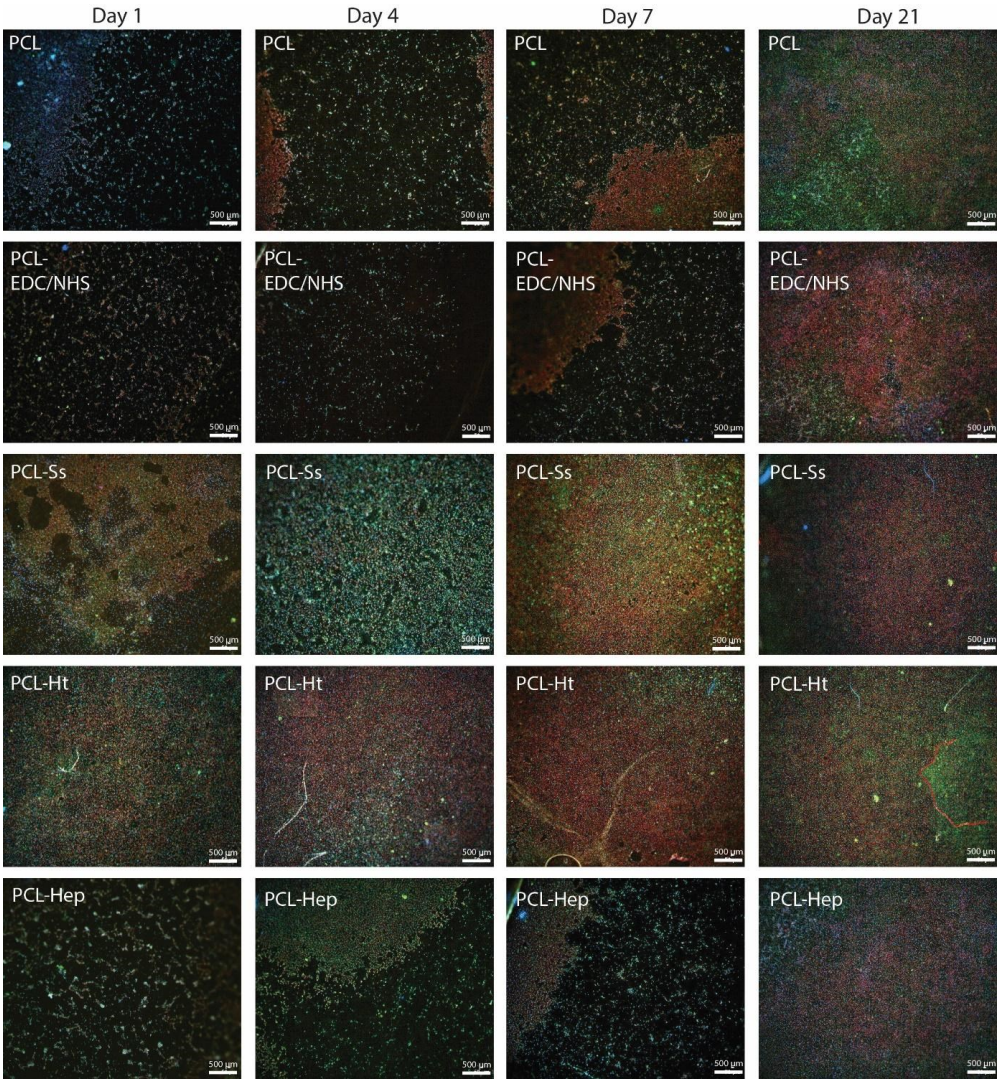

Figure S4.8. Immunostaining of human microvascular endothelial cells (hMVECs) during 21-day culture on naked PCL, PCL-EDC/NHS, PCL-Ss, PCL-Ht, and PCL-Hep. Cells were stained with Ve-Cadherin (red), von Willebrand Factor (VWF, green), and DAPI (blue). Images were captured at different time points (day 1, day 4, day 7, and day 21. Magnification 4x (scale bar 500µm).

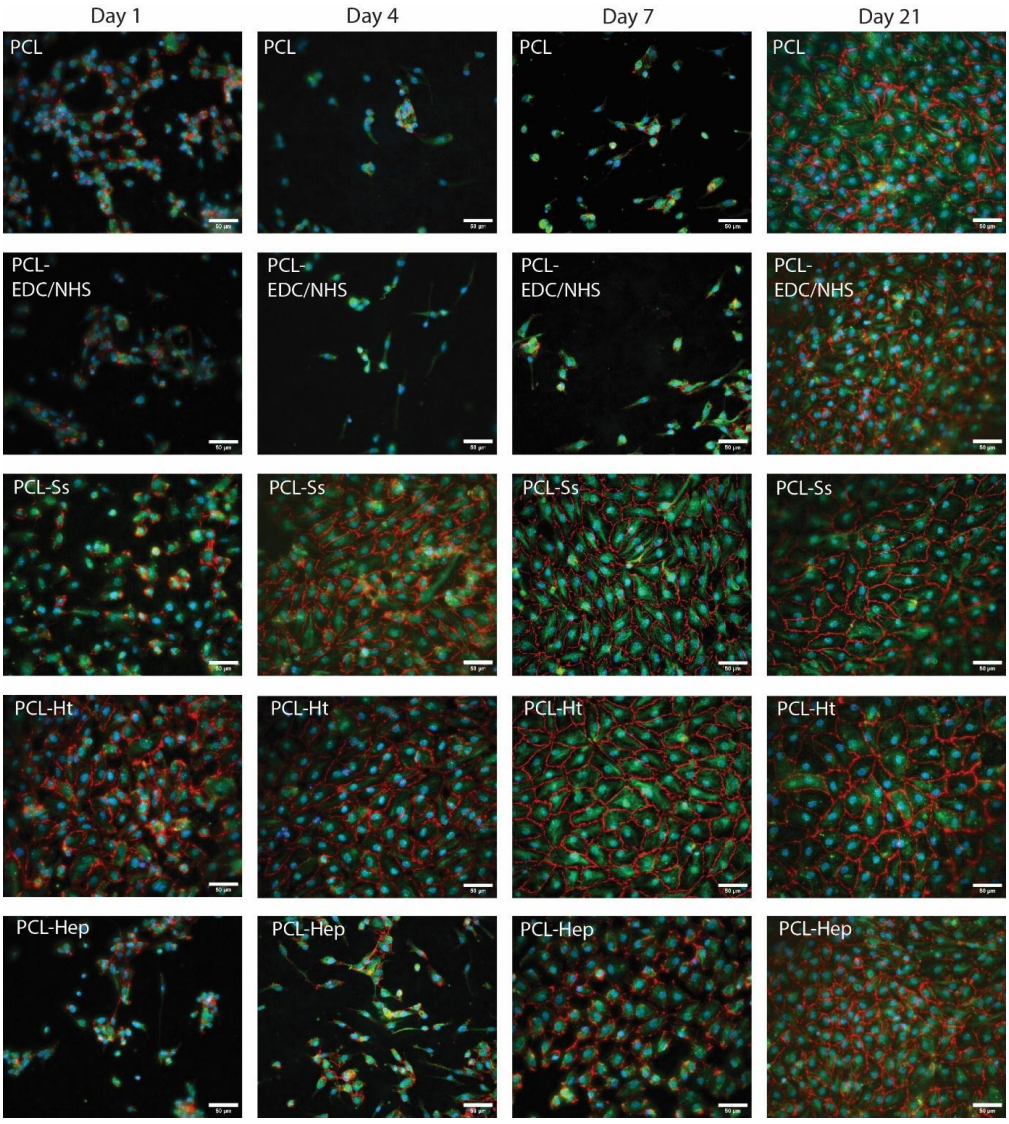

Figure S4.9. Immunostaining of human microvascular endothelial cells (hMVECs) during 21-day culture on naked PCL, PCL-EDC/NHS, PCL-Ss, PCL-Ht, and PCL-Hep. Cells were stained with Ve-Cadherin (red), von Willebrand Factor (VWF, green), and DAPI (blue). Images were captured at different time points (day 1, day 4, day 7, and day 21. Magnification 40x (scale bar 50µm).

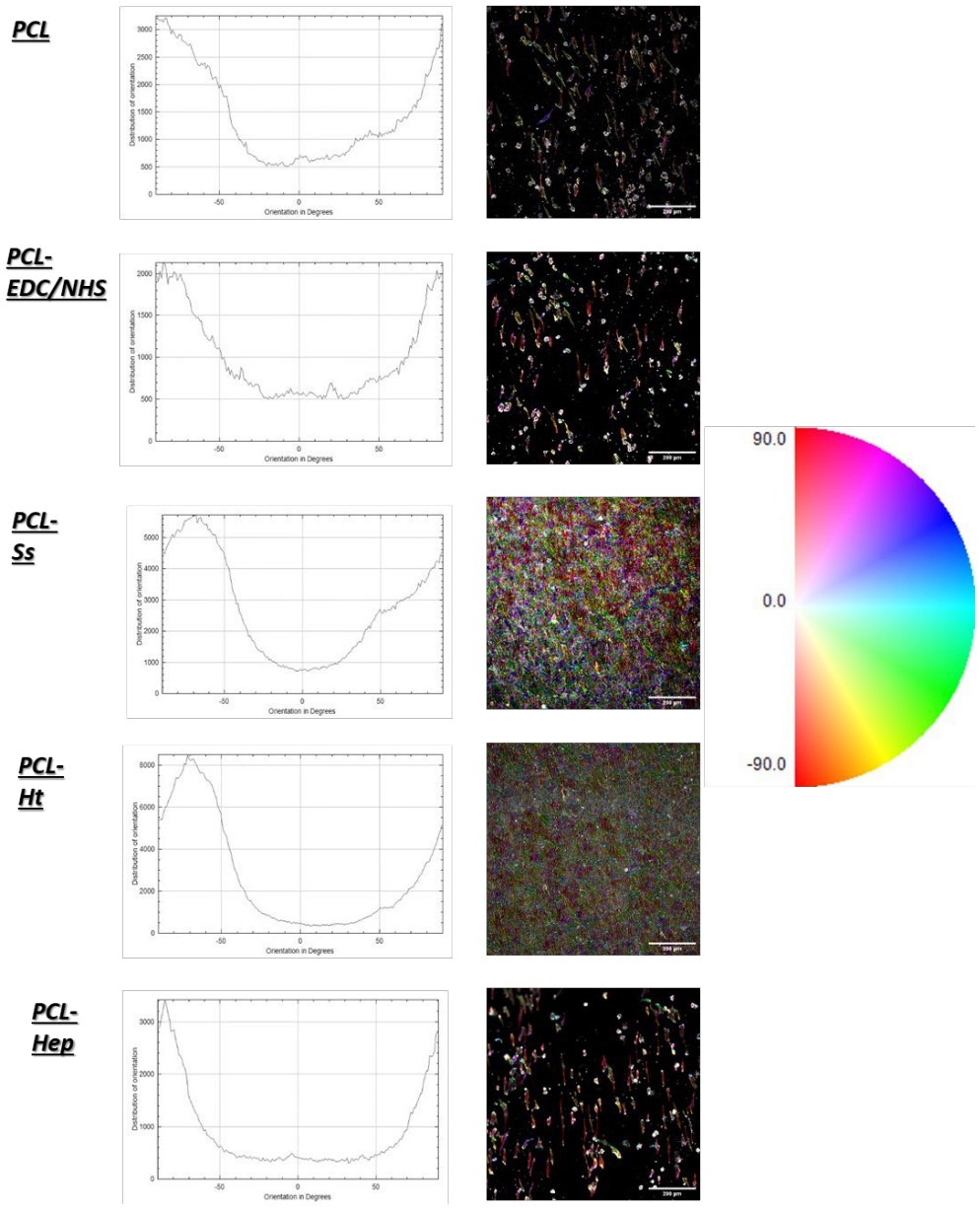

Figure S4.10. Quantification of the alignment of F-actin fibers of hMVECs cultured on the surface of PCL electrospun scaffolds with aligned nanofibers. Different colors represent different F-actins orientations following the color wheel in the figure. Magnification 10x (scale bar 200µm).

References

[1] C. Spadaccio, A. Rainer, R. Barbato, M. Trombetta, M. Chello, B. Meyns, The long-term follow-up of large-diameter Dacron® vascular grafts in surgical practice: A review, Journal of Cardiovascular Surgery 60 (2019) 501–513. https://doi.org/10.23736/S0021-9509.16.08061-7.

[2] F.O. Obiweluozor, G.A. Emechebe, D.W. Kim, H.J. Cho, C.H. Park, C.S. Kim, I.S. Jeong, Considerations in the Development of Small-Diameter Vascular Graft as an Alternative for Bypass and Reconstructive Surgeries: A Review, Cardiovasc Eng Technol 11 (2020) 495–521. https://doi.org/10.1007/s13239-020-00482-y.

[3] B. Ratner, Vascular Grafts: Technology Success/ Technology Failure, BME Front 4 (2023). https://doi.org/10.34133/bmef.0003.

[4] S. Pashneh-Tala, S. MacNeil, F. Claeyssens, The tissue-engineered vascular graft - Past, present, and future, Tissue Eng Part B Rev 22 (2016) 68–100. https://doi.org/10.1089/ten.teb.2015.0100.

[5] P. Zilla, D. Bezuidenhout, P. Human, Prosthetic vascular grafts: Wrong models, wrong questions and no healing, Biomaterials 28 (2007) 5009–5027. https://doi.org/10.1016/j.biomaterials.2007.07.017.

[6] C.W. Tsao, A.W. Aday, Z.I. Almarzooq, C.A.M. Anderson, P. Arora, C.L. Avery, C.M. Baker-Smith, A.Z. Beaton, A.K. Boehme, A.E. Buxton, Y. Commodore-Mensah, M.S.V. Elkind, K.R. Evenson, C. Eze-Nliam, S. Fugar, G. Generoso, D.G. Heard, S. Hiremath, J.E. Ho, R. Kalani, D.S. Kazi, D. Ko, D.A. Levine, J. Liu, J. Ma, J.W. Magnani, E.D. Michos, M.E. Mussolino, S.D. Navaneethan, N.I. Parikh, R. Poudel, M. Rezk-Hanna, G.A. Roth, N.S. Shah, M.P. St-Onge, E.L. Thacker, S.S. Virani, J.H. Voeks, N.Y. Wang, N.D. Wong, S.S. Wong, K. Yaffe, S.S. Martin, Heart Disease and Stroke Statistics - 2023 Update: A Report from the American Heart Association, Circulation 147 (2023) E93–E621. https://doi.org/10.1161/CIR.0000000000001123.

[7] J. Ji, H. Xu, C. Li, J. Luo, Small-Caliber Tissue-Engineered Vascular Grafts Based on Human-Induced Pluripotent Stem Cells: Progress and Challenges, Tissue Eng Part B Rev 29 (2023) 441–455. https://doi.org/10.1089/ten.teb.2023.0005.

[8] G.G. Flores-Rojas, B. Gómez-Lazaro, F. López-Saucedo, R. Vera-Graziano, E. Bucio, E. Mendizábal, Electrospun Scaffolds for Tissue Engineering: A Review, Macromol 3 (2023) 524–553. https://doi.org/10.3390/macromol3030031.

[9] A. Hasan, A. Memic, N. Annabi, M. Hossain, A. Paul, M.R. Dokmeci, F. Dehghani, A. Khademhosseini, Electrospun scaffolds for tissue engineering of vascular grafts, Acta Biomater 10 (2014) 11–25. https://doi.org/10.1016/j.actbio.2013.08.022.

[10] S. Nazarnezhad, F. Baino, H.W. Kim, T.J. Webster, S. Kargozar, Electrospun nanofibers for improved angiogenesis: Promises for tissue engineering applications, Nanomaterials 10 (2020) 1–35. https://doi.org/10.3390/nano10081609.

[11] Y. Zhuang, C. Zhang, M. Cheng, J. Huang, Q. Liu, G. Yuan, K. Lin, H. Yu, Challenges and strategies for in situ endothelialization and long-term lumen patency of vascular grafts, Bioact Mater 6 (2021) 1791–1809. https://doi.org/10.1016/j.bioactmat.2020.11.028.

[12] V.M. Merkle, D. Martin, M. Hutchinson, P.L. Tran, A. Behrens, S. Hossainy, J. Sheriff, D. Bluestein, X. Wu, M.J. Slepian, Hemocompatibility of poly(vinyl alcohol)-gelatin core-shell electrospun nanofibers: A scaffold for modulating platelet deposition and activation, ACS Appl Mater Interfaces 7 (2015) 8302–8312. https://doi.org/10.1021/acsami.5b01671.

[13] B. Sivaraman, R.A. Latour, The relationship between platelet adhesion on surfaces and the structure versus the amount of adsorbed fibrinogen, Biomaterials 31 (2010) 832–839. https://doi.org/10.1016/j.biomaterials.2009.10.008.
[14] M. Shojaee, C.A. Bashur, Compositions Including Synthetic and Natural Blends for Integration and Structural Integrity: Engineered for Different Vascular Graft Applications, Adv Healthc Mater 6 (2017). https://doi.org/10.1002/adhm.201700001.
[15] B.B.J. Leal, N. Wakabayashi, K. Oyama, H. Kamiya, D.I. Braghirolli, P. Pranke, Vascular Tissue Engineering: Polymers and Methodologies for Small Caliber Vascular Grafts, Front Cardiovasc Med 7 (2021). https://doi.org/10.3389/fcvm.2020.592361.
[16] M.X. Li, Q.Q. Wei, H.L. Mo, Y. Ren, W. Zhang, H.J. Lu, Y.K. Joung, Challenges and advances in materials and fabrication technologies of small-diameter vascular grafts, Biomater Res 27 (2023). https://doi.org/10.1186/s40824-023-00399-2.
[17] K. Razmjooee, S. Saber-Samandari, H. Keshvari, S. Ahmadi, Improving anti thrombogenicity of nanofibrous polycaprolactone through surface modification, J Biomater Appl 34 (2019) 408–418. https://doi.org/10.1177/0885328219855719.
[18] A.J. Lepedda, G. Nieddu, M. Formato, M.B. Baker, J. Fernández-Pérez, L. Moroni, Glycosaminoglycans: From Vascular Physiology to Tissue Engineering Applications, Front Chem 9 (2021). https://doi.org/10.3389/fchem.2021.680836.
[19] S. Aslani, M. Kabiri, S. HosseinZadeh, H. Hanaee-Ahvaz, E.S. Taherzadeh, M. Soleimani, The applications of heparin in vascular tissue engineering, Microvasc Res 131 (2020). https://doi.org/10.1016/j.mvr.2020.104027.
[20] S.Y. Zhou, L. Li, E. Xie, M.X. Li, J.H. Cao, X. Bin Yang, D.Y. Wu, Small-diameter PCL/PU vascular graft modified with heparin-aspirin compound for preventing the occurrence of acute thrombosis, Int J Biol Macromol 249 (2023). https://doi.org/10.1016/j.ijbiomac.2023.126058.
[21] C. Nie, L. Ma, C. Cheng, J. Deng, C. Zhao, Nanofibrous Heparin and Heparin-Mimicking Multilayers as Highly Effective Endothelialization and Antithrombogenic Coatings, Biomacromolecules 16 (2015) 992–1001. https://doi.org/10.1021/bm501882b.
[22] L. Qin, Y. Yang, W. Mao, Anticoagulant Property of a Sulfated Polysaccharide with Unique Structural Characteristics from the Green Alga Chaetomorpha aerea, Mar Drugs 21 (2023). https://doi.org/10.3390/md21020088.
[23] V.H. Pomin, P.A.S. Mourão, Structure, biology, evolution, and medical importance of sulfated fucans and galactans, Glycobiology 18 (2008) 1016–1027. https://doi.org/10.1093/glycob/cwn085.
[24] C.G. Panagos, D.S. Thomson, C. Moss, A.D. Hughes, M.S. Kelly, Y. Liu, W. Chai, R. Venkatasamy, D. Spina, C.P. Page, J. Hogwood, R.J. Woods, B. Mulloy, C.D. Bavington, D. Uhrín, Fucosylated chondroitin sulfates from the body wall of the sea cucumber Holothuria forskali: Conformation, selectin binding, and biological activity, Journal of Biological Chemistry 289 (2014) 28284–28298. https://doi.org/10.1074/jbc.M114.572297.
[25] V.H. Pomin, Holothurian fucosylated chondroitin sulfate, Mar Drugs 12 (2014) 232–254. https://doi.org/10.3390/md12010232.
[26] Q. Li, C. Cai, Y. Chang, F. Zhang, R.J. Linhardt, C. Xue, G. Li, G. Yu, A novel structural fucosylated chondroitin sulfate from Holothuria Mexicana and its effects on growth factors binding and anticoagulation, Carbohydr Polym 181 (2018) 1160–1168. https://doi.org/10.1016/j.carbpol.2017.10.100.
[27] G. Nieddu, G. Obino, C. Ciampelli, A. Brunetti, T. Cubeddu, R. Manconi, G.A. Stocchino, G.A. Deiana, M. Formato, A.J. Lepedda, Purification of an Acidic Polysaccharide with

Anticoagulant Activity from the Marine Sponge Sarcotragus spinosulus, Mar Drugs 22 (2024). https://doi.org/10.3390/md22030139.

[28] N.E. Ustyuzhanina, M.I. Bilan, A.S. Dmitrenok, N.E. Nifantiev, A.I. Usov, Fucosylated chondroitin sulfates from the sea cucumbers Holothuria tubulosa and Holothuria stellati, Carbohydr Polym 200 (2018) 1–5. https://doi.org/10.1016/j.carbpol.2018.07.035.

[29] N.E. Ustyuzhanina, M.I. Bilan, N.Y. Anisimova, S.P. Nikogosova, A.S. Dmitrenok, E.A. Tsvetkova, E.G. Panina, N.P. Sanamyan, S.A. Avilov, V.A. Stonik, M. V. Kiselevskiy, A.I. Usov, N.E. Nifantiev, Fucosylated Chondroitin Sulfates with Rare Disaccharide Branches from the Sea Cucumbers Psolus peronii and Holothuria nobilis: Structures and Influence on Hematopoiesis, Pharmaceuticals 16 (2023). https://doi.org/10.3390/ph16121673.

[30] G. Kazemzadeh, N. Jirofti, H. Kazemi Mehrjerdi, M. Rajabioun, S.A. Alamdaran, D. Mohebbi-Kalhori, M.S. Mirbagheri, R. Taheri, A review on developments of in-vitro and in-vivo evaluation of hybrid PCL-based natural polymers nanofibers scaffolds for vascular tissue engineering, Journal of Industrial Textiles 52 (2022). https://doi.org/10.1177/15280837221128314.

[31] B. Sowmya, A.B. Hemavathi, P.K. Panda, Poly (ε-caprolactone)-based electrospun nano-featured substrate for tissue engineering applications: a review, Prog Biomater 10 (2021) 91–117. https://doi.org/10.1007/s40204-021-00157-4.

[32] M.A. Rodríguez-Soto, C.A. Polanía-Sandoval, A.M. Aragón-Rivera, D. Buitrago, M. Ayala-Velásquez, A. Velandia-Sánchez, G. Peralta Peluffo, J.C. Cruz, C. Muñoz Camargo, J. Camacho-Mackenzie, J.G. Barrera-Carvajal, J.C. Briceño, Small Diameter Cell-Free Tissue-Engineered Vascular Grafts: Biomaterials and Manufacture Techniques to Reach Suitable Mechanical Properties, Polymers (Basel) 14 (2022). https://doi.org/10.3390/polym14173440.

[33] K.E. Kubow, V.D. Shuklis, D.J. Sales, A.R. Horwitz, Contact guidance persists under myosin inhibition due to the local alignment of adhesions and individual protrusions, Sci Rep 7 (2017). https://doi.org/10.1038/s41598-017-14745-7.

[34] A.K. Gaharwar, M. Nikkhah, S. Sant, A. Khademhosseini, Anisotropic poly (glycerol sebacate)-poly (-caprolactone) electrospun fibers promote endothelial cell guidance, Biofabrication 7 (2015). https://doi.org/10.1088/1758-5090/7/1/015001.

[35] A. Rashad, S. Mohamed-Ahmed, M. Ojansivu, K. Berstad, M.A. Yassin, T. Kivijärvi, E.B. Heggset, K. Syverud, K. Mustafa, Coating 3D Printed Polycaprolactone Scaffolds with Nanocellulose Promotes Growth and Differentiation of Mesenchymal Stem Cells, Biomacromolecules 19 (2018) 4307–4319. https://doi.org/10.1021/acs.biomac.8b01194.

[36] S. Sarkar, K.M. Sales, G. Hamilton, A.M. Seifalian, Addressing thrombogenicity in vascular graft construction, J Biomed Mater Res B Appl Biomater 82 (2007) 100–108. https://doi.org/10.1002/jbm.b.30710.

[37] J.L. Chen, Q.L. Li, J.Y. Chen, C. Chen, N. Huang, Improving blood-compatibility of titanium by coating collagen-heparin multilayers, Appl Surf Sci 255 (2009) 6894–6900. https://doi.org/10.1016/j.apsusc.2009.03.011.

[38] P.A.S. Mourão, Perspective on the use of sulfated polysaccharides from marine organisms as a source of new antithrombotic drugs, Mar Drugs 13 (2015) 2770–2784. https://doi.org/10.3390/md13052770.

[39] W. Zhang, W. Jin, V.H. Pomin, F. Zhang, R.J. Linhardt, Interactions of marine sulfated glycans with antithrombin and platelet factor 4, Front Mol Biosci 9 (2022). https://doi.org/10.3389/fmolb.2022.954752.

[40] E. V. Sokolova, A.O. Byankina, A.A. Kalitnik, Y.H. Kim, L.N. Bogdanovich, T.F. Solov'Eva, I.M. Yermak, Influence of red algal sulfated polysaccharides on blood coagulation and platelets activation in vitro, J Biomed Mater Res A 102 (2014) 1431–1438. https://doi.org/10.1002/jbm.a.34827.
[41] N.E. Ustyuzhanina, N.A. Ushakova, K.A. Zyuzina, M.I. Bilan, A.L. Elizarova, O. V. Somonova, A. V. Madzhuga, V.B. Krylov, M.E. Preobrazhenskaya, A.I. Usov, M. V. Kiselevskiy, N.E. Nifantiev, Influence of fucoidans on hemostatic system, Mar Drugs 11 (2013) 2444–2458. https://doi.org/10.3390/md11072444.
[42] P. Sawadkar, N. Mandakhbayar, K.D. Patel, J.O. Buitrago, T.H. Kim, P. Rajasekar, F. Lali, C. Kyriakidis, B. Rahmani, J. Mohanakrishnan, R. Dua, K. Greco, J.H. Lee, H.W. Kim, J. Knowles, E. García – Gareta, Three dimensional porous scaffolds derived from collagen, elastin and fibrin proteins orchestrate adipose tissue regeneration, J Tissue Eng 12 (2021). https://doi.org/10.1177/20417314211019238.
[43] J.A. Eble, The Extracellular Matrix in Health and Disease, Current pharmaceutical design, 15(12), 1275–1276 (2009) https://doi.org/10.2174/138161209787846694.
[44] S.N. Rodrigues, I.C. Gonçalves, M.C.L. Martins, M.A. Barbosa, B.D. Ratner, Fibrinogen adsorption, platelet adhesion and activation on mixed hydroxyl-/methyl-terminated self-assembled monolayers, Biomaterials 27 (2006) 5357–5367. https://doi.org/10.1016/j.biomaterials.2006.06.010.
[45] K. Iliou, S. Kikionis, E. Ioannou, V. Roussis, Marine Biopolymers as Bioactive Functional Ingredients of Electrospun Nanofibrous Scaffolds for Biomedical Applications, Mar Drugs 20 (2022). https://doi.org/10.3390/md20050314.
[46] P.R. Souza, A.C. de Oliveira, B.H. Vilsinski, M.J. Kipper, A.F. Martins, Polysaccharide-based materials created by physical processes: From preparation to biomedical applications, Pharmaceutics 13 (2021). https://doi.org/10.3390/pharmaceutics13050621.
[47] M.M.A. Sacramento, J. Borges, F.J.S. Correia, R. Calado, J.M.M. Rodrigues, S.G. Patrício, J.F. Mano, Green approaches for extraction, chemical modification and processing of marine polysaccharides for biomedical applications, Front Bioeng Biotechnol 10 (2022). https://doi.org/10.3389/fbioe.2022.1041102.
[48] R. Kalpana Manivannan, N. Sharma, V. Kumar, I. Jayaraj, S. Vimal, M. Umesh, A comprehensive review on natural macromolecular biopolymers for biomedical applications: Recent advancements, current challenges, and future outlooks, Carbohydrate Polymer Technologies and Applications 8 (2024). https://doi.org/10.1016/j.carpta.2024.100536.
[49] M. Jin, J. Shi, W. Zhu, H. Yao, D.A. Wang, Polysaccharide-Based Biomaterials in Tissue Engineering: A Review, Tissue Eng Part B Rev 27 (2021) 604–626. https://doi.org/10.1089/ten.teb.2020.0208.
[50] H.M. Muir1, A Modified Uranic Acid Carbazole Reaction, 1962.
[51] M. Idini, P. Wieringa, S. Rocchiccioli, G. Nieddu, N. Ucciferri, M. Formato, A. Lepedda, L. Moroni, Glycosaminoglycan functionalization of electrospun scaffolds enhances Schwann cell activity, Acta Biomater 96 (2019) 188–202. https://doi.org/10.1016/j.actbio.2019.06.054.
[52] T. D. Goddard and D. G. Kneller, SPARKY 3, (2000).
[53] T. Liu, Y. Liu, Y. Chen, S. Liu, M.F. Maitz, X. Wang, K. Zhang, J. Wang, Y. Wang, J. Chen, N. Huang, Immobilization of heparin/poly-L-lysine nanoparticles on dopamine-coated surface to create a heparin density gradient for selective direction of platelet and vascular cells behavior, Acta Biomater 10 (2014) 1940–1954. https://doi.org/10.1016/j.actbio.2013.12.013.

[54] Z. Dai, J. Ronholm, Y. Tian, B. Sethi, X. Cao, Sterilization techniques for biodegradable scaffolds in tissue engineering applications, J Tissue Eng 7 (2016). https://doi.org/10.1177/2041731416648810.

[55] C.D. Georgiou, I. Papapostolou, Assay for the quantification of intact/fragmented genomic DNA, Anal Biochem 358 (2006) 247–256. https://doi.org/10.1016/j.ab.2006.07.035.

Chapter 5
Tunable Bioresorbable Scaffolds with Marine Sulfated Polysaccharides for Small-Caliber Vascular Grafts: A Multi-Layered Strategy Combining Electrospinning and 4-Axis Printing

Gabriele Obino[a,b]; Alberto Sensini[b,c]; Tim ten Brink[b]; Gabriele Nieddu[a]; Tristan Bodet[b]; Giovanni Andrea Deiana[d]; Martijn van Griensven[c]; Marilena Formato[a]; Antonio J Lepedda[a] and Lorenzo Moroni[b]

[a]Department of Biomedical Sciences, University of Sassari, Viale San Pietro, 43b, 07100 Sassari, Italy
[b] Department of Complex Tissue Regeneration, MERLN Institute for Technology-Inspired Regenerative Medicine, Maastricht University, 6200 MD Maastricht, The Netherlands
[C] Department of Cell Biology-Inspired Tissue Engineering MERLN Institute for Technology-Inspired Regenerative Medicine, Maastricht University, 6200 MD Maastricht, The Netherlands
[d]Department of Medicine, Surgery and Pharmacy, University of Sassari, Viale San Pietro, 43b, 07100 Sassari, Italy

The content of this chapter has been published in *Advanced Healthcare Materials* https://doi.org/10.1002/adhm.202505314

Abstract

The development of small-caliber tissue-engineered vascular grafts (sTEVGs) presents several challenges, including achieving balanced endothelialization, facilitating smooth muscle cell infiltration, preventing leakage, and ensuring adequate anti-thrombogenic properties, all while maintaining mechanical strength sufficient to withstand physiological pressures, surgical handling, and suturing.

In this study, we created a multi-layered polycaprolactone (PCL)-based sTEVG using a combination of electrospinning and 4-axis printing techniques, providing precise control over scaffold porosity, fiber alignment, and tunable mechanical properties and dimensions. To improve both biocompatibility and hemocompatibility, the PCL nanofibers were functionalized with sulfated polysaccharides purified from the body wall of the marine invertebrate *Holothuria tubulosa*, which significantly enhanced endothelialization and provided strong anti-thrombogenic properties, with no significant effects on bulk mechanics of the graft.

The inner layer, composed of tightly packed aligned electrospun nanofibers, supported a rapid formation of a mature endothelium, evaluated using human umbilical vein endothelial cells (HUVECs), while preventing graft leakage even at supraphysiological pressure (>1100 mmHg). The middle layers, made of circumferential electrospun nanofibers and 4-axis printed microfibers, increased overall porosity, enabling effective adhesion, orientation and infiltration by human coronary artery smooth muscle cells (HCASMCs), a crucial step to produce a functional tunica media regulating blood flow and maintaining blood pressure. The outer layer, consisting of random electrospun nanofibers, contributed significantly to the mechanical properties of the graft such as elasticity, toughness, burst pressure, and resistance to physiological vessel pressures.

Overall, the developed four-layer construct, with its enhanced tunable mechanical and biological properties, shows promise in sTEVG applications representing a valuable customizable/off-the-shelf alternative to autologous grafts.

Keywords: small-caliber tissue-engineered vascular grafts; marine sulfated polysaccharides; electrospinning; 4-Axis printing; endothelialization

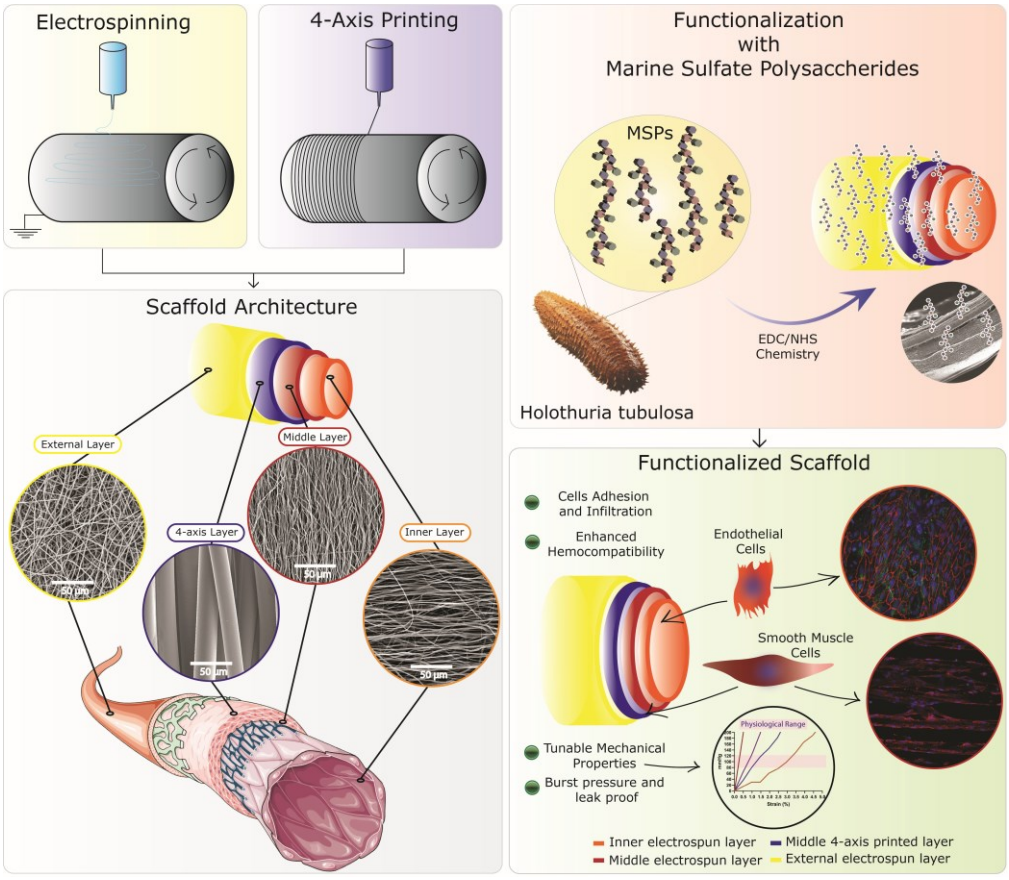

Graphical Abstract: Schematic overview of the fabrication and functionalization of multi-layered small-caliber vascular scaffolds. The scaffold was fabricated by combining electrospinning and 4-axis printing to create a multi-layered tubular structure with tunable mechanics. Functionalization with marine sulfated polysaccharides enhanced bioactivity, hemocompatibility, and cell adhesion, yielding a biomimetic small-caliber vascular graft.

Introduction

Cardiovascular diseases (CVDs), including those related to small-caliber vessels, such as Coronary Artery Disease (CAD) and Peripheral Artery Disease (PAD), are among the leading causes of morbidity and mortality worldwide [1-3]. Their prevalence continues to rise due to lifestyle factors and an aging global population [4,5]. For many patients, conventional treatment options, such as coronary artery bypass grafting, rely heavily on the availability of suitable autologous vessels. However, in a significant number of cases, patients have vessels that are either unsuitable for grafting due to poor quality or are simply unavailable in sufficient quantities [6]. This lack of optimal grafting material drives the need for alternative solutions, such as Tissue-Engineered Vascular Grafts (TEVGs), which have the potential to aid vascular surgery by providing an off-the-shelf alternative to autologous grafts [7-9].

While current TEVGs are effective for large-caliber vessels with an internal diameter greater than 6 mm, their application to smaller-caliber vessels, such as coronary arteries, has proven far more problematic. Small-caliber vessels face unique challenges, particularly the high incidence of early graft occlusion. This occlusion is primarily due to poor endothelialization and adverse interactions between blood proteins and the scaffold material, which can lead to thrombosis [10-13]. Therefore, the development of small-caliber TEVGs (sTEVGs) must focus on promoting rapid endothelialization while preventing platelet activation and clot formation. Additionally, grafts need to support cell migration, proliferation, and tissue remodeling in situ to achieve long-term functionality and integration with the native vasculature [14].

Despite advances in TEVG technology, several challenges remain, particularly for smaller vessels. Intimal hyperplasia, compliance mismatch, infection, and the long-term adaptation of the graft to the host vessel environment, especially in pediatric patients, continue to present significant obstacles to clinical success [15,16]. A promising approach to addressing these challenges involves the use of bioresorbable scaffolds, which mimic the native extracellular matrix (ECM) while guiding the formation of new tissue during the scaffold's degradation process. By carefully controlling the degradation rate, such scaffolds can provide temporary mechanical support until the host tissue has sufficiently remodeled and replaced the scaffolds' biomaterial.

Among the various fabrication techniques explored for the development of sTEVGs, electrospinning is widely used because it allows for the fabrication of nanofiber scaffolds that closely mimic the size and orientation of ECM protein fibers. These nanofibers provide numerous sites for cell attachment,

promoting cell colonization and tissue integration [14,17,18]. However, one of the key limitations of electrospun TEVG is the low porosity, due to the small fiber diameter. This low porosity impairs smooth muscle cell (SMC) infiltration and limits the deposition of ECM, which are critical for the long-term stability and functionality of the graft [14,19,20]. Furthermore, electrospun scaffolds can struggle to maintain their tubular structure after bending, a factor that limits their utility in surgical applications where flexibility and durability are essential.

To overcome these limitations, we have developed a four-layered polycaprolactone (PCL)-based sTEVG using a combination of electrospinning and 4-axis printing techniques. The first two layers of the scaffold are composed of electrospun nanofibers, with fibers aligned axially (First layer), facing the lumen of the tubular graft, or circumferentially (Second layer) to mimic the orientation of ECM in native vessels. The third layer consists of circumferential microfibers obtained by 4-axis printing (4-axis layer), which increases the porosity of the scaffold and facilitates SMC infiltration and ECM production. The final layer consists of randomly oriented electrospun nanofibers (External electrospun layer; EEL), which provide structural protection and prevent damage to the underlying layers. This multi-layered design ensures that the scaffold has varying pore sizes across its structure, with smaller pores in the inner layers to prevent leakage and larger pores in the middle layers to promote cell migration and infiltration, while maintaining overall scaffold integrity.

Alongside its mechanical and structural optimizations, scaffold's hemocompatibility was improved by PCL nanofibers functionalization with sulfated polysaccharides from *Holothuria tubulosa*. These marine-derived polysaccharides were chosen due to their known anticoagulant properties [21]. as well as their potential to improve hemocompatibility and endothelialization of nanofibrous PCL, as previously described [22].

In this study, we evidenced rapid endothelialization across the lumen surface of the scaffold, with human umbilical vein endothelial cells (HUVECs) forming a confluent monolayer within 3 days. Additionally, human coronary artery smooth muscle cells (HCASMCs) infiltrated the various strata of the middle layer while maintaining robust alpha smooth muscle actin expression, indicative of a contractile phenotype essential for optimal vascular wall function. Mechanical testing of the scaffolds demonstrated a non-linear behavior, with tunable properties such as elastic modulus, yield stress, and burst pressure. This tunability is achieved through the multi-layer design,

where individual layers can be adjusted in thickness or removed as needed, enabling precise customization of the scaffold's mechanical characteristics to meet specific vascular requirements.
Overall, the multi-layered, bioresorbable sTEVG, with its enhanced mechanical properties, anti-thrombotic features, and superior endothelialization, might represent a valuable off-the-shelf, ECM customizable alternative to autologous grafts, with important implications on the quality of life of CVD patients requiring bypass surgery.

Results

Scaffold design: production and fabrication

SEM images (Figure 5.1) confirmed the successful fabrication of a four-layered PCL sTEVG with distinct micro- and nano-architectures in each stratum. The inner layer (Figure 5.1A) comprised densely packed electrospun nanofibers aligned along the graft axis. Directly above this, a second electrospun layer (Figure 5.1B) featured nanofibers wrapped around the circumference of the graft, mimicking the native medial layer's fiber arrangement that resists vessel expansion under pressure, reproducing the hoop-stress–bearing organization of the medial ECM. The third layer (Figure 5.1C) consisted of circumferentially deposited microfibers produced by a 4-axis printing system, which created a more open, porous network designed to facilitate smooth muscle cell infiltration and de novo ECM deposition. Finally, an outermost electrospun layer of randomly oriented nanofibers (Figure 5.1D) enveloped the construct, providing a protective “adventitial” sheath that stabilizes the underlying structure and guards against delamination. Across all layers, fiber diameter and inter-fiber spacing appeared uniform, and no defects or discontinuities were observed, demonstrating robust control over scaffold morphology and layer integration (Figure 5.1E,F).

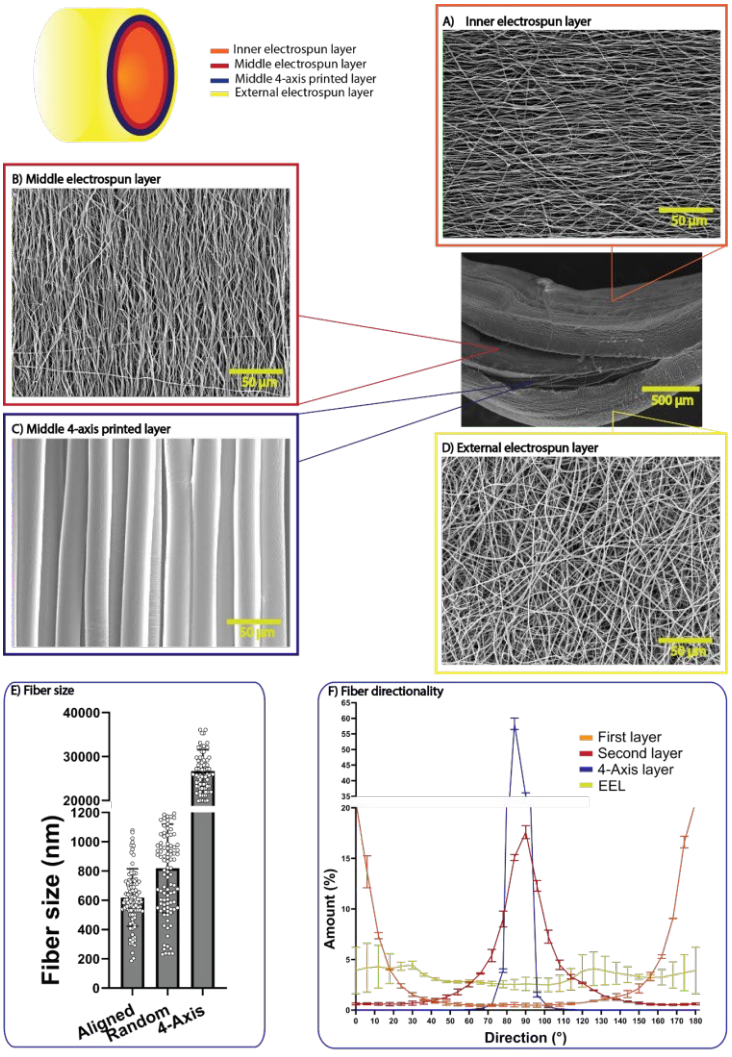

Figure 5.1. Scanning electron micrographs of the four distinct scaffold strata and a scheme of transverse section of the assembled graft. (A) Inner electrospun layer with nanofibers aligned parallel to the graft axis (×500; scale bar = 50 µm). (B) Second electrospun layer with nanofibers wrapped circumferentially (×500; scale bar = 50 µm). (C) 4-axis–printed microfiber layer with microfibers circumferentially aligned (×500; scale bar = 50 µm). (D) Outermost electrospun layer with randomly oriented nanofibers, forming an adventitia-like protective sheath (×500; scale bar = 50 µm). (E) Fiber size in the different layer. (F) Fiber directionality distribution of the different layers. Results expressed as mean ± SD (n = 5).

Spectroscopic, Colorimetric, and Elemental Characterization of Scaffold Functionalization

The success of the scaffold functionalization was evaluated using a combination of complementary techniques and assays. ATR-FTIR analysis revealed characteristic peaks at 3400 and 1650 cm−1, indicating effective crosslinking via EDC/NHS chemistry. Specifically, the broad peak at 3400 cm−1 corresponds to –OH and –NH stretching vibrations, while the peak at 1650 cm−1 corresponds to amide stretching. These peaks were observed only in the scaffolds functionalized with Ht and Hep (PCL-Ht and PCL-Hep), and were absent in untreated PCL scaffolds, confirming the chemical incorporation of marine sulfated polysaccharides onto the scaffold surfaces (Figure S5.1). In addition, Toluidine Blue staining, followed by quantitative analysis, was employed to assess the distribution and density of the functionalized polysaccharides across the scaffolds. The results showed a uniform distribution of the staining throughout the scaffold and revealed an average of 0.89 µg of sulfated polysaccharides per mg of scaffold for PCL-Hep and 1.78 µg/mg for PCL-Ht (Figure S5.2B,C).

The TBO assay was also used in our previous study to verify the functionalization stability over 1 month of incubation at 37°C in PBS and after storage for 12 months at room temperature in dry conditions. This demonstrated that the functionalization strategy and protocol exhibit excellent stability under both dry and physiological conditions [22].

This finding was further supported by EDX analysis, which provided semi-quantitative insights into the surface elemental composition and confirmed the presence of sulfur-containing groups derived from the polysaccharides. The analysis showed that sulfur accounted for an average of 0.045% of the total mass of the scaffolds in PCL-Hep and 0.07% in PCL-Ht (Figure S5.2A). Together, these methods provided robust and convergent evidence of the successful crosslinking of marine sulfated polysaccharides onto the PCL scaffolds.

Mechanical Characterization of Four-Layer Bioresorbable Vascular Graft

Uniaxial tensile testing of the electrospun and printed layers (V5.1) revealed a clear trade-off between extensibility and strength. The innermost aligned nanofiber layer (First layer) was the most compliant, reaching very high elongation before failure, but it exhibited the lowest elastic modulus, toughness to yield and yield stress (Figure 5.2C–E) of all configurations. Successive

addition of layers (circumferential nanofibers, printed microfibers, and an outer random nanofiber layer) progressively stiffened the construct (Figure 5.2C). In the stress–strain curves (Figure 5.2B), each extra layer shifted the curve upward: elastic modulus (Figure 5.2C) and toughness (Figure 5.2D) increased monotonically from the single-layer scaffold to the full four-layer graft. The four-layered scaffold had the greatest toughness and highest elastic modulus. Importantly, the physiologically relevant zone of the stress-strain curves is the pre-yield one, defined by the yield force, yield stress, and yield strain. Beyond yield, the residual part of the curve mainly serves as a safety margin, delaying rupture if yield stress is exceeded. Thus, while the first layer provided high deformability with limited strength, the four-layer assembly combined inner-layer compliance with outer-layer strength, resulting in superior energy absorption and structural reliability (Figure 5.2). The same observation can be appreciated by analyzing the net mechanical stress and elastic moduli of the different TEVG layers (Figure S5.3). Surface chemistry had only minor effects on bulk mechanics (Figure 5.3 and Figure S5.4). All PCL scaffolds retained a non-linear ductile (non-linear stress–strain) behavior (Figure 5.3A). Only PCL-Ht displayed a slight reduction in elastic modulus (Figure 5.3B), which did not compromise overall mechanical integrity (Figure 5.3). Importantly, all functionalized scaffolds preserved high deformability comparable to unmodified PCL (Figure 5.3C–E).

Burst pressure testing revealed remarkable improvements with scaffold layering (Figure 5.4). Direct burst experiments were conducted only on the fully assembled four-layer tubular scaffolds using a customized platform (V5.2), showing that PCL–EDC/NHS grafts withstood ~1467 ± 208 mmHg before rupture, while even the chemically modified variants, PCL–Ht and PCL–Hep, reached ~1123 ± 68 mmHg and ~1192 ± 81 mmHg, respectively (Figure 5.4B). All constructs exceeded 1000 mmHg, well above physiological systolic pressure, indicating strong *in vivo* pressure resistance. In contrast, indirect burst pressures for individual layers and intermediate assemblies were estimated using Laplace's law based on ring tensile data (Figure 5.4C,D). These calculations showed a clear layer-dependent increase: the innermost nanofiber layer had the lowest theoretical burst (~362 ± 31 mmHg), while the full four-layer configuration reached a predicted burst of ~10 759 ± 776 mmHg. This >25-fold increase highlights how successive layering—particularly the incorporation of circumferential fibers, microfibers, and the outer sheath—contributed synergistically to wall tension capacity and hoop strength. Importantly, the direct burst results showed minimal difference

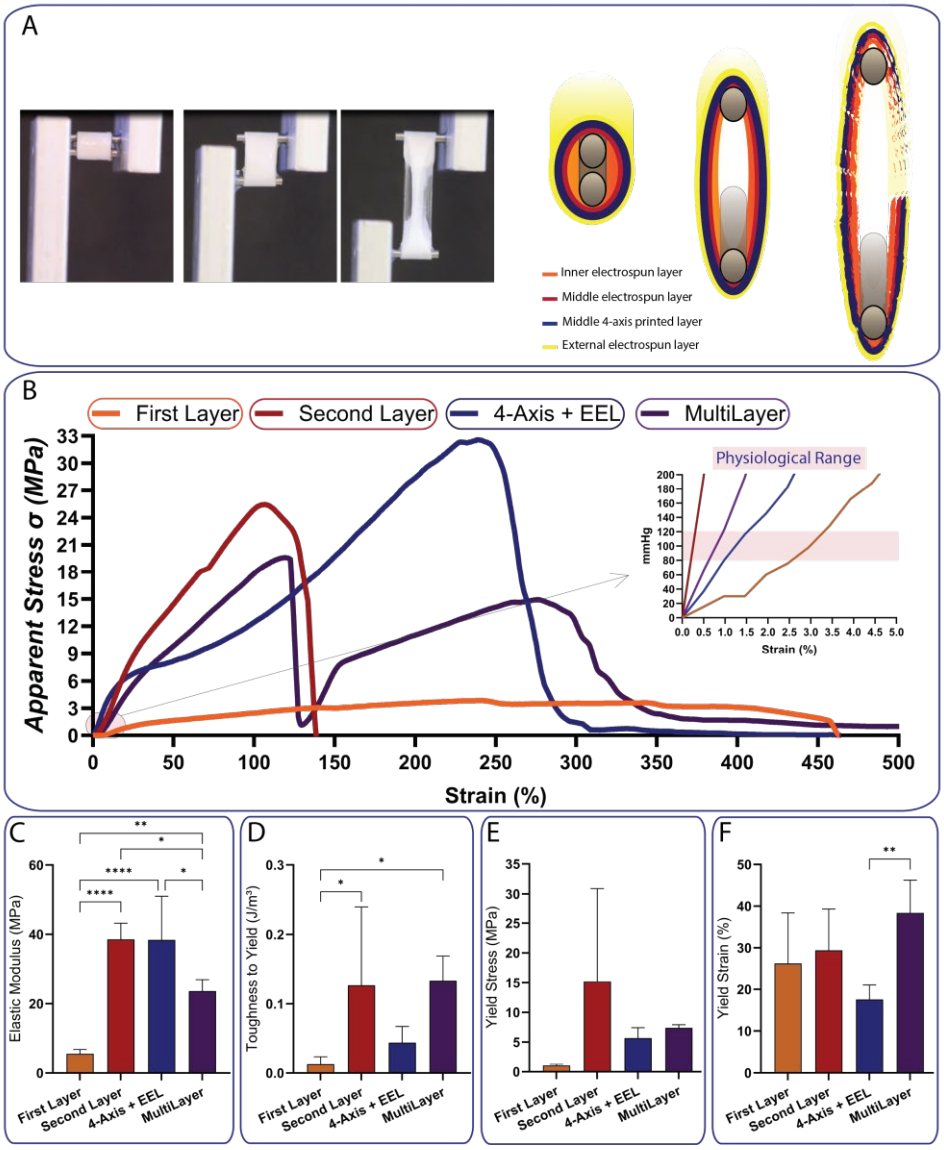

Figure 5.2. Mechanical characterization of multilayered TEVGs. (A) Tensile testing setup and schematic of the scaffold architecture. (B) Representative apparent stress-strain curves for scaffolds with increasing numbers of layers. (C) Apparent elastic modulus, (D) apparent toughness to yield, (E) apparent yield stress and (F) yield strain for each scaffold configuration. Data: mean ± SD (n = 5). Statistics: ordinary one-way ANOVA followed by Tukey's multiple comparisons test. **p*-value < 0.05; ***p*-value < 0.01; *****p*-value < 0.0001.

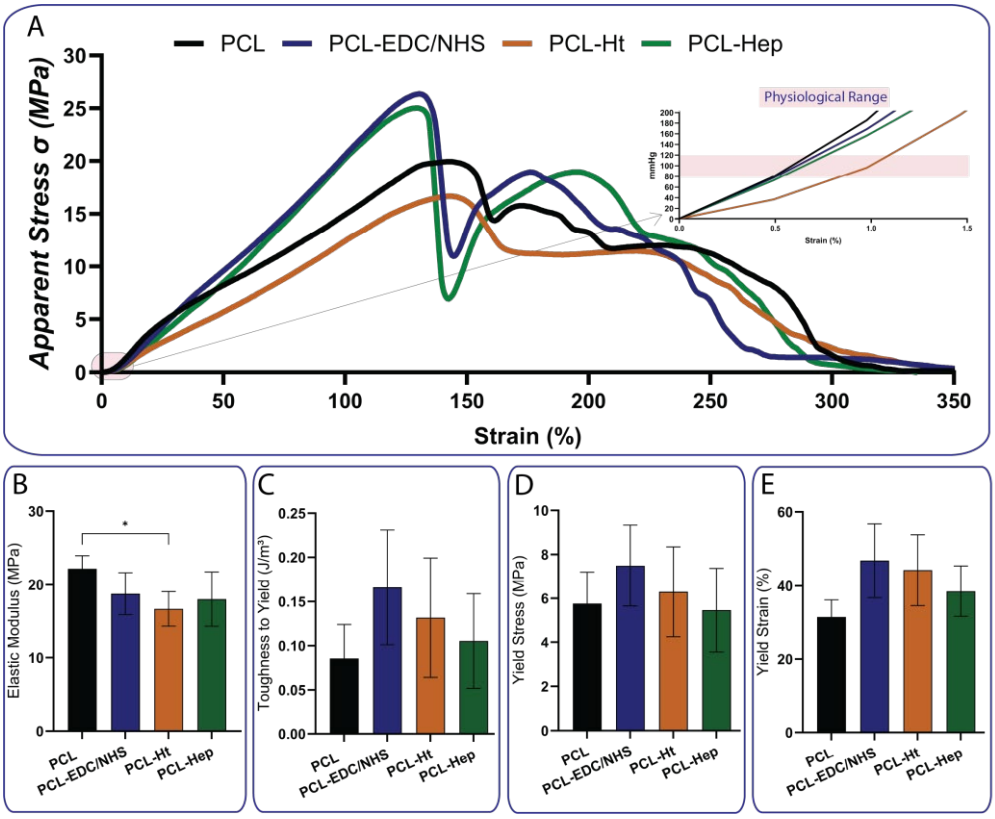

Figure 5.3. Mechanical properties of functionalized TEVGs. (A) Representative apparent stress–strain curves for PCL, PCL–EDC/NHS, PCL–Ht, and PCL–Hep scaffolds. (B) apparent elastic modulus, (C) apparent toughness to yield, (D) apparent yield stress and (E) yield strain for each scaffold functionalization. Data: mean ± SD (n = 5). Statistics: ordinary one-way ANOVA followed by Tukey's multiple comparisons test. *p-value < 0.05.

between surface chemistries (PCL–EDC/NHS, PCL–Ht, PCL–Hep), all performing in the same supraphysiological range (>11 000 mmHg). This confirms that the structural architecture, not the surface modification, was the dominant determinant of burst pressure. In summary, the combination of theoretical and experimental results demonstrates that the multilayer design provides robust pressure resistance, far exceeding clinical benchmarks, and remains mechanically sound regardless of surface treatment (Figure 5.4). Scaffold mechanics can be finely tuned by adding or removing individual layers (Figure S5.5). The incorporation of the compliant inner nanofiber layer

markedly lowered the overall elastic modulus and increased extensibility, yielding a more elastic construct. Conversely, the addition of the circumferential nanofiber layer, and particularly the inclusion of two copies of that layer substantially raised both elastic modulus and yield strength, producing a more resistant scaffold (Figure S5.3). Compliance of the individual layers and of the multilayer TEVG, both before and after functionalization with sulfated polysaccharides, was calculated from the stress–strain curves (Figure S5.6). The inner nanofiber layer exhibited the highest compliance, followed by the multilayer TEVG (both functionalized and non-functionalized). In contrast, the second electrospun layer and the 4-axis + EEL configuration showed the lowest compliance and highest stiffness (Figure S5.6). By selectively adjusting layer number and order, it was possible to precisely balance scaffold elasticity, compliance, and mechanical strength.

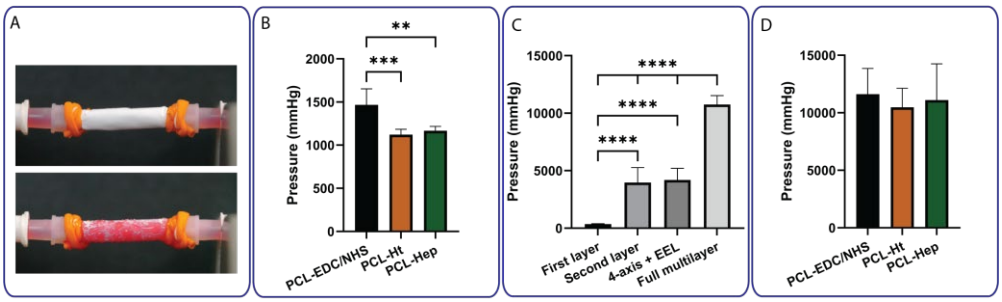

Figure 5.4. Burst pressure analysis of TEVGs. (A) Custom setup for direct burst pressure measurement. (B) Direct burst pressure values for 4-layer TEVGs with different surface chemistries. (C) Theoretical burst pressure calculated for scaffolds with increasing layer numbers and for the 4-layer construct. (D) Theoretical burst pressure for different functionalized scaffolds. Data: mean ± SD (n = 3). Statistics: ordinary one-way ANOVA followed by Tukey's multiple comparisons test. ***p*-value < 0.01; ****p*-value < 0.001; *****p*-value < 0.0001.

HUVECs culture on Vascular Scaffolds

HUVECs were seeded onto the luminal surface of the scaffolds and cultivated for 21 days under static conditions (Figure 5.5) and 7 days under dynamic flow (Figure 5.6). Quantitative assessment via DNA content was performed at days 1, 10, and 21 for statically cultured constructs (Figure S5.7), complemented by comprehensive immunofluorescence analysis of the tissue-engineered vascular graft (TEVG) surface.

Static Culture Outcomes

Under static conditions, HUVECs demonstrated differential colonization patterns depending on scaffold surface modification. Ht-treated scaffolds (PCL-Ht) supported significantly more rapid and extensive endothelial coverage compared to both PCL-EDC/NHS controls and PCL-Hep. By day 21, endothelial cells on Ht-treated scaffolds exhibited characteristics of a mature, functional endothelium characterized by a confluent monolayer without intercellular gaps and pronounced cellular alignment along the nanofiber orientation axis (Figure 5.5).

Dynamic Flow Cultivation Results

In the dynamic flow system setup (Figure S5.8), initial cellular attachment (6 hours post-static seeding) revealed incomplete coverage across all scaffold types (Figure 5.6 top panel). Notably, both PCL-Ht and PCL-Hep scaffolds demonstrated substantially higher initial cell adhesion compared to unmodified PCL constructs. Immunocytochemical analysis at this early timepoint showed positive expression of von Willebrand factor (vWF) with clear nuclear staining, while VE-cadherin, a critical adherens junction protein essential for endothelial barrier function, remained undetectable, confirming the immature state of the nascent endothelium.

Following 7 days of cultivation under physiological flow conditions, endothelial cells across all scaffold types began expressing VE-cadherin at cell-cell interfaces, indicating the initiation of adherens junction formation. This expression pattern is consistent with the known role of VE-cadherin in establishing intercellular connections during endothelial maturation. Significantly, only Ht-treated scaffolds supported the development of a near-confluent endothelial monolayer, with cells exhibiting fully formed adherens junctions and adopting the characteristic hexagonal cobblestone morphology associated with functional endothelium (Figure 5.6 bottom panel).

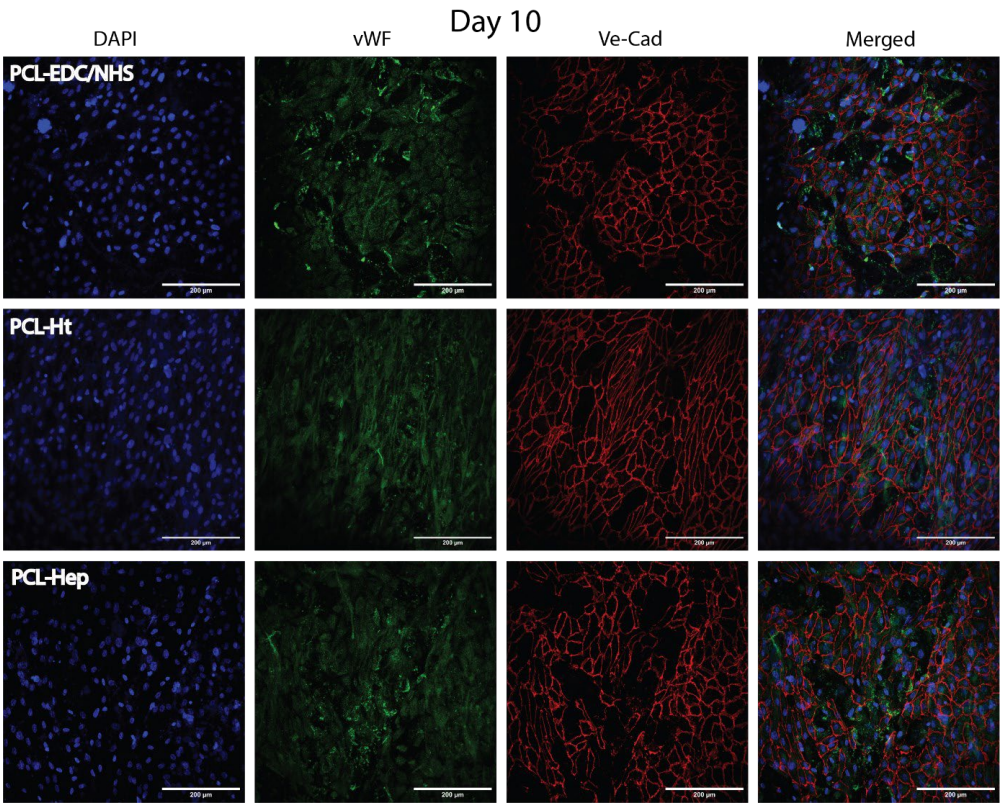

Figure 5.5. Immunofluorescent staining of HUVECs cultured under static conditions for 10 days on the luminal surface of TEVGs with different surface functionalizations: PCL-EDC/NHS, PCL-Ht, and PCL-Hep. Nuclei are stained with DAPI (blue), cell-cell junctions are labeled with VE-Cadherin (red), and von Willebrand Factor (vWF) is shown in green. Images were acquired at 25× magnification. Scale bar: 200 µm.

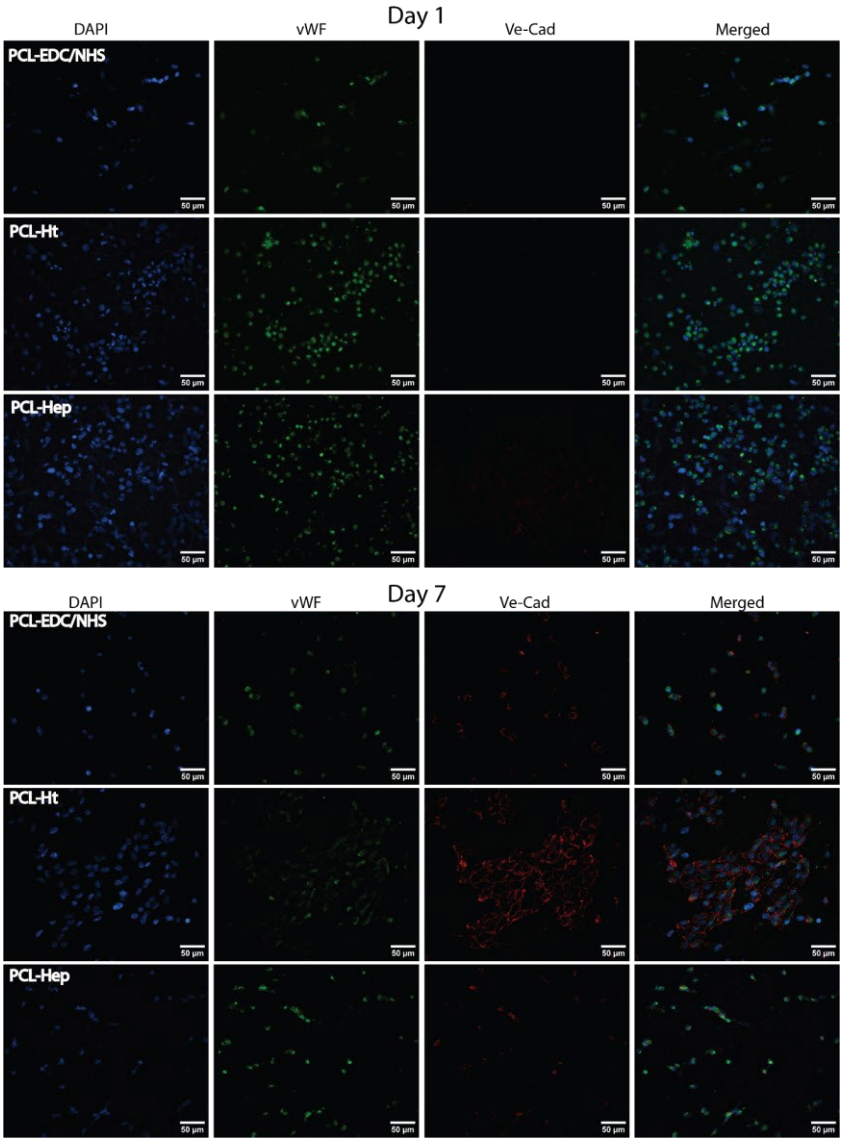

Figure 5.6. Immunofluorescent staining of HUVECs cultured under dynamic flow conditions on the luminal surface of TEVGs (PCL-EDC/NHS, PCL-Ht, and PCL-Hep). Top panel represents cells at Day 1 post-seeding; the bottom panel shows cells after 7 days of dynamic culture. Nuclei are stained with DAPI (blue), VE-Cadherin marks cell-cell junctions (red), and von Willebrand Factor (vWF) indicates endothelial phenotype (green). Images acquired at 40× magnification. Scale bar: 50 µm.

CASMC Attachment, Proliferation, and Morphological Response to Scaffold Chemistry

CASMCs were seeded onto the microfiber outer layer of each scaffold and cultured under static conditions for 21 days (Figures 5.7 and S5.9). Confocal microscopy z-stack analysis demonstrated robust cell infiltration across all scaffold types (Figure 5.7 and V5.3, V5.4 and V5.5). Quantitative DNA assay results revealed comparable cell attachment and proliferation among PCL-EDC/NHS, PCL-Ht, and PCL-Hep scaffolds at early timepoints (days 1 and 10), with no statistically significant differences observed (Figure S5.9). However, by day 21, both PCL-Ht and PCL-EDC/NHS scaffolds maintained significantly higher cell populations compared to PCL-Hep scaffolds ($p < 0.001$), indicating a potential inhibitory effect of heparin on long-term CASMC maintenance. Longitudinal analysis of DNA content across timepoints revealed relatively stable cell populations on PCL-Ht and PCL-EDC/NHS scaffolds throughout the culture period, while PCL-Hep scaffolds exhibited a significant decrease in cell number by day 21.

α-SMA immunofluorescence analysis revealed striking phenotypic differences dependent on scaffold chemistry. CASMCs cultured on PCL-Ht scaffolds exhibited the characteristic contractile phenotype, with elongated, spindle-shaped morphology aligned parallel to fiber orientation. These cells displayed well-defined α-SMA-positive stress fibers and developed multilayered structures resembling the native arterial tunica media architecture (Figure 5.7). In contrast, CASMCs on PCL-EDC/NHS surfaces predominantly adopted rounded or partially spread morphologies, forming small, loosely associated clusters with intermittent and diffuse α-SMA expression (Figure 5.7, middle panel). The most pronounced phenotypic deviation occurred on PCL-Hep scaffolds, where CASMCs assembled into dense spheroidal aggregates with minimal cellular elongation and disrupted α-SMA fiber organization, maintaining similar overall cell numbers until day 10 (Figure 5.7, bottom panel). Collectively, these findings demonstrate that while scaffold chemistry minimally influences initial CASMCs attachment and early proliferation, it substantially impacts long-term cell retention and phenotypic maintenance, with PCL-Ht scaffolds best supporting the contractile CASMCs phenotype critical for vascular tissue engineering applications.

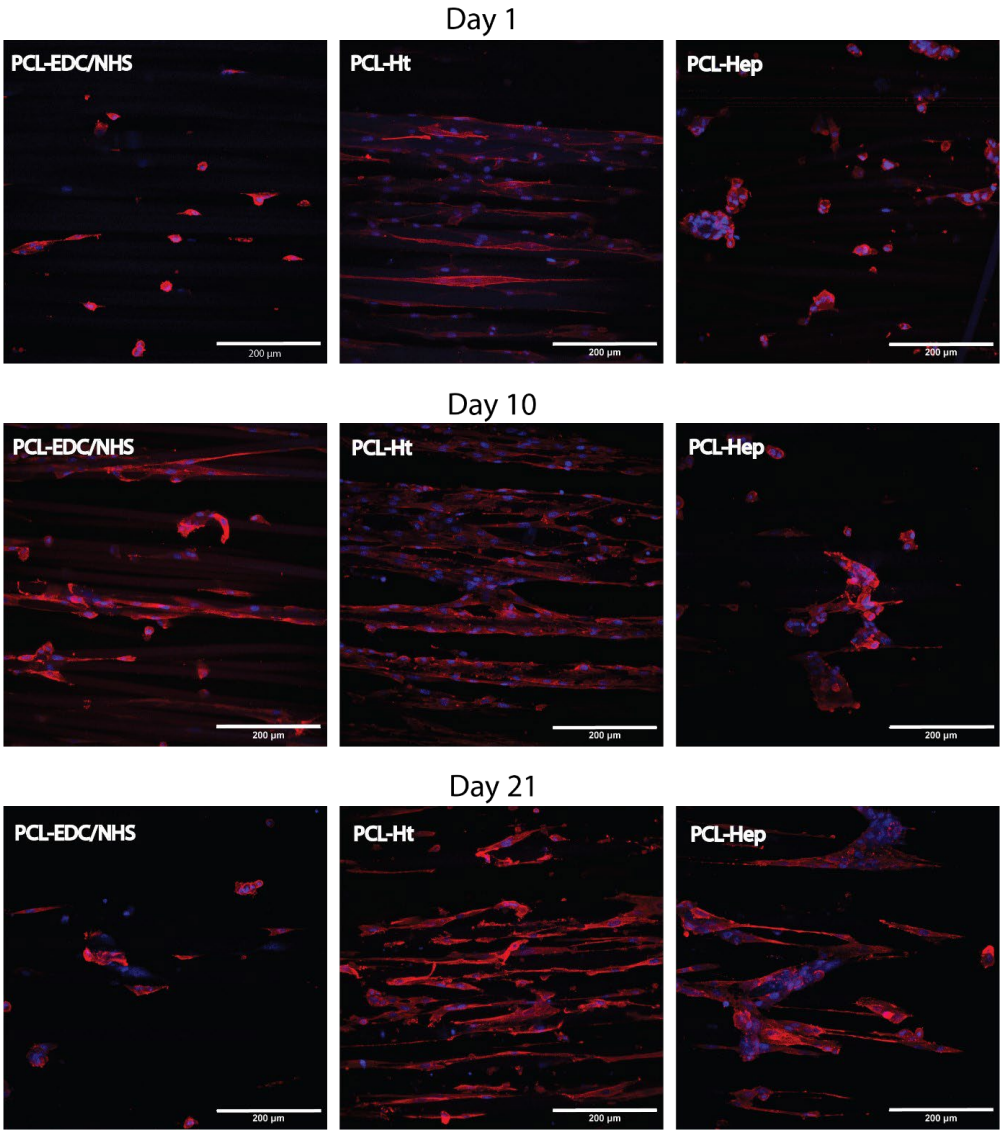

Figure 5.7. Immunofluorescent staining of CASMCs cultured under static conditions on the external surface of functionalized tubular scaffolds (PCL-EDC/NHS, PCL-Ht, and PCL-Hep). CASMCs were seeded on the microfiber outer layer of scaffolds. Red fluorescence indicates α-smooth muscle actin (α-SMA), while blue fluorescence (DAPI) marks nuclei. Images acquired at 25× magnification. Scale bar: 200 µm.

Discussion

Biomimetic Scaffold Architecture

The extracellular matrix (ECM) of vascular arteries is characterized by a complex, multilayered architecture and a distinct cellular composition, with each layer contributing uniquely to the overall vascular function [23, 24]. The intima, media, and adventitia each plays a crucial role in maintaining vessel integrity: the intima minimizes thrombosis, the media, particularly in elastic arteries, dampens the pulsatile pressure generated by cardiac output, and in the muscular arteries, such as the coronary vessels, dynamically regulate blood flow to meet the metabolic demands of the myocardium. This intricately orchestrated structure is essential for preventing clot formation, inhibiting leakage, and ensuring the effective transmission and modulation of hemodynamic forces throughout the vascular network. Numerous researchers have sought to engineer vascular grafts that replicate the complex architecture, fiber size, and orientation of native blood vessels [25]. Electrospinning provides a versatile method to fabricate nanofibers with dimensions and alignment similar to ECM proteins, enhancing surface area and cellular adhesion. However, electrospun scaffolds alone often exhibit limited pore size, which restricts effective cell infiltration and remodeling [18]. Conversely, advanced techniques like melt electrowriting and 3D printing can create open, porous scaffolds that improve cellular infiltration [26-30]. Yet, the associated larger pore sizes may compromise barrier function, increasing the risk of leakage.

Our approach addresses these limitations by combining electrospinning and 4-axis printing to create a multilayer scaffold that mimics the layered structure of native vessels. The innermost layer of aligned electrospun nanofibers offers a dense, compliant, and adhesive substrate that supports endothelial alignment and monolayer formation. The adjacent circumferential electrospun layer adds tunable stiffness and toughness. Centrally, a printed microfiber layer introduces a porous architecture that enables SMC infiltration and circumferential alignment on different strata, resembling the tunica media. Finally, an outer layer of randomly oriented nanofibers simulates the adventitia, reinforcing the scaffold and preventing delamination.

Effective sTEVG development faces significant challenges due to thrombogenic properties and poor endothelialization of the synthetic scaffold. To enhance endothelialization and reduce leakage, many researchers have applied protein coatings such as fibrin or collagen/gelatin. However, these

coatings are subject to degradation over time, leading to cell detachment, which may trigger platelet activation and thrombosis [31-34].
Building on our previous work, we leveraged the well-established anticoagulant properties of fucosylated chondroitin sulfate isolated from the echinoderm *Holothuria tubulosa* [21]. to improve the hemocompatibility and endothelialization of nanofibrous PCL scaffolds, while simultaneously reducing platelet adhesion and aggregation [22]. In this study, the previously established approach was applied to engineer an innovative graft that combines the superior mechanical properties of the fourlayer bioresorbable PCL scaffold with the biological properties of these intriguing polysaccharides [22]. Interestingly, as they are covalently immobilized on the scaffold surface via EDC/NHS chemistry, their biological effects arise from stable surface presentation rather than sustained release.

Mechanical properties

The four-layer PCL scaffold exhibits mechanical properties and architecture tailored to mimic native vessels. Its burst pressure and tensile strength match or exceed those of autologous grafts. The soft, aligned nanofiber inner layer provides low-strain compliance and a non-linear stress–strain response similar to arteries [35], while the circumferential nanofiber, printed microfiber, and outer random-fiber layers reinforce hoop strength and prevent delamination.
Importantly, the circumferential layer produced by 4-axis printing contributes not only to mechanical reinforcement but also to interlayer integration: during deposition, molten PCL microfilaments partially fuse with the underlying electrospun nanofibrous layer, promoting mechanical continuity without disrupting nanofiber morphology. Subsequently, the outer randomly oriented electrospun layer is deposited directly onto the assembled structure, enabling fiber integration with the printed layer and further unifying the scaffold. In addition, progressive cellular infiltration and ECM deposition within the graft are expected to enhance interlayer cohesion over time, potentially reducing the risk of long-term delamination following implantation. This layered strategy effectively decouples graft strength from compliance, avoiding the maladaptive stiffness of PET/ePTFE [36].
Burst pressure was assessed using two complementary approaches: a direct fluidic test, and an indirect estimation derived from tensile force at failure using a modified form of Laplace's law. The direct method involved real-time internal pressurization of the scaffolds within a closed-loop system, capturing the influence of geometric deformation, potential leakage, and material

imperfections. In contrast, the indirect method offered a theoretical estimation using an idealized model, assuming a perfectly cylindrical geometry with thin walls, to convert tensile force into theoretical burst pressure. Measured burst pressures ranged from 1100 to 1700 mmHg, with indirect calculations reaching over 10 000 mmHg. These values compare favorably with native vessel benchmarks—for example, saphenous veins (1600–2400 mmHg) and internal mammary arteries (3200–4225 mmHg) [11, 37, 38]. and are consistent with earlier-generation TEVGs, which typically targeted burst pressures of 1500–3500 mmHg [37, 39]. Importantly, all fully assembled scaffolds, regardless of surface functionalization, exhibited equivalent high-level burst performance, confirming that mechanical integrity is predominantly governed by scaffold architecture rather than surface chemistry [40].

Reported tensile strengths for native vessels vary widely due to methodological differences, with moduli ranging from ∼1.5 MPa to >40 MPa [41-44]. Such variability arises from differing approaches to modulus calculation. Some studies define elastic modulus as the steepest linear slope prior to failure, emphasizing structural strength, while others focus on the initial, low-strain region of the curve, reflecting physiological compliance. For instance, Yokoyama et al. used the linear portion of the stress–strain curve dominated by elastin (strain 0–0.6) to define an "elastin-associated" modulus, which closely matched native compliance in the physiological strain range [45]. Similarly, Soletti et al. explicitly defined elastic modulus as the slope of the stress–strain curve within physiological arterial pressure (∼80–120 mmHg), emphasizing the importance of evaluating compliance in the actual functional range [44]. In contrast, Bouchet et al. analyzed bilinear ePTFE behavior and selected the higher modulus (∼17.4 MPa), derived from the final linear region, to represent mechanical strength under near-failure conditions [46]. Such methodological differences highlight why reported elastic modulus values should be interpreted with caution [18]. In line with studies that emphasize structural strength, we calculated the elastic modulus as the slope of the linear segment of the stress–strain curve before yield. Our scaffold, while stiffer than some native vessels, retains ductile, non-linear behavior due to its layered design. For comparison, Han et al. fabricated a three-layer electrospun graft (inner PLCL/gelatin, middle PLGA, outer PCL) whose tensile strength (5.2 ± 0.7 MPa) and modulus (35.9 ± 7.7 MPa) greatly exceeded that of a porcine coronary artery (2.6 and 1.0 MPa, respectively) [47, 48]. Likewise, Wu et al. reported radial strength ∼5.1 MPa, matching the human aorta and exceeding coronary values [47]. Our multilayered structure delivers comparable

performance to what is reported in the literature while preserving inner-layer compliance, enabling graded stiffness and mechanical anisotropy as in native arteries [47, 49, 50]. To assess physiological performance, we separately derived compliance from the stress–strain curve in the approximate arterial pressure range (~80–120 mmHg). The inner electrospun layer exhibited high compliance, mimicking the elastic behavior of native elastin fibers, while the outer layers showed reduced compliance, reflecting the load-bearing role of collagen in native vessel walls. However, translating tensile data into physiologically relevant compliance entails limitations [51]. The stress–strain approach inherently assumes idealized vessel geometry and material properties: a long, cylindrical, thin-walled, homogeneous, and incompressible tube. In reality, native vessels exhibit taper, branches, residual stresses, and complex multi-layered architecture, all of which affect local mechanical responses [51, 52]. Thus, while our stress–strain-based compliance analysis offers a useful approximation, it should be interpreted in light of these geometric and biomechanical assumptions.

Relative to conventional synthetic grafts, the multilayer design offers distinct mechanical advantages. Standard materials like Dacron (PET) and ePTFE are very stiff [36, 53] and virtually noncompliant, which causes a compliance mismatch at anastomoses [54]. This mismatch is implicated in intimal hyperplasia and graft failure [54]. Our bioresorbable scaffold, in contrast, offers a native-like mechanical profile. The elastic inner layer allows axial and circumferential stretch, while outer layers resist radial deformation. This layered design mimics the functional anisotropy of native arteries and may reduce intimal hyperplasia and graft failure.

In the context of TEVG literature, these results are encouraging. Earlier work has shown that layering can decouple compliance and strength: for example, adding helical or circumferential reinforcement to a fibrous scaffold dramatically boosts burst pressure without compromising endothelial-friendly compliance as demonstrated by our scaffolds [47]. The polysaccharide surface coatings (Ht, Hep) modestly weakened individual fibers but did not prevent the full four-layer graft from achieving native-level bursts. In fact, even the weakest functionalized graft exceeded 1000 mmHg by a comfortable margin. Importantly, all graft variants after full assembly performed similarly in burst, indicating that any minor effects of polysaccharide functionalization are overcome by the structural architecture.

Finally, because the graft is bioresorbable, mechanical integrity will evolve as tissue forms. Ideally, polymer strength should degrade in concert with new

extracellular matrix deposition to avoid aneurysm [55]. Our high initial stiffness ensures safety at implantation, and the layered architecture may allow gradual load transfer: as the inner PCL nanofibers soften or degrade, SMC-deposited collagen in the media can take up stress.

A key advantage of our multilayer scaffold is its finely tunable mechanical profile, achieved through strategic adjustment of layer composition and architecture. The supplementary analysis demonstrates that scaffold elastic modulus, toughness, and tear resistance can be precisely modulated by adding or omitting specific structural layers. For instance, incorporating the most elastic inner nanofiber layer reduces elastic modulus while enhancing extensibility and toughness, offering compliance closer to that of native vessels. In contrast, adding or doubling the circumferentially aligned nanofiber layer substantially increases the elastic modulus, yield strength, and tear resistance. Such mechanical tunability is especially important for applications like coronary artery bypass grafting, where grafts must endure continuous cyclic strain, dynamic curvature, and localized compressive forces imposed by myocardial motion. The modularity of the scaffold also supports patient- and site-specific customization: its layered configuration can be adapted to match the mechanics of different vascular beds, from high-flow arteries to more compliant veins. This adaptability enhances the translational potential of the platform, allowing graft performance to be tailored to specific clinical contexts and anatomical demands.

Endothelialization and Hemocompatibility

Rapid endothelialization is essential for long-term graft patency and thromboresistance. Among the scaffold variants, those functionalized with *Holothuria tubulosa*-derived sulfated polysaccharides (PCL-Ht) demonstrated the most favorable endothelial response. Under static HUVEC culture conditions, PCL-Ht scaffolds promoted the formation of a functional endothelium, outperforming both PCL-Hep and PCL-EDC/NHS controls. Within a few days of culture, endothelial cells established confluent, uniformly aligned monolayers with evident cell-cell interactions, indicative of advanced structural organization and endothelial maturation.

Under physiological flow, only PCL-Ht scaffolds developed near-confluent cobblestone endothelium by day 7, with well-defined VE-cadherin junctions. These findings align with our previous study [22]. The enhanced endothelial response likely stems from two factors. First, the Ht polysaccharides increase scaffold hydrophilicity and present bioactive sulfate motifs that support cell

adhesion and anti-thrombosis properties, as seen in other studies of marine sulfated polysaccharides [22]. Second, the aligned nanofibrous topography itself exerts a strong contact-guidance effect: endothelial cells preferentially adhere to and elongate along aligned fibers, which accelerates monolayer formation [56]. In summary, the combination of the inner aligned layer and the Ht functionalization promoted an early, functional and anti-thrombogenic endothelial barrier, a critical first step to prevent thrombosis and maintain graft patency.

Smooth Muscle Cell Infiltration and Phenotype

While endothelial integrity is essential for luminal patency, medial integration by contractile smooth muscle cells (SMCs) is equally critical to long-term vascular function. The mid-layer, fabricated using 4-axis printing, supported extensive SMC infiltration across all scaffold variants, reflecting the design's high porosity. Early after seeding (days 1–10), CASMC attachment and proliferation were comparable on all scaffolds. However, by day 21 we observed stark differences driven by surface chemistry. Heparin-functionalized grafts (PCL-Hep) exhibited a pronounced drop in CASMC numbers ($p<0.001$), whereas PCL-Ht and non-coated scaffolds maintained high cell counts. Heparin is a known vascular SMC mitosis inhibitor—its antiproliferative effect has been documented for decades [57]—and our data suggest that the immobilized heparin on the graft surface impaired long-term CASMC survival or proliferation. Moreover, the physical phenotype was remarkably altered: on PCL-Hep, CASMCs formed dense, rounded spheroids with minimal α–smooth muscle actin organization. By contrast, CASMCs on PCL-Ht remained well-spread, elongated and aligned to the fibers, with abundant α-SMA stress fibers and multilayered structures resembling the native tunica media.

The heparin-associated phenotype is consistent with the literature: surface-bound heparan sulfates (and heparin) render the substrate anti-adhesive to SMCs, disrupting focal adhesions and preventing normal cytoskeletal tension [58]. Lundmark et al. demonstrated that smooth muscle cells on fibronectin coated with heparin lose focal contacts and stress fibers [58]—mirroring our observations on PCL-Hep. In contrast, PCL-Ht scaffolds appear to preserve the contractile phenotype of the CASMCs limiting excess proliferation. PCL-Ht grafts uniquely support both rapid endothelial sealing and stable CASMC colonization in a contractile state—two key requirements for long-term graft integration.

Future Perspectives and Clinical Implications

This multilayer, bioresorbable scaffold represents a compelling platform for next-generation small-caliber vascular grafts. Its modular architecture offers the flexibility to tailor mechanical and biological properties to specific clinical contexts. For example, increasing the inner-layer thickness while reducing circumferential reinforcement may yield more compliant grafts suitable for low-pressure venous systems, whereas augmenting the circumferential fiber content could enhance radial strength for high-pressure muscular arteries. Compared to traditional electrospun PCL grafts—which suffer from low compliance, slow degradation, poor cell infiltration, and mid-term calcification [59, 60]—our layered architecture mitigates these limitations by distributing mechanical loads and enhancing biofunctionality. Notably, long-term studies suggest that persistent PCL strands may trigger neointimal calcification, likely due to osteochondrogenic transformation of smooth muscle cells under chronic mechanical stress [61, 62]. In contrast, the effective cell infiltration observed in our study may mitigate this pathological response.

Future optimization could involve polymer blends with distinct degradation kinetics or mechanical properties, as well as layer-specific functionalization to independently modulate endothelial and smooth muscle behavior.

Furthermore, in vivo studies in relevant animal models are mandatory to evaluate native ECM deposition, scaffold resorption, and long-term integration under physiological conditions. Ultimately, the synergistic combination of rapid endothelialization, stable smooth muscle integration, and tunable mechanical behavior positions this scaffold as a promising candidate for clinical translation. With further development, particularly in terms of bioreactor-based preconditioning and scalable fabrication, this platform may enable the production of patient-specific, off-the-shelf vascular grafts that overcome the key limitations of current synthetic options.

Conclusion

We developed and validated a modular, multilayered bioresorbable vascular graft that integrates tailored mechanical performance with endothelial and smooth muscle cell compatibility. By strategically combining electrospun and four-axis printed layers, we achieved a scaffold with tunable stiffness, high burst resistance, and structural integrity suitable for arterial applications. Surface functionalization with marine-derived polysaccharides supported endothelialization and hemocompatibility without compromising mechanical

properties. The graft's design flexibility enables adaptation to site-specific vascular demands, making it a promising platform for next-generation tissue-engineered vascular replacements.

Materials and methods

The vascular scaffold was engineered as a multilayer tubular construct consisting of an inner electrospun layer with fibers aligned in the axial direction (First layer), a second electrospun layer (Second layer) with fibers aligned circumferentially, followed by a central circumferentially aligned microfiber layer produced by 4-axis printing (4-axis layer), and an external electrospun layer (EEL) of randomly oriented nanofibers. These layers were fabricated sequentially as described below in the 'Scaffold design' section.

Chemicals and Reagents

Polycaprolactone (PCL, 80 kDa MW; Sigma-Aldrich). Hexafluoro-2-propanol (HFIP; Biosolve B.V.). 1,6-hexamethylenediamine (HMDA; Sigma-Aldrich) 2-propanol (Sigma-Aldrich) *N*-(3-Dimethylaminopropyl)-*N*′-ethylcarbodiimide (EDC; Sigma-Aldrich) and *N*-Hydroxysuccinimide (NHS; Sigma-Aldrich); 2-(N-Morpholino)ethanesulfonic acid (MES; Sigma-Aldrich) buffer.

Toluidine Blue O (TBO) and Heparin sodium salt from porcine intestinal mucosa (Hep) were purchased from Sigma-Aldrich. The marine sulfate polysaccharides were isolated from *Holothuria tubulosa* in our laboratory according to the previous reports [21, 22]. For *in vitro* testing, HUVECs (PromoCell; Cat. No. C-12203) and CASMCs (Lonza Bioscience; Cat. No. CC-2583) were cultured using Endothelial Cell Growth Medium (EGM-2; Sigma-Aldrich, Cat. No. C-22011) and SmGM™-2 Smooth Muscle Cell Growth Medium-2 BulletKit™ (Lonza Bioscience; Cat. No. CC-3182), respectively. Xanthomonas campestris and Glycerol solution were purchased from Sigma-Aldrich and used for mimicking blood rheology.

Scaffold design: production and fabrication

For the first two electrospun layers (first layer and second layer), a polymer solution was prepared by dissolving 13% (w/v) polycaprolactone (PCL, 80 kDa MW) in hexafluoro-2-propanol (HFIP; Biosolve B.V., the Netherlands) under continuous stirring overnight. The solution was then electrospun using a blunt 20-gauge stainless steel hypodermic needle (internal diameter 0.8 mm, Unimed). To ensure a homogeneous deposition the needle was set to move

along the length of the collector with a speed of 30 mm/s. Electrospinning was performed under controlled conditions (temperature = 25°C, relative humidity = 35%) with the following parameters: an applied voltage of 18.5 kV, a needle-to-collector distance of 15 cm, and a flow rate of 1 mL/h. A stainless-steel mandrel (60 mm diameter) was used as the collector, which rotation was set at 5800 rpm (Peripheral speed ≈ 18 m/s.) to obtain aligned fibers. During this process, nanofibers were collected on an aluminum foil placed on the collector for 45 minutes. Following deposition, the resulting PCL meshes were carefully rolled onto a 4 mm diameter, 10 cm long aluminum mandrel such that the inner layer had fibers aligned along the mandrel's axis, to allow the correct HUVECs orientation, while the second layer exhibited circumferential fiber alignment, to allow CASMCs orientation.

On top of the first 2 electrospun layers, a central circumferentially aligned microfiber layer was fabricated using a 4-axis printing system [26, 63]. The preformed two-layer electrospun construct, mounted on the 4 mm mandrel, was incorporated into this system. PCL (80 kDa MW) was melted at 150°C for 30 minutes in a heated metal cartridge and subsequently extruded through a 260 μm diameter nozzle (25G encapsulation needle, DL Technology) under a pressure of 7 bar. The mandrel, secured to a DC motor (Unimat 12 V DC powered by a Voltcraft LPS1153 power supply, Conrad), rotated at 1060 rpm (Peripheral speed ≈ 0.222 m/s) while the printhead traversed the collector at a speed of 0.75 mm/s over 10 passes, depositing the middle microfiber layer. This layer exhibited increased porosity, facilitating CASMC infiltration and alignment, while simultaneously offering protection against delamination of the inner layers.

Finally, the composite construct (comprising the two electrospun layers and the printed middle layer) was transferred back to the electrospinning system to form the outermost layer. Using the same PCL-HFIP solution (13% w/v) as before, this final external electrospun layer (EEL) was obtained collecting the nanofibers for 15 minutes with the following settings: 18.5 kV applied voltage, 150 mm working distance, and 1 mL/h flow rate. The 4 mm mandrel speed was set at 1000 rpm (Peripheral speed ≈ 0.209 m/s) to produce randomly oriented fibers. This last step formed an external nanofibrous layer that reinforced the scaffold and further mimicked the native extracellular matrix of the vascular adventitia.

Scanning electron microscopy investigation

For the characterization of fiber morphology and size, samples were first sputter-coated with gold (Quorum Technologies SC7620). Scanning electron microscopy (SEM) images were then acquired using a JSM-IT200 microscope (Jeol Ltd.) at varying magnifications, with an accelerating voltage of 100 kV and a working distance of 11 mm. Subsequent image processing and analysis were performed to quantify fiber diameter and orientation using the Fiji image processing package (GNU General Public License), based on measurements from three samples with 35 observations each.
The nanofiber orientation was investigated with the "Directionality" plugin of ImageJ [64]. This approach allowed us to quantify the number of nanofibers within a given angle range from the axis, using a "Local Gradient Orientation" method, following a previously validated procedure [65]. The analysis was performed on 3 images per layer (magnification = 1000x) along the different principal orientations of fibers with respect of the scaffold's axis and the results reported as mean and standard deviation.

Marine sulfated polysaccharides purification and quantification

Marine sulfated polysaccharides were purified following the protocol described by Nieddu et al. [21] with minor modifications. In brief, body wall fragments from *Holothuria tubulosa* were sequentially treated with absolute ethanol and acetone to achieve dehydration and delipidation. The dehydrated tissues were rehydrated in 0.1 M sodium acetate buffer (pH 6.0) and subsequently digested with papain. After centrifugation, the supernatant was subjected to anion-exchange chromatography on a DEAE-Sephacel column, and the 1.5 M lithium chloride-eluted fractions, referred to as Ht (*H. tubulosa*), were quantified for hexuronic acid (UA) content using the Bitter and Muir method [66].

Scaffold Functionalization via Aminolysis and EDC/NHS Crosslinking of Sulfated Polysaccharides

As previously described by Obino et al. [22], PCL scaffolds were functionalized using a two-step protocol. In the first step, scaffolds underwent aminolysis by incubating with a 6% (w/v) solution of 1,6-hexamethylenediamine (HMDA) in 2-propanol at 37°C for 2 hours. This treatment was followed by successive washes with 2-propanol and distilled water to remove residual HMDA. In the subsequent step, the aminolyzed scaffolds were soaked in a solution containing 166 μg_{UA}/mL of Ht or

unfractionated heparin (Hep), prepared in 0.1 M EDC/NHS dissolved in 2-(N-morpholino)ethanesulfonic acid (MES) buffer at pH 5 and incubated for 24 hours at room temperature, then thoroughly washed with PBS to eliminate any unreacted reagents. Following functionalization, scaffolds were classified into four groups: PCL, referring to untreated polycaprolactone scaffolds; PCL-EDC/NHS, representing scaffolds subjected to aminolysis and EDC/NHS crosslinking in the absence of polysaccharides; PCL-Hep, scaffolds functionalized with heparin; and PCL-Ht, scaffolds functionalized with sulfated polysaccharides derived from *Holothuria tubulosa*.

Mechanical Characterization of Multilayered sTEVGs

Mechanical properties of multilayered tubular scaffolds were evaluated using an ElectroForce 3200 Series III mechanical tester (TA Instruments) equipped with a 45 N load cell. Circumferential tensile tests were conducted at a strain rate of 25%/s until sample failure following ISO 7198:2016 guidelines [67]. As clamping system, custom-made capstan grips, consisting of two 1.5 mm-diameter stainless steel circular pins were employed.
Scaffolds were cut into tubular segments of 5 mm length and tested after 24-hour PBS immersion at 37°C. The test was captured using a camera (DMC-G3, Panasonic) with a macrolens (Panagor 90 mm f2.8, Komine).

Scaffold configuration tested

Various scaffold configurations were evaluated to assess the contribution of each layer to the overall performance. The following individual and combined layers were tested: (i) the first electrospun layer alone (first Layer), (ii) the second electrospun layer alone (second Layer), (iii) the 4-axis printed layer (4-axis) combined with the electrospun external layer (EEL), and (iv) the full layered construct (MultiLayer). Additional configurations are presented in the supplementary information and include: the sTEVG without the 4-axis layer, and a sTEVG with a duplicated second electrospun layer. Furthermore, the fully assembled four-layer scaffold was also evaluated after surface functionalization. The tested functionalized conditions included: unmodified PCL (PCL), PCL activated with EDC/NHS chemistry (PCL–EDC/NHS), PCL functionalized with heparin (PCL–Hep), and PCL functionalized with sulfate polysaccharides from *Holothuria tubulosa* (PCL–Ht).

Dimensional Analysis

Wall thickness measurements were acquired using a Nikon SMZ25 automated stereomicroscope with ring LED illumination. For each scaffold, 20

equidistant thickness measurements were taken from high-resolution images (5× magnification) and analyzed via ImageJ (v1.53), with results expressed as mean ± standard deviation.

Mechanical Parameter Calculation

The mechanical properties of scaffolds were calculated adopting two different approaches. At first, the apparent stress (σ_a), accounting only the geometrical properties of scaffolds, was obtained as follows:

$$\sigma = \frac{F}{A}$$

Where F is the force (N) recorded and A the area (mm^2), defined as:

$$A = 2 \cdot l \cdot t$$

Where l is the width (mm^2) and t the wall thickness (mm^2) of the tested tubular scaffold.

The second consolidated method was the evaluation of the net stress (σ_n), which allows to evaluate the mechanical properties of the specimen avoiding the contribution of its internal porosity [68-71]. The net stress was calculated by dividing the apparent stress by the volume fraction (v) of the specimens. The v was calculated by using the equation:

$$v = \frac{w}{(L \cdot A \cdot \rho)}$$

Where w is the weight of the specimen (g), L is the gauge length of the specimen (mm), A is the area of the specimen as previously defined, ρ is the density of PCL (ρPCL = 1.145 g/cm^3). The weight of each specimen was calculated using a precision balance (MG214Ai-M, VWR International, Radnor, USA). The following indicators were considered: Yield Force (F_Y), Yield Stress (σ_Y), Yield Strain (ε_Y), Elastic Modulus (E), Failure Force (F_F), Failure Stress (σ_F), Failure Strain (ε_F), Toughness to Yield (W_Y), Toughness to Failure (W_F) (these last two values calculated by using the trapezoid method as the integral of the area under the stress-strain curves).

To calculate the elastic modulus, a procedure adapted from a well-established method was employed [68]. Briefly, the initial toe region, corresponding to the first 5% of the failure stress, was excluded from each stress–strain curve to ensure comparability across samples and to mark the onset of the linear elastic region. This step avoids including into the calculation of the elastic modulus,

the initial toe-region where the nanofibers are recovering from their wavy-shape before the application of the load. Next, a preliminary yield point was visually estimated, and an initial linear regression was performed on the region extending from the start of the linear region to 50% of the strain span between this point and the tentative yield point. To minimize operator bias, a second line parallel to this regression was offset by 2% strain. The official yield point was then defined as the intersection between this offset line and the stress–strain curve. The elastic modulus was calculated as the slope of a second linear regression between the start of the linear region and the official yield point.
As far as σ_Y and yield strain (ε_Y) are concerned, they were determined by evaluating the meeting point between the stress-strain curve and a straight line, having modulus equal to the calculated elastic modulus, horizontally shifted by 2% with respect to the linear section of the stress-strain curve. For all experiments, five specimens per condition were analyzed.
The volume fraction of each layer and of the whole scaffolds also allowed the calculation of the percentage porosity (P) of samples as follows:

$$P\ (\%) = (1 - \nu) \cdot 100$$

Compliance Estimation from Pressure–Strain Curves

Compliance was estimated from the low-pressure region of the pressure–strain curves, specifically within the physiological range typical of human arteries (80–120 mmHg). For each construct, the strain values at 80 mmHg and 120 mmHg were extracted directly from the plots. Compliance was then calculated as the change in strain ($\Delta\varepsilon$) divided by the corresponding change in pressure (ΔP), following the expression:

$$Compliance = \frac{\Delta\varepsilon}{\Delta P} = \left(\frac{\varepsilon 120 - \varepsilon 80}{120\ mmHg - 80\ mmHg}\right) x\ 100$$

This formulation is derived from the classical definition of vascular compliance:

$$Compliance = \frac{\Delta D / D0\varepsilon}{\Delta P}$$

where D_0 is the initial diameter and ΔD is the change in diameter due to pressurization. Under the assumption of small deformations and uniform radial expansion, circumferential strain (ε) can be approximated as $\Delta D/D_0$. Therefore, strain per unit pressure serves as a valid proxy for relative

compliance. The resulting compliance values are normalized and expressed in terms of percent strain per mmHg (%mmHg) over the 80–120 mmHg range.

Burst pressure analysis

Direct burst pressure measurements were conducted using a custom-built testing platform designed for direct evaluation of scaffold mechanical integrity. Tubular scaffolds (length: 30 mm) were firmly mounted between two Teflon connectors (internal diameter: 3 mm). To ensure a leak-free seal, the scaffold ends were secured with rubber bands. The assembled system was incorporated into a closed-loop fluidic circuit for a real-time pressure monitoring, which included a microfluidic flow controller (OB1 MK4 – ELVEFLOW) and a high-precision liquid mass flow sensor (ELVEFLOW; flow range: 40–1000 µL/min; maximum pressure: 15 bar).

The system delivered a controlled, stepwise increase in internal pressure through the fluidic circuit. The pressure was continuously recorded until scaffold failure (burst event), which was both visually confirmed and captured using a high-resolution camera (Panasonic DMC-G3, The Netherlands) equipped with a Panagor 80 mm f/2.8 macro lens (Komine, Japan).

To closely replicate the hemodynamic conditions and non-Newtonian rheology of blood, a blood-mimicking fluid was prepared with the following composition: 0.075% (w/v) xanthan gum (XG), 50% (v/v) distilled water, and 50% (v/v) glycerol (Sigma Aldrich, US). This formulation was selected based on literature demonstrating its ability to approximate both the viscosity (3.5–4.5 mPa·s) and shear-thinning behavior characteristic of human blood, particularly at varying shear rates and vessel diameters [72, 73]. The addition of xanthan gum was essential to reproduce the non-Newtonian properties of blood, wherein viscosity increases at lower shear rates due to red blood cell aggregation, a phenomenon critical for physiological relevance in small vessel testing. To increase the visual contrast during perfusion and pressure testing, a red food colorant was added to the solution.

Pressure data were acquired continuously using the ELVEFLOW Smart Interface (ESI) software and the burst pressure was defined as the maximum pressure recorded immediately prior to scaffold rupture. Each scaffold type was tested in quintuplicate (n=5), and results were reported as mean ± standard deviation.

In parallel, an indirect estimation of burst pressure was performed by applying a modified form of Laplace's law, which relates the tensile rupture force to internal pressure in a thin-walled cylindrical geometry, using the following definition, as already reported [74]:

$$BP = \frac{F(N)}{L_0 Df}$$

where F is the failure force measured in tensile testing, L_0 is the initial unloaded internal diameter of the scaffold, and Df is the internal diameter at the point of failure. This indirect method allows for comparison between pressurization-induced rupture and tensile-derived mechanical performance, providing complementary validation of scaffold strength.

Spectroscopic, Colorimetric, and Elemental Characterization of Scaffold Functionalization

The chemical composition and surface functionalization of the electrospun scaffolds were characterized using Attenuated Total Reflectance Fourier Transform Infrared Spectroscopy (ATR-FTIR) spectroscopy, Toluidine Blue O (TBO) assay, and energy-dispersive X-ray spectroscopy (EDX).

ATR-FTIR Analysis

ATR-FTIR analysis was performed using a Nicolet™ iS50 spectrometer (Thermo Fisher Scientific, the Netherlands) equipped with an attenuated total reflectance (ATR) module. Spectra were collected in the 400–4000 cm^{-1} range at a resolution of 0.5 cm^{-1}, averaging 32 scans per sample. Prior to measurement, scaffolds were cut into sections and pressed against the ATR crystal to ensure optimal contact. Background spectra were recorded under identical conditions and subtracted to minimize atmospheric interference. FTIR analysis served to verify the presence of functional groups related to the crosslinking chemistry. These data were consistent with a previously published analysis, which confirmed successful crosslinking of sulfated polysaccharides to PCL-based scaffolds [22].

Toluidine Blue O (TBO) Assay

Quantification of sulfated polysaccharide incorporation was carried out using a modified Toluidine Blue O (TBO) assay. Scaffolds (PCL-Ht, PCL-Hep, and PCL-EDC/NHS as control) were incubated in a TBO working solution (0.04% w/v in 0.01 M HCl, 0.2 M NaCl) under agitation for 1 hour. After incubation, samples were washed five times for 10 minutes with 0.2 M NaCl to remove unbound dye and subsequently transferred to an elution solution (50% ethanol in 0.01 M HCl) for complete dye extraction overnight. The eluted dye was quantified by measuring absorbance at 630 nm using a CLARIOstar Plus plate reader. For standard curve preparation, 1 mL of the TBO working solution was

combined with 100 µL of a Hep solution of known concentrations (0 µg/ml; 0.5 µg/ml; 1 µg/ml; 2.5 µg/ml; 5 µg/ml). This mixture was incubated at 37°C with gentle shaking for 1 hour, during which the Hep–TBO complex spontaneously formed and precipitated. The mixture was then centrifuged at 300 rcf for 10 minutes, after which the supernatant was discarded. The precipitate was carefully rinsed five times with the washing solution to ensure complete removal of any unbound TBO. Finally, 1 mL of the elution solution was added to dissolve the precipitate, releasing the bound TBO, and the absorbance of the resulting solution was measured at 630 nm. Before the elution step, scaffolds were imaged using a SMZ25 stereomicroscope (Nikon Instruments, Japan) with an episcopic LED illumination ring to provide uniform reflected light.

Energy-dispersive X-ray spectroscopy (EDX)

Elemental analysis was performed using EDX to detect the presence of sulfur as an indicator of sulfated polysaccharide incorporation. Scaffold samples were mounted on stubs, sputter-coated with a conductive layer of carbon (EM ACE600 High Vacuum Sputter Coater - Leica Microsystems), and analyzed using the JSM-IT200 microscope. PCL-Ht and PCL-Hep scaffolds were compared to unmodified PCL to confirm the presence of sulfur atoms associated with sulfate groups introduced during functionalization.

HUVECs Static Seeding and Culture

HUVECs were obtained from PromoCell GmbH (Cat. No. C-12203) and cultured in Endothelial Cell Growth Medium (EGM-2, Sigma-Aldrich, Cat. No. C-22011) following the manufacturer's guidelines. Tubular sTEVGs were fabricated with a 4 mm internal diameter and sectioned into 5 mm segments. To ensure sterilization, scaffolds were immersed in 70% ethanol three times for 15 minutes each, air-dried overnight, and subsequently rinsed with phosphate-buffered saline (PBS). HUVECs were then seeded onto the luminal surface of the scaffolds at a density of 2×10^6 cells/mL. The cell-seeded constructs were maintained under static conditions in a humidified incubator at 37°C and 5% CO_2, with the culture medium refreshed every 48 hours. At defined time points (days 1, 4, 7, 14, and 21 post-seeding), assessments of cell metabolic activity, proliferation, and morphology were performed to evaluate scaffold biocompatibility and cellular response.

HUVECs Dynamic Culture

For dynamic culture, sTEVGs were fabricated with a 4 mm internal diameter and sectioned into 30 mm segments, sterilized and positioned within a custom-built bioreactor chamber. HUVECs were seeded into the luminal surface at the cell density of 2×10^6 cells/mL. To promote uniform cell distribution, the chambers were rotated of 90° every 20 minutes during the first 2 hours and every hour for additional 4 hours. Then, cells were allowed to adhere for 24 hours under static conditions. Following this initial seeding phase, the bioreactor chamber was connected to a peristaltic pump, which applied a continuous flow of culture medium at a rate of 1 mL/min (Shear stress ≈ 0.027 dyn/cm²) for 7 days.

CASMCs Static Seeding and Culture

Human coronary artery smooth muscle cells (CASMCs) were obtained from Lonza Bioscience (Cat. No. CC-2583) and cultured in SmGM™-2 Smooth Muscle Cell Growth Medium-2 BulletKit™ (Lonza Bioscience, Cat. No. CC-3182). sTEVGs scaffolds, featuring a 4 mm internal diameter, were fabricated, sectioned into tubular segments of 5 mm length and placed in Eppendorf tubes of 0.5 mL. Then, they were sterilized with 70% ethanol washing, rinsed with PBS and placed in 48 multi well plates. To prevent unwanted colonization of the lumen, the scaffolds were filled with a 1.5% agarose gel. CASMCs were then seeded on the scaffolds at a density of $6x10^5$ cells/mL by adding 1 mL of cell suspension to each scaffold. To promote uniform cell distribution, the tubes were rotated 90° every 20 minutes during the first 2 hours and every hour for additional 4 hours. Following seeding, the scaffolds were transferred to non-treated 48-well plates for overnight incubation; the next day, constructs were relocated to fresh plates to remove any cells that had adhered to the well surfaces. Finally, the CASMC-seeded scaffolds were maintained under static conditions in a humidified incubator at 37°C and 5% CO_2 for 21 days, with medium changes occurring every 48 hours.

Statistical analysis

Statistical analysis was performed using GraphPad Prism version 10.0. Results are reported as mean ± standard deviation of at least three independent experiments. Differences among multiple groups at various time points were assessed using a 2-way ANOVA analysis followed by Tukey's multiple comparisons test (DNA analysis). An ordinary one-way ANOVA followed by Tukey's multiple comparisons test was conducted on mechanical

characterization, burst pressure and compliance data. For the stress–strain curves, the median curve was used for graphical representation.
A p-value of less than 0.05 was considered statistically significant (*p-value < 0.05; **p-value < 0.01; ***p-value < 0.001; ****p-value < 0.0001).

Acknowledgements

This work was supported by the European Union — NextGenerationEU (DM 737/2021, RISORSE 2021–2022, 2022-2023) [CUP J55F21004240001]. T.T.B. and L.M. also acknowledge the project 3D-MENTOR (with project number 18647) of the VICI research programme, which is financed by the Dutch Research Council (NWO). A.S. also acknowledges The European Commission and the Horizon Europe Marie Postdoctoral Fellowship project 3NTHESES (n. 101061826) for funding.

Supporting Information

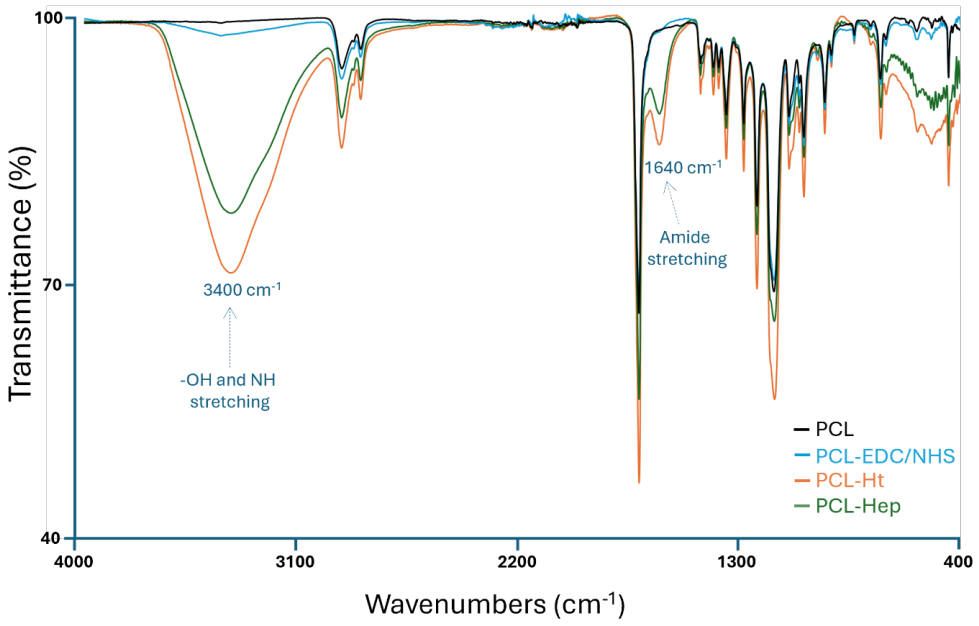

Figure S5.1. ATR-FTIR spectra of naked PCL, aminolyzed PCL treated with EDC/NHS (PCL-EDC/NHS), PCL functionalized with Hep (PCL-Hep), or with polysaccharides from Ht (PCL-Ht).

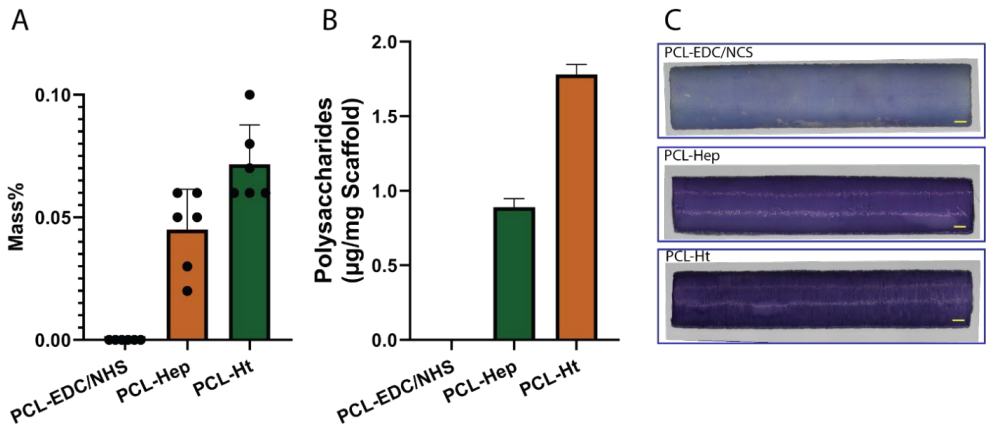

Figure S5.2. Characterization of scaffold functionalization through EDX (A), TBO assay quantification (B) and TBO qualitative staining (C). Scale bar: 1mm.

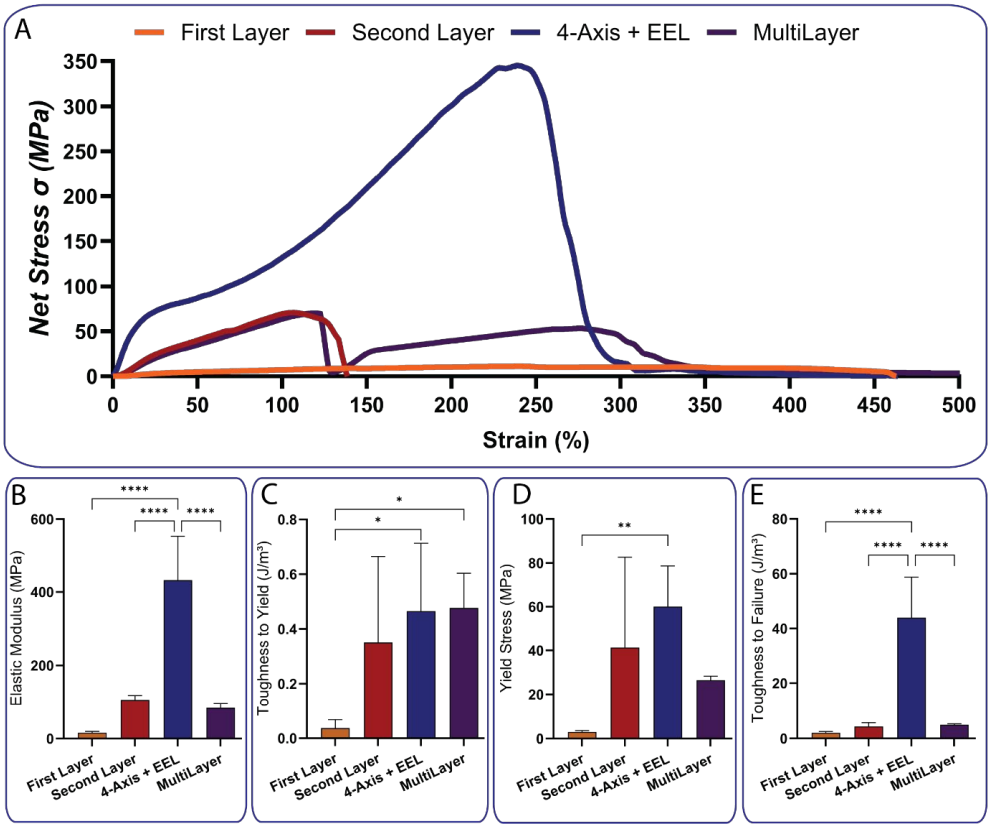

Figure S5.3. Mechanical characterization of multilayered TEVGs. (A) Representative net stress-strain curves for scaffolds with increasing numbers of layers. (B) Net elastic modulus, (C) net toughness to yield, (D) net yield stress and (E) net toughness to failure for each scaffold configuration. Data: mean ± SD (n=5). Statistics: ordinary one-way ANOVA followed by Tukey's multiple comparisons test. **p*-value < 0.05; ***p*-value < 0.01; *****p*-value < 0.0001.

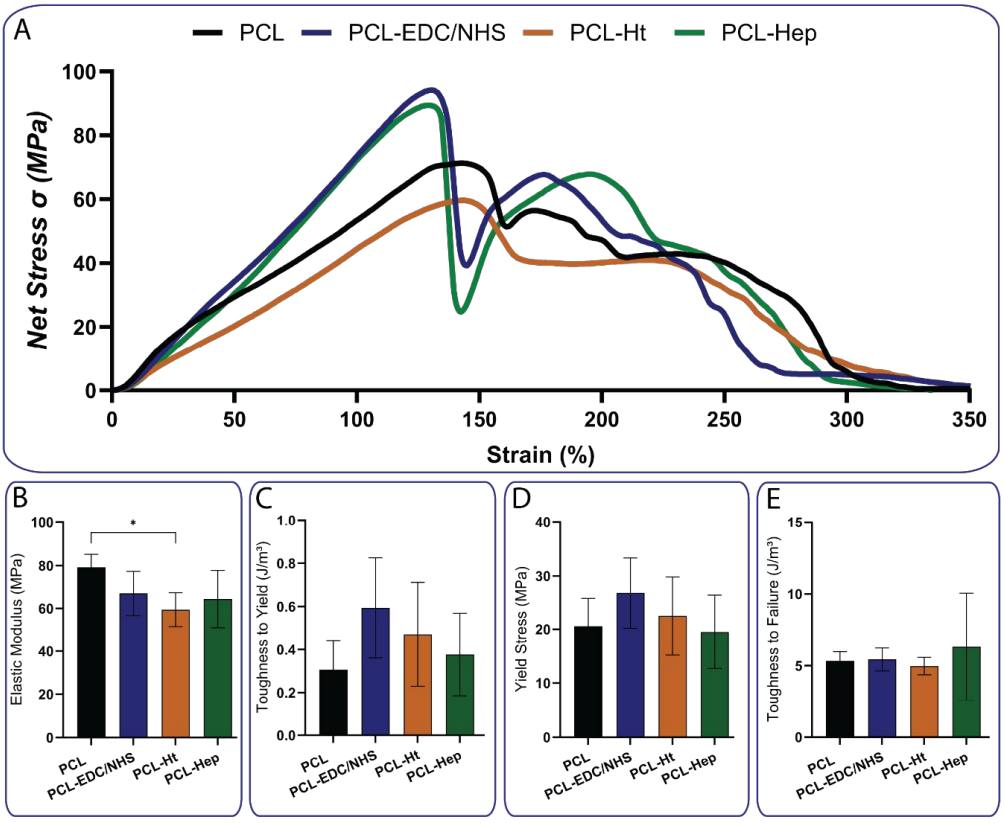

Figure S5.4. Mechanical properties of functionalized TEVGs. (A) Representative net stress–strain curves for PCL, PCL–EDC/NHS, PCL–Ht, and PCL–Hep scaffolds. (B) Net elastic modulus. (C) net toughness to yield (D) net yield stress, and (E) net toughness to failure for each scaffold functionalization. Data: mean ± SD (n=5). Statistics: ordinary one-way ANOVA followed by Tukey's multiple comparisons test. **p*-value < 0.05.

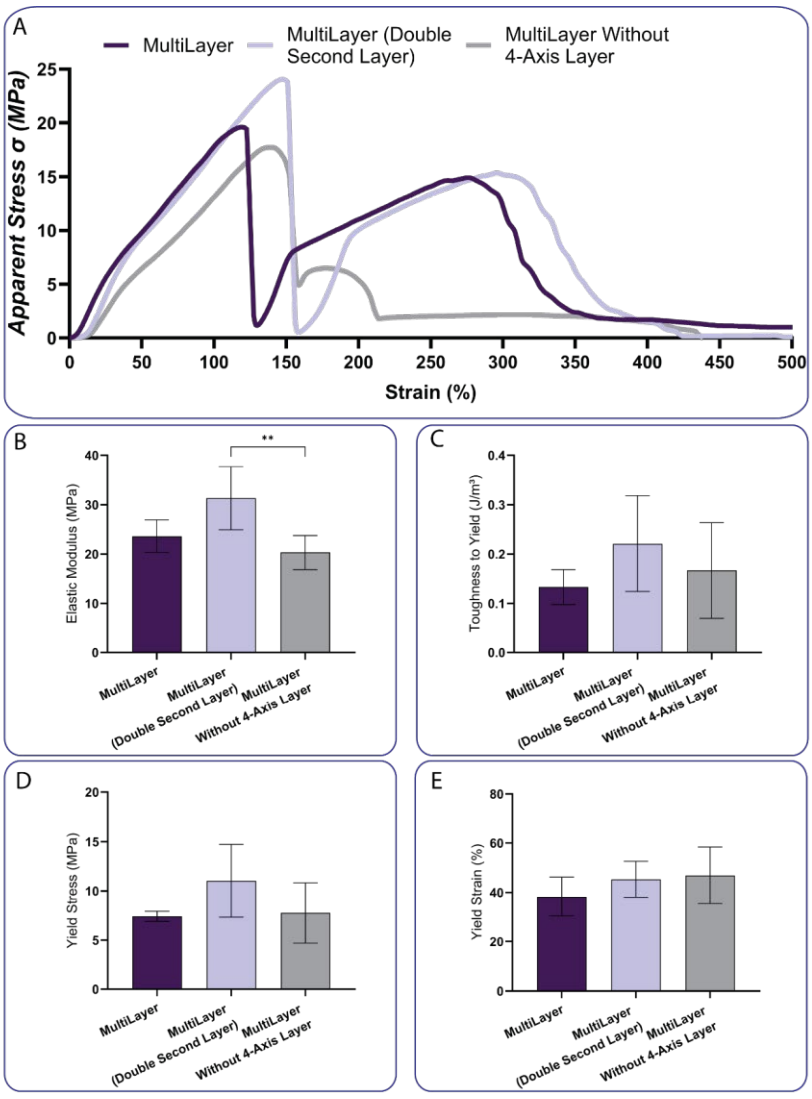

Figure S5.5. Mechanical tuning of the multilayer TEVG through scaffold design. (A) Representative stress–strain curves for scaffolds with different layer configurations, showing the effect of adding or omitting specific layers, (B) elastic modulus across configurations, (C) apparent toughness to yield, (D) apparent yield stress (E) and yield strain of each configuration. Data: mean ± SD (n=5). Statistics: ordinary one-way ANOVA followed by Tukey's multiple comparisons test. ***p*-value < 0.01.

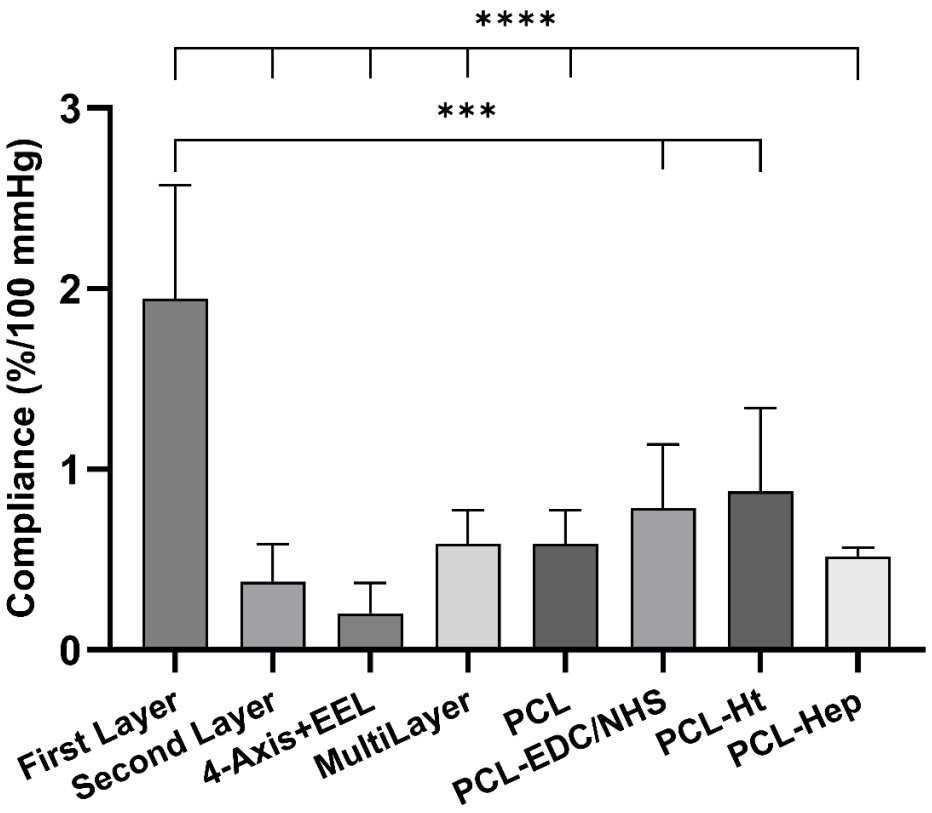

Figure S5.6. Compliance of the different layers and multilayer conformations. Data: mean ± SD (n=5). Statistics: ordinary one-way ANOVA followed by Tukey's multiple comparisons test. ****p*-value < 0.001; *****p*-value < 0.0001

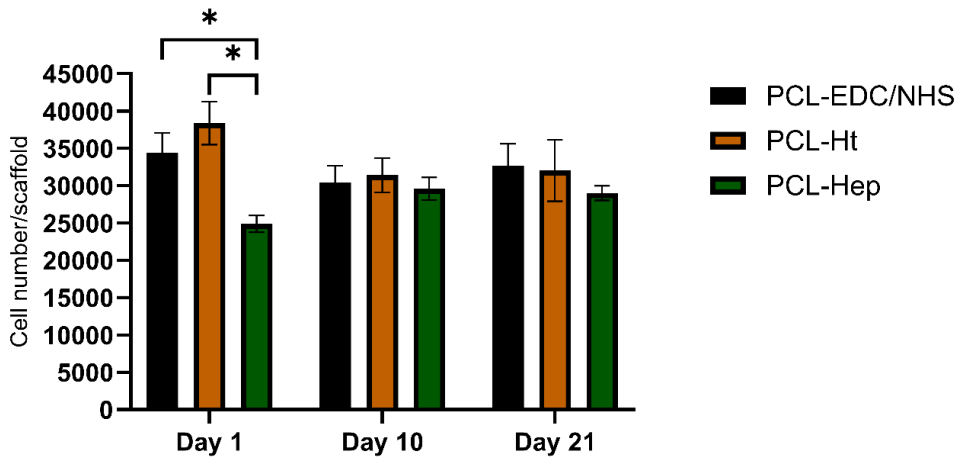

Figure S5.7. DNA quantification of HUVECs, expressed in cell number per scaffold, on PCL-EDC/NHS, PCL-Ht, and PCL-Hep scaffolds at days 1, 10, and 21. Data: mean ± SD (n=3). Statistics: 2-way ANOVA analysis followed by Tukey's multiple comparisons test. *p-value < 0.05.

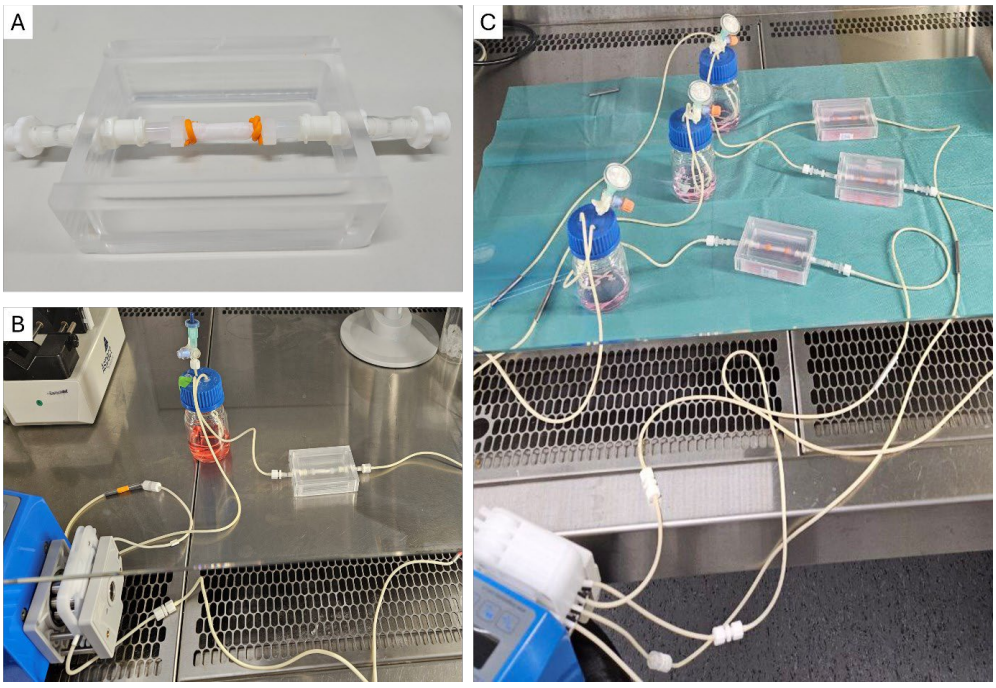

Figure S5.8. Custom-built bioreactor system for HUVEC dynamic culture. **A***)* Chamber design for tubular scaffold mounting. B-C) Complete perfusion setup integrating culture medium reservoirs, peristaltic pump, and bioreactor chambers for parallel dynamic culture experiments.

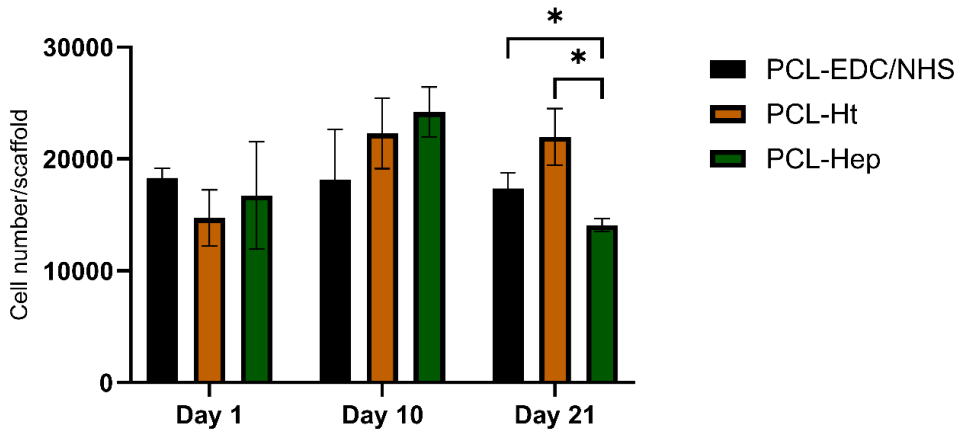

Figure S5.9. DNA quantification of CASMCs, expressed in cell number per scaffold, on PCL-EDC/NHS, PCL-Ht, and PCL-Hep scaffolds at days 1, 10, and 21. Data: mean ± SD (n=3). Statistics: 2-way ANOVA analysis followed by Tukey's multiple comparisons test. *p-value < 0.05.

	Failure Force (N)	*Failure Strain (%)*	*Failure Stress (N/mm^3)*	*Yield stress (MPa)*	*Yield strain (%)*	*Elastic Modulus (MPa)*	*Thoughness to Yield (J/m^3)*	*Thoughness to Failure (J/m^3)*
First Layer	3.9 ± 0.2	270.3 ± 32.4	3.9 ± 0.2	1.1 ± 0.2	26.3 ± 12.1	5.6 ± 1.2	0.013 ± 0.011	0.037 ± 0.031
Second Layer	23.5 ± 7.1	116.5 ± 8.1	24.4 ± 7.4	15.2 ± 15.7	29.4 ± 9.9	38.6 ± 4.6	0.127 ± 0.113	0.351 ± 0.313
4-Axis+EEL	34.9 ± 10.1	236.6 ± 22.8	33.9 ± 9.8	5.7 ± 1.8	17.6 ± 3.4	38.4 ± 12.6	0.044 ± 0.023	0.465 ± 0.247
MultiLayer	63.6 ± 3.3	127.1 ± 8.2	20.3 ± 1.0	7.4 ± 0.5	38.3 ± 7.9	23.6 ± 3.4	0.133 ± 0.036	0.476 ± 0.127
PCL	64.2 ± 6.8	137.1 ± 8.9	20.5 ± 2.2	5.8 ± 1.4	31.5 ± 4.7	22.2 ± 1.7	0.086 ± 0.038	0.306 ± 0.137
PCL-EDC/NHS	70.3 ± 13.0	134.9 ± 4.5	22.6 ± 3.9	7.5 ± 1.8	46.7 ± 10.0	18.7 ± 2.9	0.166 ± 0.065	0.593 ± 0.232
PCL-Ht	64.0 ± 9.6	136.7 ± 4.8	20.4 ± 3.1	6.3 ± 2.0	44.2 ± 9.6	16.6 ± 2.2	0.132 ± 0.067	0.471 ± 0.241
PCL-Hep	66.6 ± 18.8	129.0 ± 2.2	21.3 ± 6.0	5.5 ± 1.9	38.5 ± 6.8	18.0 ± 3.7	0.105 ± 0.054	0.376 ± 0.191
Multilayer Double 2 Layer	104.3 ± 27.1	134.0 ± 20.7	28.6 ± 7.4	11.0 ± 3.7	45.4 ± 7.3	31.4 ± 6.4	0.221 ± 0.097	0.660 ± 0.290
Multilayer Without 4-Axis	44.5 ± 14.3	134.9 ± 3.9	22.2 ± 7.2	7.8 ± 3.1	46.9 ± 11.5	20.3 ± 3.5	0.167 ± 0.097	0.429 ± 0.249

Table S5.1. Apparent mechanical properties of the scaffolds evaluated under uniaxial tensile testing. Parameters reported include failure force (F_F), failure strain (ε_F), failure stress (σF), yield stress (σ_Y), yield strain (ε_Y), elastic modulus (E), toughness to yield (W_Y), and toughness to failure (W_F). Data are expressed as mean (M) ± standard deviation (SD).

	Failure Stress (N/mm^3)	*Yield stress (MPa)*	*Elastic Modulus (MPa)*	*Thoughness to Yield (J/m^3)*	*Thoughness to Failure (J/m^3)*	*Volume Fraction*	*Porosity (%)*
First Layer	11.3 ± 0.7	3 ± 0.6	16 ± 3.6	0.718 ± 0.166	2.057 ± 0.477	0.35	65.1
Second Layer	67.6 ± 20.5	41.2 ± 41.3	89.1 ± 36.8	1.585 ± 0.488	4.402 ± 1.355	0.36	64
4-Axis+EEL	359 ± 103	60.1 ± 18.6	433.4 ± 119.7	4.146 ± 1.401	43.939 ± 14.847	0.094	90.57
MultiLayer	72.6 ± 3.7	26.5 ± 1.8	84.5 ± 12.0	1.405 ± 0.096	5.021 ± 0.342	0.28	72.02
PCL	73.2 ± 7.8	20.6 ± 5.1	79.3 ± 6.1	1.492 ± 0.181	5.331 ± 0.646	0.28	72.02
PCL-EDC/NHS	80.8 ± 14.0	26.8 ± 6.6	67.0 ± 10.4	1.521 ± 0.222	5.436 ± 0.793	0.28	72.02
PCL-Ht	73.1 ± 10.9	22.5 ± 7.3	59.4 ± 8.0	1.393 ± 0.171	4.978 ± 0.610	0.28	72.02
PCL-Hep	76.1 ± 21.5	19.5 ± 6.8	64.4 ± 13.2	1.768 ± 1.045	6.318 ± 3.736	0.28	72.02
Multilayer Double 2 Layer	85.3 ± 22.1	32.9 ± 11.1	93.5 ± 19.0	1.944 ± 0.486	5.800 ± 1.449	0.34	66.5
Multilayer Without 4-Axis	57.1 ± 18.4	19.9 ± 7.9	51.6 ± 8.8	1.496 ± 0.453	3.843 ± 1.163	0.39	61.1

Table S5.2. Net mechanical properties of the scaffolds normalized for the material volume fraction (ν). Reported values include net failure stress, net yield stress, net elastic modulus, net toughness to yield, and net toughness to failure. Data are presented as mean (M) ± standard deviation (SD). Volume fraction and porosity were also reported as single value per each scaffold conformation.

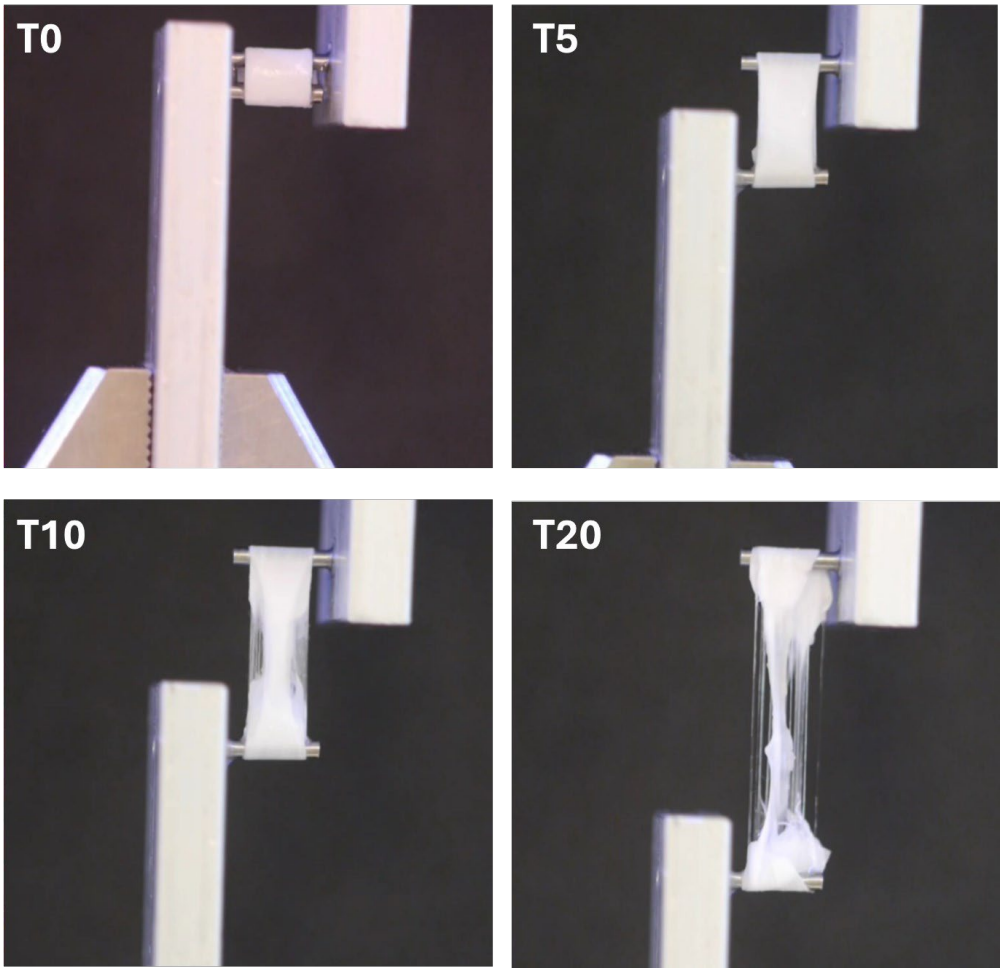

V5.1. Representative frames from a tensile test video of the tubular scaffold. The images show the sample at different time points (T0, T5, T10, and T20) during uniaxial tensile testing, illustrating progressive elongation and deformation until failure.

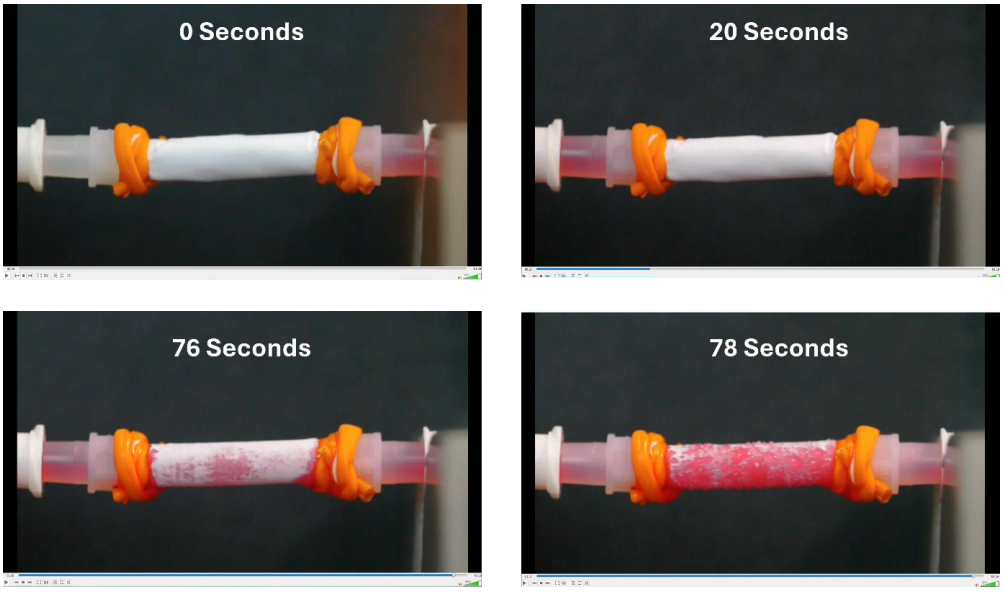

V5.2. Representative frames from the burst pressure test of the vascular scaffold. Sequential images (0–78 seconds) show the gradual pressurization of the scaffold until burst.

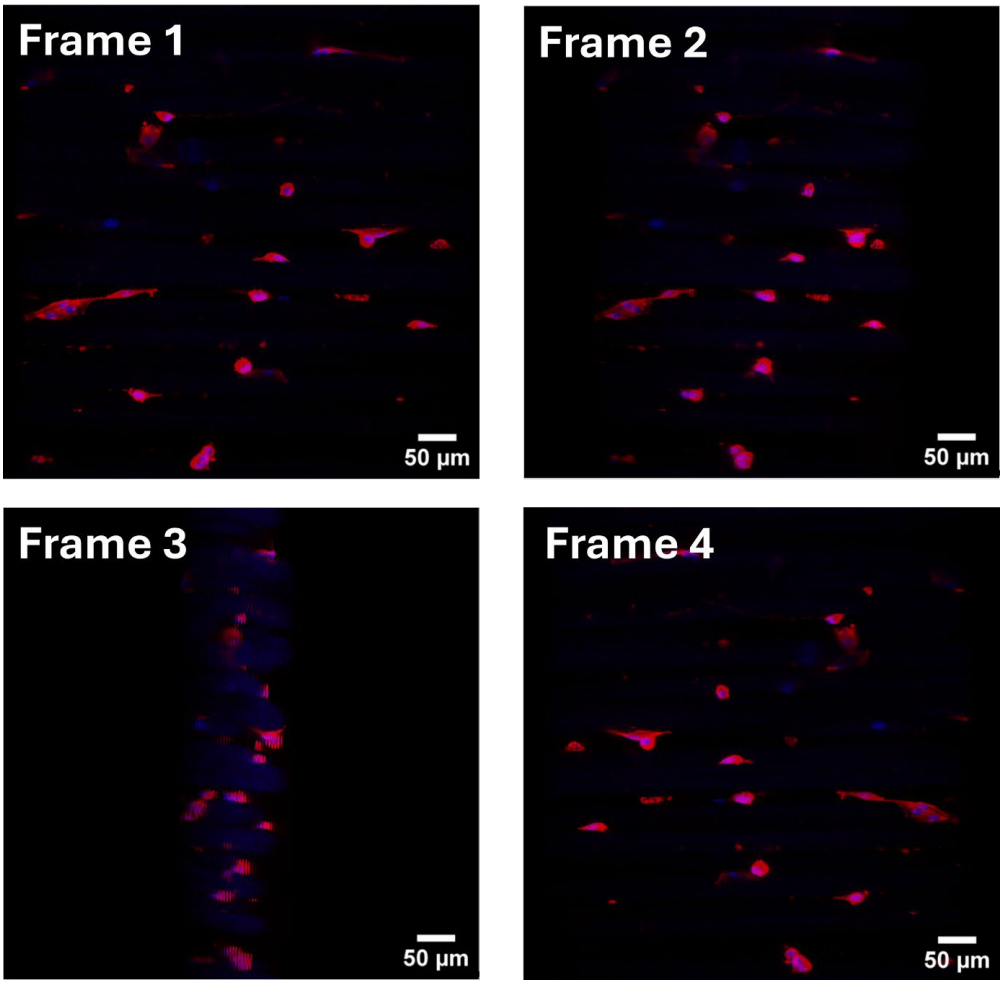

V5.3. Representative frames extracted from a z-stack video of immunofluorescent staining of CASMCs cultured under static conditions on the external surface of not functionalized PCL tubular scaffolds. CASMCs were seeded on the microfiber outer layer of the scaffolds. Red fluorescence indicates α-smooth muscle actin (α-SMA), while blue fluorescence (DAPI) marks cell nuclei. Images were acquired at 25× magnification. Scale bar: 50 µm.

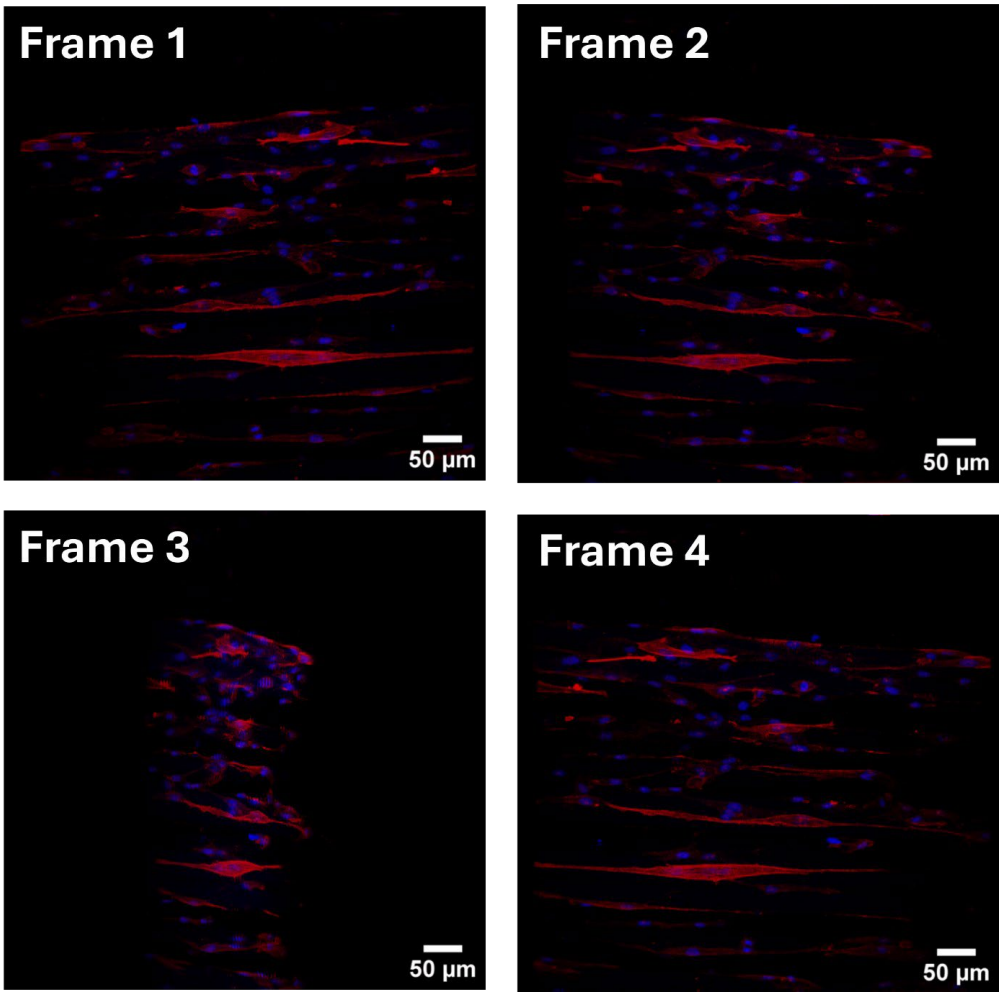

V5.4. Representative frames extracted from a z-stack video of immunofluorescent staining of CASMCs cultured under static conditions on the external surface of PCL-Ht tubular scaffolds. CASMCs were seeded on the microfiber outer layer of the scaffolds. Red fluorescence indicates α-smooth muscle actin (α-SMA), while blue fluorescence (DAPI) marks cell nuclei. Images were acquired at 25× magnification. Scale bar: 50 µm.

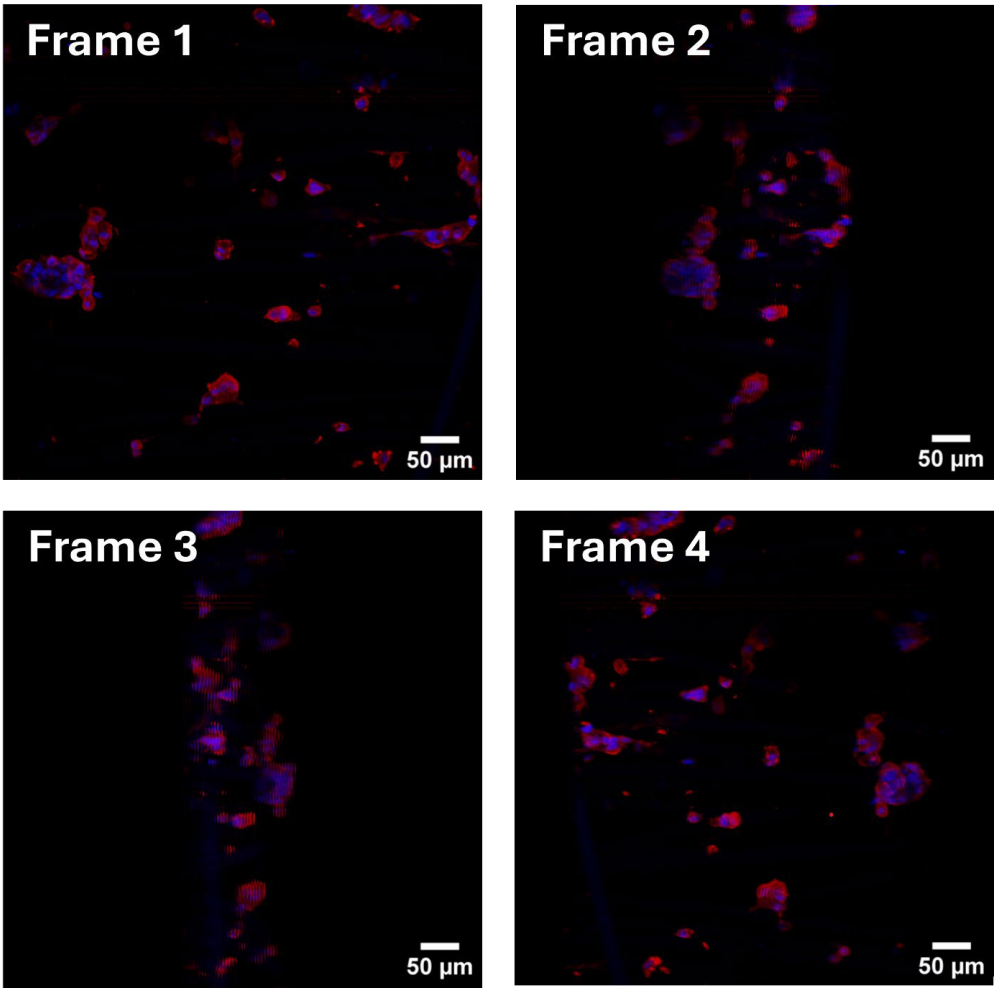

V5.5. Representative frames extracted from a z-stack video of immunofluorescent staining of CASMCs cultured under static conditions on the external surface of PCL-Hep tubular scaffolds. CASMCs were seeded on the microfiber outer layer of the scaffolds. Red fluorescence indicates α-smooth muscle actin (α-SMA), while blue fluorescence (DAPI) marks cell nuclei. Images were acquired at 25× magnification. Scale bar: 50 µm.

References

[1] G. A. Roth, G. A. Mensah, C. O. Johnson, et al., "Global Burden of Cardiovascular Diseases and Risk Factors 1990–2019," *Journal of the American College of Cardiology* 76 (2020): 2982–3021, https://doi.org/10.1016/j.jacc.2020.11.010.

[2] R. Bauersachs, U. Zeymer, J. B. Brière, C. Marre, K. Bowrin, and M. Huelsebeck, "Burden of Coronary Artery Disease and Peripheral Artery Disease: A Literature Review," Cardiovascular Therapeutics (2019): 8295054, https://doi.org/10.1155/2019/8295054.

[3] M. Drozd, M. Pujades-Rodriguez, F. Sun, et al., "Causes of Death in People With Cardiovascular Disease: A UK Biobank Cohort Study," Journal of the American Heart Association 10 (2021): 023188, https://doi.org/10.1161/JAHA.121.023188.

[4] L. J. Dominguez, A. Galioto, A. Ferlisi, et al., "Barbagallo Ageing, Lifestyle Modifications, and Cardiovascular Disease in Developing Countries," The Journal of Nutrition 10, no. 2 (2006): 143–149.

[5] J. C. Kohn, M. C. Lampi, C. A. Reinhart-King, and F. Genet, "Age-Related Vascular Stiffening: Causes and Consequences," Frontiers in Genetics 30 (2015): 112, https://doi.org/10.3389/fgene.2015.00112.

[6] R. Scott, E. H. Blackstone, P. M. McCarthy, et al., "Isolated Bypass Grafting of the Left Internal Thoracic Artery to the Left Anterior Descending Coronary Artery," The Journal of Thoracic and Cardiovascular Surgery 120 (2000): 173–184, https://doi.org/10.1067/mtc.2000.107280.

[7] N. L'Heureux, N. Dusserre, A. Marini, S. Garrido, L. de la Fuente, and T. McAllister, "Technology Insight: The Evolution of Tissue-Engineered Vascular Grafts–From Research to Clinical Practice," Nature Clinical Practice Cardiovascular Medicine 4 (2007): 389–395, https://doi.org/10.1038/ncpcardio0930.

[8] E. Benrashid, C. C. McCoy, L. M. Youngwirth, et al., "Tissue Engineered Vascular Grafts: Origins, Development, and Current Strategies for Clinical Application," Methods (San Diego, Calif) 99 (2016): 13–19, https://doi.org/10.1016/j.ymeth.2015.07.014.

[9] S. Lampridis and S. J. George, "Nonautologous Grafts in Coronary Artery Bypass Surgery: A Systematic Review," Annals of Thoracic Surgery 112 (2021): 2094–2103, https://doi.org/10.1016/j.athoracsur.2020.11.028.

[10] J. Ji, H. Xu, C. Li, and J. Luo, "Small-Caliber Tissue-Engineered Vascular Grafts Based on Human-Induced Pluripotent Stem Cells: Progress and Challenges," Tissue Engineering Part B: Reviews 29 (2023): 441–455, https://doi.org/10.1089/ten.teb.2023.0005.

[11] S. Pashneh-Tala, S. MacNeil, and F. Claeyssens, "The Tissue-Engineered Vascular Graft—Past, Present, and Future," Tissue Engineering Part B: Reviews 22 (2016): 68–100, https://doi.org/10.1089/ten.teb.2015.0100.

[12] B. B. J. Leal, N. Wakabayashi, K. Oyama, H. Kamiya, D. I. Braghirolli, and P. Pranke, "Vascular Tissue Engineering: Polymers and Methodologies for Small Caliber Vascular Grafts," Frontiers in Cardiovascular Medicine 11 (2021): 592361, https://doi.org/10.3389/fcvm.2020.592361.

[13] J. J. Devan Ohst, "Development of Novel, Bioresorbable, Small-Diameter Electrospun Vascular Grafts," Journal of Tissue Science & Engineering 2015, 06, https://doi.org/10.4172/2157-7552.1000151.

[14] M. X. Li, Q. Q. Wei, H. L. Mo, et al., "Challenges and Advances in Materials and Fabrication Technologies of Small-Diameter Vascular Grafts," Biomaterials Research 27 (2023): 58, https://doi.org/10.1186/s40824-023-00399-2.

[15] A. Post, P. Diaz-Rodriguez, B. Balouch, et al., "Elucidating the Role of Graft Compliance Mismatch on Intimal Hyperplasia Using an Ex Vivo Organ Culture Model," Acta Biomaterialia 89 (2019): 84–94, https://doi.org/10.1016/j.actbio.2019.03.025.

[16] E. J. Benjamin, M. J. Blaha, S. E. Chiuve, et al., "Heart Disease and Stroke Statistics-2017 Update: A Report From the American Heart Association," Circulation 135 (2017): 146—e603, https://doi.org/10.1161/CIR.0000000000000485.

[17] G. G. Flores-Rojas, B. Gómez-Lazaro, F. López-Saucedo, R. Vera-Graziano, and E. Bucio, "Electrospun Scaffolds for Tissue Engineering: A Review," Macromol 3 (2023): 524–553, https://doi.org/10.3390/macromol3030031.

[18] A. Hasan, A. Memic, N. Annabi, et al., "Electrospun Scaffolds for Tissue Engineering of Vascular Grafts," Acta Biomaterialia 10 (2014): 11–25, https://doi.org/10.1016/j.actbio.2013.08.022.

[19] S. A. Pineda-Castillo, H. Acar, M. S. Detamore, G. A. Holzapfel, and C. H. Lee, "Modulation of Smooth Muscle Cell Phenotype for Translation of Tissue-Engineered Vascular Grafts," Tissue Engineering Part B: Reviews 29 (2023): 574–588, https://doi.org/10.1089/ten.teb.2023.0006.

[20] R. Busch, A. Strohbach, S. Rethfeldt, et al., "New Stent Surface Materials: The Impact of Polymer-Dependent Interactions of Human Endothelial Cells, Smooth Muscle Cells, and Platelets," Acta Biomaterialia 10 (2014): 688–700, https://doi.org/10.1016/j.actbio.2013.10.015.

[21] G. Nieddu, G. Obino, C. Ciampelli, A. Brunetti, T. Cubeddu, R. Manconi, G.A. Stocchino, G.A. Deiana, M. Formato, A.J. Lepedda, Purification of an Acidic Polysaccharide with Anticoagulant Activity from the Marine Sponge Sarcotragus spinosulus, Mar Drugs 22 (2024). https://doi.org/10.3390/md22030139.

[22] G. Obino, G. Nieddu, M. Nagy, H. Ippel, T. Cubeddu, H.M.H. Spronk, T.M. Hackeng, M. Formato, A.J. Lepedda, L. Moroni, Marine-derived sulfated polysaccharides enhance hemocompatibility and endothelialization of nanofibrous PCL for vascular graft applications, Cell Biomaterials (2025) 100155. https://doi.org/10.1016/j.celbio.2025.100155.

[23] J. A. Eble, "Editorial [Hot Topic: The Extracellular Matrix in Health and Disease(Executive Editor: Johannes A. Eble)]," Current pharmaceutical design 15, no. 12 (2009): 1275–1276, https://doi.org/10.2174/138161209787846694.

[24] J. E. Wagenseil and R. P. Mecham, "Vascular Extracellular Matrix and Arterial Mechanics," Physiological Reviews 89 (2009): 957–989, https://doi.org/10.1152/physrev.00041.2008.

[25] S. Ozdemir, J. Oztemur, H. Sezgin, and I. Yalcin-Enis, "The Effect of Polymer Type and Fiber Orientation on the Compliance Properties of Electrospun Vascular Grafts," Fibres and Textiles 30 (2023): 67–71, https://doi.org/10.15240/tul/008/2023-1-011.

[26] K. A. van Kampen, J. Fernández-Pérez, M. Baker, C. Mota, and L. Moroni, "Transpapillary Iontophoretic Delivery of Resveratrol Loaded Transfersomes for Localized Delivery to Breast Cancer," Biomaterials Advances 139 (2022): 213085, https://doi.org/10.1016/j.bioadv.2022.212972.

[27] B. M. Baker, A. O. Gee, R. B. Metter, et al., "The Potential to Improve Cell Infiltration in Composite Fiber-Aligned Electrospun Scaffolds by the Selective Removal of Sacrificial

Fibers," Biomaterials 29 (2008): 2348–2358, https://doi.org/10.1016/j.biomaterials.2008.01.032.

[28] J. M. Ameer, P. R. Anil Kumar, and N. Kasoju, "Strategies to Tune Electrospun Scaffold Porosity for Effective Cell Response in Tissue Engineering," Journal of Functional Biomaterials 10 (2019): 30, https://doi.org/10.3390/jfb10030030.

[29] P. Gupta and B. B. Mandal, "Recent Progress in Functional Materials for Selective Detection and Removal of Mercury(II) Ions," Advanced Functional Materials 31 (2021): 2006168, https://doi.org/10.1002/adfm.202100027.

[30] M. Bartolf-Kopp, L. de Silva, A. J. W. P. Rosenberg, J. Groll, D. Gawlitta, and T. Jungst, "Graphene-Assisted Assembly of Electrically and Magnetically Conductive Ceramic Nanofibrous Aerogels Enable Multifunctionality," Advanced Functional Materials 34 (2024): 2314653, https://doi.org/10.1002/adfm.202311797.

[31] T. A. Horbett, "Fibrinogen adsorption to biomaterials," Journal of Biomedical Materials Research Part A 106 (2018): 2777–2788, https://doi.org/10.1002/jbm.a.36460.

[32] S. N. Rodrigues, I. C. Gonçalves, M. C. L. Martins, M. A. Barbosa, and B. D. Ratner, "Fibrinogen Adsorption, Platelet Adhesion and Activation on Mixed Hydroxyl-/Methyl-Terminated Self-Assembled Monolayers," Biomaterials 27 (2006): 5357–5367, https://doi.org/10.1016/j.biomaterials.2006.06.010.

[33] B. Sivaraman and R. A. Latour, "The Relationship Between Platelet Adhesion on Surfaces and the Structure Versus the Amount of Adsorbed Fibrinogen," Biomaterials 31 (2010): 832–839, https://doi.org/10.1016/j.biomaterials.2009.10.008.

[34] M. Carrabba, M. Fagnano, M. T. Ghorbel, et al., "Development of a Novel Hierarchically Biofabricated Blood Vessel Mimic Decorated With Three Vascular Cell Populations for the Reconstruction of Small-Diameter Arteries," Advanced Functional Materials 34 (2024): 2300621, https://doi.org/10.1002/adfm.202300621.

[35] E. Claes, J. M. Atienza, G. V. Guinea, et al., "Mechanical Properties of Human Coronary Arteries," Annual International Conference of the IEEE Engineering in Medicine and Biology Society (2010): 3792–3795, https://doi.org/10.1109/IEMBS.2010.5627560.

[36] M. A. Hiob, S. She, L. D. Muiznieks, and A. S. Weiss, "Biomaterials and Modifications in the Development of Small-Diameter Vascular Grafts," ACS Biomaterials Science & Engineering 3 (2017): 712–723, https://doi.org/10.1021/acsbiomaterials.6b00220.

[37] G. Singh, J. Cordero, B. Wiles, et al., "Development of In Vitro Bioengineered Vascular Grafts for Microsurgery and Vascular Surgery Applications," Plastic and Reconstructive Surgery 7 (2019): E2264, https://doi.org/10.1097/GOX.0000000000002264.

[38] G. Konig, T. N. McAllister, N. Dusserre, et al., "Mechanical Properties of Completely Autologous Human Tissue Engineered Blood Vessels Compared to Human Saphenous Vein and Mammary Artery," Biomaterials 30 (2009): 1542–1550, https://doi.org/10.1016/j.biomaterials.2008.11.011.

[39] P. Mallis, A. Kostakis, C. Stavropoulos-Giokas, and E. Michalopoulos, "Future Perspectives in Small-Diameter Vascular Graft Engineering," Bioengineering 7 (2020): 160, https://doi.org/10.3390/bioengineering7040160.

[40] G. Niu, E. Sapoznik, P. Lu, et al., "Fluorescent Imaging of Endothelial Cells in Bioengineered Blood Vessels: The Impact of Crosslinking of the Scaffold," Journal of Tissue Engineering and Regenerative Medicine 10 (2016): 955, https://doi.org/10.1002/term.1876.

[41] V. A. Kumar, J. M. Caves, C. A. Haller, et al., "Acellular Vascular Grafts Generated From Collagen and Elastin Analogs," Acta Biomaterialia 9 (2013): 8067–8074, https://doi.org/10.1016/j.actbio.2013.05.024.

[42] D. L. Donovan, S. P. Schmidt, S. P. Townshend, G. O. Njus, and W. V. Sharp, "Material and Structural Characterization of Human Saphenous Vein," Journal of Vascular Surgery 12 (1990): 531–537, https://doi.org/10.1067/mva.1990.22707.

[43] M. Stekelenburg, M. C. M. Rutten, L. H. E. H. Snoeckx, and F. P. T. Baaijens, "Dynamic Straining Combined With Fibrin Gel Cell Seeding Improves Strength of Tissue-Engineered Small-Diameter Vascular Grafts," Tissue Engineering Part A 15, no. 5 (2009): 1081–1089, https://doi.org/10.1089/ten.tea.2008.0183.

[44] L. Soletti, Y. Hong, J. Guan, et al., "A Bilayered Elastomeric Scaffold for Tissue Engineering of Small Diameter Vascular Grafts," Acta Biomaterialia 6 (2010): 110–122, https://doi.org/10.1016/j.actbio.2009.06.026.

[45] U. Yokoyama, Y. Tonooka, R. Koretake, et al., "Arterial Graft With Elastic Layer Structure Grown From Cells," Scientific Reports 7 (2017): 140, https://doi.org/10.1038/s41598-017-00237-1.

[46] M. Bouchet, M. Gauthier, M. Maire, A. Ajji, and S. Lerouge, "Towards Compliant Small-Diameter Vascular Grafts: Predictive Analytical Model and Experiments," Materials Science and Engineering: C 100 (2019): 715–723, https://doi.org/10.1016/j.msec.2019.03.023.

[47] A. P. Rickel, X. Deng, D. Engebretson, and Z. Hong, "Electrospun Nanofiber Scaffold for Vascular Tissue Engineering," Materials Science and Engineering: C 129 (2021): 112373, https://doi.org/10.1016/j.msec.2021.112373.

[48] F. Han, X. Jia, D. Dai, et al., "Performance of a Multilayered Small-Diameter Vascular Scaffold Dual-Loaded With VEGF and PDGF," Biomaterials 34 (2013): 7302–7313, https://doi.org/10.1016/j.biomaterials.2013.06.006.

[49] C. Bellini, A. W. Caulk, G. Li, G. Tellides, and J. D. Humphrey, "Biomechanical Phenotyping of the Murine Aorta: What Is the Best Control?," Journal of Biomechanical Engineering 139, no. 4 (2017): 0445011–0445016, https://doi.org/10.1115/1.4035551.

[50] C. Singh, C. Wong, and X. Wang, "Medical Textiles as Vascular Implants and Their Success to Mimic Natural Arteries," Journal of Functional Biomaterials 6 (2015): 500–525, https://doi.org/10.3390/jfb6030500.

[51] M. Reusser, K. S. Hunter, S. R. Lammers, and K. R. Stenmark, "Validation of a Pressure Diameter Method for Determining Modulus and Strain of Collagen Engagement for Long Branches of Bovine Pulmonary Arteries," Journal of Biomechanical Engineering 134 (2012): 054501, https://doi.org/10.1115/1.4006686.

[52] M. J. A. Williams, R. A. H. Stewart, C. J. S. Low, and G. T. Wilkins, "Assessment of the Mechanical Properties of Coronary Arteries Using Intravascular Ultrasound: An In Vivo Study," The International Journal of Cardiovascular Imaging 15 (1999): 287–294.

[53] D. B. Camasão and D. Mantovani, "The mechanical Characterization of Blood Vessels and Their Substitutes in the Continuous Quest for Physiological-Relevant Performances. A Critical Review," Materials Today Bio 10 (2021): 100106, https://doi.org/10.1016/j.mtbio.2021.100106.

[54] S. Ozdemir, I. Yalcin-Enis, B. Yalcinkaya, and F. Yalcinkaya, "An Investigation of the Constructional Design Components Affecting the Mechanical Response and Cellular Activity of Electrospun Vascular Grafts," Membranes (Basel) 12 (2022): 929, https://doi.org/10.3390/membranes12100929.

[55] J. Chen, D. Zhang, L. P. Wu, and M. Zhao, “Current Strategies for Engineered Vascular Grafts and Vascularized Tissue Engineering,” Polymers (Basel) 15 (2023): 2015, https://doi.org/10.3390/polym15092015.
[56] X. Li, X. Wang, D. Yao, et al., “Effects of Aligned and Random Fibers With Different Diameter on Cell Behaviors,” Colloids and Surfaces B: Biointerfaces 171 (2018): 461–467, https://doi.org/10.1016/j.colsurfb.2018.07.045.
[57] A. C. Gilotti, W. Nimlamool, R. Pugh, et al., “Heparin Responses in Vascular Smooth Muscle Cells Involve cGMP-Dependent Protein Kinase (PKG),” Journal of Cellular Physiology 229 (2014): 2142–2152, https://doi.org/10.1002/jcp.24677.
[58] K. Lundmark, P. K. Tran, M. G. Kinsella, A. W. Clowes, T. N. Wight, and U. Hedin, “Perlecan Inhibits Smooth Muscle Cell Adhesion to Fibronectin: Role of Heparan Sulfate,” Journal of Cellular Physiology 188 (2001): 67–74, https://doi.org/10.1002/jcp.1094.
[59] Y. Pan, X. Zhou, Y. Wei, et al., “Small-Diameter Hybrid Vascular Grafts Composed of Polycaprolactone and Polydioxanone Fibers,” Scientific Reports 7 (2017): 3615, https://doi.org/10.1038/s41598-017-03851-1.
[60] S. de Valence, J. C. Tille, D. Mugnai, et al., “Long Term Performance of Polycaprolactone Vascular Grafts in a Rat Abdominal Aorta Replacement Model,” Biomaterials 33 (2012): 38–47, https://doi.org/10.1016/j.biomaterials.2011.09.024.
[61] A. A. Dokuchaeva, A. B. Mochalova, T. P. Timchenko, et al., Polymers (Basel) 14 (2022): 3313, https://doi.org/10.3390/polym14163313.
[62] M. X. Li, Q. Q. Wei, H. L. Mo, et al., “Challenges and Advances in Materials and Fabrication Technologies of Small-Diameter Vascular Grafts,” Biomaterials Research 27 (2023): 0399, https://doi.org/10.1186/s40824-023-00399-2.
[63] J. Fernández-Pérez, K. A. van Kampen, C. Mota, M. Baker, and L. Moroni, “Flexible, Suturable, and Leak-Free Scaffolds for Vascular Tissue Engineering Using Melt Spinning,” ACS Biomaterials Science & Engineering 9 (2023): 5006–5014, https://doi.org/10.1021/acsbiomaterials.3c00535.
[64] J. Schindelin, I. Arganda-Carreras, E. Frise, et al., “Fiji: An Open-Source Platform for Biological-Image Analysis,” Nature Methods 9 (2012): 676–682, https://doi.org/10.1038/nmeth.2019.
[65] A. Sensini, L. Cristofolini, M. L. Focarete, et al., “High-Resolution X-ray Tomographic Morphological Characterisation of Electrospun Nanofibrous Bundles for Tendon and Ligament Regeneration and Replacement,” Journal Of Microscopy 272 (2018): 196–206, https://doi.org/10.1111/jmi.12720.
[66] H. M. Muir, “A Modified Uranic Acid Carbazole Reaction,” Analytical Biochemistry 4 (1962): 330–334.
[67] International Organization for Standardization, ISO 7198:2016 Cardiovascular Implants and Extracorporeal Systems — Vascular Prostheses — Tubular Vascular Grafts and Vascular Patches, 2016.
[68] A. Sensini, C. Gualandi, M. L. Focarete, et al., “Multiscale Hierarchical Bioresorbable Scaffolds for the Regeneration of Tendons and Ligaments,” Biofabrication 11 (2019): 035026, https://doi.org/10.1088/1758-5090/ab20ad.
[69] A. Sensini, C. Gotti, J. Belcari, et al., “Morphologically Bioinspired Hierarchical Nylon 6,6 Electrospun Assembly Recreating the Structure and Performance of Tendons and Ligaments,” Medical Engineering & Physics 71 (2019): 79, https://doi.org/10.1016/j.medengphy.2019.06.019.

[70] A. Sensini, R. D'Anniballe, C. Gotti, et al., "Bi-Material Nanofibrous Electrospun Junctions: A Versatile Tool to Mimic the Muscle–Tendon Interface," Materials & Design 242 (2024): 113015, https://doi.org/10.1016/j.matdes.2024.113015.

[71] A. Sensini, O. Stamati, G. Marchiori, et al., "Full-Field Strain Distribution in Hierarchical Electrospun Nanofibrous Poly-L(Lactic) Acid/Collagen Scaffolds for Tendon and Ligament Regeneration: A Multiscale Study," Heliyon 10 (2024): e26796, https://doi.org/10.1016/j.heliyon.2024.e26796.

[72] N. Perrira, A. S. Shuib, S. W. Phang, and A. S. Muda, "Experimental Investigation of Blood Mimicking Fluid Viscosity for Application in 3D-Printed Medical Simulator," Journal of Physics: Conference Series 2222 (2022): 012016, https://doi.org/10.1088/1742-6596/2222/1/012016.

[73] C. Completo, V. Geraldes, and V. Semiao, "Rheological and Dynamical Characterization of Blood Analogue Flows in a Slit," International Journal of Heat and Fluid Flow 46 (2014): 17–28, https://doi.org/10.1016/j.ijheatfluidflow.2013.12.008.

[74] V. Laterreur, J. Ruel, F. A. Auger, et al., "Comparison of the Direct Burst Pressure and the Ring Tensile Test Methods for Mechanical Characterization of Tissue-Engineered Vascular Substitutes," Journal of the Mechanical Behavior of Biomedical Materials 34 (2014): 253–263, https://doi.org/10.1016/j.jmbbm.2014.02.017.

Chapter 6
Incorporation of Notoginsenoside Fc into PCL Scaffolds to Enhance Endothelialization and Inhibit Platelet Aggregation

Gabriele Obino[a,b]; Luojiao Huang[c]; Alix Lemaître[b]; Martijn van Griensven[c]; Berta Cillero-Pastor[c]; Marilena Formato[a]; Antonio J Lepedda[a] and Lorenzo Moroni[b]

[a]Department of Biomedical Sciences, University of Sassari, Viale San Pietro, 43b, 07100 Sassari, Italy
[b] Department of Complex Tissue Regeneration, MERLN Institute for Technology-Inspired Regenerative Medicine, Maastricht University, 6200 MD Maastricht, The Netherlands
[C] Department of Cell Biology-Inspired Tissue Engineering MERLN Institute for Technology-Inspired Regenerative Medicine, Maastricht University, 6200 MD Maastricht, The Netherlands

Abstract

Small-diameter tissue-engineered vascular grafts require rapid endothelialization and antithrombogenic properties to maintain long-term patency. Conventional strategies employ heparin coatings to reduce thrombosis and promote cell colonization. However, heparin alone may not fully prevent platelet adhesion and has drawbacks such as animal-derived sourcing and effects on vascular smooth muscle cell function. Notoginsenoside Fc (NgFc), a saponin isolated from *Panax notoginseng*, is known to potently inhibit platelet aggregation and support endothelial repair. We fabricated electrospun tubular poly(ε-caprolactone) (PCL) scaffolds loaded with NgFc to provide controlled drug release. Liquid chromatography – Mass sprectromety (LC–MS) analysis confirmed successful NgFc incorporation, Integrity and burst release under physiological conditions. NgFc-loaded scaffolds greatly enhanced human umbilical vein endothelial cells (HUVECs) attachment and growth from early timepoints, with increased expression of mature endothelial markers (e.g. VE–cadherin). Platelet adhesion assays showed a marked, dose-dependent reduction in platelet attachment on NgFc-containing scaffolds (0.1% and 1% NgFc), whereas plasma clotting times (aPTT, PT) were unchanged. These results indicate that NgFc-PCL scaffolds accelerate endothelialization while significantly reducing thrombogenicity, making them promising candidates for small-caliber vascular grafts.

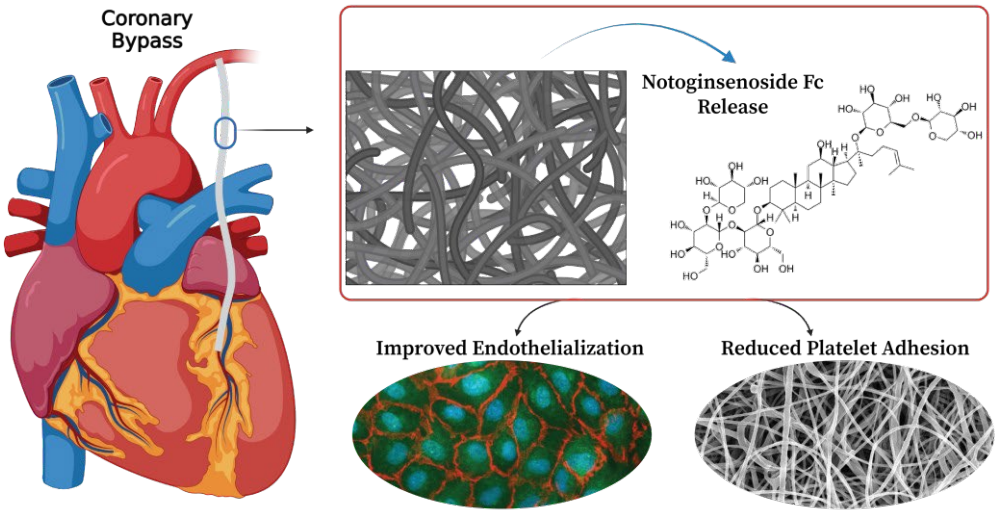

Graphical abstract: Electrospun PCL meshes loaded with NgFc were developed as small-caliber vascular grafts for coronary bypass applications. The bioactive release of NgFc enhances endothelialization while reducing platelet adhesion, supporting hemocompatibility and vascular regeneration. Figure partially created with BioRender.com under academic license.

Keywords: electrospinning; saponins; vascular grafts; Notoginsenoside Fc (NgFc); Small-diameter tissue-engineered vascular grafts; Hemocompatibiliy

Introduction

Cardiovascular disease often necessitates bypass grafting with vascular conduits. While large-caliber synthetic grafts (e.g. ePTFE, Dacron®) perform well, small-diameter (<6 mm) grafts suffer poor patency due to early thrombosis and neointimal hyperplasia [1]. In fact, lack of a confluent endothelial layer on a graft lumen is a major limitation leading to protein adsorption, platelet activation, and clot formation [2,3]. Thus, small tissue-engineered vessel grafts (sTEVGs) must promote rapid endothelialization and resist thrombosis and excessive smooth muscle growth to remain patent [4].

Heparin coatings are widely used to improve hemocompatibility of vascular scaffolds. Heparin's highly sulfated, negatively charged structure binds antithrombin III and growth factors (e.g. VEGF, FGF), reducing thrombosis and potentially stabilizing angiogenic factors [5–9]. Heparinized grafts have shown enhanced endothelial cell adhesion and prolonged clotting times [10]. For example, heparin-coated PTFE grafts support HUVEC proliferation while inhibiting smooth muscle proliferation [10,11]. However, even heparinized surfaces can permit some platelet attachment and may suppress vascular cell function in unexpected ways [12,13]. Adverse effects of heparin (e.g. bleeding, heparin-induced thrombocytopenia) and its animal origin limit its use in certain patients. These issues motivate alternative bioactive strategies.

Recently, small bioactive molecules have been explored as graft coatings to achieve dual anti-platelet and pro-endothelial effects. In this context, *Panax notoginseng* saponins are of interest [14,15]. In particular, Notoginsenoside Fc (NgFc) is a triterpenoid saponin reported to inhibit platelet aggregation and accelerate endothelial repair [16,17]. Liu et al. showed that NgFc suppressed thrombin-, collagen-, and ADP-induced platelet aggregation by downregulating the PLCγ_2 signaling cascade *in vitro* and significantly reduced arterial thrombosis *in vivo* [18]. In a separate study, NgFc treatment accelerated reendothelialization and alleviated neointimal hyperplasia following arterial injury in diabetic rats [19]. These findings suggest that NgFc could serve as a biocompatible antithrombotic and pro-endothelial agent.

In this study, we investigated NgFc as a small bioactive molecule for incorporation into tissue-engineered vascular grafts (TEVGs). Tubular electrospun PCL scaffolds were fabricated, leveraging the material's well-established biocompatibility and mechanical properties [20], and loaded them with NgFc. Electrospinning produces a fibrous matrix that mimics native extracellular matrix, promoting cell colonization [21–23]. NgFc incorporation and release were confirmed by LC–MS. We then assessed endothelialization

by culturing HUVECs on the scaffolds, investigating cell coverage and endothelial marker expression (e.g. VE–cadherin, Thbs2, KLF2, eNOS). In parallel, we analysed platelet adhesion on the scaffold surfaces and plasma coagulation times (aPTT, PT). This study demonstrates that PCL grafts incorporating NgFc substantially enhance early endothelial coverage and markedly reduce platelet adhesion *in vitro*, supporting their potential to improve small-caliber graft performance.

Material and methods

Chemicals and Reagents

NgFc and Ginsenoside Rg1 (GRg1, internal standard, IS) were purchased from TargetMol (TargetMol Chemicals Inc. Boston, MA, USA).
PCL (80kDa MW) was purchased from Sigma-Aldrich (Merck KGaA, Darmstadt, Germany); Hexafluoro-2-propanol (HFIP) was purchased from Biosolve B.V. (Biosolve B.V., Valkenswaard, the Netherlands).

2D Cytotoxicity Analysis

The potential cytotoxicity of NgFc was evaluated on human umbilical vein endothelial cells (HUVECs) at two time points: 24 and 72 hours post-treatment. Cells were seeded at a density of 5,000 cells per well in 96-well plates and allowed to adhere and stabilize for 24 hours under standard culture conditions (37 °C, 5% CO_2). Following stabilization, cells were treated with increasing concentrations of Notoginsenoside NgFc (0 μM, 3 μM, 6 μM, 12 μM, 25 μM, 50 μM, 100 μM, 200 μM, 400 μM, 800 μM, and 1200 μM), which was solubilized in DMSO. A control group treated with the highest DMSO concentration used in the test conditions (vehicle control) was included to account for any potential cytotoxic effects of the solvent. Cell viability and cytotoxicity were assessed using the PrestoBlue™ Cell Viability Reagent (Thermo Fisher Scientific, Waltham, MA, USA) and the CyQUANT™ LDH Cytotoxicity Assay Kit (Thermo Fisher Scientific, Waltham, MA, USA; Cat. No. C20302), respectively, following the manufacturers' protocols. The PrestoBlue assay was used to determine metabolic activity, while the LDH assay measured membrane integrity by quantifying lactate dehydrogenase release from damaged or dead cells. In addition to metabolic and cytotoxic evaluations, immunofluorescence staining was performed at 72 hours to assess endothelial phenotype and monolayer integrity. Cells were fixed and stained for von Willebrand factor (vWF) and vascular endothelial (VE)-cadherin, with

nuclear counterstaining using DAPI. Images were acquired by using a Nikon Eclipse Ti2 Inverted Microscope (Nikon Corporation, Tokyo, Japan) and analyzed using ImageJ (Fiji) software.

Scaffold preparation

The electrospinning solution was prepared by dissolving 13% (w/v) PCL in HFIP under continuous stirring overnight. NgFc was incorporated into the PCL solution at two different concentrations (0.1% and 1% w/w relative to PCL). For this purpose, NgFc powder was first dissolved in absolute ethanol, and the resulting solution was then added to the PCL-HFIP mixture to achieve a final ethanol concentration of 10%. Electrospun scaffolds were produced after 45 minutes of electrospinning using the following parameters: voltage, 18.5 kV; needle-to-collector distance, 15 cm; and flow rate, 1 mL/h.

For scaffold collection, a stainless-steel mandrel with a diameter of 6 cm was used for planar scaffolds, while a 4 mm diameter mandrel was employed for tubular scaffolds. The mandrel rotation speed was set at 100 rpm. To ensure uniform fiber deposition, a blunt 20-gauge stainless steel hypodermic needle (internal diameter 0.8 mm; Unimed, Switzerland) was programmed to move along the length of the collector during electrospinning. All procedures were conducted under controlled environmental conditions, with the temperature maintained at 25 °C and relative humidity at 35%.

Scanning Electron Microscopy (SEM) Investigation

For the characterization of the electrospun fibers, a layer of gold coating (Quorum Technologies SC7620, UK) was applied over the samples. Images were captured by using a JSM-IT200 microscope (Jeol ltd., the Netherlands) at 2 different magnification 1500x and 5000×, with an accelerating voltage of 100 kV and a working distance of 11 mm. The subsequent image processing and analysis was performed to determine fiber diameter (n = 3 samples × 35 measurements each) by using Fiji image processing package (GNU General Public License).

LC–MS/MS Analysis of Notoginsenoside Fc: Detection, Stability, and Release

The quantification and analysis of NgFc presence, stability, and release were performed using a LC–MS/MS system, with reference to the method developed by Wang et al. [24]. Chromatographic separation was carried out on a Waters Acquity UPLC system equipped with an ACQUITY UPLC Peptide

BEH C18 analytical column (50 × 1 mm, 1.7 µm particle size), protected by a Vanguard™ BEH C18 guard column (5 × 2.1 mm, 1.7 µm). The column temperature was maintained at 45 °C throughout the analysis. The mobile phase consisted of water (A) and acetonitrile (B), delivered at a flow rate of 0.1 mL/min. The gradient elution profile was as follows: 0–1.5 min, 10–100% B; 1.5–2 min, 100–10% B; and 2–4.5 min, re-equilibration at 10% B.

Mass spectrometric detection was conducted on a Waters Xevo TQ-S Triple Quadrupole Mass Spectrometer equipped with an electrospray ionization (ESI) source operating in negative ion mode. The optimized parameters were capillary voltage, 2.5 kV; sampling cone voltage, 40 V; desolvation temperature, 300 °C; desolvation gas flow, 650 L/h; cone gas flow, 190 L/h; and nebulizer pressure, 7.0 bar. Multiple reaction monitoring (MRM) mode was employed for quantification. The selected precursor-to-product ion transition for NgFc was *m/z* 604.56 → 783.94, with a collision energy of 24 eV. The precursor-to-product ion transition for internal standard (GRg1) was *m/z* 799.9 → 637.64, with a collision energy of 24 eV.

Quantitative analysis using LC−MS/MS with an internal standard was performed to determine NGFc concentration in the released medium sample. A stock solution of NgFc was prepared at 1.0 mg/mL in Milli-Q water and serially diluted to obtain working solutions at concentrations of 0.5, 1.0, 2.0, 5.0, 10.0, 15.0, and 20.0 µg/mL. A stock solution of IS was prepared at 1.0 mg/mL in Milli-Q water and diluted to obtain a working solution with 40.0 µg/mL. Each NGFc working solution (40 µL) was spiked with IS working solution (40 µL) and analyzed to construct the standard calibration curve.

Release test was performed by incubating PCL scaffolds containing NgFc in the quantities of 0%, 0.1% or 1.0% in different external matrices, including water, methanol, Endothelial Cell Growth Medium (EGM-2, PromoCell GmbH, Heidelberg, Germania, Cat. No. C-22011). Samples of the release media were collected after 24h. For medium samples, 50 µL of the collected solution was mixed with 100 µL of methanol, vortexed for 30 s, and centrifuged at 15,000 rpm for 10 min to precipitate denatured proteins. 40 µL of supernatant was added with IS working solution (40 µL) and analyzed by LC–MS/MS. For water and methanol release samples, 50 µL of each was centrifuged at 15,000 rpm for 10 min to remove insoluble particles. 40 µL of supernatant was added with IS working solution (40 µL) and analyzed by LC–MS/MS.

Platelet Adhesion Assays

As described in previous research [13], for platelet adhesion assays, 3.2% sodium citrate anticoagulated blood was centrifuged at 250 g for 15 minutes to isolate the platelet-rich plasma (PRP). The supernatant consisting of the PRP was carefully collected, and the platelet concentration was adjusted to 20 x 10^9 platelets per liter with autologous PPP. Platelet adhesion was assessed by adding 300 µL of the PRP to each scaffold in a 24-well plate followed by incubation at 37 °C for 1 hour, to allow platelets to adhere. Then, scaffolds were gently rinsed three times with phosphate-buffered saline (PBS) to remove any non-adherent platelet. This washing step was crucial to minimize background and ensure that only platelets firmly attached to the scaffold surface were counted.

Platelets Fluorescence Microscopy and SEM Analysis

Scaffolds were first fixed using a 1% (w/v) paraformaldehyde (PFA) solution in phosphate-buffered saline (PBS) to preserve their structural integrity and immobilize adhered platelets. Subsequently, platelets were permeabilized with a 1% sodium dodecyl sulfate (SDS) solution in PBS to enable staining of intracellular components.

For the staining procedure, scaffolds were incubated with CF647 Phalloidin (Biotium; 1:200) to visualize F-actin cytoskeletal structures, providing insights into platelet adhesion and morphology on the scaffold surfaces.

After staining, scaffolds were thoroughly rinsed with PBS followed by fluorescence microscopy analysis using Eclipse Ti2 Inverted Microscope (Nikon Corporation, Tokyo, Japan) and picture were elaborated using ImageJ Fiji image analysis software.

For SEM analysis scaffolds were fixed in 2.5% glutaraldehyde in phosphate buffer, followed by post-fixation in 1% osmium tetroxide in 0.1 M sodium cacodylate buffer for 1 hour. Samples were then dehydrated through a graded ethanol series (70%, 90%, 100%), and a thin gold coating was applied using a SC7620 sputter coater (Quorum Technologies, UK). SEM images were captured using a JSM-IT200 microscope (Jeol Ltd., The Netherlands), providing high-resolution visualization of platelet morphology and scaffold surface characteristics. Analyses were performed on PCL-NgFc (0%), PCL-NgFc (0,1%) and PCL-NgFc (1%).

Biocompatibility Assays

Human umbilical vein endothelial cells (HUVECs) were obtained from PromoCell GmbH (PromoCell GmbH, Heidelberg, Germany, Cat. No. C-12203) and cultured in Endothelial Cell Growth Medium (EGM-2, PromoCell GmbH, Heidelberg, Germania, Cat. No. C-22011) following the manufacturer's guidelines. Scaffolds were placed in 24-well plates and underwent chemical sterilization by immersion in 70% ethanol three times for 15 minutes each [25]. After sterilization, scaffolds were completely air-dried and rinsed with PBS. Subsequently, scaffolds were secured at the bottom of the wells using a rubber O-ring. HUVECs were seeded onto the scaffolds at a density of 100,000 cells per scaffold. The cells were cultured for 12 days under standard conditions (37 °C, 5% CO_2), with medium changed every 48 hours.

Metabolic Activity: PrestoBlue Assay

To assess metabolic activity, PrestoBlue reagent (Thermo Fisher Scientific, Waltham, MA, USA) was used. At every time point, scaffolds were incubated with 450 µL of PrestoBlue solution for 45 minutes at 37 °C, 5% CO_2. Then, 200 µL of the solution was transferred into a black bottom 96-well plate and fluorescence intensities were measured using a microplate reader (CLARIOstar Plus. Ortenberg, Germany) at an excitation wavelength of 560 nm and an emission wavelength of 590 nm, according to the manufacturer's instructions.

Immunofluorescence Microscopy Analysis

Scaffolds were washed with PBS to remove residual medium, followed by cell fixation with 3.7% (w/v) paraformaldehyde for 15 minutes. Then, scaffolds were further washed with PBS and cells permeabilized using 0.1% Triton X-100. To block nonspecific binding sites, scaffolds were incubated with a PBS solution containing 3% (w/v) bovine serum albumin (BSA) and 0.05% (v/v) Tween-20 (blocking solution), for 30 minutes.

Scaffolds were then incubated overnight at 4°C with primary antibodies, including an anti-von Willebrand Factor (vWF) antibody produced in rabbit (1:200 dilution; Sigma-Aldrich; Cat. No. F3520) and Alexa Fluor® 647 Mouse Anti-Human CD144-Vascular Endothelial Cadherin (VE-Cad) (1:1000 dilution; BD Pharmingen™; Cat. No. 561567) in blocking solution. After three washes of 5 minutes each with PBS containing 0.05% Tween-20 on an orbital shaker, scaffolds were incubated for 15 minutes with Phalloidin (1:1000 dilution; Thermo Fisher Scientific, Waltham, MA, USA; Cat. No. A12379), to

stain actin filaments, and DAPI (1:1000 dilution; Thermo Fisher Scientific; Cat. No. 10184322), to stain cell nuclei. Donkey anti-Rabbit IgG secondary antibody, Alexa Fluor™ 488 (1:1000 dilution; Thermo Fisher Scientific; Cat. No. A-21206), was then applied at room temperature for 1 hour to detect the vWF primary antibody. Finally, scaffolds were washed with PBS to remove unbound secondary antibodies and mounted onto glass slides for visualization using a Nikon Eclipse Ti2 Inverted Microscope (Nikon Corporation, Tokyo, Japan). Immunostaining images were analyzed using ImageJ (Fiji) software.

qPCR Analysis

At each experimental time point, electrospun scaffolds were retrieved and gently rinsed with cold PBS. Samples were then immersed in 1 mL of TRIzol® Reagent (Sigma-Aldrich, St. Louis, MO, USA) and homogenized. Total RNA was extracted by standard phenol–chloroform separation. The RNA pellet was washed with 75% ethanol, briefly air-dried, and resuspended in RNase-free water. RNA concentration and purity were determined spectrophotometrically (NanoDrop™ 2000, Thermo Fisher Scientific, Waltham, MA, USA). cDNA synthesis was performed from 500 ng total RNA using the RT² First Strand Kit (Qiagen GmbH, Hilden, Germany) on a C1000 Touch™ Thermal Cycler (Eppendorf AG, Hamburg, Germany) according to the manufacturer's protocol. Quantitative real-time PCR was carried out in 10 µL reactions using RT² SYBR® Green qPCR Mastermix (Qiagen GmbH, Hilden, Germany) with 250nM of each primer. Gene-specific primers targeted human endothelia cells are listed in table 1. Glyceraldehyde-3-phosphate dehydrogenase (GAPDH) was chosen as the housekeeping control. Amplification was performed on a CFX96™ Real-Time PCR Detection System (Bio-Rad Laboratories, Hercules, CA, USA) under the following cycling conditions: initial activation, 95 °C for 10 min; 40 cycles of denaturation at 95 °C for 15 s and annealing/extension at 60 °C for 1 min; followed by melt-curve analysis from 65 °C to 95 °C. Each sample was run in technical triplicate, and no-template controls were included on every plate. Relative gene expression was calculated using the $2^{-}\Delta\Delta Ct$ method, normalizing targets to GAPDH and expressing results relative to the 24-hour, untreated control group.

Table 1. List of primer sequences, used to target human endothelia cells-specific mRNAs.

	Primers Sequences	
	Forward	Reverse
GAPDH	GGTGGTCTCCTCTGACTTCAACA	GTGGTCGTTGAGGGCAATG
Thrombomodulin	GCCCATGGGAGCTGGTTAGA	GGCCTGACTTGGCCTGCTAC
NOTCH4	AGCTCTGGAAAGAGGGTTTAAG	CTCCTGTGGCCTGTCTTATTT
KLF2	GCAAGACCTACACCAAGAGTTCG	CATGTGCCGTTTCATGTGC
CD31	GCAACACAGTCCAGATAGTCGT	GACCTCAAACTGGGCATCAT
STAT3	CCCTTGGATTGAGAGTCAAG	AAGCGGCTATACTGCTGGTC
BAX	CATCATGGGCTGGACATTG	GGGACATCAGTCGCTTCAGT
TRPM7	TTGACATTGCCAAAAATCATGT	CTTGTTCCAAGGATCCAACC
eNOS	CAGCAACGCTACCACGAAGA	TGCGTATGCGGCTTGTCA

Statistical Analysis

Statistical analysis was performed using GraphPad Prism version 10.0. Data from metabolic activity assays and DNA quantification were analyzed for statistical significance. Differences among multiple groups at various time points were assessed using a 2-way ANOVA analysis followed by Tukey's multiple comparisons test. An ordinary one-way ANOVA followed by Tukey's multiple comparisons test was conducted for the aPTT and PT data. A p-value of less than 0.05 was considered statistically significant (*p-value < 0.05; **p-value < 0.01; ***p-value < 0.001; ****p-value < 0.0001). Results are presented as the mean ± standard deviation (SD) of at least three independent experiments.

Results

Cytotoxicity of NgFc in HUVECs

Representative immunofluorescence (vWF/VE-cadherin) images after 72 h of NgFc exposure (200–1200 μM) showed well-spread, confluent endothelial monolayers at all concentrations up to 800 μM (Figure1 A–D). At the highest dose (1200 μM), minor disruptions in cell density were observed, but overall cell morphology remained largely intact. Quantitative assays corroborated these findings: PrestoBlue metabolic activity at 24 h and 72 h was statistically comparable across the 0–800 μM range, with only a slight decline at 1200 μM (Figure 6.1E). In parallel, LDH release (percent dead cells) remained very low for all groups at 24 h and increased only marginally by 72 h (Figure 6.1F). Specifically, even at 1200 μM NgFc, cell viability by metabolic assay was >~80–90% of control and LDH-positive cells did not exceed ~20–25%. These data indicate that NgFc did not significantly compromise HUVECs viability across the tested concentrations: metabolic activity was maintained, and cytotoxicity remained minimal up to 1200 μM. Analysis of the dose–response profiles revealed a mostly flat relationship up to a critical threshold. At 24 h post-treatment, metabolic activity was near-control levels for all doses (indicating minimal acute toxicity), and LDH release was similarly negligible. By 72 h, a modest dose-dependent trend emerged: the PrestoBlue signal showed only a slight decrease with increasing dose (reflecting normal proliferation saturation rather than overt toxicity), whereas LDH leakage rose slightly at the highest concentration. Importantly, no concentration ≤800 μM caused a statistically significant loss in metabolic function or membrane integrity at either time point. A discernible cytotoxic threshold appeared only at the highest dose (1000–1200 μM) by 72 h, where ~20% of cells showed membrane damage (Figure 6.1F). Thus, NgFc cytotoxicity in this 2D HUVEC model is minimal below ~800 μM, with only mild toxicity evident at supraphysiological levels (near 1 mM) and prolonged exposure.

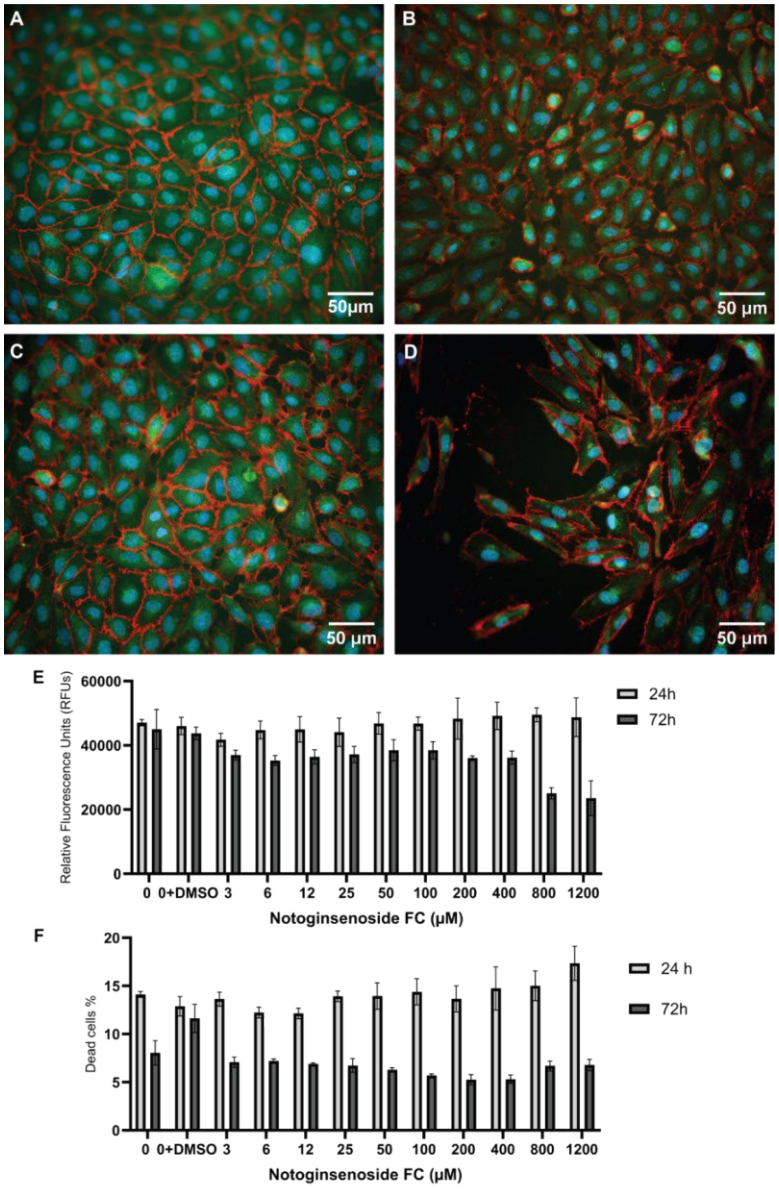

Figure 6.1. HUVEC 2D Cytotoxicity Analysis. A–D) Representative immunofluorescence images of HUVECs after 72 h exposure to NgFc at concentrations of 200 µM (A), 400 µM (B), 800 µM (C), and 1200 µM (D). E) Quantification of HUVEC metabolic activity at 24 h and 72 h post-treatment, assessed by PrestoBlue™ assay. F) Percentage of dead HUVECs at 24 h and 72 h post-treatment, determined by LDH release assay.

Scaffold fabrication, NgFc loading and release

Electrospun scaffolds loaded with NgFc were successfully fabricated and fiber morphology homogeneity was analyzed using SEM (Figure 6.2). LC–MS analysis confirmed incorporation and the structural integrity of Notoginsenoside NgFc into the electrospun PCL scaffolds (Figure 6.3). In release studies under physiological conditions, both 0.1% and 1% NgFc scaffolds exhibited a pronounced initial burst of drug release in methanol, while less pronounced in growth medium and distilled water solutions.

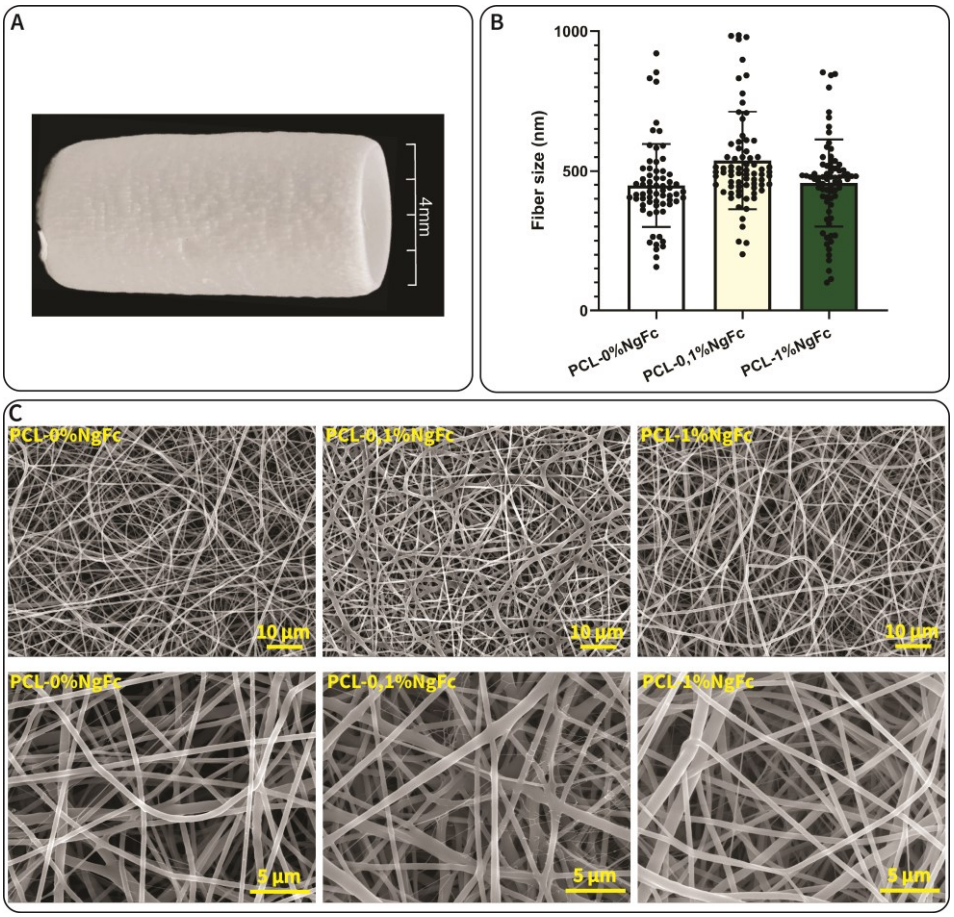

Figure 6.2. Morphological characterization of electrospun nanofibers. A) Representative photograph of a tubular electrospun scaffold. B) Histogram of fiber-diameter distributions in scaffolds with and without NgFc. C) SEM micrographs of the nanofibers at 1,500× (scale bar: 10 µm) and 5,000× (scale bar: 5 µm) magnifications.

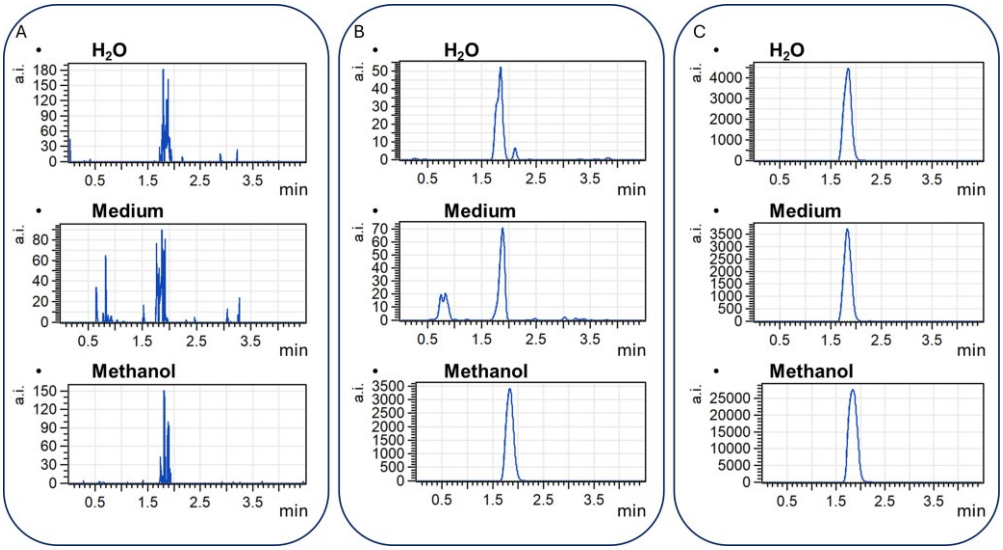

Figure 6.3. Representative chromatograms of NgFc release after 24 h incubation in different media (H_2O, culture medium, and methanol) from control electrospun scaffolds (A) and scaffolds containing two NgFc loadings: 0.1% (B), and 1% (C), with respect to PCL weight. Peaks correspond to NgFc elution, highlighting the effect of solvent and loading concentration on release behavior.

Endothelial Cell Adhesion and Proliferation

Immunofluorescence analysis of human umbilical vein endothelial cells (HUVECs) cultured on the scaffolds revealed a clear enhancement in cell adhesion and surface colonization following NgFc incorporation. At 48 hours post-seeding, cells on the PCL control scaffolds exhibited sparse distribution, forming isolated clusters with limited spreading. In contrast, both PCL scaffold conditions incorporating 0.1% and 1% NgFc demonstrated markedly greater surface coverage, with more extensive cell spreading and cytoskeletal organization (Figure 6.4), indicating improved adhesion and early colonization.

Metabolic activity, as assessed by the PrestoBlue assay, did not differ significantly between groups at each time point; however, a consistent increase in fluorescence intensity was observed across days 1, 5, and 12 in all conditions, reflecting progressive HUVEC proliferation over time (Figure S6.1). Despite comparable metabolic trends, the structural organization of the endothelial layer varied notably between groups.

By day 12, PCL-NgFc scaffolds supported the development of a confluent and morphologically mature endothelial monolayer, as evidenced by well-distributed expression of VE-cadherin and von Willebrand factor (vWF). These markers indicate the establishment of robust intercellular junctions and advanced endothelial maturation. However, it is noteworthy that localized detachment of the monolayer was observed, particularly on the PCL-1%NgFc scaffolds. In these regions, the endothelial sheet appeared to delaminate from the scaffold surface, suggesting potential disruption of cell–matrix interactions despite otherwise favorable endothelialization. Conversely, PCL control scaffolds continued to exhibit discontinuous coverage with persistent gaps, limited cell spreading, and clustering. These features are indicative of suboptimal focal adhesion and a lack of full endothelial maturation (Figure 6.5). The persistence of such discontinuities over time underscores the limited bioactivity of unmodified PCL in supporting sustained endothelialization.

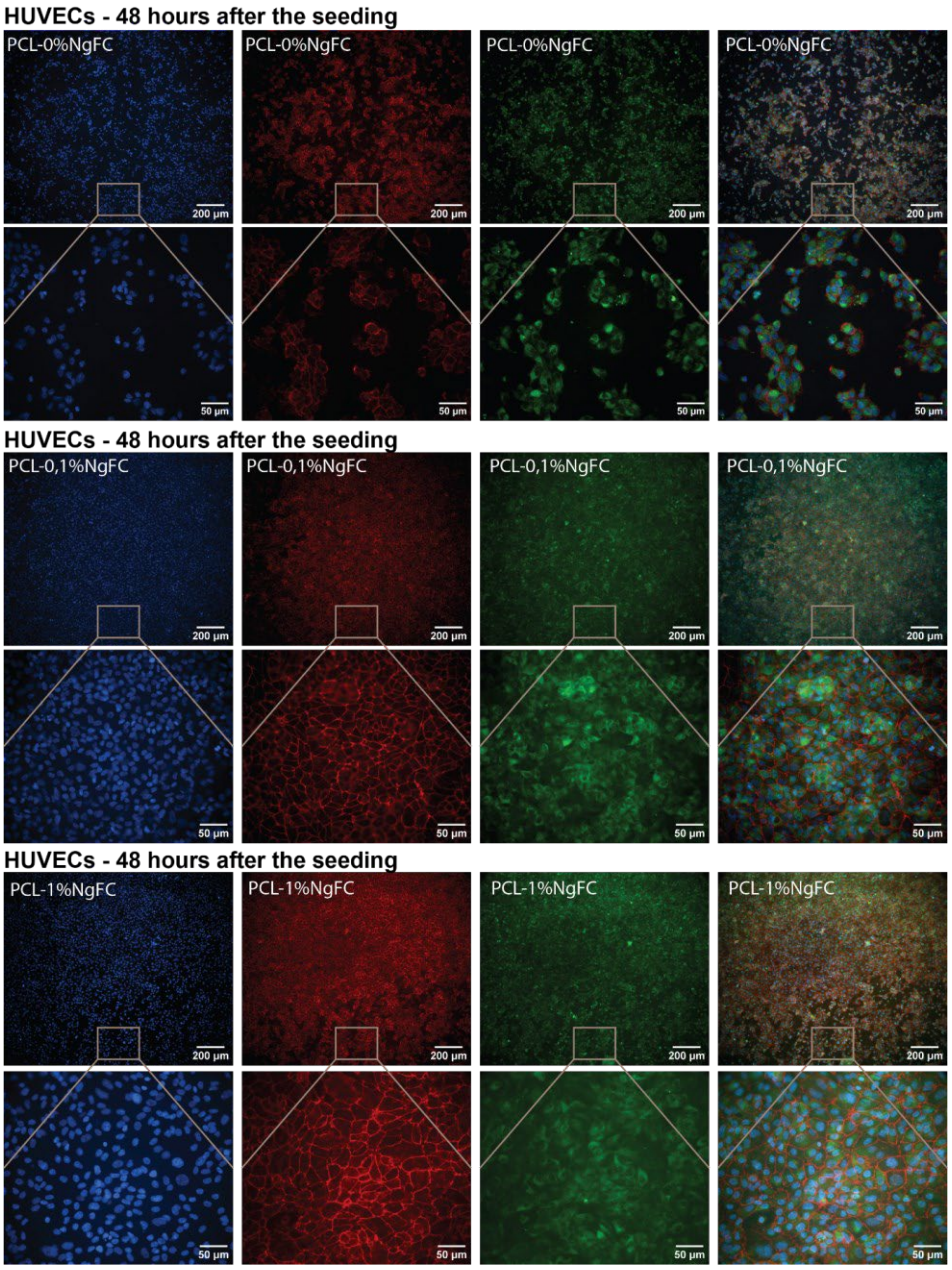

Figure 6.4. Immunofluorescence of HUVECs on electrospun scaffolds at 48 h post-seeding (Day 1). Nuclei are stained with DAPI (blue), VE-cadherin (red), and vWF (green). Main images: 4× magnification (scale bar: 200 µm); insets: 40× magnification (scale bar: 50 µm).

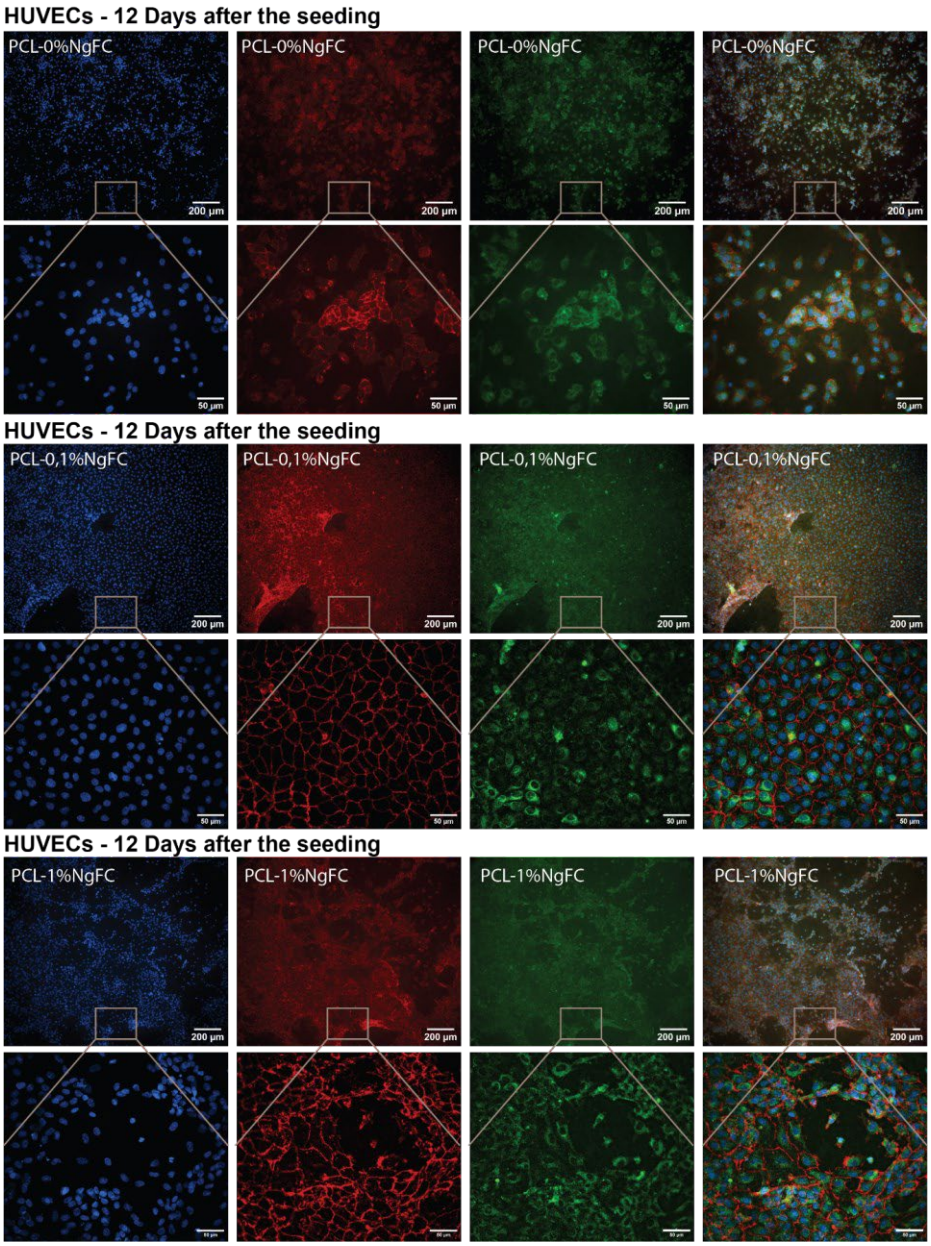

Figure 6.5. Immunofluorescence of HUVECs on electrospun scaffolds at Day 12. Nuclei are stained with DAPI (blue), VE-cadherin (red), and vWF (green). Main images: 4× magnification (scale bar: 200 µm); insets: 40× magnification (scale bar: 50 µm)

Endothelial gene expression

Gene expression analysis of HUVECs cultured on PCL-NgFc scaffolds (0%, 0.1%, 1%) was evaluated on Day 1 and Day 12 (Figure 6.6). TRPM7 expression was consistently upregulated on Day 12 compared to Day 1 across all scaffold conditions. Thrombomodulin expression was upregulated in the PCL- 1%NgFc condition on Day 12 and was almost absent in all scaffolds on Day 1. STAT3 expression was significantly higher on Day 12 than on Day 1 for all scaffolds, showing slightly differences across all conditions. BAK and Notch4 were expressed at both time points, but no significant variations were observed between conditions or time points. KLF2 expression was detected exclusively in the 0.1% and 1% NgFc conditions on Day 12 and was undetectable in scaffolds without NgFc (PCL-0%NgFc) or on Day 1 in all conditions. CD31 expression increased markedly on Day 12 compared to Day 1, showing an approximately 8-fold upregulation, yet with no statistical significant differences between scaffolds.

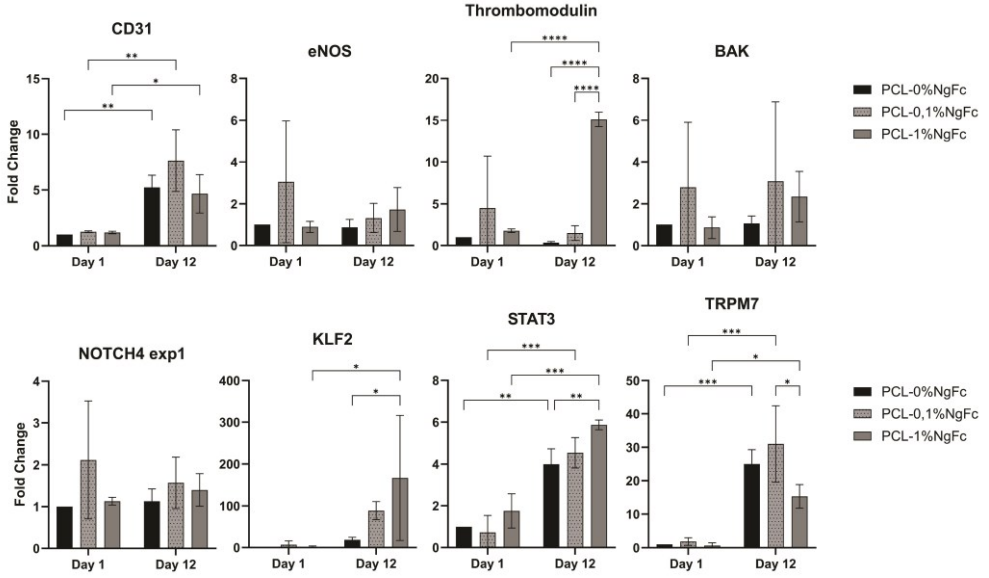

Figure 6.6. Quantitative gene expression analysis of endothelial-related markers in HUVECs cultured on NgFc-loaded electrospun PCL scaffolds. Relative mRNA expression levels of CD31, eNOS, Thrombomodulin, BAK, NOTCH4, KLF2, STAT3, and TRPM7 were quantified by qPCR after 1 and 12 days of culture on electrospun PCL scaffolds containing 0% (control), 0.1%, or 1% NgFc.

Platelet adhesion

Scanning electron microscopy revealed stark differences in platelet attachment (Figure 6.7C). The PCL control surface was densely covered with adherent, activated platelets, whereas NgFc-containing scaffolds showed dramatically fewer platelets. In the 0.1% NgFc group, a moderate reduction was visible; in the 1% NgFc group the surface was essentially free of adhered platelets. These results demonstrate that NgFc strongly inhibits platelet attachment to the scaffold.

Coagulation cascade interference

Despite the dramatic antiplatelet effect, NgFc had no detectable impact on plasma coagulation. Activated partial thromboplastin time (aPTT) and prothrombin time (PT) were essentially identical for all scaffold groups. In particular, no prolongation of aPTT or PT was seen in the NgFc-PCL groups compared to PCL (Figures 6.8 A and B); all values remained within normal human plasma range. This indicates that NgFc incorporation did not appreciably alter clotting factor activity under our assay conditions.

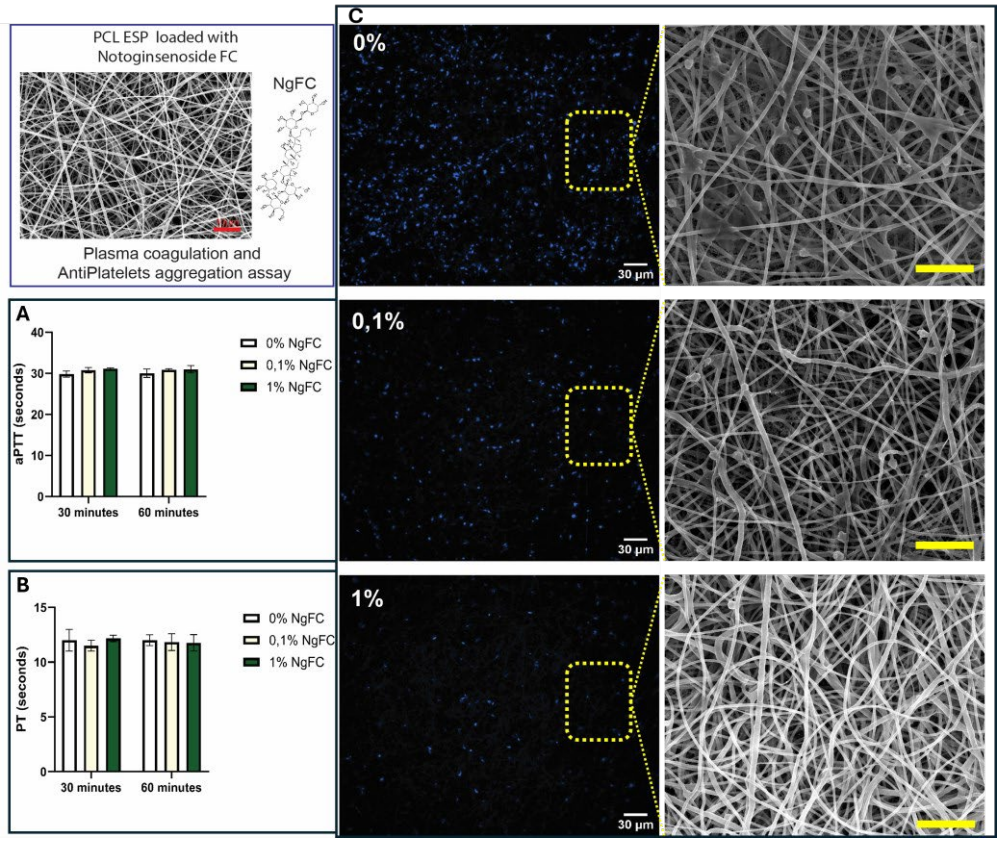

Figure 6.7. Anticoagulation and Platelet Adhesion Analysis **A)** Activated partial thromboplastin time (aPTT) of plasma incubated on scaffold surfaces. **B)** Prothrombin time (PT) of plasma incubated on scaffold surfaces. **C)** Representative images of platelet adhesion on PCL scaffolds containing, 0.1%, or 1% NgFc: Phalloidin-stained platelets (Blue; 60× magnification; scale bar: 30 µm) and SEM micrographs (2,000× magnification; scale bar: 10 µm).

Discussion

In this study, we demonstrate that the incorporation of NgFc into electrospun PCL scaffolds generates a dual-function vascular graft that simultaneously promotes rapid endothelialization and significantly reduces platelet adhesion. Prior to incorporation into scaffolds, the cytotoxicity profile of NgFc was evaluated in 2D HUVEC cultures. Across a wide range of concentrations (up to 1200 µM),

The negligible cytotoxicity of NgFc up to ~800 μM suggests a broad safety margin for scaffold-based delivery. NgFc did not induce significant cytotoxic effects at either 24 or 72 hours, as evidenced by maintained metabolic activity and low levels of cell death. Endothelial cells remained well-spread and confluent, indicating that NgFc is well tolerated and suitable for biofunctionalization of vascular scaffolds. The early burst release of NgFc from the hydrophobic PCL matrix ensures immediate availability at the graft surface, yielding a high local concentration capable of triggering rapid biological responses [26–29]. This burst release is a well-documented phenomenon in PCL systems, driven by the polymer's hydrophobicity and nanofiber porosity, and has been leveraged in various biomedical applications, including vascular grafts and wound dressings [29–33]. In this system, NgFc is rapidly liberated upon implantation, generating high local concentrations at the graft surface. Crucially, our viability data imply that these initial burst concentrations will remain within the non-toxic range for endothelial cells, providing a potent stimulatory pulse without harming the nascent endothelium. Remarkably, NgFc-loaded grafts supported the rapid formation of an endothelial monolayer, with HUVECs reaching confluence in a significantly shorter timeframe compared to bare PCL controls. This finding is consistent with prior reports that NgFc enhances endothelial repair. For example, Liu et al. found that NgFc treatment accelerated reendothelialization after arterial injury in diabetic rats [19]. In their system, NgFc restored autophagy and thereby increased endothelial proliferation and migration under diabetic stress [19]. Our *in vitro* results are consistent with these reports: NgFc markedly boosted early HUVECs attachment and morphology organization on PCL electrospuns scaffolds, suggesting that the drug is bioactive *in situ* and can drive quick formation of an endothelial monolayer. Moreover, HUVECs cultured on NgFc embedded scaffolds showed a pronounced expression of VE-cad indicating stronger formation of intercellular junctions. Increased VE-cadherin suggests a more mature, confluent endothelial barrier on the graft lumen.

Endothelial gene expression analysis revealed a clear time-dependent maturation of HUVECs on all PCL-NgFc scaffolds, as evidenced by the upregulation of TRPM7, STAT3, and CD31 at day 12 compared to day 1. The strong induction of CD31 (8-fold) underscores the establishment of endothelial junctions and functional identity during prolonged culture. Interestingly, NgFc concentration selectively influenced certain regulatory genes: KLF2 was induced only in 0.1% and 1% scaffolds at day 12, while Thrombomodulin

expression was exclusive to the 1% condition, suggesting that higher NgFc content may promote an anti-inflammatory and anticoagulant endothelial phenotype. In contrast, Notch4 expression remained stable across conditions and timepoints, indicating its role as a constitutive endothelial marker rather than a dynamic regulator under these conditions. The uniform STAT3 upregulation across all scaffolds implies a general activation of pro-survival and angiogenic signaling during culture, independent of NgFc concentration. Collectively, these findings suggest that while temporal factors drive the baseline endothelial maturation, scaffold composition—particularly higher NgFc content—can further enhance protective and homeostatic endothelial pathways, which may be advantageous for vascular tissue engineering applications. Critically, NgFc endowed the scaffolds with pronounced antiplatelet activity. The dose-dependent reduction in platelet adhesion on PCL-NgFc versus bare PCL might indicate that NgFc actively prevents platelet-surface interactions. This is in line with the known antiplatelet mechanism of NgFc: Yingqiu Liu et al. reported that NgFc strongly inhibited thrombin-, collagen- and ADP-induced platelet aggregation by suppressing the PLCγ_2 signaling cascade [18]. *In vivo*, NgFc treatment significantly reduced arterial thrombosis in a rat model [18]. Our adhesion assay extends these findings to the context of a biomaterial interface, showing that passive contact with NgFc-loaded fibers is sufficient to impair platelet attachment. Importantly, the lack of change in aPTT and PT indicates that NgFc does not act as a heparin-like anticoagulant in plasma. Instead, NgFc's effect is platelet specific. This differs from heparin coatings, which prolong clotting times but may not fully eliminate platelet binding. Here, NgFc provided antithrombogenicity without altering coagulation assays, suggesting a lower risk of systemic anticoagulation side effects.

Taken together, these results highlight the value of NgFc as a dual-function graft additive. NgFc, a small bioactive saponin appears to simultaneously create a more pro-healing surface for ECs and a less thrombogenic surface for platelets. In practice, a small-diameter vascular graft that can rapidly attract endothelial cells while discouraging clot formation would greatly improve patency.

In the literature, several strategies have demonstrated the potential of rapid drug delivery systems to improve TEVG performance. Matsuzaki et al. reported that heparin-embedded arterial grafts, despite releasing most of the heparin within 24 hours, significantly improved vessel patency by preventing early arterial occlusion [34]. Similarly, small peptides have been incorporated

into electrospun PCL grafts to enhance hemocompatibility and promote vascular regeneration. Other bioactive release strategies have focused on nitric oxide (NO) due to its central role in vascular homeostasis, NO is a key endothelium-derived mediator that suppresses platelet activation, inhibits smooth muscle cell proliferation, and promotes endothelial repair [35–38]. Recent advances have demonstrated that combining NO release with antifouling surface chemistries can closely mimic the native antithrombotic phenotype. Releasing membranes functionalized with polycarboxybetaine (pCB) coatings synergistically reduced platelet adhesion and fibrinogen adsorption, achieving antithrombotic protection far superior to either modality alone [39]. This multimodal strategy highlights the potential of NO-releasing approaches to accelerate endothelialization while simultaneously minimizing thrombogenicity. Moreover, Li et al. developed NO-generating PCL/S-nitrosated keratin scaffolds that supported rapid endothelialization, inhibited smooth muscle cell proliferation, and formed a confluent endothelial monolayer within one month post-implantation, owing to the controlled NO release that improved blood compatibility and increased CD31 expression [40]. Compared with these systems, NgFc offers a distinct mechanism of action, selectively targeting platelet PLCγ_2 signaling while avoiding systemic anticoagulation. Together, these complementary approaches illustrate the broader design space for hemocompatible vascular grafts, where endothelial-mimetic strategies such as NO release and targeted small-molecule delivery (NgFc) may be used alone or in combination to optimize both thromboresistance and endothelial integration. Other multifunctional approaches have also shown promise: Fan et al. combined heparin, the endothelial cell-capturing peptide LXW-7, and carbon monoxide (CO) nanogenerators into acellular blood vessels, achieving rapid endothelialization within 14 days, reduced neointimal hyperplasia, and long-term patency through anti-inflammatory and anti-thrombogenic effects [41]. In this context, our study provides proof of concept for the use of NgFc to enhance hemocompatibility and anti-thrombogenicity of electrospun vascular grafts. Future work will focus on tuning NgFc release through polymer blends and combining it with well-established agents like heparin [6,42,43] or fucosylated chondroitin sulfate [13] to further optimize graft performance.

Conclusion

Electrospun PCL scaffolds incorporating NgFc molecules significantly enhance endothelial cell coverage and maturation while markedly suppressing

platelet adhesion. These findings support the notion that NgFc confers dual bioactivity to vascular grafts: i) accelerating reendothelialization as previously shown *in vivo* [19]; and ii) inhibiting thrombosis consistent with known antiplatelet pathways [17,18]. The data justify further development of Fc-loaded grafts for small-caliber vessel replacement, where rapid healing and antithrombogenicity are both required for success.

Supporting Information

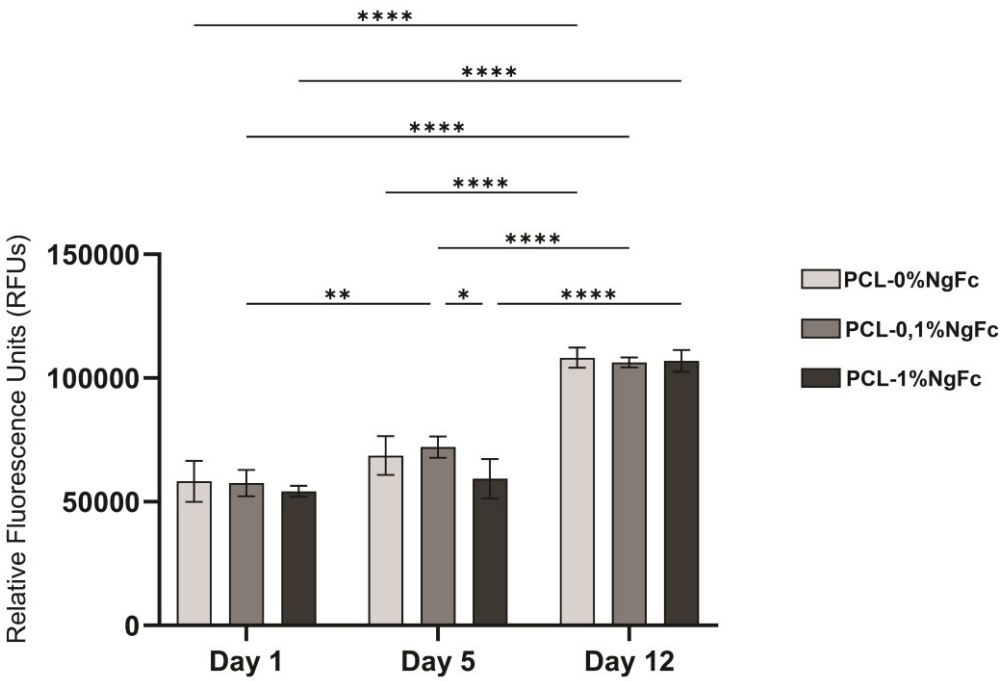

Figure S6.1. Metabolic activity of HUVECs cultured on the scaffolds. HUVECs were seeded on naked electrospun PCL scaffolds (Controls) and scaffolds containing 0.1%, or 1% NgFc, and metabolic activity was assessed at Day 1, Day 5, and Day 12 of culture.

References

[1] A. Fayon, P. Menu, R. El Omar, Cellularized small-caliber tissue-engineered vascular grafts: looking for the ultimate gold standard, NPJ Regen Med 6 (2021). https://doi.org/10.1038/s41536-021-00155-x.

[2] B. Sivaraman, R.A. Latour, The relationship between platelet adhesion on surfaces and the structure versus the amount of adsorbed fibrinogen, Biomaterials 31 (2010) 832–839. https://doi.org/10.1016/j.biomaterials.2009.10.008.

[3] S.N. Rodrigues, I.C. Gonçalves, M.C.L. Martins, M.A. Barbosa, B.D. Ratner, Fibrinogen adsorption, platelet adhesion and activation on mixed hydroxyl-/methyl-terminated self-assembled monolayers, Biomaterials 27 (2006) 5357–5367. https://doi.org/10.1016/j.biomaterials.2006.06.010.

[4] Y. Zhuang, C. Zhang, M. Cheng, J. Huang, Q. Liu, G. Yuan, K. Lin, H. Yu, Challenges and strategies for in situ endothelialization and long-term lumen patency of vascular grafts, Bioact Mater 6 (2021) 1791–1809. https://doi.org/10.1016/j.bioactmat.2020.11.028.

[5] J.L. Chen, Q.L. Li, J.Y. Chen, C. Chen, N. Huang, Improving blood-compatibility of titanium by coating collagen-heparin multilayers, Appl Surf Sci 255 (2009) 6894–6900. https://doi.org/10.1016/j.apsusc.2009.03.011.

[6] S. Aslani, M. Kabiri, S. HosseinZadeh, H. Hanaee-Ahvaz, E.S. Taherzadeh, M. Soleimani, The applications of heparin in vascular tissue engineering, Microvasc Res 131 (2020). https://doi.org/10.1016/j.mvr.2020.104027.

[7] C. Nie, L. Ma, C. Cheng, J. Deng, C. Zhao, Nanofibrous Heparin and Heparin-Mimicking Multilayers as Highly Effective Endothelialization and Antithrombogenic Coatings, Biomacromolecules 16 (2015) 992–1001. https://doi.org/10.1021/bm501882b.

[8] T. Liu, Y. Liu, Y. Chen, S. Liu, M.F. Maitz, X. Wang, K. Zhang, J. Wang, Y. Wang, J. Chen, N. Huang, Immobilization of heparin/poly-L-lysine nanoparticles on dopamine-coated surface to create a heparin density gradient for selective direction of platelet and vascular cells behavior, Acta Biomater 10 (2014) 1940–1954. https://doi.org/10.1016/j.actbio.2013.12.013.

[9] S.E. Sakiyama-Elbert, Incorporation of heparin into biomaterials, Acta Biomater 10 (2014) 1581–1587. https://doi.org/10.1016/j.actbio.2013.08.045.

[10] K. Tardalkar, T. Marsale, N. Bhamare, J. Kshersagar, L. Chaudhari, M.G. Joshi, Heparin Immobilization of Tissue Engineered Xenogeneic Small Diameter Arterial Scaffold Improve Endothelialization, Tissue Eng Regen Med 19 (2022) 505–523. https://doi.org/10.1007/s13770-021-00411-7.

[11] A.C. Gilotti, W. Nimlamool, R. Pugh, J.B. Slee, T.C. Barthol, E.A. Miller, L.J. Lowe-Krentz, Heparin responses in vascular smooth muscle cells involve cGMP-dependent protein kinase (PKG), J Cell Physiol 229 (2014) 2142–2152. https://doi.org/10.1002/jcp.24677.

[12] S.Y. Zhou, L. Li, E. Xie, M.X. Li, J.H. Cao, X. Bin Yang, D.Y. Wu, Small-diameter PCL/PU vascular graft modified with heparin-aspirin compound for preventing the occurrence of acute thrombosis, Int J Biol Macromol 249 (2023). https://doi.org/10.1016/j.ijbiomac.2023.126058.

[13] G. Obino, G. Nieddu, M. Nagy, H. Ippel, T. Cubeddu, H.M.H. Spronk, T.M. Hackeng, M. Formato, A.J. Lepedda, L. Moroni, Marine-derived sulfated polysaccharides enhance hemocompatibility and endothelialization of nanofibrous PCL for vascular graft applications, Cell Biomaterials (2025) 100155. https://doi.org/10.1016/j.celbio.2025.100155.

[14] L.J. Ma, F. Liu, Z.F. Zhong, J.B. Wan, Comparative study on chemical components and anti-inflammatory effects of Panax notoginseng flower extracted by water and methanol, J Sep Sci 40 (2017) 4730–4739. https://doi.org/10.1002/jssc.201700641.

[15] Z. Ju, J. Li, H. Han, L. Yang, Z. Wang, Analysis of bioactive components and multi-component pharmacokinetics of saponins from the leaves of Panax notoginseng in rat plasma after oral administration by LC–MS/MS, J Sep Sci 41 (2018) 1512–1523. https://doi.org/10.1002/jssc.201701042.

[16] H.-S. Jang, H. Jaeschke, B. Jiao, H. Chen, Y. Xu, D. Gui, fmed Copyright, M. Wei, Y. Gao, D. Cheng, H. Zhang, W. Zhang, Y. Shen, Q. Huang, X. An, B. Wang, Z. Yu, N. Wang, Notoginsenoside Fc ameliorates renal tubular injury and mitochondrial damage in acetaminophen-induced acute kidney injury partly by regulating SIRTT/SODD pathway, Frontiers in medicine, *9*, 1055252. (2023) https://doi.org/10.3389/fmed.2022.1055252.

[17] C. He, J. Li, N. Xu, R. Wang, Z. Li, L. Yang, Z. Wang, Pharmacokinetics, bioavailability, and metabolism of Notoginsenoside Fc in rats by liquid chromatography/electrospray ionization tandem mass spectrometry, J Pharm Biomed Anal 109 (2015) 150–157. https://doi.org/10.1016/j.jpba.2015.02.038.

[18] Y. Liu, T. Liu, K. Ding, Z. Liu, Y. Li, T. He, W. Zhang, Y. Fan, W. Ma, L. Cui, X. Song, Phospholipase Cγ2 signaling cascade contribute to the antiplatelet effect of notoginsenoside Fc, Front Pharmacol 9 (2018). https://doi.org/10.3389/fphar.2018.01293.

[19] J. Liu, C. Jiang, X. Ma, L. Feng, J. Wang, Z. Peng, Notoginsenoside Fc Accelerates Reendothelialization following Vascular Injury in Diabetic Rats by Promoting Endothelial Cell Autophagy, J Diabetes Res 2019 (2019). https://doi.org/10.1155/2019/9696521.

[20] Y. Pan, X. Zhou, Y. Wei, Q. Zhang, T. Wang, M. Zhu, W. Li, R. Huang, R. Liu, J. Chen, G. Fan, K. Wang, D. Kong, Q. Zhao, Small-diameter hybrid vascular grafts composed of polycaprolactone and polydioxanone fibers, Sci Rep 7 (2017). https://doi.org/10.1038/s41598-017-03851-1.

[21] A. Hasan, A. Memic, N. Annabi, M. Hossain, A. Paul, M.R. Dokmeci, F. Dehghani, A. Khademhosseini, Electrospun scaffolds for tissue engineering of vascular grafts, Acta Biomater 10 (2014) 11–25. https://doi.org/10.1016/j.actbio.2013.08.022.

[22] S. Ozdemir, I. Yalcin-Enis, B. Yalcinkaya, F. Yalcinkaya, An Investigation of the Constructional Design Components Affecting the Mechanical Response and Cellular Activity of Electrospun Vascular Grafts, Membranes (Basel) 12 (2022). https://doi.org/10.3390/membranes12100929.

[23] J.J. Devan Ohst, Development of Novel, Bioresorbable, Small-Diameter Electrospun Vascular Grafts, J Tissue Sci Eng 06 (2015). https://doi.org/10.4172/2157-7552.1000151.

[24] C. He, J. Li, N. Xu, R. Wang, Z. Li, L. Yang, Z. Wang, Pharmacokinetics, bioavailability, and metabolism of Notoginsenoside Fc in rats by liquid chromatography/electrospray ionization tandem mass spectrometry, J Pharm Biomed Anal 109 (2015) 150–157. https://doi.org/10.1016/j.jpba.2015.02.038.

[25] Z. Dai, J. Ronholm, Y. Tian, B. Sethi, X. Cao, Sterilization techniques for biodegradable scaffolds in tissue engineering applications, J Tissue Eng 7 (2016). https://doi.org/10.1177/2041731416648810.

[26] Y. Jiang, Y. Guo, H. Wang, X. Wang, Q. Li, Hydrogel coating based on dopamine-modified hyaluronic acid and gelatin with spatiotemporal drug release capacity for quick endothelialization and long-term anticoagulation, Int J Biol Macromol 230 (2023). https://doi.org/10.1016/j.ijbiomac.2022.123113.

[27] Y. Wang, B. Ma, A. Yin, B. Zhang, R. Luo, J. Pan, Y. Wang, Polycaprolactone vascular graft with epigallocatechin gallate embedded sandwiched layer-by-layer functionalization for enhanced antithrombogenicity and anti-inflammation, Journal of Controlled Release 320 (2020) 226–238. https://doi.org/10.1016/j.jconrel.2020.01.043.
[28] D. Wang, X. Wang, Z. Zhang, L. Wang, X. Li, Y. Xu, C. Ren, Q. Li, L.S. Turng, Programmed Release of Multimodal, Cross-Linked Vascular Endothelial Growth Factor and Heparin Layers on Electrospun Polycaprolactone Vascular Grafts, ACS Appl Mater Interfaces 11 (2019) 32533–32542. https://doi.org/10.1021/acsami.9b10621.
[29] I. Sebe, P. Szabó, B. Kállai-Szabó, R. Zelkó, Incorporating small molecules or biologics into nanofibers for optimized drug release: A review, Int J Pharm 494 (2015) 516–530. https://doi.org/10.1016/j.ijpharm.2015.08.054.
[30] D.C. Ardila, E. Tamimi, T. Doetschman, W.R. Wagner, J.P. Vande Geest, Modulating smooth muscle cell response by the release of TGFβ2 from tubular scaffolds for vascular tissue engineering, Journal of Controlled Release 299 (2019) 44–52. https://doi.org/10.1016/j.jconrel.2019.02.024.
[31] M. Ghazalian, S. Afshar, A. Rostami, S. Rashedi, S.H. Bahrami, Fabrication and characterization of chitosan-polycaprolactone core-shell nanofibers containing tetracycline hydrochloride, Colloids Surf A Physicochem Eng Asp 636 (2022). https://doi.org/10.1016/j.colsurfa.2021.128163.
[32] S. Chan Park, M.J. Kim, K. Choi, J. Kim, S.O. Choi, Influence of shell compositions of solution blown PVP/PCL core-shell fibers on drug release and cell growth, RSC Adv 8 (2018) 32470–32480. https://doi.org/10.1039/c8ra05485a.
[33] T. Abudula, K. Gauthaman, A. Mostafavi, A. Alshahrie, N. Salah, P. Morganti, A. Chianese, A. Tamayol, A. Memic, Sustainable drug release from polycaprolactone coated chitin-lignin gel fibrous scaffolds, Sci Rep 10 (2020). https://doi.org/10.1038/s41598-020-76971-w.
[34] J. Li, N. Zhuo, J. Zhang, Q. Sun, J. Si, K. Wang, D. Zhi, The loading of C-type natriuretic peptides improved hemocompatibility and vascular regeneration of electrospun poly(ε-caprolactone) grafts, Acta Biomater 151 (2022) 304–316. https://doi.org/10.1016/j.actbio.2022.08.032.
[35] Z. Yang, Y. Yang, K. Xiong, X. Li, P. Qi, Q. Tu, F. Jing, Y. Weng, J. Wang, N. Huang, Nitric oxide producing coating mimicking endothelium function for multifunctional vascular stents, Biomaterials 63 (2015) 80–92. https://doi.org/10.1016/j.biomaterials.2015.06.016.
[36] K.A. Amoako, C. Archangeli, H. Handa, T. Major, M.E. Meyerhoff, G.M. Annich, R.H. Bartlett, Thromboresistance characterization of extruded nitric oxide-releasing silicone catheters, ASAIO Journal 58 (2012) 238–246. https://doi.org/10.1097/MAT.0b013e31824abed5.
[37] T.C. Major, D.O. Brant, C.P. Burney, K.A. Amoako, G.M. Annich, M.E. Meyerhoff, H. Handa, R.H. Bartlett, The hemocompatibility of a nitric oxide generating polymer that catalyzes S-nitrosothiol decomposition in an extracorporeal circulation model, Biomaterials 32 (2011) 5957–5969. https://doi.org/10.1016/j.biomaterials.2011.03.036.
[38] H. Zhang, G.M. Annich, J. Miskulin, K. Osterholzer, S.I. Merz, R.H. Bartlett, M.E. Meyerhoff, Nitric oxide releasing silicone rubbers with improved blood compatibility: preparation, characterization, and in vivo evaluation, 2002.
[39] K.A. Amoako, H.S. Sundaram, A. Suhaib, S. Jiang, K.E. Cook, Multimodal, Biomaterial-Focused Anticoagulation via Superlow Fouling Zwitterionic Functional Groups Coupled with

Anti-Platelet Nitric Oxide Release, Adv Mater Interfaces 3 (2016). https://doi.org/10.1002/admi.201500646.

[40] P. Li, D. Jin, J. Dou, L. Wang, Y. Wang, X. Jin, X. Han, I.K. Kang, J. Yuan, J. Shen, M. Yin, Nitric oxide-releasing poly(ε-caprolactone)/S-nitrosylated keratin biocomposite scaffolds for potential small-diameter vascular grafts, Int J Biol Macromol 189 (2021) 516–527. https://doi.org/10.1016/j.ijbiomac.2021.08.147.

[41] Y. Fan, J. Pei, Y. Qin, H. Du, X. Qu, W. Li, B. Huang, J. Tan, Y. Liu, G. Li, M. Ke, Y. Xu, C. Zhu, Construction of tissue-engineered vascular grafts with enhanced patency by integrating heparin, cell-adhesive peptide, and carbon monoxide nanogenerators into acellular blood vessels, Bioact Mater 34 (2024) 221–236. https://doi.org/10.1016/j.bioactmat.2023.12.015.

[42] M. Zhang, C.H.H. Chan, J.P. Pauls, C. Semenzin, C. Ainola, H. Peng, C. Fu, A.K. Whittaker, J.F. Fraser, Investigation of Heparin-loaded Poly(ethylene glycol)-based Hydrogels as Anti-thrombogenic Surface Coatings for Extracorporeal Membrane Oxygenation, Journal of Materials Chemistry B (2022) https://doi.org/10.1039/D2TB00379A.

[43] J.M.M. Heyligers, H.J.M. Verhagen, J.I. Rotmans, C. Weeterings, P.G. De Groot, F.L. Moll, T. Lisman, Heparin immobilization reduces thrombogenicity of small-caliber expanded polytetrafluoroethylene grafts, J Vasc Surg 43 (2006) 587–591. https://doi.org/10.1016/j.jvs.2005.10.038.

Chapter 7
General Discussion

This chapter reflects on the scientific and translational implications of this work, discussing how the research evolved from the exploration of natural bioactive molecules to their integration into bioresorbable, bioactive scaffolds, concluding in the design of biomimetic architectures that replicate the structural and functional complexity of native blood vessels.

Introduction

The development of functional substitutes for small-caliber blood vessels remains one of the most pressing challenges in cardiovascular tissue engineering. Despite decades of research (figure 7.1), the clinical translation of artificial vascular grafts has been limited by thrombosis, intimal hyperplasia, inadequate compliance, and the difficulty of achieving rapid and stable endothelialization, not to mention the distinct requirements of different vessels within the human body.

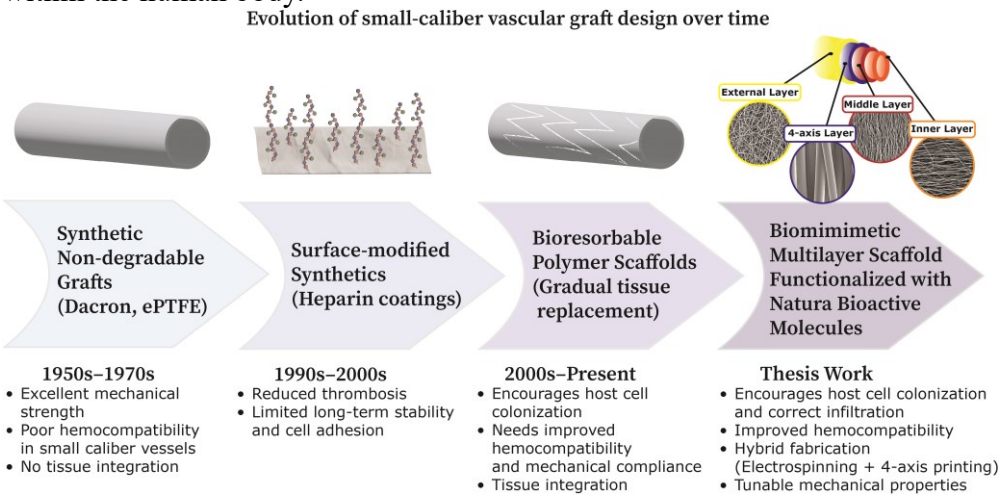

Figure 7.1. Evolution of small-caliber vascular graft design over time. Schematic overview illustrating the progressive evolution of vascular graft technologies from early synthetic non-degradable materials toward advanced biomimetic multilayer scaffolds.

Vascular Grafts: Current Clinical Options and Limitations

The clinically available synthetic vascular grafts on the market are predominantly non-biodegradable and highly stable polymers, engineered to minimize blood protein adsorption and platelet adhesion while maintaining adequate blood perfusion to replace defective native vessels. Among these materials, polyethylene terephthalate (PET, commercially known as Dacron) and expanded polytetrafluoroethylene (ePTFE, GORE-TEX®) represent the most widely used synthetic grafts in vascular surgery [1].

Dacron was first introduced into the clinical field in the 1950s, following its experimental application by Michael E. DeBakey in 1954, and the subsequent development of knitted Dacron grafts in 1957 [2,3]. In contrast, ePTFE was discovered later, in 1969, by Robert W. Gore, and its first vascular graft was commercially released in 1975 [4,5]. These materials marked a major technological advance in the history of vascular surgery, providing strong, infection-resistant, and easily manufactured conduits capable of withstanding systemic arterial pressures and long-term implantation.

Their clinical success has been particularly evident in large-caliber vessels, such as the aorta, where high blood flow velocities limit the interaction between blood components and the graft surface, thus reducing the likelihood of thrombosis [6,7]. However, their performance dramatically declines in small-diameter applications (below 6 mm), where slower hemodynamics and longer residence times of blood elements promote protein adsorption, platelet adhesion, and thrombus formation, often culminating in graft occlusion [8].

Although these polymers were originally designed to reduce nonspecific protein adsorption, they cannot achieve a truly non-fouling surface. Their partial protein and cell adhesion is not sufficient to support the formation of a continuous and protective endothelial layer, yet it is enough to trigger undesirable biological reactions, such as smooth muscle cell proliferation and neointimal hyperplasia [9,10]. Thus, neither Dacron nor ePTFE can be considered ideal materials: their surfaces are neither completely inert nor biologically instructive. On one hand, an ideal non-fouling material should entirely prevent nonspecific protein adsorption, platelet adhesion, and pathological cell proliferation. On the other, an ideal bioactive and biodegradable material should promote selective protein adsorption and support a controlled sequence of cellular events, such as endothelialization, smooth muscle cell organization, and extracellular matrix deposition, leading to the regeneration of a functional vascular wall. Dacron and ePTFE fail to meet either of these paradigms for small caliber vessels, providing neither a truly complete passive nor a regenerative interface.

For this reason, significant research has been devoted to surface modification strategies aimed at improving the hemocompatibility of these polymers. Various approaches have been explored, including heparin immobilization [11], PEGylation [12], endothelial cell seeding, and bioactive coatings, all with the goal of imparting non-fouling or pro-endothelial properties [13,14]. More recent studies have demonstrated that zwitterionic polymers, polyethylene glycol (PEG), and poly(2-oxazoline) coatings exhibit remarkable resistance to

nonspecific adsorption of proteins and cells, representing one of the most promising classes of non-fouling surface technologies [15,16].
In parallel, attention has increasingly shifted toward the development of bioresorbable materials, capable of combining mechanical integrity with biological integration. Unlike inert polymers, these materials should allow controlled protein adsorption, possibly without protein denaturation, thereby guiding cell adhesion, proliferation, and extracellular matrix (ECM) deposition. Such grafts are designed to provide temporary mechanical support during tissue regeneration and then gradually degrade, being ultimately replaced by newly synthesized native ECM [17].
It is precisely this second, tissue regenerative approach that forms the foundation of the research presented in this thesis. The work focuses on the development of bioresorbable vascular grafts functionalized with natural bioactive molecules to promote physiological vascular remodeling. Specifically, this study introduces novel biofunctionalization strategies based on marine sulfated polysaccharides (MSPs) and Notoginsenoside Fc (NgFc), integrating them into advanced, tunable scaffold architectures that combine electrospinning and 4-axis 3D printing. These complementary fabrication techniques provide both mechanical stability and structural precision, enabling controlled porosity for smooth muscle cell infiltration and fiber alignment for proper endothelial orientation. Altogether, this integrated design aims to achieve a functional, biomimetic, and fully resorbable vascular graft, capable of guiding host tissue regeneration while ensuring hemodynamic stability and long-term compatibility.

Engineering the Luminal Surface to Enhance Hemocompatibility and Endothelialization of Tissue-Engineered Vascular Grafts (TEVGs)

The hemocompatibility of the luminal surface is the single most critical factor determining TEVGs success, as nonspecific protein adsorption and denaturation, followed by platelet adhesion and thrombus formation, can ultimately lead to rapid occlusion. While heparin coatings have long been considered the gold standard for improving hemocompatibility, they have never provided a fully effective solution for small-caliber vessel grafts. Moreover, their clinical use presents several drawbacks, including limited stability [18], potential immunogenicity, and the risk of uncontrolled

anticoagulant release possibly leading to heparin-induced thrombocytopenia [18,19].

In this context, marine sulfated polysaccharides (MSPs) have emerged as a promising alternative to heparin. As explored in **Chapter 2**, MSPs are structurally diverse, highly sulfated glycans that mimic key features of the native endothelial glycocalyx. These molecules can interact with coagulation factors, modulate inflammation, and promote endothelial regeneration. **Chapter 2** summarizes current knowledge on MSP structure–function relationships, anticoagulant mechanisms, and endothelial support, highlighting strategies for their functionalization onto electrospun and 3D-printed scaffolds. In addition, it reviews *in vitro* and *in vivo* evidence supporting their potential and discusses current challenges and future directions for clinical translation. Collectively, these insights establish MSPs as versatile and underexplored biomolecules capable of overcoming persistent barriers in vascular tissue engineering.

In **Chapter 3**, we specifically purified MSPs from two marine organisms: *Holothuria tubulosa* and *Sarcotragus spinosulus*. *H. tubulosa* is a well-characterized source of MSPs, extensively studied in the literature for its anticoagulant and pro-regenerative properties. In contrast, *S. spinosulus* represents a previously unexplored species, offering a potentially unique structural repertoire of sulfated polysaccharides that may provide distinct bioactive functions. Two anticoagulant MSPs from this study were selected and subsequently applied in **Chapter 4** for the functionalization of electrospun PCL scaffolds, where they produced a substantial enhancement in hemocompatibility and endothelialization compared to scaffolds functionalized with unfractionated heparin. Importantly, *S. spinosulus* MSPs may introduce novel molecular motifs capable of modulating coagulation and vascular cell behavior in ways not previously observed with conventional MSP sources. Despite these promising outcomes, the precise molecular structures of these MSPs remain incompletely characterized, and further studies are required to fully elucidate their structural features and bioactive mechanisms before a possible clinical use. The results presented in this thesis demonstrate that MSPs can effectively serve to engineer the luminal interface between the material and blood components, representing a promising alternative to heparin.

Like heparin, MSPs possess anticoagulant activity, a high negative charge density, and structural similarity to glycosaminoglycans, which reduces nonspecific protein adsorption and denaturation caused by hydrophobic

interactions, enabling them to bind and stabilize key angiogenic growth factors such as VEGF and FGF-2 [20–22]. Importantly, MSP-functionalized scaffolds not only reduced platelet adhesion but also promoted rapid and complete endothelialization within a few days, thereby contributing to thrombosis prevention. Compared to heparin-functionalized scaffolds, MSPs showed superior support for endothelial cell growth and stability showing a more effective antithrombotic profile. These dual benefits are highly desirable as long-term graft patency.

Mechanical Performance and Scaffold Design

Beyond hemocompatibility, the mechanical and structural design of TEVGs is fundamental for their successful clinical translation. Scaffolds must withstand arterial pressures, exhibit sufficient burst strength, match the compliance of the native vessel to avoid flow disturbances and intimal hyperplasia, and possess adequate porosity to allow effective infiltration and colonization by vascular cells without compromising structural integrity or causing fluid leakage.

In **Chapter 5**, we designed a biomimetic scaffold architecture aimed at addressing the major requirements for TEVGs, utilizing the same PCL functionalized with MSPs that had demonstrated promising hemocompatibility and endothelialization in **Chapter 4**. Electrospinning and 4-axis printing were combined to produce multilayered scaffolds with tunable architecture and mechanical properties. This hybrid strategy enabled the integration of distinct functionalities within a single graft: a hemocompatible, leak-free inner layer promoting endothelialization; two middle layers designed to support smooth muscle cell infiltration, extracellular matrix deposition, and mechanical resilience; and an external layer mimicking the tunica adventitia, providing structural support and protection.

The multilayer construct developed in this work exhibited mechanical integrity compatible with small-caliber vessel applications. More importantly, their design allowed precise tuning of scaffold mechanical properties, enabling adaptation to the specific requirements of different vascular environments, ranging from veins to arteries.

In the literature, there is an extensive variety of electrospun TEVGs, fabricated from polymers such as PCL, biodegradable polyurethanes, natural polymers like decellularized ECM, or blends of these and other materials [23,24]. However, electrospinning alone often cannot satisfy all the functional and mechanical requirements of small-caliber vascular grafts. Purely electrospun scaffolds can be difficult to handle; when bent, they may not fully recover their

tubular shape, potentially leading to structural collapse. Moreover, the dense fiber structure typical of electrospun scaffolds can impede immediate cell infiltration, which may only occur as the polymer degrades. This delayed colonization is problematic, as it can increase the risk of aneurysm or early graft failure if the newly synthesized ECM is not established in time to provide mechanical support.

On the other hand, 4-axis printing has been shown to produce scaffolds with excellent handling and mechanical robustness, yet the resulting high porosity often requires pre-seeding of smooth muscle and endothelial cells, followed by prolonged *in vitro* culture, before transplantation is feasible [25,26].

By combining electrospinning and 4-axis printing, we were able to integrate the advantages of both techniques while minimizing their respective limitations. This hybrid strategy produced scaffolds with graded porosity across layers, enabling leak-free constructs, rapid formation of a confluent endothelial monolayer within a few days, and proper smooth muscle cell infiltration into the medial layer.

The growing interest in multilayered TEVGs reflects the need to better mimic native vessel architecture, reproducing the intima, media, and adventitia with appropriate fiber orientation, density, and functionality. Existing examples in the literature often rely on complex geometrical setups and coatings such as fibrin or ECM-derived materials to enhance cell compatibility [27–29]. However, these coatings can inadvertently promote platelet adhesion and are prone to rapid degradation, leading to partial or complete detachment of cells over time. In contrast, our scaffolds demonstrated robust and rapid endothelialization due to covalently bound MSPs, which provide stable bioactive cues without these drawbacks.

The multilayered architecture not only recapitulated native fiber orientation and porosity but also supported correct endothelial alignment and smooth muscle cell organization within the medial layer. Moreover, the scaffold design successfully reproduced the J-shaped mechanical behavior characteristic of native vessels. The axially aligned nanofiber inner layer provided higher compliance, while the circumferential nanofiber, 4-axis printed microfiber, and outer random-nanofiber layers collectively reinforced hoop strength and prevented delamination, together resulting in a nonlinear J-shaped stress–strain response comparable to that of native arterial tissue [30]. This hierarchical, layered configuration effectively decoupled graft strength from compliance, thereby avoiding the maladaptive stiffness commonly observed in conventional PET and ePTFE grafts [31].

By integrating hybrid fabrication with bioactive functionalization, this work provides a versatile and biomimetic platform that combines hemocompatibility, cellular guidance, and mechanical resilience. Such an approach represents a significant step toward the development of clinically relevant, bioresorbable small-caliber vascular grafts that can seamlessly integrate with host tissue and restore physiological vascular function.

Smooth Muscle Cell Integration and Vascular Remodeling

A common limitation of heparin-functionalized grafts is their inhibitory effect on smooth muscle cell (SMC) proliferation and organization. Heparin is a well-known inhibitor of vascular SMC mitosis, and its antiproliferative effect has been well documented [32]. While this property may be beneficial for preventing intimal hyperplasia, excessive inhibition of SMC activity compromises the development of a functional medial layer, which is essential for maintaining vessel tone and supporting long-term remodeling.

In **Chapter 5**, the results demonstrated that the mid-layer, fabricated using 4-axis printing, supported extensive SMC infiltration across all scaffold variants, reflecting the design's porosity of the medial layer. However, clear morphological differences were observed depending on the surface chemistry. Scaffolds functionalized with heparin showed rounded cells distributed in clusters, with minimal α–smooth muscle actin (α-SMA) organization, whereas SMCs on MSP-functionalized scaffolds remained well-spread, elongated, and aligned along the fibers, with abundant α-SMA stress fibers and multilayered structures resembling contractile SMCs in the native tunica media. These results represent a significant advancement toward achieving long-term patency in TEVGs, as functional layers of contractile SMCs are fundamental for TEVGs.

Only a limited number of studies have examined SMC infiltration and organization within vascular grafts, and further investigation is still needed to understand how to balance SMC colonization to prevent intimal hyperplasia and calcification while ensuring sufficient ECM deposition by the synthetic SMC phenotype. Ideally, in TEVG development, an initial phase of ECM production by synthetic SMCs should be followed by their transition to a contractile phenotype, ultimately leading to the formation of a well-organized and functional tunica media[33].

Research on heparin-functionalized TEVGs has mostly focused on hemocompatibility and endothelialization. However, one of the few studies addressing SMC behavior on heparinized PCL electrospun scaffolds, conducted by Cao et al., showed that heparin surface modification enhanced SMC infiltration compared to unmodified PCL. This was mainly due to increased surface hydrophilicity. Yet, immunofluorescence imaging revealed a clustered localization of SMCs within the scaffold [33], consistent with our findings for heparin-functionalized PCL. In contrast, the MSP-functionalized scaffolds in our study displayed a homogeneous SMC distribution with elongated morphology and well-organized α-SMA fibers, as shown in our immunofluorescence analyses (**Chapter 5**). Collectively, these results further demonstrate that MSP-functionalized scaffolds supported SMC spreading, alignment, and maintenance of a contractile phenotype. By supporting both rapid endothelialization and SMCs medial integration, MSP-based scaffolds move closer to the long-sought goal of TEVG development: the synchronized regeneration of all vascular wall layers.

Natural Bioactive Molecules: Expanding the Toolbox with NgFc

In **Chapter 6** we explored the potential of Notoginsenoside Fc (NgFc) as a novel bioactive molecule for vascular graft functionalization. This class of saponins have been investigated for their anticoagulant and vasoprotective properties [34–36]; however, its application in TEVGs remains virtually unexplored. Proof-of-concept experiments conducted in this work demonstrated that NgFc can be successfully incorporated into electrospun scaffolds and released, producing positive effects on hemocompatibility and endothelialization.

Comparable strategies in the literature have employed other small bioactive molecules to modulate vascular cell behavior and prevent thrombosis. For example, resveratrol, a polyphenolic antioxidant, has been incorporated into vascular graft materials (e.g., electrospun PLCL fibers) to mitigate oxidative stress and inflammation. Zhang *et al.* developed bilayer PCL/PLCL grafts loaded with S-nitrosated keratin (an NO donor) and resveratrol, where the resveratrol-containing layer reduced oxidative damage and inflammation while supporting endothelialization without intimal hyperplasia, thrombosis, or calcification [37]. Similarly, resveratrol-releasing polyurethane (PU) scaffolds exhibited markedly improved hemocompatibility, with prolonged

clotting times, reduced hemolysis, and minimal platelet attachment. These scaffolds facilitated the formation of a confluent endothelial monolayer while suppressing SMC proliferation, providing both antithrombotic protection and rapid endothelial coverage [38].

Other bioactive release strategies have focused on nitric oxide (NO) due to its central role in vascular homeostasis. NO acts as an endothelium-derived mediator that suppresses platelet activation, inhibits SMC proliferation, and promotes endothelial repair [39–42]. Compared with these systems, NgFc offers a distinct mechanism of action, selectively targeting platelet Phospholipase Cγ_2 signaling [36] while avoiding systemic anticoagulation and enhancing endothelial colonization. Although preliminary, these findings open a promising research direction—exploring natural small molecules as complementary bioactive agents alongside polysaccharides and proteins. For instance, combining MSPs with NgFc could yield synergistic effects by coupling the potent anticoagulant activity of sulfated polysaccharides with the vasoprotective and anti-inflammatory properties of saponins. This approach aligns with a growing trend in regenerative medicine: harnessing naturally derived compounds to design multifunctional biomaterials. Moreover, it contributes to the diversification of biofunctionalization strategies, moving beyond traditional mammalian-derived components and drawing inspiration from small molecules obtained from natural sources such as plants or marine organisms.

Limitations, Future Perspectives, and Conclusions

While this thesis significantly advances the field of vascular tissue engineering by demonstrating the successful incorporation of marine sulfated polysaccharides (MSPs) and Notoginsenoside Fc (NgFc) into multilayered bioresorbable scaffolds, several challenges remain before these strategies can be translated into clinical practice. Most experiments were performed under controlled *in vitro* conditions, which cannot fully replicate the complex physiological environment of the human vasculature. *In vivo* validation under dynamic hemodynamic conditions will therefore be essential to confirm the hemocompatibility, endothelialization, remodeling capacity, and long-term functionality of MSP- and NgFc-functionalized grafts. Factors such as immune response, hemodynamic shear stress, and patient-specific comorbidities may critically influence scaffold integration and remodeling, warranting extensive preclinical studies in relevant animal models. A structured, stepwise in vivo validation strategy should therefore be implemented. Initial proof-of-concept

studies could be performed in small animal models, such as rat abdominal aorta or carotid artery interposition models (1.5–2 mm diameter), which enable rapid assessment of acute thrombosis, endothelialization, inflammatory response, and early neotissue formation over 4–12 weeks. These models are particularly suitable for mechanistic evaluation of macrophage polarization, endothelial coverage, and early remodeling processes.

Subsequent validation under clinically relevant hemodynamic conditions would require large animal models, such as rabbit carotid or porcine carotid/coronary artery models (3–6 mm diameter), which more closely resemble human vascular biomechanics and coagulation profiles. Mid- to long-term studies (3–12 months) should assess graft patency, compliance matching, intimal hyperplasia, ECM depositionsmooth muscle cell organization, and scaffold degradation kinetics.

Another important consideration is the synchronization between scaffold degradation and tissue regeneration. Although polycaprolactone (PCL) provides excellent mechanical strength and processability, its slow degradation may impede full tissue replacement and remodeling. Future studies should explore the use of alternative or blended polymers, such as poly(lactic-co-glycolic acid) (PLGA), poly(L-lactic acid) (PLLA), or poly(ester urethanes), to fine-tune degradation kinetics and achieve a resorption rate that more closely matches neotissue formation. Furthermore, the concept of selective or gradient functionalization across scaffold layers presents an exciting opportunity to achieve spatial control over cellular responses: for instance, incorporating antithrombogenic cues on the luminal surface while promoting smooth muscle and extracellular matrix organization within the medial or adventitial regions. This layer-specific approach could be further enhanced by combining multiple bioactive agents, such as MSPs with growth factors or signaling molecules, to create a more physiologically relevant microenvironment that orchestrates cell recruitment, differentiation, and matrix remodeling.

Looking ahead, future work should also focus on developing more physiological dynamic *in vitro* platforms that better replicate physiological flow, pressure, and cyclic strain, such as bioreactors with pulsatile perfusion, possibly integrating immune response studies. Furthermore, the integration of computational modeling and data-driven design could accelerate the optimization of scaffold geometry, porosity, and functionalization gradients to predict long-term mechanical and biological performance.

Another promising direction lies in the exploration of multifunctional bioactive systems. Combining polysaccharides with small molecules such as

NgFc with nitric oxide donors, antioxidant agents (e.g., resveratrol), or anti-inflammatory peptides could yield synergistic effects that balance endothelialization, hemocompatibility, and controlled SMC proliferation.

Finally, from a translational standpoint, scalability and reproducibility represent key challenges. The extraction and standardization of marine polysaccharides must ensure consistent composition, purity, and bioactivity to meet regulatory and manufacturing requirements. Establishing reliable sourcing and quality control protocols will be essential to guarantee the safety and efficacy of these materials for clinical applications. In parallel, advances in additive manufacturing and automated electrospinning/printing systems could facilitate the scalable fabrication of patient-specific grafts, while adherence to Good Manufacturing Practice (GMP) guidelines and early regulatory engagement will be critical for clinical translation.

Despite these limitations, the findings presented in this thesis lay a solid foundation for the development of next-generation, multifunctional vascular grafts. By coupling molecular bioactivity with structural design and controlled degradation, these approaches move closer to realizing small-caliber tissue-engineered vascular grafts that are hemocompatible, mechanically compliant, and capable of orchestrating the synchronized regeneration of all vascular wall layers, bringing the vision of a durable and fully bioresorbable vascular substitute within reach.

References

[1] J. Chlupáč, E. Filová, L. Bačáková, L. Bačáková, Blood Vessel Replacement: 50 years of Development and Tissue Engineering Paradigms in Vascular Surgery, Physiol. Res 58 (2009) 119–139. www.biomed.cas.cz/physiolres.

[2] O.C. JULIAN, Dacron Tube and Bifurcation Arterial Prostheses Produced to Specification, AMA Arch Surg 78 (1959) 260. https://doi.org/10.1001/archsurg.1959.04320020082012.

[3] Md. Anisuzzaman, Michael E. DeBakey: A cardio-vascular surgeon whose innovations revolutionized the treatment of heart and blood vessel, Journal of Thoracic Disease and Cardiothoracic Surgery 2 (2021) 01–04. https://doi.org/10.31579/2693-2156/018.

[4] R. Suy, A. Nevelteen, D. Deleersnijder, G. Dewaele, K. Seghers, J. Hendrickx, G. Stalpaert, The expanded polytetrafluorethylene (PTFE) graft as a vascular substitute., J Cardiovasc Surg (Torino) 21 (1980) 321–8.

[5] R.C. Kester, Reinforced Expanded Polytetrafluoroethylene (Gore-Tex) Grafts for Haemodialysis, Biomater Med Devices Artif Organs 6 (1978) 331–340. https://doi.org/10.3109/10731197809119792.

[6] S.G. Friedman, R.S. Lazzaro, L.N. Spier, C. Moccio, A.J. Tortolani, A prospective randomized comparison of Dacron and polytetrafluoroethylene aortic bifurcation grafts, Surgery 117 (1995) 7–17. https://doi.org/10.1016/S0039-6060(05)80223-5.

[7] J. Ji, H. Xu, C. Li, J. Luo, Small-Caliber Tissue-Engineered Vascular Grafts Based on Human-Induced Pluripotent Stem Cells: Progress and Challenges, Tissue Eng Part B Rev 29 (2023) 441–455. https://doi.org/10.1089/ten.teb.2023.0005.

[8] M.X. Li, Q.Q. Wei, H.L. Mo, Y. Ren, W. Zhang, H.J. Lu, Y.K. Joung, Challenges and advances in materials and fabrication technologies of small-diameter vascular grafts, Biomater Res 27 (2023). https://doi.org/10.1186/s40824-023-00399-2.

[9] A. Lejay, B. Bratu, S. Kuntz, N. Neumann, F. Heim, N. Chakfé, Calcification of Synthetic Vascular Grafts: A Systematic Review, EJVES Vasc Forum 60 (2023) 1–7. https://doi.org/10.1016/j.ejvsvf.2023.05.013.

[10] R. Zizhou, X. Wang, S. Houshyar, Review of Polymeric Biomimetic Small-Diameter Vascular Grafts to Tackle Intimal Hyperplasia, ACS Omega 7 (2022) 22125–22148. https://doi.org/10.1021/acsomega.2c01740.

[11] J.M.M. Heyligers, H.J.M. Verhagen, J.I. Rotmans, C. Weeterings, P.G. de Groot, F.L. Moll, T. Lisman, Heparin immobilization reduces thrombogenicity of small-caliber expanded polytetrafluoroethylene grafts, J Vasc Surg 43 (2006) 587–591. https://doi.org/10.1016/j.jvs.2005.10.038.

[12] A. Venault, Y. Chang, H.-H. Hsu, J.-F. Jhong, H.-S. Yang, T.-C. Wei, K.-L. Tung, A. Higuchi, J. Huang, Biofouling-resistance control of expanded poly(tetrafluoroethylene) membrane via atmospheric plasma-induced surface PEGylation, J Memb Sci 439 (2013) 48–57. https://doi.org/10.1016/j.memsci.2013.03.041.

[13] X. Ren, Y. Feng, J. Guo, H. Wang, Q. Li, J. Yang, X. Hao, J. Lv, N. Ma, W. Li, Surface modification and endothelialization of biomaterials as potential scaffolds for vascular tissue engineering applications, Chem Soc Rev 44 (2015) 5680–5742. https://doi.org/10.1039/C4CS00483C.

[14] B.D. Ratner, S.J. Bryant, Biomaterials: Where We Have Been and Where We Are Going, Annu Rev Biomed Eng 6 (2004) 41–75. https://doi.org/10.1146/annurev.bioeng.6.040803.140027.

[15] K. Amoako, R. Ukita, K.E. Cook, Antifouling Zwitterionic Polymer Coatings for Blood-Bearing Medical Devices, Langmuir 41 (2025) 2994–3006. https://doi.org/10.1021/acs.langmuir.4c04532.

[16] S. Jana, M. Roels, M.N. Leiske, Y. Bernhard, B.G. De Geest., K. Van Hecke, R. Hoogenboom, Poly(2-Hydroxymethyl-2-Oxazoline) as Super-Hydrophilic Antifouling Polymer, Angewandte Chemie International Edition 64 (2025). https://doi.org/10.1002/anie.202424873.

[17] Y. Zhuang, C. Zhang, M. Cheng, J. Huang, Q. Liu, G. Yuan, K. Lin, H. Yu, Challenges and strategies for in situ endothelialization and long-term lumen patency of vascular grafts, Bioact Mater 6 (2021) 1791–1809. https://doi.org/10.1016/j.bioactmat.2020.11.028.

[18] R.A. Hoshi, R. Van Lith, M.C. Jen, J.B. Allen, K.A. Lapidos, G. Ameer, The blood and vascular cell compatibility of heparin-modified ePTFE vascular grafts, Biomaterials 34 (2013) 30–41. https://doi.org/10.1016/j.biomaterials.2012.09.046.

[19] E. Luong-Van, L. Grøndahl, K.N. Chua, K.W. Leong, V. Nurcombe, S.M. Cool, Controlled release of heparin from poly(ε-caprolactone) electrospun fibers, Biomaterials 27 (2006) 2042–2050. https://doi.org/10.1016/j.biomaterials.2005.10.028.

[20] S. Aslani, M. Kabiri, S. HosseinZadeh, H. Hanaee-Ahvaz, E.S. Taherzadeh, M. Soleimani, The applications of heparin in vascular tissue engineering, Microvasc Res 131 (2020). https://doi.org/10.1016/j.mvr.2020.104027.

[21] C. Nie, L. Ma, C. Cheng, J. Deng, C. Zhao, Nanofibrous Heparin and Heparin-Mimicking Multilayers as Highly Effective Endothelialization and Antithrombogenic Coatings, Biomacromolecules 16 (2015) 992–1001. https://doi.org/10.1021/bm501882b.

[22] S.Y. Zhou, L. Li, E. Xie, M.X. Li, J.H. Cao, X. Bin Yang, D.Y. Wu, Small-diameter PCL/PU vascular graft modified with heparin-aspirin compound for preventing the occurrence of acute thrombosis, Int J Biol Macromol 249 (2023). https://doi.org/10.1016/j.ijbiomac.2023.126058.

[23] A.P. Rickel, X. Deng, D. Engebretson, Z. Hong, Electrospun nanofiber scaffold for vascular tissue engineering, Materials Science and Engineering C 129 (2021). https://doi.org/10.1016/j.msec.2021.112373.

[24] A. Hasan, A. Memic, N. Annabi, M. Hossain, A. Paul, M.R. Dokmeci, F. Dehghani, A. Khademhosseini, Electrospun scaffolds for tissue engineering of vascular grafts, Acta Biomater 10 (2014) 11–25. https://doi.org/10.1016/j.actbio.2013.08.022.

[25] J. Fernández-Pérez, K.A. van Kampen, C. Mota, M. Baker, L. Moroni, Flexible, Suturable, and Leak-free Scaffolds for Vascular Tissue Engineering Using Melt Spinning, ACS Biomater Sci Eng 9 (2023) 5006–5014. https://doi.org/10.1021/acsbiomaterials.3c00535.

[26] K.A. van Kampen, J. Fernández-Pérez, M. Baker, C. Mota, L. Moroni, Fabrication of a mimetic vascular graft using melt spinning with tailorable fiber parameters, Biomaterials Advances 139 (2022). https://doi.org/10.1016/j.bioadv.2022.212972.

[27] M.B. Browning, D. Dempsey, V. Guiza, S. Becerra, J. Rivera, B. Russell, M. Höök, F. Clubb, M. Miller, T. Fossum, J.F. Dong, A.L. Bergeron, M. Hahn, E. Cosgriff-Hernandez, Multilayer vascular grafts based on collagen-mimetic proteins, Acta Biomater 8 (2012) 1010–1021. https://doi.org/10.1016/j.actbio.2011.11.015.

[28] D. Radakovic, J. Reboredo, M. Helm, T. Weigel, S. Schürlein, E. Kupczyk, R.G. Leyh, H. Walles, J. Hansmann, A multilayered electrospun graft as vascular access for hemodialysis, PLoS One 12 (2017). https://doi.org/10.1371/journal.pone.0185916.

[29] F. Han, X. Jia, D. Dai, X. Yang, J. Zhao, Y. Zhao, Y. Fan, X. Yuan, Performance of a multilayered small-diameter vascular scaffold dual-loaded with VEGF and PDGF, Biomaterials 34 (2013) 7302–7313. https://doi.org/10.1016/j.biomaterials.2013.06.006.

[30] E. Claes, J.M. Atienza, G. V. Guinea, F.J. Rojo, J.M. Bernal, J.M. Revuelta, M. Elices, Mechanical properties of human coronary arteries, in: 2010 Annual International Conference of the IEEE Engineering in Medicine and Biology Society, EMBC'10, 2010: pp. 3792–3795. https://doi.org/10.1109/IEMBS.2010.5627560.

[31] M.A. Hiob, S. She, L.D. Muiznieks, A.S. Weiss, Biomaterials and Modifications in the Development of Small-Diameter Vascular Grafts, ACS Biomater Sci Eng 3 (2017) 712–723. https://doi.org/10.1021/acsbiomaterials.6b00220.

[32] A.C. Gilotti, W. Nimlamool, R. Pugh, J.B. Slee, T.C. Barthol, E.A. Miller, L.J. Lowe-Krentz, Heparin responses in vascular smooth muscle cells involve cGMP-dependent protein kinase (PKG), J Cell Physiol 229 (2014) 2142–2152. https://doi.org/10.1002/jcp.24677.

[33] J. Cao, X. Geng, J. Wen, Q. Li, L. Ye, A. Zhang, Z. Feng, L. Guo, Y. Gu, The penetration and phenotype modulation of smooth muscle cells on surface heparin modified poly(ε-caprolactone) vascular scaffold, J Biomed Mater Res A 105 (2017) 2806–2815. https://doi.org/10.1002/jbm.a.36144.

[34] J. Liu, C. Jiang, X. Ma, L. Feng, J. Wang, Z. Peng, Notoginsenoside Fc Accelerates Reendothelialization following Vascular Injury in Diabetic Rats by Promoting Endothelial Cell Autophagy, J Diabetes Res 2019 (2019). https://doi.org/10.1155/2019/9696521.

[35] C. He, J. Li, N. Xu, R. Wang, Z. Li, L. Yang, Z. Wang, Pharmacokinetics, bioavailability, and metabolism of Notoginsenoside Fc in rats by liquid chromatography/electrospray ionization tandem mass spectrometry, J Pharm Biomed Anal 109 (2015) 150–157. https://doi.org/10.1016/j.jpba.2015.02.038.

[36] Y. Liu, T. Liu, K. Ding, Z. Liu, Y. Li, T. He, W. Zhang, Y. Fan, W. Ma, L. Cui, X. Song, Phospholipase Cγ2 signaling cascade contribute to the antiplatelet effect of notoginsenoside Fc, Front Pharmacol 9 (2018). https://doi.org/10.3389/fphar.2018.01293.

[37] J. Zhang, Y. Wang, Y. Sun, Z. Zhou, F. Liu, X. Zhang, C. Kong, J. Yuan, M. Yin, D. Wang, Bilayer vascular grafts incorporated with S-nitrosated keratin nanoparticles and resveratrol to enhance long-term nitric oxide release and endothelialization, Acta Biomater 203 (2025) 291–305. https://doi.org/10.1016/j.actbio.2025.07.060.

[38] S. Asadpour, H. Yeganeh, F. Khademi, H. Ghanbari, J. Ai, Resveratrol-loaded polyurethane nanofibrous scaffold: viability of endothelial and smooth muscle cells, Biomedical Materials 15 (2019) 015001. https://doi.org/10.1088/1748-605X/ab4e23.

[39] Z. Yang, Y. Yang, K. Xiong, X. Li, P. Qi, Q. Tu, F. Jing, Y. Weng, J. Wang, N. Huang, Nitric oxide producing coating mimicking endothelium function for multifunctional vascular stents, Biomaterials 63 (2015) 80–92. https://doi.org/10.1016/j.biomaterials.2015.06.016.

[40] K.A. Amoako, C. Archangeli, H. Handa, T. Major, M.E. Meyerhoff, G.M. Annich, R.H. Bartlett, Thromboresistance characterization of extruded nitric oxide-releasing silicone catheters, ASAIO Journal 58 (2012) 238–246. https://doi.org/10.1097/MAT.0b013e31824abed5.

[41] T.C. Major, D.O. Brant, C.P. Burney, K.A. Amoako, G.M. Annich, M.E. Meyerhoff, H. Handa, R.H. Bartlett, The hemocompatibility of a nitric oxide generating polymer that catalyzes S-nitrosothiol decomposition in an extracorporeal circulation model, Biomaterials 32 (2011) 5957–5969. https://doi.org/10.1016/j.biomaterials.2011.03.036.

[42] H. Zhang, G.M. Annich, J. Miskulin, K. Osterholzer, S.I. Merz, R.H. Bartlett, M.E. Meyerhoff, Nitric oxide releasing silicone rubbers with improved blood compatibility: preparation, characterization, and in vivo evaluation, 2002.

Chapter 8
Thesis Impact

This chapter examines the scientific, economic, and societal implications of this research, emphasizing its contribution to sustainable biomaterial innovation and the development of clinically applicable small-caliber vascular grafts.

Natural Bioactive Molecules: Driving Innovation and Sustainable Solutions

Natural molecules have long served as the cornerstone of modern pharmacology. Among these natural discoveries, aspirin is one of the most remarkable examples. Originating from willow bark (*Salix alba*), used for over 3,500 years as a natural remedy for pain and fever, it was later isolated and synthesized as acetylsalicylic acid in 1897 and became one of the world's most widely used drugs. Its evolution, from a traditional plant extract to a cornerstone of modern medicine, perfectly illustrates how nature's chemistry continues to inspire therapeutic innovation [1]. Just a few decades after aspirin's emergence, another natural discovery revolutionized healthcare: the accidental identification of *Penicillium notatum* by Alexander Fleming in 1928, which led to the birth of penicillin [2], the moment when humanity learned to harness nature's own defense mechanisms to combat infection. Penicillin changed the course of human history, opening the antibiotic era and redefining the boundaries of survival and healing.

Together, these landmark discoveries illustrate how nature has long been the world's greatest chemist, offering molecular blueprints of extraordinary complexity and efficacy. Even today, natural products remain a vast and largely untapped reservoir of bioactive molecules, refined through millions of years of evolution. Their study continues to inspire modern biotechnology, guiding us toward new therapeutic frontiers and sustainable innovations in human health with molecules shaped by thousands of years of evolution.

Modern research tools, such as high-throughput screening platforms, combinatorial chemistry, and robotic automation, allow for the systematic exploration of this molecular diversity, enabling the identification and application of natural compounds with unprecedented efficiency. Among the diverse biological sources, marine organisms occupy a particularly promising position. Marine biodiversity, including sponges, algae, and echinoderms such as holothurians (sea cucumbers), harbors unique metabolites evolved under extreme environmental conditions, resulting in bioactivities rarely found in terrestrial sources. These marine-derived compounds not only offer new therapeutic opportunities but also align with the principles of the blue economy, fostering sustainable innovation through the responsible use of marine resources.

Beyond their biomedical potential, these natural compounds can contribute to bioremediation and economic diversification, promoting eco-sustainable

models of development. For instance, valorizing marine by-products or cultivating bioactive species could support local economies while restoring marine ecosystems. This circular approach, where environmental conservation and biotechnological innovation reinforce each other, represents an emerging frontier in sustainable biotechnology.

In this thesis, natural bioactive molecules were harnessed to improve key functional properties required for the development of effective small-caliber vascular grafts. This research provides an innovative strategy to engineer vascular devices that could generate substantial economic and healthcare impact.

Cardiovascular diseases remain the leading cause of mortality worldwide, with almost half a million patients requiring coronary artery bypass graft (CABG) procedures each year [3,4], and the demand continues to rise due to aging populations, sedentary lifestyles, pollution, and genetic predispositions. However, the limited availability of autologous vessels and the poor long-term outcomes of synthetic grafts create a pressing need for readily available, bioresorbable, and functional vascular substitutes.

The development of an off-the-shelf, bioresorbable vascular graft, capable of immediate implantation, physiological remodeling, and integration with host tissue, could transform the clinical landscape. Such a solution would not only reduce surgical complexity and healthcare costs but also save lives in emergency settings where autologous grafts are unavailable or unsuitable.

The following sections of this chapter examine in detail the scientific, technological, biomedical, societal, and environmental impacts of this work, outlining how the integration of natural bioactive molecules and advanced biofabrication strategies contributes to both the progress of vascular tissue engineering and the promotion of sustainable biotechnology.

Scientific and Technological Impact

This thesis advances the field of vascular tissue engineering by introducing innovative biofunctionalization strategies that integrate natural bioactive molecules with advanced scaffold fabrication technologies. The incorporation of marine sulfated polysaccharides (MSPs) and Notoginsenoside Fc (NgFc) into bioresorbable tissue-engineered vascular grafts (TEVGs) represents a novel and promising contribution to the field. Combined with hybrid biofabrication methods, specifically electrospinning and 4-axis printing, these approaches enabled the design of multilayered scaffolds that mimic the structural hierarchy of native vessels, combining mechanical robustness,

controlled porosity supporting cells infiltration across different scaffold layers, and biological functionality.
From a scientific standpoint, this work provides new insights into the interplay between material bioactivity, hemocompatibility, and vascular cell behavior. MSPs were shown not only to reduce platelet adhesion but also to promote endothelialization, while maintaining smooth muscle cells contractile phenotype. Meanwhile, NgFc emerged as a promising natural molecule capable of enhancing both hemocompatibility and endothelialization. Together, these findings highlight the potential of natural compounds to enhance biomaterial performance by modulating cell–material interactions in a biologically inspired and sustainable manner.
Technologically, this work demonstrates the potential of combining electrospinning and 4-axis printing to create scaffolds with precisely controlled mechanical and architectural properties. This hybrid strategy bridges the gap between structure and function, providing a versatile and tunable platform adaptable to various vascular applications. Moreover, the modularity of this system opens the possibility of incorporating other bioactive agents or tailoring scaffold designs for different vessel types, from veins to arteries, representing a scalable path toward clinically relevant devices.

Biomedical and Clinical Impact

According to the American Heart Association, global deaths from cardiovascular diseases have increased substantially, rising from over 12 million in 1990 to more than 19 million in 2021, with approximately 46% of these deaths attributable to ischemic heart disease (mainly due to coronary artery disease) [5]. However, when focusing on high-income countries (e.g. Australia, Austria, Belgium, Canada, France, Germany, Italy, Japan, the United Kingdom, and the United States, The Netherlands, among others), an opposite trend is observed. In these nations, cardiovascular-related deaths have decreased from 3,165,240 in 1990 to 2,883,088 in 2021, with approximately 75% of these deaths attributable to ischemic heart disease [5]. This decline highlights the impact of preventive measures targeting behavioral and environmental risk factors. Improvements in diet, smoking cessation (including the reduction of secondhand smoke exposure), moderation of alcohol intake, and promotion of physical activity, together with better control of environmental risks such as air pollution, temperature extremes, and lead exposure, have collectively contributed to this reduction. Notably, household air pollution—still a major global environmental risk for cardiovascular

disease—is almost absent in high-income regions, underlining the importance of socioeconomic and infrastructural factors in prevention outcomes.

Despite these advances, cardiovascular diseases remain the leading cause of mortality worldwide, and surgical interventions continue to face significant challenges. One of the most persistent problems in cardiovascular surgery is the lack of a reliable small-caliber vascular graft suitable for long-term implantation. Although modern medicine and therapeutic resources have greatly reduced mortality and morbidity through pharmacological and surgical advancements, the absence of an effective artificial conduit for vessels smaller than 6 mm remains a major limitation. Current synthetic grafts, such as expanded polytetrafluoroethylene (ePTFE) and polyethylene terephthalate (PET) [6], frequently fail in small-diameter applications due to thrombosis, compliance mismatch, and partial endothelialization, resulting in graft occlusion and poor long-term patency. Similarly, tissue-engineered vascular grafts (TEVGs) have not yet achieved consistent clinical performance, as they still require substantial improvement in terms of cellular colonization, hemocompatibility, mechanical compliance, and controlled biodegradation. Consequently, surgical revascularization in small vessels still relies on autologous grafts, restricting treatment options for patients lacking suitable donor vessels.

The scaffolds developed in this thesis address these challenges through the synergistic integration of bioactive molecules and structural design, representing a new generation of regenerative vascular substitutes. By promoting rapid endothelialization and balanced smooth muscle cell organization, these scaffolds have the potential to reduce thrombosis and enhance long-term graft patency. Such features are essential for achieving functional remodeling, enabling the gradual degradation of the scaffold while supporting the formation of native-like vascular tissue. Clinically, these innovations could decrease the need for repeated interventions, improve long-term patient outcomes, and broaden the scope of treatable cardiovascular conditions. Furthermore, the translational potential of this approach extends beyond vascular grafts: natural bioactive molecules such as MSPs and NgFc could be incorporated into stent coatings, vascular patches, or other implantable devices, thereby expanding their clinical applicability and facilitating progressive integration into existing cardiovascular therapies.

Economic, Societal, and Environmental Impact

From an economic standpoint, cardiovascular diseases (CVDs) represent not only the leading cause of mortality worldwide but also one of the greatest financial burdens on healthcare systems. In the United States alone, the total cost of CVDs in 2021 was estimated at $417.9 billion, including both direct and indirect expenses. Of this, $233.3 billion corresponded to direct costs, including expenditures for physicians, hospital and clinical services, prescribed medications, and home health care. By comparison, the direct costs associated with all neoplasms (cancers) in the same year were $173.3 billion, underscoring the substantial economic weight of cardiovascular disease. The remaining $184.6 billion represented indirect costs, primarily due to lost productivity from premature cardiovascular-related deaths, that is, the economic value of work and societal contributions lost due to early mortality from CVD [5].

The development of reliable small-caliber vascular grafts could therefore have a significant economic impact. By reducing the need for repeat surgeries and eliminating secondary harvesting procedures to obtain autologous vessels for coronary or peripheral bypass operations, healthcare costs could be substantially lowered. Beyond the direct savings from shorter operative times and fewer complications, indirect economic benefits would also arise from faster patient recovery, reduced long-term morbidity, and improved quality of life. This will collectively decrease the overall financial burden of cardiovascular disease on both patients and healthcare systems.

From a market perspective, the global vascular graft market, within which small-caliber grafts represent a clinically critical yet commercially challenging segment, is projected to reach USD 1.7–2.8 billion by 2030, depending on the source and market definition, with steady compound annual growth rates expected over the next decade [7].

Major commercial products dominating clinical practice for large and some small-diameter bypasses include heparin-bonded ePTFE grafts, such as *GORE® PROPATEN®* (W. L. Gore & Associates), available in diameters of 4–8 mm and currently indicated for peripheral artery disease [8]; biologic conduits such as *Artegraft® Collagen Vascular Graft* (LeMaitre), based on heparin coating but contraindicated for venous or low-pressure systems [9]; and emerging tissue-engineered solutions like *Humacyte's Human Acellular Vessel (HAV)*, which is progressing through regulatory pathways for small-diameter applications and currently approved by the FDA only for vascular trauma repair [10].

Our NgFc- and MSP-functionalized multilayer scaffolds differ from these existing solutions on several practical and mechanistic fronts, underscoring their translational and economic potential. First, MSP functionalization preserves hemocompatibility while promoting balanced endothelialization and contractile SMC colonization, key factors associated with improved long-term patency in preclinical models. Second, unlike biologic xenografts derived from animal tissues or complex cell-based products, MSPs and NgFc are renewable, naturally derived molecules (from marine and plant sources), offering a lower-cost, scalable, and ethically favorable supply chain that reduces dependence on mammalian-derived materials. Third, the hybrid fabrication approach (electrospinning + 4-axis printing) enables layer-specific and selective functionalization, for instance, antithrombogenic cues on the luminal surface combined with pro-regenerative signals in the medial layer. This design allows a single construct to address multiple failure modes (thrombosis, compliance mismatch, and poor medial remodeling) that conventional single-material grafts cannot. Collectively, these attributes could translate into clinical advantages, reduced graft failure rates and fewer reinterventions, as well as economic value through lower lifetime treatment costs and decreased need for autologous vessel harvesting, thereby reducing both direct surgical expenses and broader indirect costs linked to lost productivity.

Beyond their scientific and clinical significance, the strategies developed in this thesis embody a sustainable and ethical approach to biomaterials research. By sourcing bioactive compounds from marine and plant origins, this work reduces reliance on animal-derived materials such as heparin, providing safer, renewable, and ethically responsible alternatives. This direction aligns with the global transition toward a bio-based circular economy, where renewable biological resources are leveraged to produce health-related materials and technologies in environmentally and socially sustainable ways.

Within this context, marine biotechnology may emerge as a key enabler, bridging marine resource valorization, ecosystem restoration, and biomedical innovation within an integrated framework (figure 8.1). The use of MSPs not only promotes environmental sustainability through responsible utilization of marine biomass but also enhances economic and ethical value via renewable sourcing and reduced dependence on animal tissues.

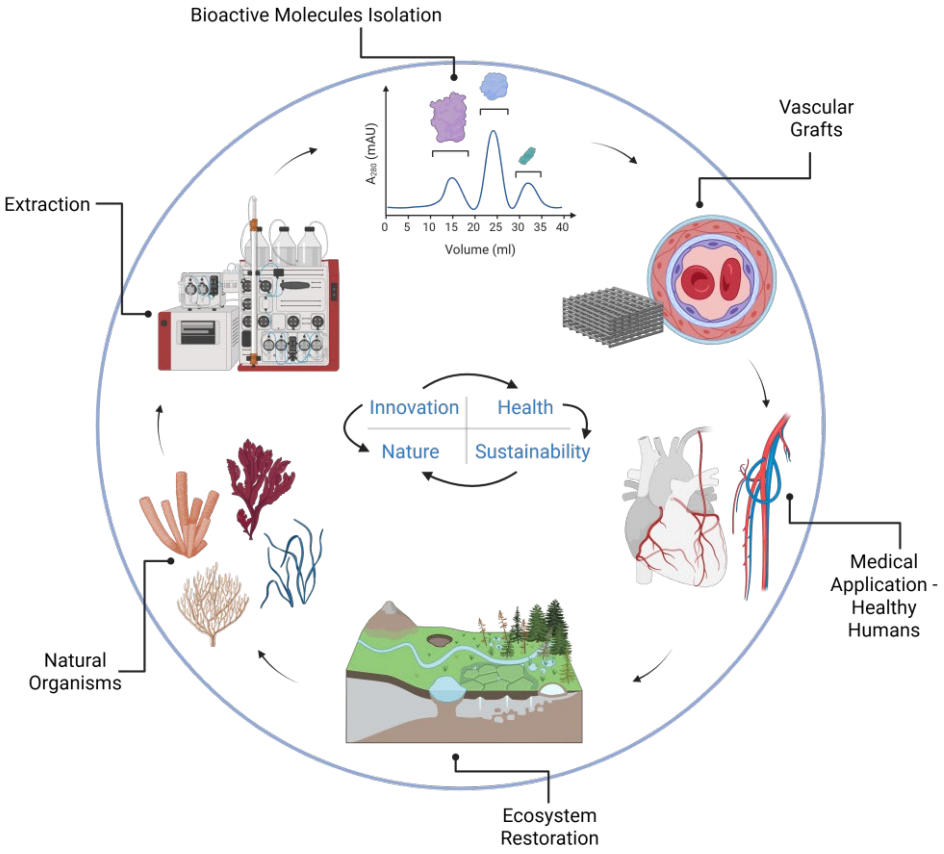

Figure 8.1. Schematic representation of the circular bioeconomy linking natural resources, bioactive molecule isolation, biomedical device fabrication, and ecosystem restoration.

References

[1] M.R. Montinari, S. Minelli, R. De Caterina, The first 3500 years of aspirin history from its roots – A concise summary, Vascul Pharmacol 113 (2019) 1–8. https://doi.org/10.1016/j.vph.2018.10.008.

[2] J.W. Bennett, K.-T. Chung, Alexander Fleming and the discovery of penicillin, in: 2001: pp. 163–184. https://doi.org/10.1016/S0065-2164(01)49013-7.

[3] R. Ramsingh, F.G. Bakaeen, Coronary artery bypass grafting: Practice trends and projections, Cleve Clin J Med 92 (2025) 181–191. https://doi.org/10.3949/ccjm.92a.23071.

[4] B.J. Bachar, B. Manna, Coronary Artery Bypass Graft, 2025.

[5] S.S. Martin, A.W. Aday, N.B. Allen, Z.I. Almarzooq, C.A.M. Anderson, P. Arora, C.L. Avery, C.M. Baker-Smith, N. Bansal, A.Z. Beaton, Y. Commodore-Mensah, M.E. Currie, M.S.V. Elkind, W. Fan, G. Generoso, B.B. Gibbs, D.G. Heard, S. Hiremath, M.C. Johansen, D.S. Kazi, D. Ko, M.H. Leppert, J.W. Magnani, E.D. Michos, M.E. Mussolino, N.I. Parikh, S.M. Perman, M. Rezk-Hanna, G.A. Roth, N.S. Shah, M. V. Springer, M.-P. St-Onge, E.L. Thacker, S.M. Urbut, H.G.C. Van Spall, J.H. Voeks, S.P. Whelton, N.D. Wong, S.S. Wong, K. Yaffe, L.P. Palaniappan, 2025 Heart Disease and Stroke Statistics: A Report of US and Global Data From the American Heart Association, Circulation 151 (2025). https://doi.org/10.1161/CIR.0000000000001303.

[6] P. Zilla, D. Bezuidenhout, P. Human, Prosthetic vascular grafts: Wrong models, wrong questions and no healing, Biomaterials 28 (2007) 5009–5027. https://doi.org/10.1016/j.biomaterials.2007.07.017.

[7] Inc. Grand View Research, Vascular Grafts Market (2024 - 2030), San Francisco, 2024. https://www.grandviewresearch.com/industry-analysis/vascular-graft-market?utm_source=chatgpt.com (accessed October 27, 2025).

[8] Gore (or W. L. Gore & Associates), GORE® PROPATEN® Vascular Graft. https://www.goremedical.com/products/propaten (accessed October 27, 2025).

[9] LeMaitre Vascular, ArteGraft Collagen Vascular Graft. https://www.lemaitre.com/products/artegraft-collagen-vascular-graft (accessed October 27, 2025).

[10] Inc. Humacyte, Acellular Tissue Engineered Vessels. https://humacyte.com/acellular-tissue-engineered-vessels/?utm_source=chatgpt.com (accessed October 27, 2025).

Appendix

Summary

Bioinspired by Nature, Designed for Flow: Engineering Functional Interfaces for Small-Caliber Vascular Grafts—the title of this PhD thesis—captures the guiding philosophy of the work and frames a coherent, progressive scientific journey driven by a single central question: how can synthetic small-caliber vascular grafts be engineered by drawing inspiration from nature to create instructive biointerfaces capable of guiding hemocompatibility, vascular regeneration, and long-term functionality under physiological flow conditions?

The thesis begins by reframing small-caliber vascular graft failure as a problem of disrupted flow at multiple levels. Early thrombosis, insufficient endothelialization, intimal hyperplasia, and compliance mismatch are not treated as isolated failure modes, but as interconnected consequences of non-physiological interactions among blood flow, vascular cells, and synthetic materials. This perspective highlights that successful graft design must simultaneously regulate blood–material interactions, cellular organization, and mechanical responses to pulsatile flow.

Within this framework, marine sulfated polysaccharides (MSPs) are identified as bioinspired candidates capable of restoring key aspects of the native endothelial interface. Rather than acting solely as anticoagulants, MSPs emerge as multifunctional molecules able to modulate coagulation cascades, platelet adhesion, endothelial behavior, inflammation, and growth factor signaling.

The thesis then focuses on the purification and characterization of sulfated polysaccharides extracted from *Holothuria tubulosa* and *Sarcotragus spinosulus*. The pronounced heterogeneity observed among the isolated polysaccharides fractions underscores the necessity of molecular control to ensure reproducible bioactivity under dynamic conditions. This stage represents a critical design checkpoint, leading to the selection of specific fractions that combine strong anticoagulant activity with cytocompatibility and are suitable for integration into flow-exposed biomaterial systems.

The preservation of MSPs bioactivity following immobilization onto biomaterial surfaces was first evaluated using electrospun polycaprolactone (PCL) scaffolds as a well-defined platform. By minimizing architectural complexity, this step isolates the contribution of the luminal biointerface to

hemocompatibility and endothelialization. The results demonstrate that MSPs-functionalized surfaces retain anticoagulant function, reduce platelet adhesion, and promote rapid formation of a confluent endothelial monolayer—an essential prerequisite for establishing a stable, flow-aligned endothelium.

Building upon these findings, the thesis advances toward graft designs that explicitly couple biological performance with flow-driven mechanical demands. By combining electrospinning and four-axis printing, multilayered vascular grafts were engineered to reproduce a biomimetic architecture inspired by the native vessel wall, enabling physiological deformation while maintaining structural integrity. This hierarchical design allows independent tuning of mechanical properties to meet the specific requirements of different vascular beds, while simultaneously promoting correct cellular organization through controlled fiber alignment and layer-specific porosity. Together, these features reflect the structural and functional hierarchy of native blood vessels.

In addition to the finely tuned and modular architecture, functionalization with MSPs enables a uniquely balanced integration of hemocompatibility and cellular colonization by combining potent anticoagulant and antithrombotic activity with rapid and stable endothelialization, while also supporting smooth muscle cell alignment and maintenance of a contractile phenotype. This coordinated regulation of blood–material interactions and vascular cell behavior enables the regeneration of a functional vessel wall capable of adapting dynamically to physiological flow conditions. In this context, MSPs function not merely as antithrombotic agents, but as instructive biointerfaces that harmonize hemocompatibility, vascular regeneration, and mechanical adaptation.

The concept of designed for flow is further extended through the exploration of complementary natural bioactive molecules. In the final study of this thesis, Notoginsenoside Fc—a triterpenoid saponin isolated from *Panax notoginseng*—is investigated as a controlled-release component within PCL-based vascular grafts. Its incorporation enables the temporal modulation of thrombogenic responses and endothelialization, introducing a dynamic layer of bioactivity that evolves alongside graft integration. This approach provides an additional modular strategy for functionalizing vascular grafts, which can be employed either independently or in combination with other bioactive tools, such as MSPs.

The concluding chapters expands the scope of this work beyond experimental validation to consider its broader scientific, societal, and economic implications. Cardiovascular diseases remain the leading cause of mortality worldwide, and the lack of reliable small-caliber vascular grafts continues to impose a substantial clinical and economic burden. Graft failure due to thrombosis or intimal hyperplasia leads to repeated surgical interventions, prolonged hospitalization, lifelong pharmacological management, and reduced quality of life for patients. In this context, the development of vascular grafts that actively promote hemocompatibility and regeneration under physiological flow conditions represents not only a scientific challenge, but a pressing societal need.

The use of surface-bound bioactivity offers a translationally realistic strategy that is compatible with scalable manufacturing and regulatory requirements. Such material-driven solutions may ultimately enable more durable and economically sustainable vascular repair technologies.

Finally, this work highlights the largely untapped potential of natural molecules as a resource for regenerative medicine. Shaped by millions of years of evolution, natural compounds—such as marine sulfated polysaccharides and plant-derived saponins—encode complex biological functions that remain only partially explored. This vast and still underinvestigated molecular reservoir offers powerful opportunities to discover new bioactive cues capable of instructing tissue regeneration and guiding biomaterial performance in ways that synthetic systems alone cannot yet replicate.

Sumenvatting

Bio-geïnspireerd door de natuur, ontworpen voor stroming: het ontwikkelen van functionele interfaces voor kleine diameter vaatprotheses.—de titel van dit proefschrift—vat de leidende filosofie van het werk samen en omvangt een samenhangende en progressieve wetenschappelijke reis, gedreven door één centrale vraag: hoe kunnen synthetische vaatprothesen met een kleine diameter worden ontworpen door inspiratie te vergaren uit de natuur, om instructieve bio-interfaces te creëren die hemocompatibiliteit, vasculaire regeneratie en langdurige functionaliteit onder fysiologische stromingscondities sturen?

Het proefschrift begint met het herdefiniëren van het falen van kleine-diameter vaatprothesen als een probleem van verstoorde stroming op meerdere niveaus. Vroege trombose, onvoldoende endothelialisatie, intima-hyperplasie en een mismatch in compliantie worden niet beschouwd als geïsoleerde mechanismen, maar als onderling verbonden gevolgen van niet-fysiologische interacties tussen bloedstroming, vasculaire cellen en synthetische materialen. Dit perspectief benadrukt dat een succesvol ontwerp van vaatprotheses gelijktijdig bloed–materiaalinteracties, cellulaire organisatie en mechanische responsen op pulserende stroming moet reguleren.

Binnen dit kader worden mariene gesulfateerde polysachariden (MSPs) geïdentificeerd als bio-geïnspireerde kandidaten die in staat zijn essentiële aspecten van de natuurlijke endothele interface te herstellen. In plaats van uitsluitend als anticoagulant te functioneren, blijken MSPs multifunctionele moleculen te zijn die stollingscascades, bloedplaatjesadhesie, vorming van het endotheel, ontstekingsprocessen en groeifactorsignalering kunnen moduleren. Hun structurele gelijkenis met natuurlijke glycosaminoglycanen suggereert een unieke capaciteit om stromingsadaptieve biologische signalen aan het bloed–materiaalinterface te reconstrueren.

Aangezien door stroming gemedieerde biologische responsen sterk afhankelijk zijn van moleculaire presentatie, richt het proefschrift zich vervolgens op de zuivering en karakterisering van gesulfateerde polysachariden afkomstig van *Holothuria tubulosa* en *Sarcotragus spinosulus*. De uitgesproken heterogeniteit die tussen de geïsoleerde fracties wordt waargenomen, benadrukt de noodzaak van moleculaire controle om reproduceerbare bioactiviteit onder dynamische omstandigheden te waarborgen. Deze fase vormt een cruciaal ontwerpmoment en leidt tot de selectie van specifieke fracties die sterke anticoagulerende activiteit combineren met

cytocompatibiliteit, en geschikt zijn voor integratie in aan stroming blootgestelde biomateriaalsystemen.
Het behoud van MSPs-bioactiviteit na immobilisatie op biomateriaaloppervlakken werd voor het eerst geëvalueerd met behulp van elektrogesponnen polycaprolacton (PCL)-scaffolds als een goed gedefinieerd platform. Door de architecturale complexiteit te minimaliseren, wordt in deze stap de bijdrage van de luminale bio-interface aan hemocompatibiliteit en endothelialisatie geïsoleerd. De resultaten tonen aan dat met MSP gefunctionaliseerde oppervlakken hun anticoagulerende functie behouden, bloedplaatjesadhesie verminderen en de snelle vorming van een confluente endotheliale monolaag bevorderen, een essentiële voorwaarde voor het ontstaan van een stabiel, aan stroming georiënteerd endotheel.
Voortbouwend op deze bevindingen beweegt het proefschrift zich richting vaatprothesen waarvan het ontwerp expliciet biologische prestaties koppelt aan stromingsgedreven mechanische eisen. Door elektrospinning te combineren met vierassig 3D-printen werden meerlaagse vaatprotheses ontwikkeld die een biomimetische architectuur reproduceren, geïnspireerd op de natuurlijke vaatwand, en die fysiologische vervorming mogelijk maken met behoud van structurele integriteit. Dit hiërarchische ontwerp maakt het mogelijk mechanische eigenschappen onafhankelijk af te stemmen op de specifieke vereisten van verschillende vaatbedden, terwijl tegelijkertijd correcte cellulaire organisatie wordt bevorderd via gecontroleerde vezeluitlijning en laag-specifieke porositeit. Samen weerspiegelen deze kenmerken de structurele en functionele hiërarchie van natuurlijke bloedvaten.
Naast de fijn afgestemde en modulaire architectuur maakt functionalisatie met MSP's een uniek gebalanceerde integratie van hemocompatibiliteit en cellulaire kolonisatie mogelijk, door krachtige anticoagulerende en antitrombotische activiteit te combineren met snelle en stabiele endothelialisatie, terwijl de uitlijning van gladde spiercellen en het behoud van een contractiel fenotype worden ondersteund. Deze gecoördineerde regulatie van bloed–materiaalinteracties en vasculair celgedrag maakt de regeneratie mogelijk van een functionele vaatwand die zich dynamisch kan aanpassen aan fysiologische stromingscondities. In deze context functioneren MSPs niet louter als antitrombotische agentia, maar als instructieve bio-interfaces die hemocompatibiliteit, vasculaire regeneratie en mechanische adaptatie harmoniseren.
Het concept designed for flow wordt verder uitgebreid door de verkenning van complementaire natuurlijke bioactieve moleculen. In de laatste studie van dit

proefschrift wordt Notoginsenoside Fc, een triterpenoïde saponine geïsoleerd uit Panax notoginseng, onderzocht als een gecontroleerd afgiftecomponent binnen PCL-gebaseerde vaatprothesen. De incorporatie ervan maakt temporele modulatie van trombogene responsen en endothelialisatie mogelijk en introduceert een dynamische laag van bioactiviteit die zich ontwikkelt parallel aan de integratie van de prothese. Deze benadering biedt een aanvullende modulaire strategie voor de functionalisatie van vaatprothesen, die zowel zelfstandig als in combinatie met andere bioactieve hulpmiddelen, zoals MSPs, kan worden toegepast.

De afsluitende hoofdstukken verbreden de reikwijdte van dit werk voorbij experimentele validatie en beschouwen de bredere wetenschappelijke, maatschappelijke en economische implicaties. Cardiovasculaire aandoeningen blijven wereldwijd de belangrijkste doodsoorzaak, en het ontbreken van betrouwbare kleine-diameter vaatprothesen legt een aanzienlijke klinische en economische last op de gezondheidszorg. Prothesefalen als gevolg van trombose of intima-hyperplasie leidt tot herhaalde chirurgische ingrepen, langdurige ziekenhuisopnames, levenslange farmacologische behandeling en een verminderde kwaliteit van leven voor patiënten. In deze context vormt de ontwikkeling van vaatprothesen die actief hemocompatibiliteit en regeneratie bevorderen onder fysiologische stromingscondities niet alleen een wetenschappelijke uitdaging, maar ook een dringende maatschappelijke noodzaak.

Het gebruik van oppervlak-gebonden bioactiviteit biedt een translationeel realistische strategie die verenigbaar is met schaalbare productie en regulatoire vereisten. Dergelijke materiaalgedreven oplossingen kunnen uiteindelijk leiden tot duurzamere en economisch houdbare technologieën voor vasculaire reconstructie.

Tot slot benadrukt dit werk het grotendeels onbenutte potentieel van natuurlijke moleculen als bron voor regeneratieve geneeskunde. Gevormd door miljoenen jaren van evolutie, natuurlijke verbindingen zoals mariene gesulfateerde polysachariden en plantaardige saponinen, bevatten complexe biologische functies die tot op heden slechts gedeeltelijk zijn verkend. Dit omvangrijke en nog onvoldoende onderzochte moleculaire reservoir biedt krachtige kansen om nieuwe bioactieve signalen te ontdekken die weefselregeneratie kunnen sturen en biomateriaalprestaties kunnen beïnvloeden op manieren die synthetische systemen alleen nog niet kunnen evenaren.

Acknowledgements

Those who know me well know that this might be the most difficult part of the entire thesis for me to write, not because it matters any less, but because I have never been particularly good at expressing this kind of gratitude without worrying that I might forget something important to mention.
And yet, here I am, writing what is probably the only section that everyone will actually read. While the rest of this thesis may (understandably) remain unexplored by many of you, I am quite certain that most of you will, by strategically skipping ahead, make it to this page.

So, I will begin, as is tradition, by thanking my supervisors, **Lorenzo** and **Antonio**. Both of you have played an incredibly important role in my development as a scientist. More than anything, I would like to thank you for always being available to listen to my concerns, for your constant support, and for believing in my ideas — probably more than I believed in them myself at times.
Your guidance went far beyond scientific advice. You taught me how to think critically, how to face challenges with resilience, and how to remain curious even when experiments refused to cooperate. Even during moments when things were not going perfectly with my health, you continued to believe in me and support me with understanding and patience. Your trust, encouragement, and humanity allowed me to grow not only professionally, but personally. For that, I am deeply grateful.
I would also like to sincerely thank **my paranymphs**, **Tim** and **Tristan**. You have not only made my days at work lighter and more enjoyable, but you have also always been there whenever I needed help — in the lab and outside of it. Your support, availability, and friendship have meant a great deal to me throughout these years. You have been far more than colleagues; you have been true friends.

Finally, I would like to thank the members of the PhD committee for taking the time to read and evaluate this thesis. I truly appreciate your effort, attention, and the valuable insights you bring to this work.

Now I want to express my deepest gratitude to my family.
To my mother — who is probably the very first reason why I started a PhD, or pursued any form of study at all. She has always prioritized my sister's and my education above everything else, even above her own personal needs. She gave us the opportunity to follow the paths we truly wanted to pursue, supporting our ambitions with strength, sacrifice, and unconditional love. Without her vision and determination, none of this would have been possible.
To my father — who may not be a man of many words (a characteristic I might have inherited) — but who has always been present in his own way. He has never questioned my career choices, always trusting my decisions and stepping in quietly whenever support was needed. His steady presence has been a constant foundation throughout this journey.
And **to my sister, Alessia** — being your older brother has always felt like a great responsibility. At times, I felt I had to set an example: in behavior, in studying, in sports, and in life in general. But you found your own way, as we all do, somewhere between our dreams and the opportunities life places in front of us. You have always supported this PhD, and in a way, you were decisive in making it happen. It was four years ago, while I was working in another research lab on a fellowship, that you sent me that message: "Send me your CV," while you were doing your internship in a biochemistry lab in Sassari. They were looking for someone with experience in regenerative medicine and marine organisms. That message eventually led to this PhD opportunity. In many ways, this journey started with you.
And throughout these years, you have always been there, giving your opinion on figures for papers, listening to my frustrations, and sharing the small victories along the way. For that, and for so much more, thank you.

I would also like to thank my grandmothers and my grandfather, as well as my uncles, aunts, and cousins. Even if they never fully understood why I decided to leave the sun and the sea (and, to be honest, I still question that choice on certain rainy days), they were always proud of me and they have always wanted the very best for me and have supported me in their own loving ways. Whether through care packages filled with homemade sweets, or simply by being there every time I return home, they have reminded me where I come from and what truly matters. Their affection and constant encouragement have been a quiet but steady source of strength throughout this journey.

Riscrivo in Italiano per voi:
A mia madre — che è probabilmente la prima vera ragione per cui ho iniziato un dottorato, o intrapreso qualsiasi percorso di studi. Ha sempre messo l'istruzione mia e di mia sorella al primo posto, sopra ogni altra cosa, persino sopra i propri bisogni personali. Ci ha dato la possibilità di seguire i percorsi che desideravamo davvero intraprendere, sostenendo le nostre ambizioni con forza, sacrificio e amore incondizionato. Senza la sua visione e la sua determinazione, nulla di tutto questo sarebbe stato possibile.
A mio padre — che forse non è un uomo di molte parole (una caratteristica che potrei aver parzialmente ereditato) — ma che è sempre stato presente a modo suo. Non ha mai messo in discussione le mie scelte professionali, fidandosi delle mie decisioni ed intervenendo silenziosamente ogni volta che c'era bisogno di supporto. La sua presenza costante è stata una base solida lungo tutto questo percorso.
E a mia sorella, Alessia — essere tuo fratello maggiore è sempre stato per me una grande responsabilità. A volte ho sentito di dover dare l'esempio: nel comportamento, nello studio, nello sport e nella vita in generale. Ma tu hai trovato la tua strada, come tutti noi, in equilibrio tra i nostri sogni e le opportunità che la vita ci mette davanti. Hai sempre sostenuto questo dottorato e, in un certo senso, sei stata determinante nel renderlo possibile. È stato quattro anni fa quando, mentre lavoravo in un altro laboratorio di ricerca con una borsa di studio, che mi hai mandato quel messaggio: "Mandami il tuo CV", mentre stavi svolgendo il tuo tirocinio in un laboratorio di biochimica a Sassari. Cercavano qualcuno con esperienza in medicina rigenerativa e organismi marini. Quel messaggio ha poi portato a questa opportunità di dottorato. In molti modi, questo percorso è iniziato con te e da te.
E in tutti questi anni sei sempre stata presente, dandomi la tua opinione sulle figure degli articoli, ascoltando le mie frustrazioni e condividendo le piccole vittorie lungo il cammino. Per questo, e per molto altro, grazie.
Desidero inoltre ringraziare le mie nonne e mio nonno, così come i miei zii, le mie zie e i miei cugini e Kiki. Anche se non hanno mai compreso del tutto perché abbia deciso di lasciare il sole e il mare (e, ad essere onesto, me lo chiedo ancora anch'io in certe giornate di pioggia), sono sempre stati orgogliosi di me e hanno sempre voluto il meglio per me, sostenendomi a modo loro con affetto e presenza. Che fosse attraverso pacchi pieni di dolci fatti in casa o semplicemente con il loro esserci ogni volta che torno a casa, mi hanno

sempre ricordato da dove vengo e cosa conta davvero. Il loro affetto e il loro incoraggiamento costante sono stati una fonte silenziosa ma solida di forza lungo tutto questo percorso

To my lifelong friends, who have stayed close despite the distance not always making things easy: Dario, Alessandro, Davide, Cristian, and all my friends from Sorso, who are always ready to grab a coffee with me during those few days each year when I return to my hometown. Time and distance have never weakened our bond, and that is something rare and invaluable.
To my high school friends — Francesco, Giommaria, Luca, Dario, Matteo, Gabriele, Marco, Roberto, and Antonio — somehow, after all these years, we are still there every week commenting on the newest chapter of *One Piece*, a story we started reading together back in high school.
You have always been there when I needed support — whether it was help with the more engineering-oriented parts of my projects, motivation during difficult moments, or simply perspective when things felt overwhelming. Together, we have learned how to face challenges that life unexpectedly places in front of us — moments that test strength. In those times especially, I understood the value of having friends who do not step back when things become heavy.
You have given me strength and motivation in ways I may not have always expressed clearly, but that I have always deeply felt.

And to the more recent people I met during my PhD:

Fabiana, **Helena**, and **Nasia**, my very first friends in the Netherlands back in 2022. You all stayed at MERLN for only a short time, but you definitely left a lasting mark. The fact that we still organize summer vacations together, and sometimes even spontaneous trips, says everything about how deep that connection was from the very beginning.
And **Nasia** — what started as a friendship during those first months in a new country, unexpectedly became something much more. Two years later, you became my partner, sharing not only this PhD journey but also everyday life with me, multiple travels and many dramas that we faced together. Your presence has been a source of strength and happiness, especially during the most demanding moments. Having you by my side has made this experience richer in every possible way. Εσύ είσαι ο θησαυρός μου.

To the people who helped me so much at the beginning of my time in Maastricht, when I was desperately trying to find a decent place to live while also dealing with some health issues: **Carlotta**, **Sophia**, and **Helen**. Your support during that uncertain period meant more than I can properly express. And **Helen**, in particular, I will never forget the kindness you showed me, allowing me to stay in your apartment for almost a month without even seeing or knowing me.
And to all the fantastic friends and colleagues in the office and in the lab, who shared with me drama, gossip, frustrations, laughs, and countless scientific discussions over these years: **Jae**, **Adrian**, **Kike**, **Niccolò**, **Zhendong**, **Luo**, **Asli**, **Vini**, **Dorian**, **Tim**, **Tristan**, **Ines**, **Vivek**, **Liline**, **Pauline**, **Fangzhou**, **Jonathan**, **Leila**, **Marie**, **Alix**, **Joanna**, **Maria Kalogeropoulou**, **Maria Papageorgiou**, **Francesca Giacomini.**, **Alberto**, **David Baratta**, **David Dimech**, **Gabriele Addario**, **Ivo**, **Kenny**, **Clarissa, Carlos**. Thank you for making these years not only scientifically stimulating, but also deeply human. Also, big thanks to the people who stayed only for a short period but that left an important mark: **Marco**, **Beatrice**, **Pra**, **Noemi**, **Daniele**, **Gabriele Gaglio**, **Riccardo.**
Special thanks for the everyday support in the lab and with the many bureaucratic procedures to **Cristina**, **Claudia**, and **Gabriele Nieddu** from the biochemistry lab in Sassari, and to Prof. **Marilena Formato**, who was always actively involved in the final revision of my work.

And thanks to the people that I met more recently between the gym and the office, **Davide**, **Nicola**, **Ebrahim**.

Last but not least, my sincere appreciation to **Martijn** for helping me many times with my projects, for always being extremely positive, and for spreading positive energy around him

Each of you, in different ways, has shaped not only this work, but the person I have become throughout these years. For that, I am deeply and sincerely grateful.

Publications

Obino G, Sensini A, Ten Brink T, Nieddu G, Bodet T, Deiana GA, van Griensven M, Formato M, Lepedda AJ, Moroni L. Tunable Bioresorbable Scaffolds With Marine Sulfated Polysaccharides for Small-Caliber Vascular Grafts: A Multi-Layered Strategy Combining Electrospinning and 4-Axis Printing. Adv Healthc Mater. **2026** Feb 2:e05314. doi: 10.1002/adhm.202505314. Epub ahead of print. PMID: 41630198.

Obino G, Nieddu G, Nagy M, Ippel H, Cubeddu T, Spronk HMH, Hackeng TM, Formato M, Lepedda AJ, Moroni L. Marine-derived sulfated polysaccharides enhance hemocompatibility and endothelialization of nanofibrous PCL for vascular graft applications. Cell Biomaterials. **2025** Nov;1(10):100155. doi:10.1016/j.celbio.2025.100155

Nieddu G, **Obino G**, Ciampelli C, Brunetti A, Cubeddu T, Manconi R, Stocchino GA, Deiana GA, Formato M, Lepedda AJ. Purification of an Acidic Polysaccharide with Anticoagulant Activity from the Marine Sponge *Sarcotragus spinosulus*. Mar Drugs. **2024** Mar 21;22(3):139. doi: 10.3390/md22030139. PMID: 38535480; PMCID: PMC10971851.

Nieddu G, Michelucci E, Formato M, Ciampelli C, **Obino G**, Signore G, Di Giorgi N, Rocchiccioli S, Lepedda AJ. Molecular Characterization of Plasma HDL, LDL, and VLDL Lipids Cargos from Atherosclerotic Patients with Advanced Carotid Lesions: A Preliminary Report. Int J Mol Sci. **2022** Oct 18;23(20):12449. doi: 10.3390/ijms232012449. PMID: 36293312; PMCID: PMC9604033.

Biography

Gabriele Obino was born and raised in Sorso (Sassari), Italy. From an early age, he was driven by a deep curiosity about how things work and a strong fascination for science and innovation. This naturally led him to pursue a Bachelor's degree in Biotechnology. After graduating, he moved to Turin to continue his academic journey with a Master's degree in Industrial Biotechnology. During these years, he developed a strong interest in regenerative medicine and carried out his Master's thesis research at the National University of Ireland, Galway. He graduated in 2020, increasingly motivated by the potential of tissue engineering and translational biomedical research.

Following his Master's degree, Gabriele worked in biotechnology and microbiology, gaining hands-on laboratory experience and refining his scientific approach. Eager to deepen his expertise in regenerative medicine, he later enrolled in a double-degree PhD program between the University of Sassari and Maastricht University.

His doctoral research focused on the development of innovative bioresorbable scaffolds for small-caliber vascular grafts, combining electrospinning and advanced 3D printing techniques. His work bridges materials science, cell biology, and bioengineering, with the goal of improving hemocompatibility and promoting rapid and functional vascular regeneration.

Beyond the laboratory, sport and nature have always been essential parts of his life. Immersing himself in natural environments allows him to disconnect, reflect, and regain perspective. Observing the balance, adaptability, and efficiency of natural systems reinforces his belief that science should learn from biology itself. This connection to nature continues to inspire his work in regenerative medicine, where the ultimate aim is to support and restore the body's intrinsic capacity to heal.